

Study of the Massive O- and WR-stars and their Associated Winds

A
THESIS SUBMITTED
To
PT. RAVISHANKAR SHUKLA UNIVERSITY, RAIPUR
FOR
THE DEGREE OF DOCTOR OF PHILOSOPHY
IN
PHYSICS
UNDER THE FACULTY OF SCIENCE

INVESTIGATOR :

Bharti Arora

ARIES, NAINITAL – 263 001

SUPERVISOR :

Dr. Jeewan C. Pandey

(Scientist – E)

ARIES, Manora Peak

Nainital – 263 001

Uttarakhand

CO-SUPERVISOR :

Dr. Nand K. Chakradhari

(Senior Assistant Professor)

S.o.S. in Physics and

Astrophysics, Pt. R.S.U.,

Raipur – 492 010

2021

Research Centre

ARYABHATTA RESEARCH INSTITUTE OF OBSERVATIONAL
SCIENCES (ARIES)

MANORA PEAK, NAINITAL 263 001, INDIA

Declaration by Candidate

I declare that the thesis entitled *Study of the Massive O- and WR-stars and their Associated Winds* is my own work conducted under the supervision of **Dr. Jeewan C. Pandey** at **Aryabhata Research Institute of observational sciencES (ARIES), Nainital, Uttarakhand, India**, and co-supervision of **Dr. Nand K. Chakradhari** at **S.o.S. in Physics and Astrophysics, Pt. Ravishankar Shukla University, Raipur, Chhattisgarh, India** approved by the Research Degree Committee. I have put in more than 300 days of attendance excluding course work with the supervisor at the center.

I further declare that to the best of my knowledge the thesis does not contain any part of any work, which has been submitted for the award of any degree either in this University or in any other University/Deemed university without proper citation.


Bharti Arora

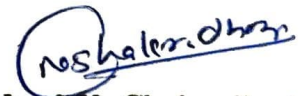
Signature of the Candidate



Dr. Jeewan C. Pandey

Signature of the Supervisor

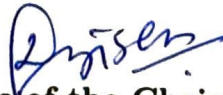
Scientist "E"
ARIES, Nainital



Dr. Nand K. Chakradhari

Signature of the Co-Supervisor

Dr. N.K. Chakradhari
(M.Sc., Ph.D., UGC-CSIR-NET)
Senior Assistant Professor
SoS in Physics & Astrophysics
Pt. Ravishankar Shukla University,
Raipur-492010, (CG) INDIA



Signature of the Chairman, DRC

CHAIRMAN,
Depos. Research Committee,
SoS in Physics & Astrophysics,
Pt. R.S. University, RAIPUR, (CG)



Director
Aryabhata Research Institute Of
Observational Sciences (ARIES)
(Under Department of Science & Technology)

Certificate by the Supervisor

This is to certify that the work entitled ***Study of the Massive O- and WR-stars and their Associated Winds*** is a piece of research work done by **Ms. Bharti Arora** under my guidance and supervision for the degree of Doctor of Philosophy in **PHYSICS** of Pt. Ravishankar Shukla University, Raipur (Chhattisgarh), India. The candidate has put in an attendance of more than 300 days excluding coursework with me.

To the best of my knowledge and belief this thesis

1. Embodies the work of the candidate herself.
2. Has duly been completed.
3. Fulfills the requirements of the Ordinance relating to the Ph.D. degree of the University;
and
4. Is up to the standard both in respect of contents and language for being referred to the examiner.

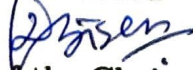


Dr. N.K. Chakradhari
(M.Sc., Ph.D., UGC-CSIR-NET)
Senior Assistant Professor
SoS in Physics & Astrophysics
Pt. Ravishankar Shukla University,
Raipur-492015, INDIA



Dr. Jeewan C. Pandey
Signature of the Supervisor
Scientist "E"
ARIES, Nainital

Forwarded



Signature of the Chairman, DRC

CHAIRMAN;
Dept. Research Committee
SoS in Physics & Astrophysics
Pt. Ravishankar Shukla University, RAIPUR, (CG)



Director
Aryabhata Research Institute Of
Observational Sciences (ARIES)
(Under Department of Science & Technology)

Declaration on Plagiarism

I declare that all materials in my thesis entitled "**Study of the Massive O- and WR-stars and their Associated Winds**" are my own work and do not involve plagiarism. I also certify that

a. No sentence, equation, diagram, table, paragraph or section has been copied verbatim from previous work unless it is placed under quotation marks and duly referenced.

b. The work presented is original and my own work. No ideas, processes, results or words of others have been presented as my own work.

c. Report on Plagiarism check is appended.

Raipur, Dated 22.07.2021

Bharti Arora
BHARTI ARORA
Name & Signature of the Candidate

Forwarded

P. S. Sen
22/07/2021
Chairman, DRC

CHAIRMAN,
Deptt. Research Commission
ICPS in Physics & Astrophysics
Jawahar University, RAIPUR, (CG)

D. Banerjee
Director
Aryabhata Research Institute Of
Observational Sciences (ARIES)
(Under Department of Science & Technology)

Urkund Analysis Result

Analysed Document: Study of the Massive O and WR_stars and their Associated Winds
(Bharti Arora).pdf (D110516196)
Submitted: 7/16/2021 1:44:00 PM
Submitted By: library_prsu@rediffmail.com
Significance: 3 %

Sources included in the report:

Thesis.pdf (D78786277)
BS_MS_thesis.pdf (D106209471)
Correlation between optical and X-ray variability of active galactic Nuclei by Pramod Karbhari
Pawar Ph.D. Physics..pdf (D26717830)
rapport.pdf (D11230138)
aditya_thesis.pdf (D40189901)
MSc_Thesis.pdf (D29557649)
MSc_Thesis.pdf (D29536914)
THE STUDY OF DISK CORONA EMISSION FROM TYPE 1 ACTIVE GALACTIC NUCLEI by Ritesh
Ghosh.pdf (D53219855)
Thesis_PGoswami.pdf (D86038185)
Thesis_PGoswami.pdf (D86038288)
Nibedita Kalita_Physics.pdf (D23552008)
16e33298-59ae-4d26-992f-3abf375227c6
56a80824-436e-4b29-921a-567f8150095d
49dca107-eb06-448b-9231-9fdb70f3301
ef0e2385-98b7-490b-a6ec-1d6a2802ce5a
ebe36546-236a-428b-add0-040e1577138b
42e122ad-424d-4dc1-97d8-7d5c3f32d5de
d2a33e88-50f3-4a45-8cb6-2a2a48de3cb2
<https://arxiv.org/pdf/2003.10262>
https://orbi.uliege.be/bitstream/2268/25492/1/theseG_Rauw.pdf
<http://adsabs.harvard.edu/pdf/2006MNRAS.371.1280D>
<https://www.aanda.org/articles/aa/pdf/2014/01/aa22539-13.pdf>
<https://arxiv.org/pdf/2004.04083>
http://www.matfis.uniroma3.it/Allegati/Dottorato/TESI/tortosa/tesi_PhD_Tortosa_Alessia.pdf

Instances where selected sources appear:

61

Copy Right Transfer Approval Form

APPENDIX - 5

Copy Right Transfer Approval Form

(Clause 14e of the Ordinance - 45)

Name of the Candidate: **Bharti Arora**
Department: **School of Studies in Physics and Astrophysics**
Degree : **Doctor of Philosophy in Physics**
University: **Pt. Ravishankar Shukla University, Raipur**
Supervisor: **Dr. Jeewan C. Pandey**
Co-Supervisor: **Dr. Nand K. Chakradhari**
Thesis Title: **Study of the Massive O- and WR-stars
and their Associated Winds**
Year of Award:

Agreement

1. I hereby declare that, if appropriate, I have obtained and attended hereto a written permission/statement from owner(s) of each third party copyrighted matter to be included in my thesis/dissertation, allowing distribution as specified below.
2. I hereby grant to the university and its agents the non-exclusive license to archive and make accessible, under the condition specified below, my thesis/dissertation, in whole or in part in all forms of media, now or hereafter known. I retain all other ownership rights to the copyright of the thesis/dissertation. I, my Supervisor and Co-Supervisor, also retain the right to use in future works (such as articles or books) all or part of this thesis, dissertation, or project report.

Condition:

1. Release the entire work for access worldwide

Bharti Arora
Signature of the Candidate

J. Pandey
Signature and Seal of the Supervisor
Scientist-VI
ARIES, Nainital

Place RAIPUR

Date 22.7.2021

D. Banerji

Director
Aryabhata Research Institute Of
Observational Sciences (ARIES)
(Under Department of Science & Technology)

Signature and Seal of the Co-Supervisor

N.K. Chakradhari
Dr. N.K. Chakradhari
(M.Sc., Ph.D., UGC-CSIR-NET)
Senior Assistant Professor
SoS in Physics & Astrophysics
Pt. Ravishankar Shukla University,
Raipur-492010, (CG) INDIA

ARIES/AC/CC/2016/01

ARYABHATTA RESEARCH INSTITUTE OF OBSERVATIONAL SCIENCES

(An autonomous Institute under the Department of Science & Technology)

Manora Peak, Nainital

Pre PhD Course work - 2015-16

*It is certified that **Ms. Bharti Arora** attended and successfully completed the Pre-PhD course work conducted at ARIES during the session August 2015- July 2016.*

*Her performance in the course work was found satisfactory and she has obtained an aggregate of **66%**.*

Wahab Uddin
(Acting Director)



Manish Naja

(Chairman, Academic Committee)

SCHOOL OF STUDIES IN PHYSICS AND ASTROPHYSICS
PT. RAVISHANKAR SHUKLA UNIVERSITY,
RAIPUR - 492010 CHHATTISGARH (INDIA)



Dr. D. P. Bisen
M. Phil, Ph. D.
Profess & Head

Phone : (M) 9406201131, 7987186589
(O) (0771) 2262864
Email : hodphysics98@gmail.com
: dpbisen@rediffmail.com

Ref. : 16.22./Phy/2021,

Raipur

Date : ... 19/07/21 ...

CERTIFICATE

This is to certify that **Bharti Arora** has given Pre-Ph.D. seminar in online mode on her thesis entitled “**Study of the Massive O- and WR- stars and their Associated Winds**” on **15.07.2021** at School of Studies in Physics & Astrophysics, Pt. Ravishankar Shukla University, Raipur (C. G.). **Bharti Arora's** presentation has been very satisfactory and DRC members have recommended for the submission of her Ph. D. Thesis.

D. P. Bisen
19/07/2021

Chairman

Departmental Research Committee
SoS in Physics & Astrophysics
Pt. Ravishankar Shukla University, Raipur (C. G.)

SCHOOL OF STUDIES IN PHYSICS AND ASTROPHYSICS
PT. RAVISHANKAR SHUKLA UNIVERSITY,
RAIPUR - 492010 CHHATTISGARH (INDIA)



Phone : (M) 9406201131, 7987186589
(O) (0771) 2262864
Email : hodphysics98@gmail.com
: dpbisen@rediffmail.com

Dr. D. P. Bisen
M. Phil, Ph. D.
Profess & Head

Ref. : ...1623/Phy/2021,

Raipur. Date : 19/07/21...

PLAGIARISM VERIFICATION REPORT

This is to certify that plagiarism check of the Ph.D. thesis submitted by **Bharti Arora** entitled “**Study of the Massive O- and WR- stars and their Associated Winds**” has been carried out by **Pt. Sunder Lal Sharma Library of Pt. Ravishankar Shukla University, Raipur (C.G.) India**. On the basis of this report it has been found that the percentage of similarity is 3%: within acceptable limit (less than 10%). Therefore almost no plagiarism was found.

Hence DRC recommends the thesis may be dispatched to the reviewers for further action.

D. P. Bisen
19/07/2021

Chairman

Departmental Research Committee
SoS in Physics & Astrophysics
Pt. Ravishankar Shukla University, Raipur (C.G)

**SCHOOL OF STUDIES IN PHYSICS AND ASTROPHYSICS
PT. RAVISHANKAR SHUKLA UNIVERSITY,
RAIPUR - 492010 CHHATTISGARH (INDIA)**



Dr. D. P. Bisen
M. Phil, Ph. D.
Profess & Head

Phone : (M) 9406201131, 7987186589
(O) (0771) 2262864
Email : hodphysics98@gmail.com
: dpbisen@rediffmail.com

Ref. : 1624/Phy/2021 ,

Raipur.

Date : 19/07/2021

CERTIFICATE OF PUBLICATION

This is to certify that **Bharti Arora** has published her research work in various reputed international journals having **Science Citation Index (SCI) with IMPACT FACTOR** as listed in Thomson Reuters which are given below:

List of Publications:

Publications in refereed journal:

1. X-ray emission characteristics of an O+O binary HD 93205
Arora, Bharti and Pandey, Jeewan Chandra, 2021, Monthly Notices of the Royal Astronomical Society (MNRAS), to be submitted, (Impact factor: 5.356)
2. Quest for the upcoming periastron passage of an episodic dust maker and particle accelerating colliding wind binary : WR 125
Arora, Bharti; Pandey, Jeewan Chandra; De Becker, Michaël; Pandey, S. B.: Charadhari, Nand Kumar; Sharma Saurabh; Kumar Brijesh, 2021, The Astronomical Journal (AJ), under review. (Impact factor: 5.838)
3. Unraveling the Nature of the Deeply Embedded Wolf-Rayet Star WR 121a
Arora, Bharti and Pandey, Jeewan Chandra, 2020, The Astrophysical Journal (ApJ), 891, 104 (Impact factor : 5.745)
4. Long term soft and hard X-ray investigation of the colliding wind WN+O binary WR 25
Arora, Bharti; Pandey, Jeewan Chandra; De Becker, Michaël, 2019, Monthly Notices of the Royal Astronomical Society, (MNRAS), 487, 2624–2638, (Impact factor: 5.536)

Conference Proceedings

1. X-ray observations of the colliding wind binary WR 25
Arora, Bharti and Pandey, Jeewan Chandra, 2018, a conference proceeding for BINA workshop, Bulletin de la Société Royale des Sciences de Liège, Vol. 87, p. 193 – 197
2. Polarization study of massive binaries with the ARIES-1.04 m telescope
Arora, Bharti; Pandey, Jeewan Chandra; Joshi, Arti; De Becker, Michaël, 2019, a conference proceeding for BINA workshop, Bulletin de la Société Royale des Sciences de Liège, Vol. 88, p. 287 – 290
3. Linear Polarization Towards Galactic Anti-center direction: the Case of Alessi 1
Singh, Sadhana; Pandey, Jeewan Chandra; Yadav, Ramakant Singh; Medhi, Biman Jyoti; Joshi, Arti; Arora, Bharti, 2019, a conference proceeding for BINA workshop, Bulletin de la Société Royale des Sciences de Liège, Vol. 88, p. 283 – 286


19/07/2021

Chairman

Departmental Research Committee
SoS in Physics & Astrophysics
Pt. Ravishankar Shukla University, Raipur (C. G.)

“For myself, I like a universe that includes much that is unknown and, at the same time, much that is knowable. A universe in which everything is known would be static and dull, as boring as the heaven of some weak-minded theologians. A universe that is unknowable is no fit place for a thinking being. The ideal universe for us is one very much like the universe we inhabit. And I would guess that this is not really much of a coincidence.”

Carl Sagan
– “Can We Know the Universe?” in M. Gardner (ed.), “The Sacred Beetle and Other Great Essays in Science” (Plume, 1986)

ACKNOWLEDGMENTS

Every stage of life is inspired by the persons we met and the series of steps taken previously. I am grateful to each and every person and the institutions where I have studied till 2015 that have actually motivated me to pursue research in Astrophysics. Additionally, I am fortunate to do Ph.D. under the beautiful and mesmerizing sky of ARIES.

My foremost thanks goes to my Ph.D. supervisor Dr. Jeewan C. Pandey. He has always given me full freedom to work the way I wanted and shown confidence in my opinions. Sir, you have been a lighthouse during my Ph.D. tenure and I never felt lost till now. He has not only been my research mentor but also the one guiding me through different scenarios of life. I am fortunate that you have been my Guru for both personal and professional fronts.

My sincere thanks to my Ph.D. co-supervisor, Dr. Nand K. Chakradhari, for guiding me through several academic endeavors. It has always been a pleasure to work with him. I express my deep regards to my scientific collaborator Dr. Michaël De Becker. Learning is always fun when it's Michaël and the things I have learnt from him during my visit to Belgium for three months are the basis of my present understanding of the subject.

I want to especially thank the director of ARIES, Dr. Dipankar Banerjee, for providing us a pleasant academic environment to work in. The fruitful discussion with ARIES faculty members during meetings and reviews has helped me to grow further in the field. My research work deeply benefited from the observational and other technical facilities provided by ARIES. I also thank Dr. D. P. Bisen and Dr. Nameeta Brahme for co-operating with me to sort out several academic formalities at Pt. Ravishankar Shukla University, Raipur.

It has always been a pleasure to be in the company of my Ph.D. batch-mates Shilpa, Gaurav, Priyanka, Rakesh, and Jayanand. The time spent with Shilpa as a room-mate is memorable. I really enjoyed the moments spent with Shilpa and Gaurav as my siblings. I have learnt a lot from Subhajeet bhayia, Arti di, Sadhana, Nikita, and Gurpreet while working under the guidance of Dr. Jeewan C. Pandey. I want to thank my other seniors and juniors with whom ARIES has always been like my home and they were my family during the last few years.

My Grandfather, Mamma, Papa, and brothers Abhishek and Shivam have been constant pillars of my journey till now without whom I could have never achieved

this milestone. Thank you for appreciating my achievements and giving me wings to fly even higher.

I owe a thanks to Dinesh, Sharmila, and Parwinder who are my all-time friends and make my day whenever we talk. Last but not least is my Thakur Ji who marks the beginning and ending point of my life.

With this, I look forward to an exciting and joyful journey ahead of my Ph.D.

Bharti

ABSTRACT

Massive stars (initial mass $> 8M_{\odot}$) are important objects within a galaxy, impacting their environments via their intense radiation fields as well as dense, supersonic winds and subsequently via supernova explosions. This thesis aims to explore the massive O-type and Wolf-Rayet (WR) stars and their associated winds in detail using multi-wavelength data sets. These are, more generally, found in binary or higher multiplicity systems with other massive stars having orbital periods from a couple of days up to a few hundred of years. WR stars are the evolved counterparts of O-type objects whose strong stellar winds gradually unravel their deeper layers. While some WRs display enhanced nitrogen and helium abundances (WN stars), others present enhanced carbon and depletion in nitrogen while helium is still highly present (WC stars). To accomplish our goal, timing and spectral studies of massive binaries have been performed by using mainly X-ray data sets. Additional optical polarimetric as well as infra-red photometric studies have also been performed. It has been attempted to investigate massive systems covering a large parameter space in terms of binary orbital parameters. Further, different spectral classes of hot stars have been considered to develop an overall view of the stellar winds of these stars. The main highlight of the present work is that several physical phenomena active in the individual stellar winds and the wind interaction region of massive binaries have been explored to assess the dynamical evolution of massive stellar outflows.

The thermal X-ray emission (0.3–10.0 keV) has been explored in the case of four massive binaries *viz.* WR 25 (O2.5If*/WN6+OB), WR 121a (WN7+abs), WR 125 (WC7ed+O9 III), and HD 93205 (O3.5 V((f))+O8 V) using data from several X-ray observatories. The long-term (~ 16 yrs) X-ray observations of WR 25 reveals phase-locked variations repeating consistently over many consecutive orbits, in agreement with an X-ray emission fully explained by thermal emission from the colliding winds in the 208-d orbit. A significant deviation of the X-ray flux with respect to the $1/D$ (D is the binary separation) trend, expected for adiabatic shocked winds, close to periastron passage is reported. In a similar line, the X-ray emission from an O+O binary HD 93205 showed typical features of a wind interacting system. On the other hand, an X-ray study of the deeply embedded WR star, WR 121a, carried out using ~ 12 yr long observations has helped to see the periodic variation of 4.1 d in its X-ray light curve for the first time. The present study indicates that WR 121a is an X-ray bright massive binary with an X-ray luminosity of $\sim 10^{34}$ erg s^{-1} , which can be explained by active wind collision between its components. The observed

phase-locked X-ray flux modulations could be due to the wind collision region being eclipsed by the secondary star in a binary orbit. The winds of both components of WR 121a appear to be radiative. Radiative inhibition and braking might be severely affecting the wind collision in this short-period massive binary system.

The thermal X-ray emission has been further explored to uncover the upcoming periastron passage in case of a particle accelerating and dust making system WR 125. The source was monitored using *AstroSat* and 3.6 m Devasthal Optical Telescope. WR 125 appeared brighter in near infra-red *K*-band during the years 2017-2021 which is attributed to another episode of dust formation similar to the one reported during the likely periastron passage at the beginning of the 1990's. This is further supported by enhanced mid infra-red emission observed during 2018-19. The source reaches a lower X-ray emission state in June, 2020 (close to the recent infrared maximum) which could be due to enhanced absorption of X-rays produced in the colliding wind region by the WC stellar wind close to the periastron in an eccentric orbit. The time interval between the previous and latest X-ray low states may indicate an orbital period of 28-29 years, in fair agreement with the recurrence time of episodic dust production.

The presence of hard X-ray emission (above 10.0 keV) is an outcome of particle acceleration in colliding wind binaries. The non-detection of the hard X-rays in WR 25, above the background level, suggested that the sensitivity of the present hard X-ray observatories is not sufficient to detect non-thermal emission from massive binaries above 10 keV, unless the wind kinetic power is large enough to significantly feed particle acceleration in the wind-wind interaction.

The optical polarimetric variations in the case of massive binaries help to unfold the inhomogeneities present in the stellar winds. The linear polarization study of a massive O5.5 V-III+O6 V-III binary, DH Cep, has revealed orbital phase-dependent modulations of the degree of polarization as well as the polarization angle which might be originating from the asymmetric circumstellar envelope.

To conclude the thesis, the multiwavelength study of massive binaries has helped to constrain the properties of the individual stellar winds as well as that of the wind interaction region. Timing and spectral studies of such systems have led to the determination of orbital elements of few massive binaries along with addressing some of the key phenomena associated with them like hydrodynamics of the shocks formed in the stellar outflows as well as wind structure, particle acceleration, dust formation, etc. in the wind interaction region.

LIST OF PUBLICATIONS

Publications in refereed journal

Published

1. Unraveling the Nature of the Deeply Embedded Wolf-Rayet Star WR 121a
[Arora, Bharti](#) and Pandey, Jeewan Chandra, 2020, The Astrophysical Journal (**ApJ**), 891, 104 (**Impact factor¹: 5.745**)
2. Long term soft and hard X-ray investigation of the colliding wind WN+O binary WR 25
[Arora, Bharti](#); Pandey, Jeewan Chandra; De Becker, Michaël, 2019, Monthly Notices of the Royal Astronomical Society, (**MNRAS**), 487, 2624–2638, (**Impact factor: 5.536**)

Papers Submitted

1. Quest for the upcoming periastron passage of an episodic dust maker and particle accelerating colliding wind binary: WR 125
[Arora, Bharti](#); Pandey, Jeewan Chandra; De Becker, Michaël; Pandey, S. B.; Chakradhari, Nand K.; Sharma, Saurabh; Kumar, Brijesh, 2021, The Astronomical Journal (**AJ**), under review, (**Impact factor: 5.838**)

To be submitted

1. X-ray emission characteristics of an O+O binary HD 93205
[Arora, Bharti](#) and Pandey, Jeewan Chandra, 2021, Monthly Notices of the Royal Astronomical Society (**MNRAS**), to be submitted, (**Impact factor: 5.356**)

Conference Proceedings (Refereed)

1. X-ray observations of the colliding wind binary WR 25
[Arora, Bharti](#) and Pandey, Jeewan Chandra, 2018, a conference proceeding for BINA workshop, Bulletin de la Société Royale des Sciences de Liège (**BSRSL**), Vol. 87, p. 193–197

¹Impact factor for the year of publication.

-
2. Polarization study of massive binaries with the ARIES-1.04 m telescope
Arora, Bharti; Pandey, Jeewan Chandra; Joshi, Arti; De Becker, Michaël, 2019, a conference proceeding for BINA workshop, Bulletin de la Société Royale des Sciences de Liège (**BSRSL**), Vol. 88, p. 287–290

 3. Linear Polarization Towards Galactic Anti-center direction: the Case of Alessi 1
Singh, Sadhana; Pandey, Jeewan Chandra; Yadav, Ramakant Singh; Medhi, Biman Jyoti; Joshi, Arti; **Arora, Bharti**, 2019, a conference proceeding for BINA workshop, Bulletin de la Société Royale des Sciences de Liège (**BSRSL**), Vol. 88, p. 283–286

NOTATIONS AND ABBREVIATIONS

The most commonly used notations and abbreviations in the thesis are given below. If a symbol has been used in a different connection than listed here, it has been explained at the appropriate place.

Notations

\AA	Angstrom
$'$, arcmin	Arc minute
$''$, arcsec	Arc second
D	Binary separation
D/a	Binary separation normalized to semi-major axis 'a'
k	Boltzmann constant
L_{bol}	Bolometric luminosity
f	Clumping factor
χ	Cooling parameter
d	Day or Days
Dec.	Declination
$^{\circ}$, deg	Degree
p	Degree of polarization
ρ	Density
r	Distance from stagnation point to the binary star center
e	Eccentricity
T_{eff}	Effective Temperature
λ_{eff}	Effective wavelength of a filter
e^{-}	Electron charge
J2000	Epoch of observation
N_H^{ism}	Equivalent hydrogen column density of interstellar medium
N_H^{local}	Equivalent hydrogen column density of local medium
N_H^{total}	Equivalent hydrogen column density (total)
ν	Frequency

G	Gravitational constant
HR	Hardness ratio
HJD	Heliocentric Julian Date
Hz	Hertz
i	Inclination
M_i	Initial mass of star on main sequence
F_B^{int}	Intrinsic flux in 0.3–10.0 keV energy range
F_S^{int}	Intrinsic flux in 0.3–2.0 keV energy range
F_H^{int}	Intrinsic flux in 2.0–10.0 keV energy range
F_X^{int}	Intrinsic flux in 3.0–10.0 keV energy range
L_X^{int}	Intrinsic X-ray luminosity
F_B^{ism}	ISM corrected flux in 0.3–10.0 keV energy range
F_S^{ism}	ISM corrected flux in 0.3–2.0 keV energy range
F_H^{ism}	ISM corrected flux in 2.0–10.0 keV energy range
F_X^{ism}	ISM corrected flux in 3.0–10.0 keV energy range
L_X^{ism}	ISM corrected X-ray luminosity
$F_{B_1}^{ism}$	ISM corrected flux in 0.3–5.0 keV energy range
$F_{H_1}^{ism}$	ISM corrected flux in 2.0–5.0 keV energy range
Jy	Jansky
JD	Julian Date
kpc	Kiloparsec (unit of distance)
ω	Longitude of periastron
m_H	Mass of the H-atom
M_\odot	Mass of the Sun
\dot{M}	Mass-loss rate
\dot{M}_1	Mass-loss rate of primary star
\dot{M}_2	Mass-loss rate of secondary star
μ	Mean molecular weight
Z	Metallicity/Abundance
mas	Milli arcsecond
$M \sin^3 i$	Minimum mass of star
$M_{pri} \sin^3 i$	Minimum mass of primary star
$M_{sec} \sin^3 i$	Minimum mass of secondary star
MJD	Modified Julian Date
q, u, q_1, u_1	Normalized Stoke's parameters at four

	position of half wave plate
$norm_1$	Normalization constant of cool component of X-ray fitting model
$norm_2$	Normalization constant of hot component X-ray fitting model
F_B^{obs}	Observed flux in 0.3–10.0 keV energy range
F_S^{obs}	Observed flux in 0.3–2.0 keV energy range
F_H^{obs}	Observed flux in 2.0–10.0 keV energy range
F_X^{obs}	Observed flux in 3.0–10.0 keV energy range
τ	Optical depth
ϕ	Orbital phase
P	Orbital period
kT_1	Plasma temperature of cool component of X-ray fitting model
kT_2	Plasma temperature of hot component of X-ray fitting model
ψ	Polarization angle
n	Power law index
$a \sin i$	Projected semi-major axis
v	Pre-shock wind velocity
V_o	Radial velocity
K	Radial velocity amplitude
χ_ν^2	Reduced chi-square
R.A.	Right Ascension
s	Second
L_\odot	Solar luminosity
M_\odot	Solar mass
Z_\odot	Solar metallicity
j	Spectral index
θ	Shock-cone half opening angle
v_∞	Terminal wind velocity
$v_{\infty,1}$	Terminal wind velocity of primary star
$v_{\infty,2}$	Terminal wind velocity of secondary star
S_ν	Thermal radio flux density
A_V	Total absorption in the visual magnitude

$T_{periastron}$	Time of periastron passage
T_{RVmax}	Time of maximum radial velocity
c	Velocity of light
λ	Wavelength
η	Wind momentum ratio
L_{wind}	Wind kinetic energy
L_X	X-ray luminosity
yr	Year

Abbreviations

ARIES	Aryabhata Research Institute of observational sciencES
ADFOSC	ARIES-Devasthal Faint Object Spectrograph and Camera
AIMPOL	Aries IMaging POLarimeter
AOS	Active Optics System
ACIS	Advanced CCD Imaging Spectrometer
ADU	Analog to Digital Unit
ARF	Ancillary Response File
AGB	Asymptotic Giant Branch
APEC	Astrophysical Plasma Emission Code
APED	Astrophysical Plasma Emission Database
Broad energy band	0.3-10.0 keV energy range
Broad ₁ energy band	0.3-5.0 keV energy range
BI	Back Illuminated
b-WR	Binary-stripped WR stars
CCD	Charge Coupled Device
CE	Common Envelope
CWB	Colliding Wind Binary
CCF	Current Calibration File
<i>dof</i>	Degrees of Freedom
DOT	Devasthal Optical Telescope
DSA	Diffusive Shock Acceleration
WNE	Early WN star

ESA	European Space Agency
EPIC	European Photon Imaging Camera
EOB	Extensible Optical Bench
E-ray	Extra-ordinary ray image
FoV	Field of view
FPMA & B	Focal plane modules A & B
FFA	Free-Free absorption
FI	Front Illuminated
FWHM	Full Width at Half Maximum
GRB	Gamma Ray Burst
HPD	Half Power Diameter
HWP	Half Wave Plate
Hard energy band	2.0-10.0 keV energy range
Hard ₁ energy band	2.0-5.0 keV energy range
HEASoft	High Energy Astrophysics Software
HR diagram	Hertzsprung-Russell diagram
IRAF	Image Reduction and Analysis Facility
IPC	Imaging Proportional Counter
IR	Infra-Red
ISM	Interstellar Matter/Medium
IC	Inverse Compton
LAXPC	Large Area Xenon Proportional Counter
WNL	Late WN star
LBV	Luminous Blue Variable
MOS	Metal-Oxide Semi-conductor
mag	magnitude (stellar)
ms-WR	Main sequence WR stars
Myr	Million year
NASA	National Aeronautics and Space Administration
NEOWISE-R	Near-Earth Object Wide-field Infrared Survey Explorer Reactivation mission
NIR	Near Infra-Red
NuSTAR	Nuclear Spectroscopic Telescope Array
ODF	Observation Data File
O-ray	Ordinary ray image

PACWB	Particle Accelerating Colliding Wind Binary
PHOT	Photometry
PC mode	Photon Counting mode
PSF	Point Spread Function
PSPC	Position Sensitive Proportional Counter
RSG	Red Super Giant
RMF	Response Matrix File
ROSAT	The ROentgen SATellite
RLOF	Roche lobe overflow
ST	Sampurnanand Telescope
SAS	Science Analysis System
SNR	Signal to Noise Ratio
SXT	Soft X-ray Telescope
Soft energy band	0.3-2.0 keV energy range
SN/SNe	Supernova/Supernovae
TANSPEC	TIFR-ARIES NIR Spectrometer
TIRCAM2	TIFR NIR Imaging Camera-II
2MASS	Two Micron All Sky Survey
UV	Ultraviolet
uGMRT	upgraded Giant Metrewave Radio Telescope
UVIT	UV Imaging Telescopes
VLT	Very Large Telescope
WR	Wolf-Rayet
WN	WR star with enhanced Nitrogen abundance
WC	WR star with enhanced Carbon abundance
WO	WR star with enhanced Oxygen abundance
w-WR	Wind-stripped WR stars
wb-WR	Wind+binary-stripped WR star
WCR	Wind Collision Region
WISE	Wide-Field Infrared Explorer
<i>W1</i>	WISE–3.4 μm band
<i>W2</i>	WISE–4.6 μm band
XIS	X-ray Imaging Spectrometer
XRT	X-ray Telescope

Contents

LIST OF FIGURES	xxxii
LIST OF TABLES	xxxiv
1 INTRODUCTION	1
1.1 Massive Stars	1
1.1.1 OB-type stars	2
1.1.2 Wolf-Rayet stars	3
1.1.2.1 Classification of WR stars	4
1.1.2.2 Evolution of WR stars	6
1.2 Physics behind stellar winds and mass loss	11
1.3 Observational phenomena related to massive stars	16
1.3.1 Thermal and non-thermal radio emission	22
1.3.2 Infra-red emission	24
1.3.3 Optical and UV emission	26
1.3.4 Thermal X-ray emission	27
1.3.5 High energy X-ray and Gamma-ray emission	29
1.3.6 Energy budget of massive binaries	30
1.4 Motivation of Thesis	31
1.5 Outline of Thesis	32
2 TELESCOPES, INSTRUMENTS, OBSERVATIONS, AND DATA PROCESSING	35
2.1 Charged Coupled Devices: The detector used for multiwavelength observations	35
2.2 X-ray telescopes and back-end detectors	36
2.2.1 <i>AstroSat</i>	36
2.2.2 <i>Chandra</i>	38
2.2.3 <i>NuSTAR</i>	39

CONTENTS

2.2.4	<i>Suzaku</i>	40
2.2.5	<i>The Neil Gehrels Swift Observatory</i>	42
2.2.6	<i>XMM-Newton</i>	43
2.3	X-ray observations and data reduction	45
2.3.1	<i>AstroSat</i>	48
2.3.2	<i>Chandra</i>	50
2.3.3	<i>NuSTAR</i>	51
2.3.4	<i>Suzaku</i>	52
2.3.5	<i>Swift</i>	52
2.3.6	<i>XMM-Newton</i>	53
2.4	X-ray analysis techniques	54
2.4.1	Timing analysis	54
2.4.2	Spectral analysis	54
2.4.2.1	Astrophysical Plasma Emission Code (APEC)	56
2.4.2.2	Photo-electric absorption model	57
2.4.2.3	X-ray flux	57
2.5	Near Infra-Red (NIR) observations	58
2.5.1	Telescope	58
2.5.2	Instrument	60
2.5.3	Observations and data reduction	60
2.6	Optical polarimetric observations	63
2.6.1	Aries IMaging POLarimeter (AIMPOL)	63
2.6.2	Observations and data processing	64
2.7	Data taken from surveys and other literature	65
3	X-RAY INVESTIGATION OF THE COLLIDING WIND BINARY WR 25	69
3.1	WR 25: An Introduction	69
3.2	The Spectra	72
3.2.1	Look at the X-ray spectra of WR 25	72
3.2.2	X-ray spectral analysis	72
3.2.2.1	<i>Suzaku</i>	75
3.2.2.2	<i>Swift</i>	75
3.2.2.3	<i>XMM-Newton</i>	75
3.2.2.4	<i>NuSTAR</i>	77
3.3	X-ray light curves analysis	82
3.3.1	Folded X-ray light curves	82

3.3.2	Flux vs. binary separation	86
3.4	Discussion	91
3.4.1	Variability of the thermal X-ray emission	91
3.4.2	Lack of non-thermal X-ray emission	96
3.4.3	Comparison with other systems	100
3.5	Conclusions	102
4	WR 121a: A SHORT PERIOD COLLIDING WIND BINARY	105
4.1	Overview	105
4.2	X-ray image analysis of WR 121a	107
4.3	X-ray timing analysis	110
4.3.1	Search for variability	110
4.3.2	Folded X-ray light curves	113
4.4	X-ray spectral analysis	113
4.5	Discussion	119
4.6	Conclusions	127
5	QUEST FOR THE UPCOMING PERIASTRON PASSAGE IN WR 125	129
5.1	Overview	129
5.2	The colliding wind binary WR 125	131
5.3	X-ray spectral and light curve analysis	132
5.4	Discussion	139
5.4.1	Dust emission	139
5.4.2	X-ray emission	142
5.4.3	Synchrotron radio emission	143
5.4.4	Toward a more complete picture	145
5.5	Conclusions	146
6	X-RAY INVESTIGATION AND OPTICAL POLARIMETRY OF MASSIVE O+O BINARIES	149
6.1	Part I: Characteristics of X-ray emission from HD 93205	149
6.1.1	X-ray light curve analysis	151
6.1.2	X-ray spectral analysis	154
6.1.3	Discussion: X-ray emission from HD 93205	158
6.2	Part II: Search for intrinsic linear polarization in DH Cep	160
6.2.1	Motivation	160
6.2.2	Discussion: Linear Polarization of DH Cep	162

CONTENTS

7	SUMMARY AND FUTURE PROSPECTS	165
7.1	Summary	165
7.2	Future prospects	168
	REFERENCES	187

List of Figures

1.1	Variation of stellar absolute magnitude or luminosity versus their surface temperature or stellar classification displayed in the Hertzsprung-Russell (HR) diagram. The figure is adopted from: https://chandra.harvard.edu/ed	
1.2	Montage of optical WN (<i>top</i>) and WC (<i>bottom</i>) spectra. The figure is adopted from Crowther (2007)	7
1.3	The evolution of a $60 M_{\odot}$ star with 0.02 metallicity undergoing mass-loss shown in the Kippenhahn diagram. The nuclear burning stages are indicated by cross-hatched areas while the convective regions have been highlighted using curly symbols. The figure is adopted from Maeder & Meynet (1987)	10
1.4	Evolutionary tracks for the formation of WR stars through the ms-WR, w-WR, wb-WR, and w-WR formation channels in the Large Magellanic Cloud ($Z = 0.008$). The figure is adopted from Shenar et al. (2019)	12
1.5	The geometrical structure of the interaction region of the primary and secondary star's winds mixing near the contact discontinuity. The figure is reproduced from Kashi & Soker (2009)	16
1.6	Illustration of first-order Fermi mechanism to explain particle acceleration by the strong shocks. The upstream and downstream regions are designated using the letters 'u' and 'd', respectively. The scattering of particles in the two regions because of magneto-hydrodynamic processes has been shown in the panels (c) and (d). All the four scenarios are explained in the text individually. The figure is taken from Longair (1994)	20

LIST OF FIGURES

1.7	Fitted spectrum for WR 147, including total (solid line), synchrotron (dashed line), and thermal (dotted line) flux. The open circles are synchrotron fluxes estimated by subtracting a thermal component from the total observed fluxes. The figure is adopted from Pittard et al. (2006)	24
1.8	Illustration of P-Cygni line profile formation in an outflow which is expanding. The figure is adopted from Owocki (2013)	27
1.9	Representation of the energy budget of stellar winds in a binary hosting wind collision. Non-thermal processes are highlighted in ‘red’ color while thermal emission phenomena are mentioned in ‘blue’. The different numbers express typical percentage of energy transferred between two consecutive boxes starting from the bolometric luminosity which is the total output energy of the star. The figure is adopted from De Becker & Raucq (2013)	31
2.1	A schematic of principal instruments onboard <i>AstroSat</i> with folded solar panels. The figure is adopted from Singh (2016)	37
2.2	Different components of <i>Chandra</i> spacecraft. The figure is adopted from: https://chandra.harvard.edu/about/spacecraft.html	39
2.3	Schematic view of <i>NuSTAR</i> , the first hard X-ray focusing telescope in 3-79 keV energy range, in stowed (bottom) and deployed (top) configurations. The figure is adopted from Harrison et al. (2013)	40
2.4	Side view of the internal structures of <i>Suzaku</i> payload upon deployment of the extensible optical bench. The figure is adopted from Mitsuda et al. (2007)	41
2.5	Schematic view of <i>Swift</i> observatory instruments. The figure is adopted from: https://www.swift.ac.uk/about/instruments.php	43
2.6	A schematic diagram of the ESA’s <i>XMM-Newton</i> observatory. This figure is adopted from Lumb et al. (2012)	44
2.7	TIRCAM2 mounted on the axial port of 3.6 m DOT. The figure is adopted from Baug et al. (2018)	59
2.8	Optical design of AIMPOL from Rautela et al. (2004) (<i>left</i>) and AIMPOL mounted at the base of ST along with 1024×1024 CCD camera (<i>right</i>).	64

3.1	<i>XMM-Newton</i> –PN false-color image of η -Carinae field in 0.3–10.0 keV energy range from observation ID 0112560201. X- and Y- axes correspond to R.A. (J2000) and Dec. (J2000), respectively.	71
3.2	FI <i>Suzaku</i> –XIS and <i>XMM-Newton</i> –MOS2 spectra of WR 25 at different orbital phases. In each panel the stars are at (almost) identical binary separation but either receding (phase<0.5) or approaching each other (phase>0.5).	73
3.3	<i>NuSTAR</i> –FPMA spectra of WR 25 without background correction (black line) and only background (red line) of observation ID 30002010005.	74
3.4	Variation of plasma temperature corresponding to hot component (kT_2) with orbital phase of WR 25 derived from <i>XMM-Newton</i> –EPIC data.	74
3.5	Spectral parameters as a function of orbital phase as observed by (a) <i>Suzaku</i> –XIS, (b) <i>Swift</i> –XRT, and (c) <i>XMM-Newton</i> –EPIC.	76
3.6	Normalization constant ($norm$) and observed X-ray flux (F_X^{obs}) as a function of orbital phase for <i>NuSTAR</i> –FPMs data.	77
3.7	X-ray light curves in broad (0.3–10.0 keV), soft (0.3–2.0 keV), and hard (2.0–10.0 keV) energy bands as observed by <i>Swift</i> –XRT. Blue triangles mark the data observed during 2007 December to 2009 June and the red filled circles correspond to 2014 August to 2016 August observations.	83
3.8	Folded X-ray light curves in broad, soft, and hard energy bands as observed by (a) FI <i>Suzaku</i> – XIS, (b) <i>Swift</i> –XRT, and (c) <i>XMM-Newton</i> –MOS2.	84
3.9	Folded X-ray light curves in 3.0–10.0 keV energy range as observed by <i>NuSTAR</i> – FPMA (upper panel) and FPMB (lower panel).	85
3.10	Observed (top) and intrinsic (bottom) X-ray flux of WR 25 as a function of binary separation in soft (F_S) and hard (F_H) energy bands as observed by <i>Suzaku</i> –XIS. The orbital phases corresponding to a few data points have also been mentioned in the figures.	87
3.11	Observed (top) and intrinsic (bottom) X-ray flux of WR 25 as a function of binary separation in soft (F_S) and hard (F_H) energy bands as observed by <i>Swift</i> –XRT. The orbital phases corresponding to a few data points have also been mentioned in the figures.	88

LIST OF FIGURES

3.12	Observed (top) and intrinsic (bottom) X-ray flux of WR 25 as a function of binary separation in soft (F_S) and hard (F_H) energy bands as observed by <i>XMM-Newton</i> –EPIC. The orbital phases corresponding to a few data points have also been mentioned in the figures.	89
3.13	(a) Observed and (b) intrinsic X-ray flux as a function of binary separation in 3.0–10.0 keV (F_X) energy band as observed by <i>NuSTAR</i> –FPMs. The orbital phases corresponding to a few data points have also been mentioned in the figures.	90
3.14	Expected evolution of the pre-shock wind velocity (v) and cooling parameter (χ) with the orbital phase for both components of WR 25. Here, secondary component of WR 25 is an O4 supergiant.	94
4.1	Merged and exposure corrected images of W43-Main from the observation IDs 18868, 17716, 18870, 18867, and 18869 (<i>left</i>) and 18887, 17717, and 18888 (<i>right</i>) of <i>Chandra</i> –ACIS-I observations in the 0.5–7.0 keV energy band. The images are binned into $\sim 0.5'' \times 0.5''$ pixels (1×1 binning). The $1.5' \times 1.2'$ region of the W43-Main around its center has been marked by a rectangle. The X- and Y-axes correspond to R.A. (J2000) and Dec. (J2000), respectively. The position of WR 121a as well as various other sources detected in the field has also been marked in the figures.	108
4.2	X-ray light curves of WR 121a in different energy bands as observed by (a) <i>XMM-Newton</i> –EPIC, and (b) <i>Chandra</i> –ACIS.	111
4.3	Lomb-Scargle (<i>top</i>), data window (<i>middle</i>), and CLEAN (<i>bottom</i>) power spectra of WR 121a in 0.5–8.0 keV energy range using data from <i>Chandra</i> –ACIS. The dashed-dotted line in the top panel shows the false alarm probability corresponding to 99% significance level.	112
4.4	Folded X-ray light curves of WR 121a in different energy bands as observed by <i>Chandra</i> –ACIS.	114
4.5	Comparison of <i>Chandra</i> –ACIS spectra of WR 121a at two different orbital phases. Black points correspond to an orbital phase ~ 0.41 and red points refer to a phase ~ 0.97	115
4.6	X-ray spectra of WR 121a as observed from MOS and PN detectors onboard <i>XMM-Newton</i> along with the best fit folded two-temperature plasma emission model (2T APEC). The lower panel shows the residual in terms of the ratio of the data and model.	116

4.7	Spectral parameters as a function of the orbital phase of WR 121a obtained from <i>Chandra</i> –ACIS (red filled circles) and <i>XMM-Newton</i> –EPIC data (green filled triangles). Here, $norm_1$ and $norm_2$ are in the units of 10^{-3} cm^{-5} , N_H^{local} in 10^{22} cm^{-2} , and F_B^{ism} , F_S^{ism} as well as F_H^{ism} are in the units of $10^{-12} \text{ erg cm}^{-2} \text{ s}^{-1}$. The downward arrows in the top panel mark the upper limits of $norm_1$ for two <i>Chandra</i> Obs. IDs (see Table 4.1).	117
4.8	Plot of eccentricity as a function of the orbital period of WR+O binaries. The location of WR 121a is shown by the dashed line. . . .	120
4.9	Variation of cooling parameter (χ) as a function of the orbital phase for WR 121a by assuming primary as a WN7 star and an O-type dwarf/giant/supergiant star as secondary.	123
4.10	Variation of half opening angle of the shock-cone formed due to collision between stellar winds of a WN7 star and an O-type dwarf/giant/supergiant star in a circular binary orbit of period 4.1 d.	126
5.1	<i>XMM-Newton</i> –PN image from the observation ID 0794581101 in 0.2–15.0 keV energy band. The position of WR 125 has been highlighted with a circle.	133
5.2	<i>XMM-Newton</i> –EPIC spectra of WR 125 from the observation IDs (a) 0794581101 (<i>top</i>) and (b) 0853980101 (<i>bottom</i>). The EPIC spectra have been fitted jointly using the model PHABS*PHABS(APEC+APEC) with parameters given in Table 5.1 for both the IDs. The lower panels show the ratio of the data to the model.	135
5.3	Observed (F^{obs} , <i>top</i>) and ISM corrected (F^{ism} , <i>bottom</i>) flux from WR 125 <i>viz.</i> F_B , F_S , and F_H in broad (0.5–10.0 keV), soft (0.5–2.0 keV), and hard (2.0–10.0 keV) energy bands, respectively. The purple circle marks the <i>Einstein</i> –IPC data point, the orange square is the <i>ROSAT</i> –PSPC flux, green pentagons are the <i>Swift</i> –XRT flux measurements while pink triangles correspond to the <i>XMM-Newton</i> –EPIC observations and blue diamonds show the <i>Astrosat</i> –SXT flux values.	137
5.4	X-ray light curve of WR 125 in 0.3–10.0 keV energy band as observed by <i>Swift</i> –XRT (green pentagons), <i>XMM-Newton</i> –PN (pink triangles), and <i>Astrosat</i> –SXT (blue diamonds). The PN and SXT count rate has been converted to that of the <i>Swift</i> –XRT using WebPIMMS.	139

LIST OF FIGURES

5.5	<i>K</i> -band light curve of WR 125 by combining data from the literature, 2MASS survey and the present study. The accuracy of data from Williams et al. (1992, 1994) is 0.05 mag.	140
5.6	NEOWISE-R <i>W1</i> and <i>W2</i> bands light curve of WR 125 by combining data from Williams (2019) and the recent observations.	141
5.7	Sketch of the likely eccentric orbit of WR 125, illustrating three specific orbital phases: (a) close to apastron, (b) intermediate phase, and (c) close to periastron. Blue spheres represent the (not to scale) radio photospheres.	144
6.1	X-ray light curves of HD 93205 as observed by <i>XMM-Newton</i> using (a) MOS1, (b) MOS2, and (c) PN in broad ₁ (0.3-5.0 keV), soft (0.3-2.0 keV), and hard ₁ (2.0-5.0 keV) energy bands.	152
6.2	Folded X-ray light curves of HD 93205 as observed by <i>XMM-Newton</i> using (a) MOS1, (b) MOS2, and (c) PN in broad ₁ (0.3-5.0 keV), soft (0.3-2.0 keV), and hard ₁ (2.0-5.0 keV) energy bands.	153
6.3	X-ray spectra of HD 93205 jointly fitted with the two temperature thermal plasma emission model for all of the eight phase bins defined in Table 6.2. The lower panel of each figure represents ratio of the data to the model.	155
6.4	Variation of different spectral parameters with orbital phase of HD 93205 obtained after X-ray spectral fitting (see Table 6.2).	156
6.5	Variation of X-ray flux in different energy bands from HD 93205 obtained after X-ray spectral fitting with orbital phase (<i>left</i>) and binary separation (D normalized to semi-major axis ‘a’) (<i>right</i>).	156
6.6	Variation of $F_{B_1}^{ism}$ from HD 93205 with orbital phase as observed by <i>XMM-Newton</i> -EPIC. The solid line shows the 1/D function, where D is the binary separation in terms of the semi-major axis.	159
6.7	Linear polarization (<i>left</i>) and polarization angle (<i>right</i>) variation of DH Cep with the orbital phase in B, V, R, and I filters running from top to bottom.	162
6.8	Linear polarization (V-band) as a function of distance towards the direction of DH Cep.	163

List of Tables

1.1	Optical classification criteria for WN, WC, and WO subtypes reproduced from van der Hucht (2001)	5
1.2	Optical emission lines used for classifying WR stars reproduced from van der Hucht (2001)	6
2.1	Log of X-ray observations of WR 25.	46
2.2	Log of X-ray observations of WR 121a and WR 125.	49
2.3	NIR observations of WR 125 with TIRCAM2	63
3.1	Orbital parameters of WR 25.	70
3.2	Best fit parameters obtained from spectral fitting of WR 25 as observed from <i>Suzaku</i> , <i>Swift</i> , and <i>XMM-Newton</i>	78
3.3	Best fit parameters obtained from spectral fitting of WR 25 as observed from <i>NuSTAR</i>	81
3.4	List of the stellar parameters adopted for the estimation of cooling parameter (χ) at the WCR of WR 25.	94
3.5	Estimates of the upper limits on the count rate for <i>NuSTAR</i> instruments at the position of WR 25.	98
4.1	Best fit parameters obtained from spectral fitting of WR 121a as observed from <i>Chandra</i> –ACIS and <i>XMM-Newton</i> –EPIC.	118
5.1	Best-fit parameters obtained from joint fitting of <i>XMM-Newton</i> –EPIC spectra of WR 125 using the model PHABS*PHABS(APEC+APEC). . .	134
5.2	Best-fit parameters obtained from joint fitting of <i>XMM-Newton</i> –EPIC spectra of WR 125 using the model PHABS*APEC.	136
5.3	Best-fit parameters obtained from spectral fitting of WR 125 using different models as observed from <i>AstroSat</i> , <i>Einstein</i> , <i>Rosat</i> , <i>Swift</i> , and <i>XMM-Newton</i>	138

LIST OF TABLES

6.1	Orbital parameters of HD 93205.	150
6.2	Best fit parameters obtained from spectral fitting of HD 93205 as observed from <i>XMM-Newton</i> -EPIC.	157
6.3	Basic parameters of the DH Cep system.	161

Chapter 1

INTRODUCTION

1.1 Massive Stars

The initial mass of a star is the determining factor of its evolution and final destiny. Massive stars having an initial mass greater than $8M_{\odot}$ are the hottest and most luminous stars, with effective temperature $T_{eff} \gtrsim 15,000$ K, and stellar luminosities between 10^4 – $10^6 L_{\odot}$. They act as cosmic engines which generate a majority of the luminosity of the star-forming galaxies. Massive stars have relatively short lifetimes of a few to 10 Myrs and they provide the most valuable signature of star formation through their ultraviolet (UV) emission which is reprocessed in several forms. This is also utilized to estimate the star formation rates (Kennicutt, 1998; Kennicutt & Evans, 2012). The interstellar gas is stirred from the UV radiation, stellar winds, and ultimate demise of massive stars through supernovae (SNe). This feedback drives the gas turbulence and triggers new generations of star formation by filling gas into the dense filaments (Elmegreen & Lada, 1977). The formation of different elements through nuclear burning occurs inside the cores of massive stars and further explosive nucleosynthesis active in SNe generates elements which contaminate the interstellar medium (ISM). The elemental yield powers the galactic chemical as well as metallicity (Z) evolution of the Universe. Upon their violent death as SNe, massive stars transform into compact objects such as black holes, neutron stars, pulsars or magnetars. The Study of stellar evolution in early environments is feasible by investigating Gamma-ray bursts (GRBs; Gehrels et al. 2009; Woosley & Bloom 2006) and SNe. However, such kind of exploration requires knowledge of the link between massive stars, their mass-loss, and the subsequent type of SN observed.

1. INTRODUCTION

The wind mass-loss is not significant for the evolution of low and intermediate mass stars (initial mass $< 8M_{\odot}$) until they reach their final transition stages from an asymptotic giant branch (AGB) star to a protoplanetary nebula. However, mass-loss can't be disregarded in the case of massive stars. Even on the main sequence, massive stars undergo mass-loss in the form of fast winds which influence their subsequent evolution. Further, this mass shedding plays a critical role in governing the type of final SN explosion. Hence, mass loss is tightly connected with the evolution of massive stars. As main sequence stars, these are classified into the spectral types O and B. The Wolf-Rayet (WR) phase of the massive stars, which is the final stage of evolution of stars with initial mass $\gtrsim 25 M_{\odot}$, experiences the most profound effects of mass loss. A brief introduction to OB and WR-stars has been given below.

1.1.1 OB-type stars

The stars having an initial mass greater than $\sim 15\text{-}20 M_{\odot}$ populate the upper left corner of the Hertzsprung-Russell (HR) diagram shown in Figure 1.1. These objects are the main-sequence stars belonging to the spectral types from O to early B-stars. O-type stars are classified into the ionization classes of 2-9. However, based on the luminosity class division, they belong to classes I, III, and V denoting supergiants, giants, and dwarfs, respectively. Similarly, ionization classes of B stars range from 0-9 and the initial masses of early B0-3 stars fill the gap from $8 M_{\odot}$. The O and early B-type stars are further classified into various spectral subtypes using He I and He II line ratios as well as Si II, Si III, and Si IV features. The important lines considered are (all line wavelengths are mentioned in \AA units): He I: $\lambda 4471$ and 4387 ; He II: $\lambda 4542$ and 4686 ; Si II: $\lambda 4128\text{-}30$; Si III: $\lambda 4552$; Si IV: $\lambda 4089$ and 4116 . The ratio $\lambda 4471$ He I/ $\lambda 4542$ He II determines O subtypes. This ratio decreases monotonically while moving towards earlier spectral types, for example, the $\lambda 4471$ line is very weak, or completely absent at O3 (Crowther, 2004).

The appearance of various emission lines is seen among most O-type stars in the optical waveband. In a few O-type stars, N III $\lambda 4634\text{-}41$ triplet as well as He II $\lambda 4686$ is present in emission as noticed by Plaskett & Pearce (1931). These stars were labeled as Of type. For example, O supergiants with He II $\lambda 4686$ and N IV $\lambda 4058$ or N III $\lambda 4640$ emission features are identified as OIf stars. Walborn (1982) first introduced the OIf/WN spectral class to designate a spectrum of the objects which have spectral features intermediate of an OIf and a WR star. Here, WN is one of the spectral types of WR stars showing enhanced emission from nitrogen and

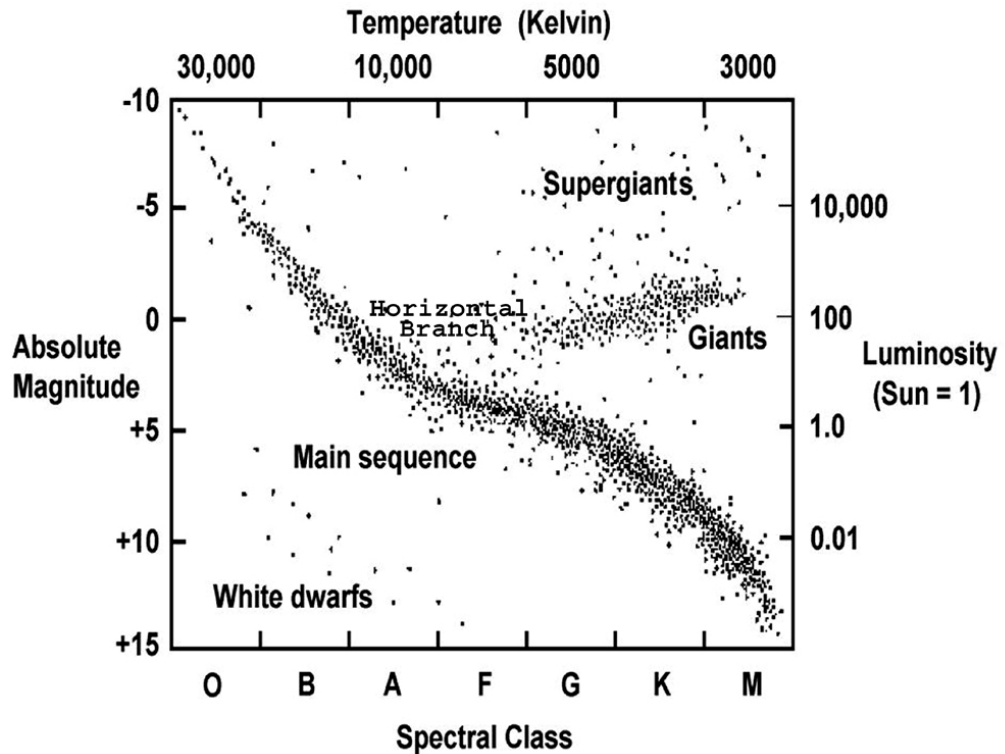


Figure 1.1: Variation of stellar absolute magnitude or luminosity versus their surface temperature or stellar classification displayed in the Hertzsprung-Russell (HR) diagram. The figure is adopted from: https://chandra.harvard.edu/edu/formal/variable_stars/bg_info.html.

helium (see Section 1.1.2). The spectra are differentiated on the basis of $H\beta$ line presence. $H\beta$ is observed as an absorption line in the case of OIf stars. There exist another category of hot stars called hot slash stars denoted by OIf/WN where $H\beta$ is observed having a P-Cygni profile, however, WR stars display it as an emission line (Crowther & Walborn, 2011).

1.1.2 Wolf-Rayet stars

The OB-type stars are believed to evolve into WR stars. Three examples of WR stars in the Cygnus region were first reported by Wolf & Rayet (1867). The broad emission lines are the main characteristic of the optical spectra of WR stars contrary to the spectra of most of the stars which are dominated by narrow absorption lines. The massive stars' spectrum consisting of rich emission lines helps to distinguish them easily by spectroscopic means at larger distances too. A wide span of ionization and excitation is covered by the broad emission lines over the blue continuum of hot

1. INTRODUCTION

stars. The formation of such unique spectral features happens in the dense stellar winds. This means that the photosphere of the early type stars is seen in the stellar outflows where the optical depth of the order of unity is achieved and emission lines are generated from further out in the winds.

1.1.2.1 Classification of WR stars

WR stars are historically classified based upon their optical spectral features which originate because of ionized helium and other heavier elements present in their atmospheres. The WR spectra mainly belong to any of three categories defined as WN, WC, and WO where emission lines from either nitrogen, carbon, or oxygen, respectively, are displayed. Here, each class exhibit enrichment of He as well (Smith, 1973; Willis, 1982). A qualitative scheme to classify WR stars was first given by Beals (1929, 1938) and further enhanced by Hiltner & Schild (1966) and Smith (1968). The advanced development of linear detectors helped to create the existing WR stars classification schemes in a completely quantitative manner.

All classification of WR stars is dependent upon ratios of emission line strengths, with a numerical suffix indicating the temperature (WN2 is hotter than WN3, which is hotter than WN4, etc.). WN subtypes range from WN2-WN5 for “early-type” (WNE), and WN7-WN11 for “late-type” (WNL) stars; WN6 can either be early or late. Similarly, WC subtypes span WC4-WC6 (early) and WC7-WC9 (late). The rare WO1-WO4 types, consisting of strong O V – O VIII lines in the spectrum, are an extension of the WC sequence (Crowther et al., 1998; Tramper et al., 2015). Generally, the spectral sequences WC and WO are well behaved and the spectra transitions smoothly between these two categories. Table 1.1 shows the classification criteria for each WR spectral subtype in the optical region using emission lines given in Table 1.2.

Additional suffixes are also appended to accommodate peculiar spectral features. For example, the presence of circumstellar dust which weakens the spectral lines in many late-type WCs is denoted with a “d”, WNs are grouped into weak-(no suffix) and broad-line (marked with a “b”) categories. WN spectra which show hydrogen emission lines are indicated with an “h”, and those with hydrogen in both emission and absorption lines bear an “ha” (see Crowther & Walborn 2011; Smith & Conti 2008). Spectroscopically, WN#ha stars display a continuation of the emission line ‘Of’ type stars having powerful stellar winds during comparatively earlier stages of evolution (Bohannon & Crowther, 1999). Additionally, WN#ha stars appear

Table 1.1: Optical classification criteria for WN, WC, and WO subtypes reproduced from [van der Hucht \(2001\)](#).

WN types	Nitrogen emission lines	Other emission criteria
WN2	N v weak or absent	He II strong
WN2.5	N v present, N IV absent	
WN3	N IV \ll N v, N III weak or absent	
WN4	N IV \simeq N v, N III weak or absent	
WN4.5	N IV $>$ N v, N III weak or absent	
WN5	N III \simeq N IV \simeq N v	
WN6	N III \simeq N IV, N v present but weak	
WN7	N III $>$ N IV, N III $<$ He II 4686Å	He I weak P-Cyg
WN8	N III \gg N IV, N III \simeq He II 4686Å	He I strong P-Cyg
WN9	N III $>$ N II, N IV absent	He I P-Cyg
WN10	N III \simeq N II	Balmer lines, He I P-Cyg
WN11	N II \simeq He II, N III weak or absent	Balmer lines, He I P-Cyg

WC types	Carbon emission lines	Other emission criteria
WC4	C IV strong, C II weak or absent	O v moderate
WC5	C III \ll C IV	C III $<$ O v
WC6	C III \ll C IV	C III $>$ O v
WC7	C III $<$ C IV	C III \gg O v
WC8	C III $>$ C IV	C II absent, O v weak or absent
WC9	C III $>$ C IV	C II present, O v weak or absent

WO types	Oxygen emission lines	Other emission criteria
WO1	O VII \geq O v, O VIII present	C III absent
WO2	O VII $<$ O v	C IV $<$ O VI, C III absent
WO3	O VII weak or absent	C IV \simeq O VI, C III absent
WO4		C IV \gg O VI, C III absent

to have more luminosity as compared to their H-free counterparts, *i.e.*, WN stars ([Hamann et al., 2006](#)). Their presence in the young clusters indicates that they have current mass $> 65M_{\odot}$ derived from cluster turn-offs ([Crowther et al., 1995](#)). Figure 1.2 gives examples of optical spectra of WN and WC stars.

As the Galactic WR star catalog has expanded out beyond the Solar Neighborhood, most of the recent additions suffer too much extinction to allow us to obtain optical spectra, and so classification using K -band lines, as in [Figer et al. \(1997\)](#), is essential. There are a wealth of WR lines between 2.0 and 2.4 μm , as shown in Table 2 of [Figer et al. \(1997\)](#), however, no single line appears in every subtype’s spectrum, requiring multiple narrow band filters to identify WR star can-

1. INTRODUCTION

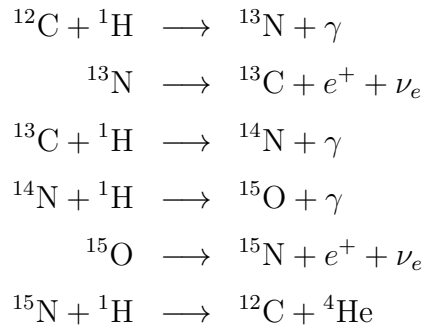
Table 1.2: Optical emission lines used for classifying WR stars reproduced from [van der Hucht \(2001\)](#).

Sequence	Lines
WN stars	He I 3888 Å, He I & He II 4027 Å, He I 4471 Å, He I 4921 Å, He I 5875 Å, He II 4200 Å, He II 4340 Å, He II 4541 Å, He II 4686 Å, He II 4861 Å, He II 5411 Å, He II 6560 Å, N II 3995 Å, N III 4634 – 4641 Å, N III 5314 Å, N IV 3479 – 3484 Å, N IV 4058 Å, N V 4603 Å, N V 4619 Å, N V 4933 – 4944 Å
WC stars	C II 4267 Å, C III 5696 Å, C III/C IV 4650 Å, C IV 5801 – 5812 Å, O V 5572 – 5598 Å
WO stars	C IV 5801 – 5812 Å, O IV 3400 Å, O V 5572 – 5598 Å, O VI 3811 – 3834 Å, O VII 5670 Å, O VIII 6068 Å

didates photometrically. At present, 667 galactic WR stars belonging to different spectral classes are known as assembled in “Galactic Wolf Rayet Catalogue v1.25” (see “<http://www.pacrowther.staff.shef.ac.uk/WRcat/>”).

1.1.2.2 Evolution of WR stars

It has generally been admitted that O stars are the progenitors of WR stars which have shed their external layers in the form of strong stellar winds or through other eruptive incidences. Massive stars produce energy to survive on the main sequence through hydrogen fusion via CNO cycle in their cores ([de Boer & Seggewiss, 2008](#)) as follows:



Among all of the reactions mentioned above, the fourth one is the slowest. Consequently, most of the initial C along with O obtained in the CNO bi-cycle reactions

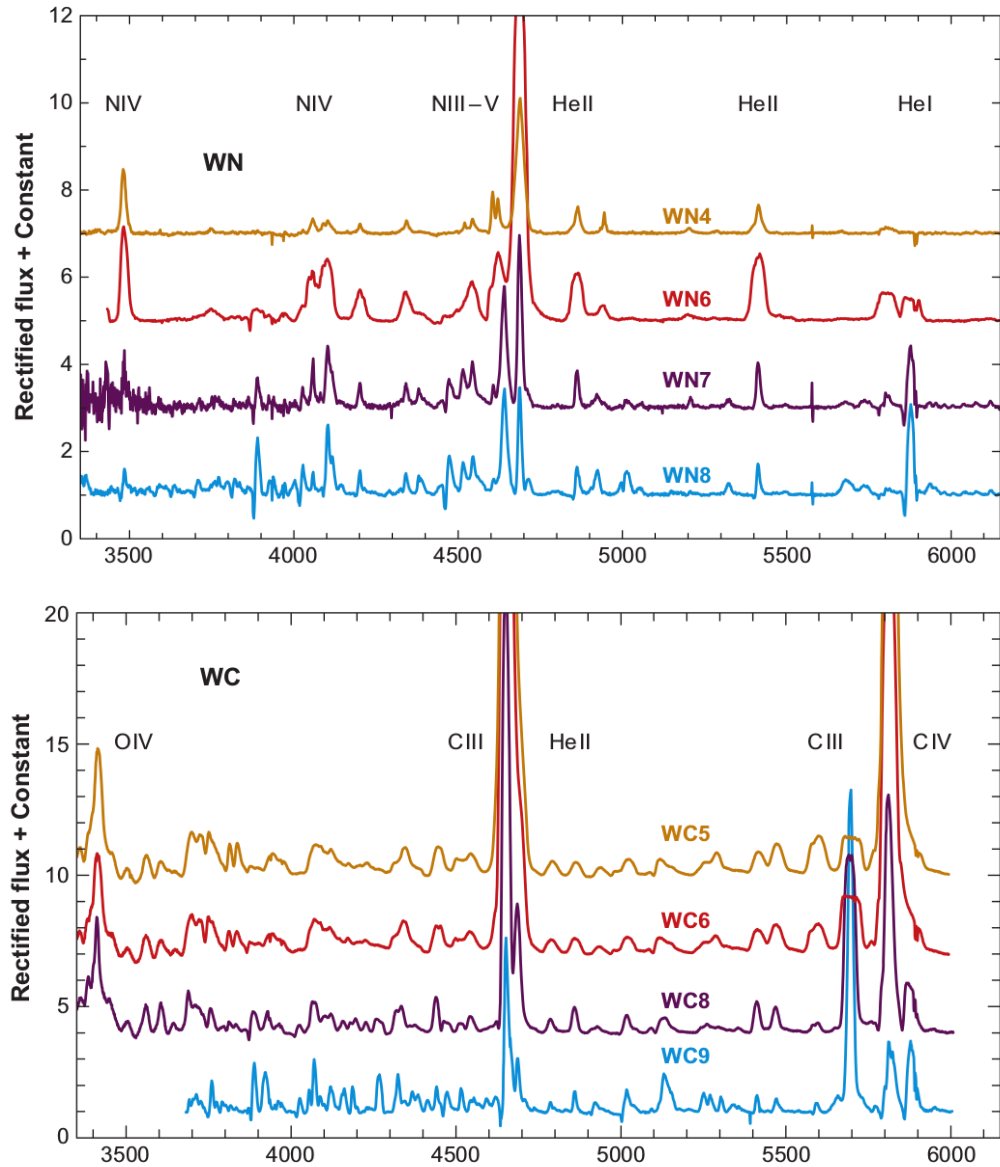
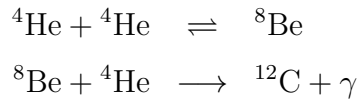


Figure 1.2: Montage of optical WN (*top*) and WC (*bottom*) spectra. The figure is adopted from [Crowther \(2007\)](#).

are transformed to N. However, total CNO nuclei stay same in number. Hydrogen is converted to helium throughout the duration when the star stays on the main sequence. If the density and temperature of the stellar core remain constant then the pressure decrease according to ideal gas law. As a result, the star would not stay in hydrostatic equilibrium any longer and must contract. This shrinkage leads to an increase in density and temperature until a new equilibrium situation is reached. If the temperature becomes high enough ($\sim 10^8$ K), further helium burning will set in

1. INTRODUCTION

the core (de Boer & Seggewiss, 2008). The fusion toward ^{12}C is a two-step process involving three α particles, thus known as the triple-alpha process:



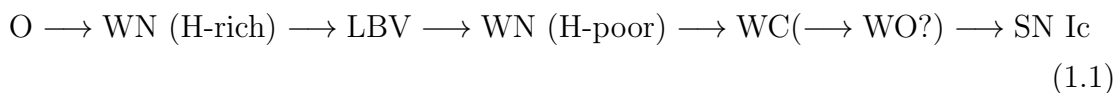
Upon sufficient accumulation of carbon nuclei, oxygen may be produced through further α captures as,



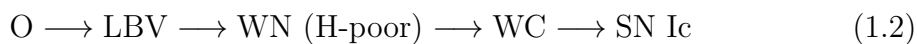
The competition in the reactions producing carbon and oxygen decides the core C/O ratio after He exhaustion. The material processed through nuclear fusion remains inside the stellar cores and cannot be noticed in the case of normal stars. On the other hand, for O stars and their successors, extreme stellar winds peel off the outer hydrogen-rich envelope. The matter present inside the convective core after nuclear processing is eventually noticed at the surface. It is also believed that mixing caused by stellar rotation together with mass-loss can facilitate nuclear processed material to reveal at the stellar surface.

It was first proposed by Conti (1975) that a massive O star may go through major mass loss in the form of winds and, as a result, initially the H-burning products and later the He-burning products existing in the stellar core are revealed at its surface. Spectroscopically, these evolutionary phases are related to the WN and WC spectral subtypes of WR stars. This general view has since been called as the ‘‘Conti scenario’’. This scenario is further supported by the discovery of intermediate stars with typical properties of Of and WR stars both (Walborn, 1977, 1982). The initial mass (M_i) of the progenitor star governs the evolutionary path followed by a massive star. For solar composition, this sequence as adapted by Crowther (2007) is given below:

for $M_i \gtrsim 75 M_\odot$,



for $75 M_\odot \gtrsim M_i \gtrsim 40 M_\odot$,



and for $40 M_{\odot} \gtrsim M_i \gtrsim 25 M_{\odot}$

$$\text{O} \longrightarrow \text{LBV/RSG} \longrightarrow \text{WN (H-poor)} \longrightarrow \text{SN Ib} \quad (1.3)$$

An O-star may either become a red supergiant (RSG) or a luminous blue variable (LBV) before attaining the WR phase. RSGs are the extremely large and cold stars. However, LBV is an exceptionally bright star whose outward radiation pressure in the external stellar layers is almost same as the inward gravitational force. This means that it can drive the expulsion of a large amount of matter from the surface in a very short time. Though the role of LBV in this chain is still poorly understood, the Conti scenario is widely accepted, implying that WC stars are at a later evolutionary stage, and come from more massive progenitors on average, than WN stars.

The evolutionary scenario of the massive star with M_i as $60 M_{\odot}$ is illustrated in Figure 1.3 (Maeder & Meynet, 1987). At the age of 3.5 Myr, when the star is evolving through the main sequence phase, strong stellar winds expose deeper layers of the star which once formed the large convective core. The products made out of H-burning via CNO cycle *i.e.* N is revealed and surface material shows He enrichment at the expense of H. Several solar masses are rapidly lost when the star is in LBV phase ($t = 3.7$ Myr) which occurs for a short time between central H and He burning. The star is identified as a WNL star during the former part of the core He burning (3.7-3.9 Myr) and later when the extreme mass-loss lead to the removal of H-rich atmosphere outside the H-burning shell, it appears as a WNE star (3.9-4.1 Myr). After 4.1 Myr, the matter enriched with N present inside the He-burning convective core is revealed in the stellar atmosphere. Later, it disappears and C and O are exposed as a result of He-burning reactions. The star spends last 0.2 Myr of its life in the WC phase and ultimately dies with a SN explosion.

The evolutionary path of a single star is decided by its initial mass as discussed in the Conti scenario above. The initial mass essential to become a WR star is further governed by the metallicity of the medium surrounding the star. It has been seen that stars born in metal-poor environments need progenitors of higher masses to do so. This fact comes as a direct consequence of the weaker line-driven winds of massive stars in low metallicity regions, as explained in Section 1.2 (Georgy et al., 2015, 2012). In addition to the initial mass and metallicity, there are many other factors such as magnetic field, rotation, binarity, etc. that influence a massive star's evolution (see Chiosi & Maeder 1986; Maeder & Meynet 2012). The presence of a

1. INTRODUCTION

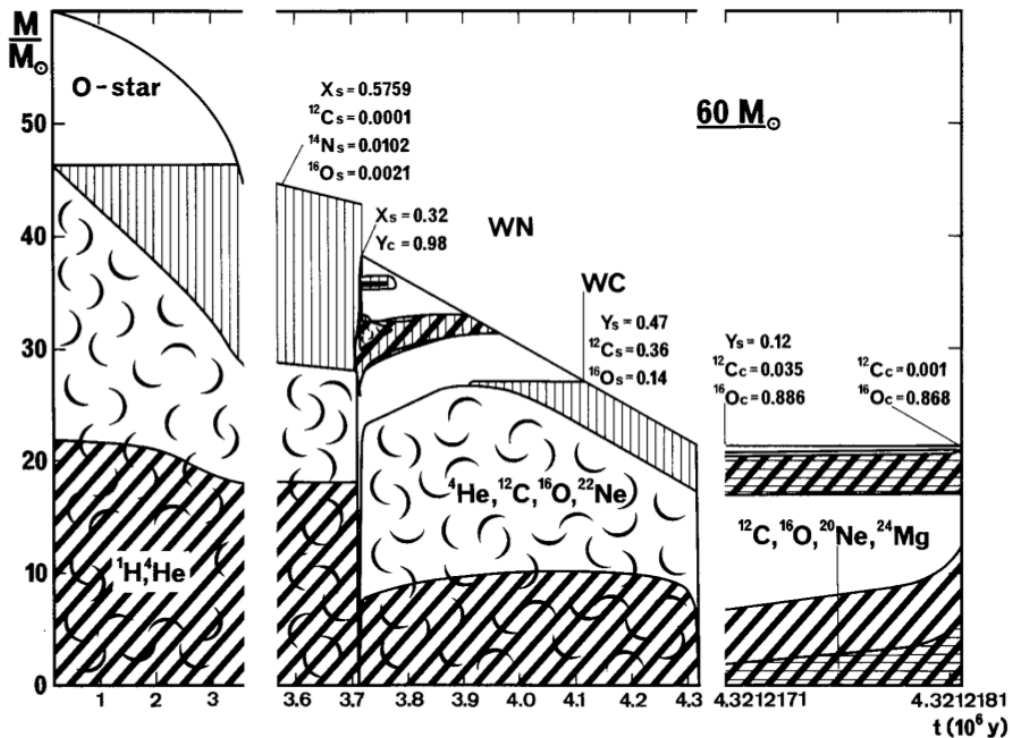


Figure 1.3: The evolution of a $60 M_{\odot}$ star with 0.02 metallicity undergoing mass-loss shown in the Kippenhahn diagram. The nuclear burning stages are indicated by cross-hatched areas while the convective regions have been highlighted using curly symbols. The figure is adopted from [Maeder & Meynet \(1987\)](#).

close companion proves to be the potential influencer. A large fraction of Galactic O stars is noticed to be existing in binary systems (see Section 1.3). Therefore, the prediction of the massive star's future deeply relies on the knowledge of its binary status.

An advanced level of complication is added to massive stars' evolution by their binarity. The binary components will grow individually as single stars when they are widely separated in the orbit. However, with the decreasing separation, the two stars will interact with each other during certain stages in their lifetimes. One possible channel of binary interaction is through Roche lobe overflow (RLOF). This occurs when the primary star's hydrogen envelope is stripped away upon interacting with the gravitational field of secondary. The primary star's mass can either be accreted by the secondary or get lost in the system through RLOF stripping leading to conservative or non-conservative mass transfer, respectively. The formation of a common envelope (CE) may also be experienced by few binaries. This phase

comes into the picture when a primary star is losing matter at a larger rate than the accretion rate of the secondary. Consequently, the secondary star’s Roche lobe is filled by the excess matter present in the system and eventually RLOF occurs. A common envelope of the material exists around the binary components with filled Roche lobes of both the stars (Iben & Livio, 1993; Podsiadlowski, 2001). Enhancement in the rotational velocity of the star, called spin-up, may also occur in binary systems where the accretion of matter onto the secondary is going on.

Therefore, there are four distinct channels of WR stars formation. The evolutionary tracks were calculated using the Binary Population and Spectral Synthesis (BPASS) code (Shenar et al., 2019). These formation channels are illustrated in Figure 1.4 and their description is given below.

1. **Main sequence WR stars** (ms-WR): These are the WR stars undergoing H-burning in the core and were “born this way” initially. They exhibit very large masses ($\gtrsim 60 M_{\odot}$ at Z_{\odot}) and give rise to strong stellar winds. Therefore, the typical WN spectra are exhibited by such stars during the main sequence phase only.
2. **Wind-stripped WR stars** (w-WR): These are the classical WR stars that came into existence through their intrinsic mass-loss in the form of winds or eruptions according to the Conti scenario described earlier. Sufficient initial mass is mandatory for a star to attain WR stage through this channel.
3. **Wind+binary-stripped WR stars** (wb-WR): The classical WR stars which were originally capable of becoming WR stars fall into this category. They have enough initial mass to become a WR star as a single object but they are a part of the binary system. Because of the binary companion, their outer envelopes are further stripped either by RLOF or via CE evolution.
4. **Binary-stripped WR stars** (b-WR): These are the classical WR stars that could never achieve the WR phase until they are accompanied by a binary companion. They lose outer layers through binary interactions only and b-WR stars have minimum initial masses extended to lower values.

1.2 Physics behind stellar winds and mass loss

The condition of hydrodynamic equilibrium is not met in massive stellar atmospheres. The radiation as well as gas pressure overcome the gravity. Consequently,

1. INTRODUCTION

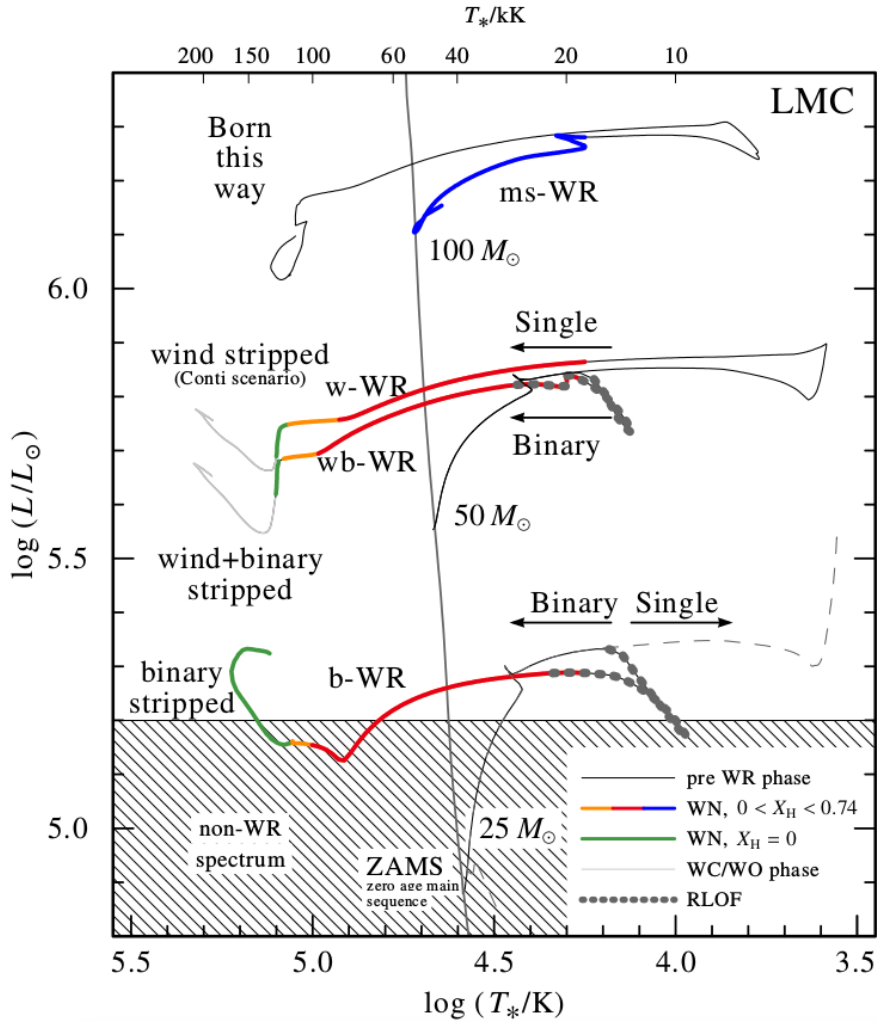


Figure 1.4: Evolutionary tracks for the formation of WR stars through the ms-WR, w-WR, wb-WR, and b-WR formation channels in the Large Magellanic Cloud ($Z = 0.008$). The figure is adopted from [Shenar et al. \(2019\)](#).

the gas flows outwards in the form of stellar winds. The continuous outflow of matter at supersonic speeds constituent the stellar winds. The winds of massive early-type stars, which are the hottest and most luminous objects, are very strong. They affect the evolution of the star itself along with the neighboring interstellar medium. The radiation pressure of the star is thought to be the driving mechanism of hot star winds.

The hot, luminous stars' winds are also called the line-driven winds as they originate from absorption in spectral lines. Massive stars mostly emit in the ultraviolet regime, where many absorption lines are seen from outer atmospheres. The momentum transfer through line-scattering is based on the fact that original

1.2 Physics behind stellar winds and mass loss

photon is emitted from the stellar photosphere in a given direction, however, the following re-emission is almost isotropic after absorption by an ion in the stellar atmosphere. Consequently, the momentum is transferred radially to the associated ion through the change in direction of the photon. Considering all such scatterings, the integrated transferred momentum is zero as the momentum transfer due to the re-emission cancels out being symmetric and the wind is accelerated radially. The resonance lines, that originate from ionic ground states or low-lying meta-stable levels, are the most efficient in accelerating the wind. The total wind plasma is accelerated by this process when the momentum gained by metal ions is shared with H and/or He present in abundance through Columb interactions. The direct transfer of momentum from the star radiation to H and/or He is less because of their few absorption lines around the maximum stellar continuum emission.

The Doppler effect has to be considered while explaining the wind acceleration from the radiation force on the plasma. The stellar photospheric radiations can interact significantly with the matter of the static atmosphere especially occupying the lower layers. Therefore, the direct radiation, having appropriate wavelength to the given spectral line, from the photosphere cannot be received by the ions in the outer layers. Hence, their acceleration is strongly diminished. Due to the outward motion of external layers, velocity gradient makes up in the stellar atmosphere. As a result, ions in the outer layers see the red-shifted photons emitted by the photosphere. Since these red-shifted photons do not interact with the intermediate layers, they can directly be absorbed by the ions in the outer atmosphere. Therefore, the Doppler effect is important to accelerate the stellar winds radiatively.

Lucy & Solomon (1970) first proposed the line driving mechanism while the most accepted line-driven wind theory called “CAK” was introduced by Castor et al. (1975). The mass loss in massive stars through line-driven stellar winds has been reviewed by Puls et al. (2008) using the standard 1D model. The mass-loss rate (\dot{M}) and terminal (maximum) velocity (v_∞) are the primary characteristics of stellar winds. Let us consider wind to be stationary, homogeneous, and spherically symmetric. According to the continuity equation, the total mass flux or \dot{M} from a spherical shell encircling the star is conserved and given as

$$\dot{M} = 4\pi r^2 \rho(r) v(r) \tag{1.4}$$

where $\rho(r)$ is the wind density and the wind velocity a distance r from the center

1. INTRODUCTION

of the star is denoted by $v(r)$. The equation of motion is presented as

$$v \frac{dv}{dr} = -\frac{GM}{r^2} - \frac{1}{\rho} \frac{dp}{dr} + g_{rad} \quad (1.5)$$

Here, the gravitational acceleration ($=GM/r^2$) is directed inwards while the gas pressure gradient force ($=dp/dr$) and total radiative acceleration (g_{rad}) are the outwards forces. The total radiative acceleration results cumulatively from the continuum and line opacity terms, *i.e.* $g_{rad} = g_{rad}^{cont} + g_{rad}^{line}$. As Equation 1.5 suggests, the total radiative acceleration has to exceed the gravity to initiate stellar wind beyond a certain point in the outer photospheric layers.

The hot stars' continuum opacity mainly comes from the Electron (Thompson) scattering. It is independent of the wavelength and may be measured as following

$$g_e = \frac{\sigma_e L_\star}{4\pi r^2 c \rho} \quad (1.6)$$

where σ_e is the electron scattering opacity and L_\star is the stellar luminosity. In fact, the overall radiative acceleration mainly arises from the line scattering process. As the bound-bound transitions are resonant in nature, therefore, intrinsically the electron scattering is much weaker than line scattering (Gayley, 1995). Sobolev (1960) realized that the radially outward motion of the gas would cause the outer atmospheric layers to see a redshifted photosphere. The blueward photons for a spectral line may, therefore, travel uninterruptedly from the photosphere until they are in resonance with that particular spectral line after red-shifting. This resonance region is associated with the geometric width called the Sobolev length and is estimated as $v_{th}/(dv/dr)$, where v_{th} is the thermal speed of the ion. Generally, Sobolev length is smaller than the typical scales of variations in the outflow caused either by opacity or velocity gradient. Therefore, the line acceleration for a single line with optical depth τ and frequency ν can approximately be given as

$$g_{rad}^{line} = \frac{L_\nu \nu}{4\pi r^2 c^2} \frac{dv}{dr} \frac{1}{\rho} (1 - e^{-\tau}) \quad (1.7)$$

where L_ν is the luminosity in spectral line of frequency ν . When $\tau < 1$, *i.e.* for optically thin lines, g_{rad}^{line} doesn't depend upon the velocity field and retains the similar form as that of Equation 1.6. Whereas, for $\tau > 1$, g_{rad}^{line} becomes significant and suggests that optically thick lines are the main drivers of the massive stars

1.2 Physics behind stellar winds and mass loss

winds. For such scenarios, g_{rad}^{line} becomes

$$g_{thick} \simeq \frac{L_{\star}}{\dot{M}c^2} v \frac{dv}{dr} \quad (1.8)$$

Here, the spatial velocity gradient (dv/dr) influences the line acceleration. The Doppler effect is the origin of such dependence and explains several peculiar characters of the radiative line driving mechanism. Thus, the force from optically thick lines remains unaffected by opacity and varies only according to the velocity gradient. If we neglect the gravity and pressure terms in equation 1.5, $v(dv/dr) \simeq g_{line}$. After substitution of $v(dv/dr)$ into Equation 1.8 provides $\dot{M} \propto L_{\star}/c^2$.

Several optically thick lines are involved in the wind acceleration actually and the mass-loss is directly related to their number. According to the CAK theory, summation of multiple lines is performed by following a line-strength distribution function where opacity is estimated using a power law. Hence, integration of the multiple lines gives the total line acceleration (e.g. Puls et al. 2000). The self-consistent solution describing the winds of hot stars is first provided by this approach. The underlying velocity of the stellar outflows is structured in the form of ‘ β -law’ which marks the key prediction of this study and is given as

$$v_r = v_{\infty} \left(1 - \frac{R_{\star}}{r} \right)^{\beta} \quad (1.9)$$

where R_{\star} is the radius of the star and v_{∞} is the wind velocity at an infinite distance from the star called ‘terminal wind velocity’. If the star is approximated as a point source then $\beta=0.5$. However, if we consider the angular size of the stellar disk, which is more realistic, $\beta \simeq 0.8$ for hot O-stars (Friend & Abbott, 1986). Further investigation and refinement of this theory has been done by Abbott & Lucy (1985), Vink et al. (2000), and Kudritzki (1996). Observationally, the typical \dot{M} for early-type stars belong to $\sim 10^{-7} - 10^{-4} M_{\odot} \text{ yr}^{-1}$ range, and v_{∞} is often of the order of $\sim 1000 - 3000 \text{ km s}^{-1}$ (Smith, 2014). More massive winds are observed in stars with more luminosity. Let us transform these quantities to the typical kinetic energy of the wind and it is found that $L_{wind} = 0.5 \dot{M} v_{\infty}^2 \sim 10^{34} - 10^{38} \text{ erg s}^{-1}$. The comparison of bolometric luminosities, $L_{bol} \sim 10^{37} - 10^{40} \text{ erg s}^{-1}$, of massive stars with their L_{wind} shows that only a tiny fraction like 0.1% or so of the total output energy of the star flows into the wind still, it is very important as already discussed.

1.3 Observational phenomena related to massive stars

Massive stars are generally found in binary or higher multiplicity systems. Although, the fraction of massive stars in binaries is not well constrained but conservatively, the lower limit is 50%. The actual fraction may probably be considerably larger (Sana et al. 2012a; Sana & Evans 2011). The winds of two stars in a massive binary interact with each other and a fraction of wind kinetic energy is transformed to heat energy. The winds interaction is the source of multiple features which can be observed throughout the electromagnetic spectrum covering from radio waves to gamma-ray regime. For example, the collision between the stellar winds in massive binaries leads to the formation of hydrodynamic shocks in the wind collision region (WCR). A schematic view of the WCR has been shown in Figure 1.5.

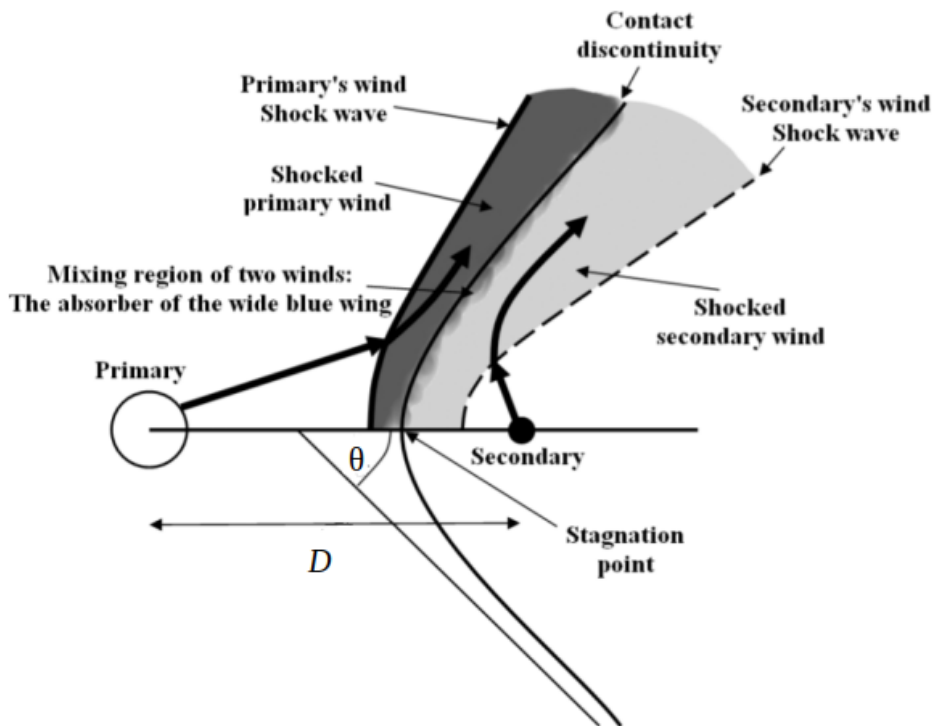


Figure 1.5: The geometrical structure of the interaction region of the primary and secondary star's winds mixing near the contact discontinuity. The figure is reproduced from Kashi & Soker (2009).

The concept of wind-wind collision has been introduced theoretically by Pri-lutskii & Usov (1976) and Cherepashchuk (1976). The interaction of the colliding

1.3 Observational phenomena related to massive stars

stellar winds will manifest itself in the form of two oppositely oriented shocks-fronts. A contact discontinuity separates the two shocks in between the stars. At each shock front, part of the kinetic energy is thermalized. The location of the wind collision is determined by comparing the wind momentum of both the stars. For the winds having comparable strength, WCR is located in between the two stars at an equal distance from both and is perpendicular to the line joining the center of the binary components. On the other hand, the shocked gas in the collision zone is wrapped around the binary component which has relatively weaker stellar wind provided the two outflows are of different strengths. Considering the spherical outflow of matter from the stars approximately radially to the shock region, the wind momentum ratio, η , governs the location where the winds meet. η is defined as

$$\eta = \frac{\dot{M}_2 v_{\infty,2}}{\dot{M}_1 v_{\infty,1}} \quad (1.10)$$

where \dot{M} is the mass-loss rate and v_{∞} defines the terminal wind velocity for the primary and secondary stars referred to as 1 and 2, respectively, (Stevens et al., 1992). The distances r_1 and r_2 are measured from the stagnation point in the location of winds interaction to the center of primary and secondary star, respectively, and are given as

$$r_1 = \frac{1}{1 + \eta^{1/2}} D, \quad r_2 = \frac{\eta^{1/2}}{1 + \eta^{1/2}} D \quad (1.11)$$

where D is the separation between the centers of two stars. To the first approximation, the shape of the wind collision zone is a cone with a half opening angle (θ) set by the value of η (Eichler & Usov, 1993) and shown in Figure 1.5.

In order to deal with the stellar wind hydrodynamics, whether single or multiple systems, an important concept of *strong shocks* have to be taken into account. Strong shocks are those hydrodynamic shocks where the upstream gas pressure is negligible as compared to the gas present in the downstream region. Upstream or the pre-shock gas is constituted of the gas which has not yet passed through the shock region, whereas the downstream or post-shock gas has already crossed that region. The ambient stellar winds, whose temperatures are given by photospheric temperature of the stars ($\sim 10^4$ K), travel with hypersonic terminal wind speeds of the order of several thousand kilometer per second. Thus, it is safe to estimate the properties of the post-shock region like density, velocity, and temperature by assuming the strong shocks limit.

1. INTRODUCTION

Let us consider a one-dimensional shock wave and the shock is assumed to be independent of time. Suppose the pre-shock gas having pressure P_0 , density ρ_0 , temperature T_0 , is traveling with velocity v_0 relative to the shock in its own rest frame. The corresponding gas properties in the post-shock region are P_1 , ρ_1 , T_1 , and v_1 . The next step is to obtain the equations of mass flux, momentum flux, and energy conservation across the shock zone.

Since the matter is neither created nor destroyed in the shock zone. Therefore, the mass flux approaching the shock region from the upstream gas per unit area and time has to be the same as that of the mass flux going out of the shock region to the downstream. Thus, the mass flux conservation equation is

$$\rho_0 v_0 = \rho_1 v_1 \quad (1.12)$$

Similarly, the momentum flux of the upstream gas ($=\rho_0 v_0$) has to be compared with that of the downstream gas ($=\rho_0 v_0 v_1$) after it passes through the shock region. The change in momentum in two regions should be arising from their pressure difference as

$$\rho_0 v_0 v_1 - \rho_0 v_0^2 = P_0 - P_1 \quad (1.13)$$

In the case of an “adiabatic” shock where the gas doesn’t cool radiatively, the total energy should also remain conserved. The work done by the gas (considered as per unit area per unit time) while moving from pre-shock to post-shock region must correspond to the energy difference of the two regions. Since this work done is related to the difference in pressure, therefore, $E_1 - E_0$ is given as

$$E_1 - E_0 = P_0 v_0 - P_1 v_1 \quad (1.14)$$

where E_0 and E_1 represent the sum of the kinetic energy and internal energy of the gas in the pre-shock and post-shock regions, respectively and are defined as below.

$$\begin{aligned} E_0 &= \rho_0 v_0 \left(\frac{1}{2} v_0^2 + \frac{1}{\gamma - 1} \frac{P_0}{\rho_0} \right), \\ E_1 &= \rho_1 v_1 \left(\frac{1}{2} v_1^2 + \frac{1}{\gamma - 1} \frac{P_1}{\rho_1} \right) \end{aligned} \quad (1.15)$$

where γ is the specific heats ratio at constant pressure and volume. Equations 1.12, 1.13, and 1.14 are used to determine the physical properties of the boundary

1.3 Observational phenomena related to massive stars

region. These are known as the *Rankine-Hugoniot* conditions. Essentially, the mass, momentum, and energy conservation are expressed by these conditions.

An important quantity for the study of shocks called *Mach Number* (M_0) is defined as the ratio of the wind velocity to the sound speed (c_s) as

$$M_0 = v_0/c_s, \quad c_s^2 = \gamma \frac{P_0}{\rho_0} \quad (1.16)$$

For the case of strong adiabatic shocks, where $M_0 \gg 1$ and $\gamma = 5/3$, the above equations can be solved to express the physical properties (like velocity, density, pressure, and temperature) of the post-shock region in terms of the corresponding quantity in the pre-shock region. The derived relations are

$$\frac{\rho_1}{\rho_0} \simeq 4, \quad \frac{v_1}{v_0} \simeq \frac{1}{4}, \quad P_1 \simeq \frac{3}{4}\rho_0 v_0^2, \quad T_1 \simeq \frac{3\mu m_H}{16k} v_0^2 \quad (1.17)$$

μ is the mean molecular weight in terms of the mass of the H-atom (m_H). For the intense shock scenario, the density of the gas perturbed by the shock becomes four times relative to the unperturbed gas. This is called the compression ratio. The pressure and temperature also increases in the post-shock region followed by the gas compression. However, the perturbed gas moves with lesser velocity than before entering the shock region.

The charged particles can be accelerated to very high energies by the astrophysical shocks. Therefore, massive binaries can act as particle accelerators by the strong shocks formed in the colliding stellar winds. The massive systems displaying such features are named as particle accelerating colliding wind binaries (PACWBs). [De Becker & Raucq \(2013\)](#) has published the first catalogue of PACWBs. The diffusive shock acceleration (DSA) is believed to be the main mechanism for accelerating particles through the formation of strong hydrodynamic shocks during the wind collision ([Bell, 1978](#); [Drury, 1983](#); [Fermi, 1949](#)). [Figure 1.6](#) illustrates the DSA mechanism presenting four scenarios separately. The upstream gas is stationary in situation (a) and U is the supersonic velocity at which the shock passes through the medium. Contrarily, the gas in the upstream region has bulk velocity $v_0 = U$ when crossing the shock region if the shock itself is stationary as in situation (b). Since strong shocks are being considered, therefore, the bulk velocity of the downstream gas $v_1 = v_0/4 = \frac{U}{4}$ (see Equation 1.17). In the rest frame of upstream gas, as in situation (c), the velocity of the downstream gas is $v'_1 = U - \frac{U}{4} = \frac{3}{4}U$. In the opposite scenario (d), the upstream gas moves with a velocity $v'_0 = \frac{3}{4}U$, where the

1. INTRODUCTION

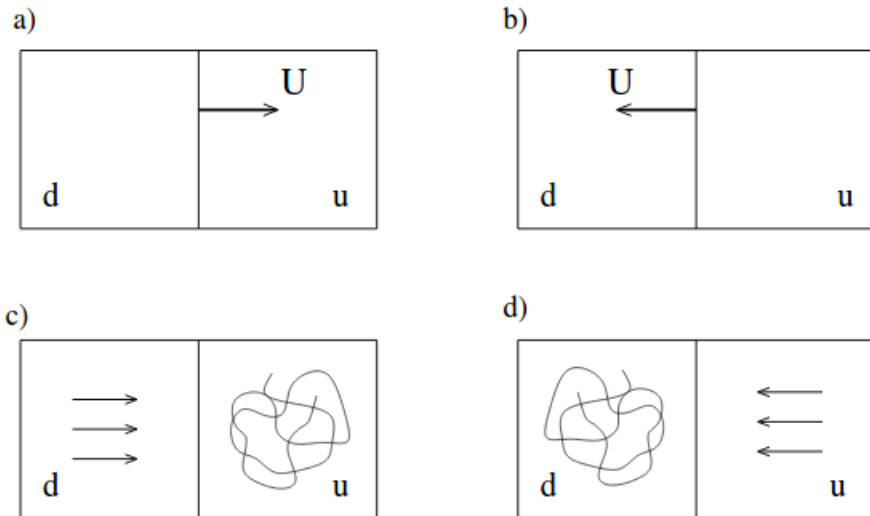


Figure 1.6: Illustration of first-order Fermi mechanism to explain particle acceleration by the strong shocks. The upstream and downstream regions are designated using the letters ‘u’ and ‘d’, respectively. The scattering of particles in the two regions because of magneto-hydrodynamic processes has been shown in the panels (c) and (d). All the four scenarios are explained in the text individually. The figure is taken from Longair (1994).

downstream gas is assumed to be at rest. Ultimately, the conclusion of the present argument is “the individual particles encounter the gas traveling with same speed when they cross the shock from any direction”.

Let us first evaluate the average increase in the particle’s energy while crossing the shock from upstream to the downstream region. Performing Lorentz transformation, the energy of the particle when it passes into the downstream region is

$$E_1 = \gamma_V(E_0 + p_x V) \quad (1.18)$$

where X-coordinate is taken to be perpendicular to the shock and $V = \frac{3}{4}U$. The shock is non-relativistic because $V \ll c$ and hence the Lorentz factor, $\gamma_V = 1$. The particles are moving at relativistic velocities, therefore, $E_0 = pc$ and hence $p_x = (E_0/c)\cos\theta$. Ultimately,

$$\Delta E = pV\cos\theta, \quad \frac{\Delta E}{E_0} = \frac{V}{c}\cos\theta \quad (1.19)$$

The particles crossing the shock arrive within an angular region of θ to $\theta+d\theta$ with the probability proportional to $\sin\theta d\theta$. Whereas, the rate of their approach to the shock

1.3 Observational phenomena related to massive stars

front is associated to the X-component of their velocities, $c \cos\theta$. At the end, the particle cross the shock front with a probability proportional to $\sin\theta\cos\theta d\theta$. Upon normalizing such that the probability distribution integral, over all the particles approaching the shock front, is equal to one *i.e.* those for which $\theta \in [0:\pi/2]$, it is found that

$$p(\theta) = 2\sin\theta\cos\theta d\theta \quad (1.20)$$

Hence, the average energy gain of the particle after shock crossing is

$$\left\langle \frac{\Delta E}{E_0} \right\rangle = \frac{V}{c} \int_0^{\pi/2} 2\cos^2\theta\sin\theta d\theta = \frac{2}{3} \frac{V}{c} \quad (1.21)$$

The velocity vector of the particle is randomized without any loss of energy when scattered into the downstream region. Later it crosses the shock again, as shown in Figure 1.6(d), followed by another fractional energy gain of $(2/3)(V/c)$. As a result, the average fractional energy gained by the particle while making one round trip across the shock region is given as

$$\left\langle \frac{\Delta E}{E_0} \right\rangle = \frac{4}{3} \frac{V}{c} \quad (1.22)$$

No such crossings exist where particles may lose energy. Hence, the process goes linearly with V/c , and is therefore very efficient in accelerating particles to relativistic speeds. The iterative nature of this process is crucial for the DSA mechanism. Once the high energy particles cross the shock-front, they begin interacting with Alfvén or magneto-hydrodynamic waves as well as magnetic turbulence present in the medium. This leads to the scattering of particles isotropically which can further pass through the shock to another direction. The resultant of this multiplication is that the particles are accelerated up to very large Lorentz factors and attain very high energies. The relativistic particles have an energy spectrum explained with a power law of the form

$$N(E) \propto E^{-n} \quad (1.23)$$

Here, n is the power-law index. When dealing with a population of relativistic electrons, n is called the electron index. Thus, the first-order Fermi acceleration mechanism proves to be a good candidate, in the context of massive stellar winds possessing strong hydrodynamic shocks, to justify the presence of relativistic particles (both hadrons and electrons) which are needed to explain many observational

features associated with massive stars. The important characteristics of massive stars observed in different wavebands are described below.

1.3.1 Thermal and non-thermal radio emission

The strong radiation fields of the massive stars ionize the stellar winds. Thus, the free electrons interact with the ions, resulting in free-free thermal emission detectable from IR to radio frequencies. The detection of radio emission from massive early-type stars has been made since the early 1980s (Abbott et al., 1981, 1980; White & Becker, 1983). The radio emission from the stellar winds of massive stars comprises of two components:

1. Thermal emission - This is the continuous thermal free-free emission arising from spherically symmetrical mass-loss flow having brightness temperature of $\sim 10^4$ K, and
2. Non-thermal emission - This component of the massive stars' radio radiation emission is mainly non-steady, variable, and is associated with relatively higher brightness temperature of $\sim 10^6$ - 10^7 K. The non-thermal synchrotron radiation from the electrons accelerated in the shocked region of the stellar winds is thought to be a reason behind this kind of emission.

Wright & Barlow (1975) and Panagia & Felli (1975) presented a model for deriving the radio and IR spectrum resulting from the free-free emission of ionized stellar winds. The emergent radio flux S_ν , under the assumptions of homogeneous and spherical winds, depends upon the different stellar parameters as follows:

$$S_\nu = 2.32 \times 10^4 \left(\frac{\dot{M}z}{v_\infty \mu} \right)^{4/3} \left(\frac{\zeta g_\nu \nu}{d^3} \right)^{2/3} \quad (1.24)$$

where g_ν is the quantum correction factor called the ‘‘Gaunt Factor’’. It is used for the semi-classical formula for the free-free radiation emission and is estimated as

$$g_\nu = 9.77 \left(1 + 0.13 \log \frac{T_e^{3/2}}{z\nu} \right) \quad (1.25)$$

Here, the different symbols like ν , d , z , μ , ζ , and T_e describe the frequency in Hz, distance to star in kpc, rms ionic charge, mean molecular weight, mean number of electrons per ion and electron temperature, respectively. S_ν is measured in Janskys

1.3 Observational phenomena related to massive stars

and can be utilized to estimate mass-loss rates. The largest uncertainties in \dot{M} derived by this method comes from errors in measuring stellar distances, composition as well as in the ionization state of the gas in the radio-emitting region. Thus, the thermal emission is the continuum radiation if mass-loss is considered to be homogeneous having constant or accelerating velocity. This emission is described by a power law of the form

$$S_\nu \propto \nu^j \tag{1.26}$$

where j is equal to about 0.6, in agreement with many observations.

On the other hand, j for non-thermal emission is found to be significantly lower than that of thermal emission and can even be negative in some cases. Additionally, high variability and non-steadiness are associated with this non-thermal component. Also, the brightness temperature associated with this emission is larger than that of the thermal emission (White & Becker, 1983). As mentioned above, non-thermal emission originates from the synchrotron radiation mechanism for which mainly two ingredients are required (White, 1985). First is the magnetic field presence, and the existence of a population of relativistic electrons is second, such that when these highly energetic charged particles gyrate around magnetic field lines, synchrotron radiation emission takes place. The scaling relation for flux density of the non-thermal emission given is as

$$S_\nu \propto \nu^{-(n-1)/2} \tag{1.27}$$

where the electron distribution is described by the index n and is equal to ~ 2 . The cosmic rays are also believed to be produced by this mechanism. The overall radio spectrum of PACWBs, in particular, is of composite nature where both the thermal as well as non-thermal processes contribute. For example, the radio spectrum for WR 147 is shown in Figure 1.7. Here, the total observed flux is illustrated by the solid line which is sum of the two types of emission. The dashed line represents the thermal emission with flux $S_\nu \propto \nu^{0.6}$, whereas the dotted line having a power law of $\nu^{-0.5}$ shows the non-thermal part of the total emission. A turn-over occurs at the low-frequency region of the spectrum due to the free-free absorption of non-thermal flux.

The intrinsic non-thermal emission is expected to be affected by several absorption processes that will change the resulting shape of the non-thermal spectrum. The combined action of the free-free absorption from the surrounding material, the Razin effect due to the surrounding plasma reducing the energy of the relativistic particles, and the synchrotron self-absorption are responsible for the low frequency

1. INTRODUCTION

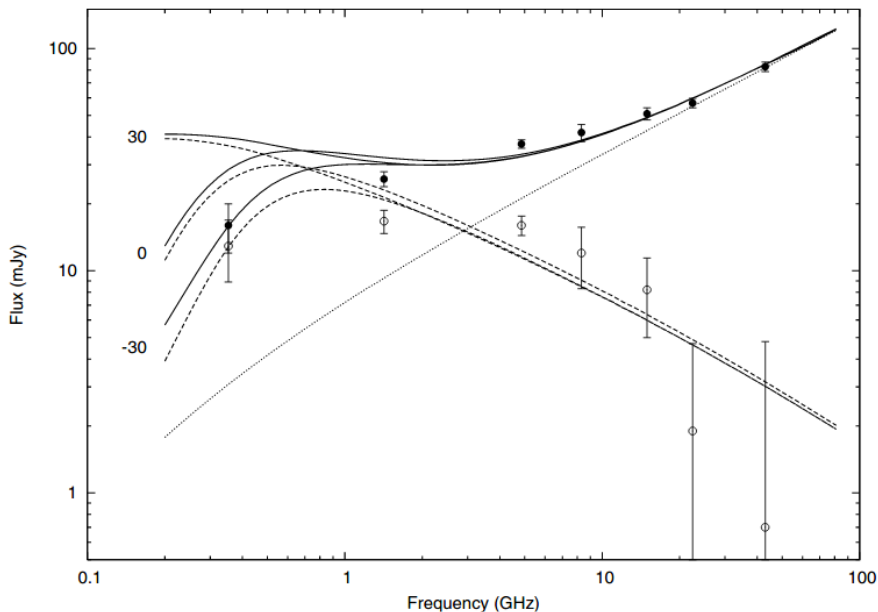


Figure 1.7: Fitted spectrum for WR 147, including total (solid line), synchrotron (dashed line), and thermal (dotted line) flux. The open circles are synchrotron fluxes estimated by subtracting a thermal component from the total observed fluxes. The figure is adopted from [Pittard et al. \(2006\)](#).

absorption (see Figure 1.7; detailed models can be found in [Dougherty et al. 2003](#)). Thus, the non-thermal flux density is expected to grow with frequency from a turn-over frequency (likely to occur at a fraction of GHz in the case of wide systems; [De Becker 2007](#)) before it becomes maximum at few GHz frequency. The turn-over frequency, and hence the maximum, is strongly dependent on the absorption process and the physical parameters of the system that is considered. The free-free absorption seems to be the dominant absorption factor as suggested by the recent models and observations.

1.3.2 Infra-red emission

The properties of the stellar wind consisting of plasma can be analyzed using the IR, (sub)millimeter, and radio continua. As it has already been mentioned in Section 1.3.1 that radio and infra-red observations show power-law spectra formed by free-free emission from the stellar winds. Other effects like velocity stratification have to be taken into account while concentrating on lower frequencies. [Wright & Barlow \(1975\)](#) already pointed it out that such phenomena are important to explain at least

1.3 Observational phenomena related to massive stars

the IR spectrum. Therefore, the infra-red spectra of the massive stars steepen and have $j \sim 0.9$. The acceleration of stellar winds is still in progress in the regions from where this emission originates (Morris et al., 1993).

Many of the WC type stars are known to have an excess infrared emission, which is usually interpreted as due to dust emission (Williams, 1995). The dust surrounding the massive stars absorb the photospheric UV radiation and the subsequent re-emission takes place in the IR wavelength regime. Scattering doesn't affect the IR radiations much while passing through dense regions. Most of the WC9 and a few WC8 stars are seen to have 1-2 orders of magnitude higher flux levels above the free-free continuum of the typical Planckian spectra of massive stars which peak near $4 \mu\text{m}$. The persistent circumstellar dust formation gives rise to their enhanced IR emission (Williams et al., 1987). The greatest difficulty to accept the dust existence in the case of massive, hot stars is that their intense radiation fields should evaporate the grains as soon as they are formed. The grains may survive under two circumstances, one is that they are shielded from the intense radiation in some way or they are located far away from the star itself. In the latter case, the density is too low at larger distances for the formation of dust and molecules in a WR wind accumulating $\sim 5 M_{\odot} \text{ yr}^{-1}$. It was suggested by Usov (1991) that the collisionally shocked WC7 stellar wind could produce dust when cooled efficiently. This effort was the first of its kind to tackle the underlying difficulty in explaining dust formation in hostile environments of some WC type stars. This emission strongly depends upon the spectral subtype. However, certain regions of higher density have to prevail in WC stellar winds than found in uniform, spherical winds to form grains efficiently. This can be attained under few circumstances e.g. clumping or disk-like structure of the winds or compression of the post-shock gas in the WCR of a colliding wind binary (CWB). There exist an ample number of evidences where we see that WR winds are clumpy rather than homogeneous (e.g. Chené et al. 2020). Also, some stars are observed to have non-spherical winds revealed in their polarimetric studies (e.g. Arora et al. 2019b). The third category also finds its place in many WR binary systems (e.g. Arora & Pandey 2020; Arora et al. 2019a). Still, it is not precisely known how grains form in the hot stellar winds where conditions are very distinct from those of cool evolved stars which show this phenomenon rather more frequently. For a better understanding of the dynamics of hot stellar winds, such phenomena have to be explored extensively.

1.3.3 Optical and UV emission

The hot, luminous stars with $\sim 30,000$ K effective temperature emit mostly in the far UV regions as per Wien's law. Therefore, a major portion of the bolometric luminosity of O- and WR- stars is made up of ultra-violet photons. However, the long-wavelength tail part of their spectral energy distributions (SEDs) is constituted by the optical waveband photons.

Being highly dense, the material present in the expanding hot star winds is optically thick to a number of atomic spectral-line transitions. The line-scattered radiation within the wind manifest itself in the form of a characteristic line profile called 'P-Cygni profile'. This nomenclature is taken from the star P-Cygni in which it was first recognized that such line profiles are indicative of mass outflow from the astrophysical sources (Morton, 1967). Figure 1.8 illustrates the process responsible for P-Cygni line profile formation. As a consequence of the Doppler effect, the resonance line from a column of material approaching the observer in the front side of the star is blueshifted. Thus, an absorption trough results when the stellar radiation is scattered out of this direction. In other words, the particular line profile is observed with reduced flux on its blue side. However, the wind material present in the lobes located on either side of this absorption column may also cause radiation scattering toward the observer. Any of the approaching or the receding hemispheres may scatter the radiation, therefore, it can either be blue- or red-shifted, respectively. Hence, the additional flux received at the observer end displays symmetrically enhanced emission on both the sides of center of the associated line. When the deficient blue-side flux is combined with this symmetric emission, an asymmetric P-Cygni line profile emerges. An apparent blueward absorption and redward emission is presented in such scenarios.

For massive stars, the P-Cygni profiles are ubiquitously seen in the UV wavelengths. These are the direct indicators of the stellar winds. The asymptotic wind speed, v_∞ , can be measured quite unambiguously from the blue edge of the absorption in these P-Cygni profiles. The saturated C IV $\lambda 1548-51$, or Si IV $\lambda 1393-1402$ P-Cygni profiles observed using Hubble Space Telescope or International Ultraviolet Explorer have provided quite accurate wind velocities for OB and WR stars (Lamers et al., 1995; Prinja et al., 1990). On the other hand, optical spectroscopic radial velocity studies of massive stars help to uncover the spectroscopic nature of stellar systems which leads to the determination of binary orbital parameters and masses

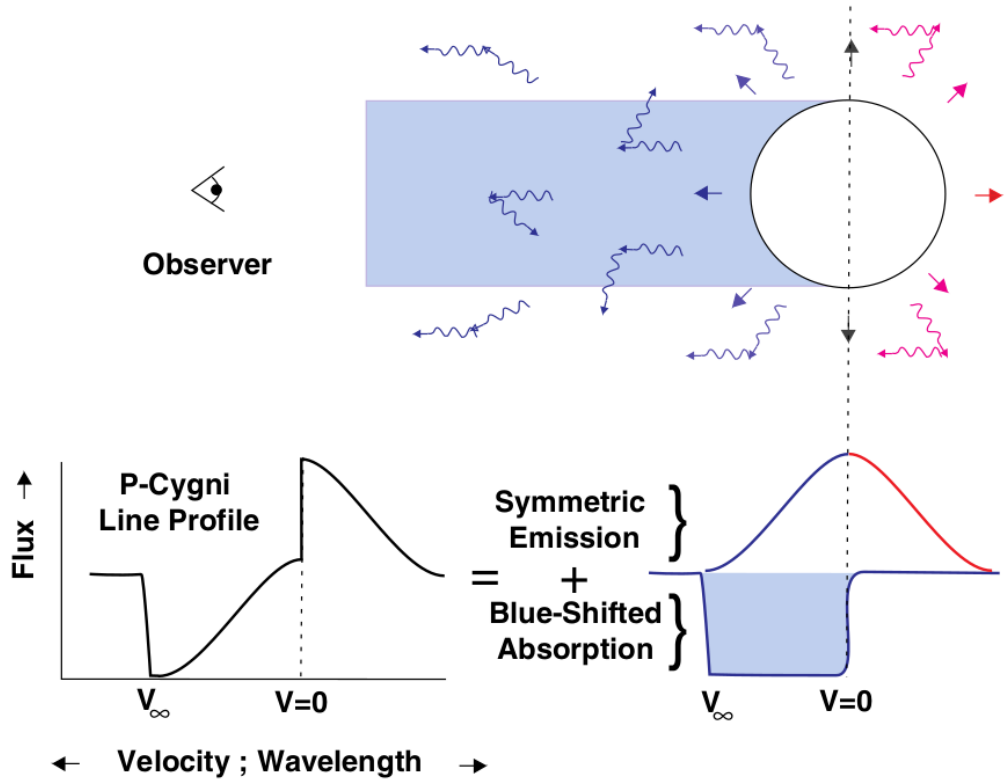


Figure 1.8: Illustration of P-Cygni line profile formation in an outflow which is expanding. The figure is adopted from [Owocki \(2013\)](#).

of the components useful for further investigation of massive star properties (e.g. [Gamen et al. 2006](#); [Morrell et al. 2001](#)).

1.3.4 Thermal X-ray emission

The high energy part of the electromagnetic spectrum is constituted by X-rays with energy from 0.1 to 100 keV. Early type stars were first detected in X-rays by *Einstein* observations of the Cyg OB2 region and the Carina Nebula ([Harnden et al. 1979](#), [Seward et al. 1979](#)). It was hard to explain the emission with coronal activity, since X-ray emission from corona should suffer significant photoelectric absorption by stellar wind, which is absent in the observed spectra. X-ray emission should arise farther out in the wind. The X-ray luminosity in the 0.2-4.0 keV band shows a strong linear correlation $L_X/L_{bol} \sim 10^{-7}$ ([Harnden et al. 1979](#), [Pallavicini et al. 1981](#)). The correlation is independent of the spectral type between A5-O3, indicating a universal mechanism for X-ray emission.

The shocks generated within the radiatively-driven winds of single O-stars are

1. INTRODUCTION

thought to emit mostly in the soft X-rays (Berghoefer et al., 1997; Lucy, 1982; Lucy & White, 1980). The line-driven winds are inherently not stable to doppler perturbations. The most suitable reason is little enhancement in the speed of a packet in the outflow will push the packet out of the underlying wind material shadow. As a result, the wind packet gets accelerated upon receiving more of the photospheric flux. Therefore, single star winds have structures and are prone to instabilities (Feldmeier et al. 1997; Owocki et al. 1988). As a result, the massive stellar winds become clumpy and produces shocks within the wind of a single star when several clumps of different velocity collide with each other throughout the outflow. The soft X-ray emission is generated in single hot stars by these distributed shocks. The typical temperature associated to the X-ray emission from single massive stars is $\sim 10^6$ K (suggesting that the shocks are not very strong). Also, they are not significantly dependent upon time. A part of this emission originates from a distance of around two stellar radii above the photosphere or may be from further interior parts of the wind as suggested by high-resolution X-ray spectroscopy of massive stars with high resolution spectrographs on-board *Chandra* and *XMM-Newton* (Cassinelli et al. 2001; Kahn et al. 2001).

An additional source producing X-ray emission in the case of massive binary systems is the wind collision in between the binary components on top of the intrinsic X-ray emission given by each star individually (Cherepashchuk 1976; Prilutskii & Usov 1976). However, wind collision is strong only if the stellar winds have attained sufficiently high velocity before colliding and they are close enough to each other as well (Stevens et al., 1992). The X-ray emission from the colliding winds can be distinguished from that of the background emission arising from the individual stars as the shocks in the wind collision are expected to have temperatures about a factor of 10 or so higher than those of the “distributed shocks” in the individual winds. Again, the individual wind has to reach their maximum velocities before interacting with one another. Further, the emission from the wind-wind collision zone shows high variability due to intrinsic alterations of the emitting region or modifications in the material characteristics present in between the observer and the WCR or both may also affect simultaneously. The massive binaries are generally X-ray brighter when compared to the apparently single stars (Pollock, 1987).

The thermal X-ray emission, described earlier, from the individual as well as WCR dominates below 10 keV in the X-ray spectrum of massive binaries. The X-ray spectrum of massive binaries presents typical features of plasma heated to

the temperature of 10^6 - 10^7 K with several emission lines. The unprecedented sensitivities along with the improved spectral resolution of X-ray detectors carried by observatories like *Chandra* and *XMM-Newton* has led to the major progress of this research field. The intense monitoring of X-ray emission modulations in the CWBs has been performed by these instruments. Additionally, the large scale surveys of several clusters and associations, where massive stars reside, by both of these satellites have refined the global view of the X-ray emitting early-type stars, and particularly massive binaries.

1.3.5 High energy X-ray and Gamma-ray emission

The thermal radiation processes completely dominate the emission in IR to soft X-rays over the non-thermal emission from the stars and/or WCR. However, the non-thermal radiations begin to reveal beyond 10 keV in the spectrum of massive binaries. The high energy particles accelerated to relativistic speeds can interact with the radiation fields of the stars along with the high density wind material of the WCR. Photons are emitted by this interaction through several phenomena like anisotropic inverse Compton (IC) scattering, relativistic bremsstrahlung, and neutral pion decay (Benaglia & Romero 2003; Eichler & Usov 1993; Pittard & Dougherty 2006; Reitberger et al. 2014).

The population of accelerated particles (mostly electrons) responsible for the synchrotron radiation gives rise to the high energy X-ray photons as well through IC scattering of the stellar UV photons. The local energy density of the radiations, and the energy and spatial distribution of electrons are the main factors deciding the IC emission. Another factor to consider is the scattering angle which defines the angle between direction of the incoming stellar photons and line of sight to the observer. Major energy of the non-thermal electrons is lost through their cooling by IC scattering in CWBs. The resultant non-thermal X-ray and gamma-ray luminosities exceed by several orders of magnitude from the radio synchrotron luminosity. Further, when the high-energy electrons pass through the Coulomb field of the wind plasma, another process of relativistic bremsstrahlung comes into play. This mechanism of radiation emission also depends upon the energy distribution along with the spatial distribution of high-energy electrons and the number density of plasma constituting the wind. Since the bremsstrahlung radiation emitted by a nucleus of mass M has intensity $\sim(M/m_e)^{-2}$ times the intensity produced by an electron, therefore, mostly the relativistic electrons are involved in the bremsstrahlung emission.

1. INTRODUCTION

If the protons, among the constituents of wind material, are also accelerated along with the electrons then they may also interact with the ambient ions. As a result, gamma-rays are produced through hadronic neutral pion decay channel as

$$p + p \longrightarrow \pi^0 + X, \quad \pi^0 \longrightarrow \gamma + \gamma \quad (1.28)$$

Similarly, the factors determining this emission are the wind plasma number density and spatial-energetic distribution of high-energy protons at this time. Therefore, non-thermal nucleons population is revealed by the process of pion decay in a similar way the population of non-thermal electrons is associated with the IC and bremsstrahlung emission mechanisms. The expected gamma-ray luminosity made up of photons with energy >100 MeV lies in the range 10^{32} - 10^{33} erg s $^{-1}$ for isolated massive stars in the typically dense surrounding medium (Benaglia et al., 2001).

1.3.6 Energy budget of massive binaries

The energy budget of astrophysical sources is addressed to find out the source of the energy which is being utilized by certain physical processes active in those scenarios. The energy budget of CWBs has been schematically illustrated in Figure 1.9. A star's bolometric luminosity is the energy reservoir of the winds flowing out of its surface. The winds are derived through radiative energy conversion into the mechanical energy. In context of the energy conversion per unit time, kinetic energy of the stellar winds is measured using the rate of matter deposition into the wind or mass-loss rate and its terminal velocity. A tiny fraction of the bolometric luminosity is converted to the wind kinetic energy ($\simeq 0.1\%$; calculated in Section 1.2). Further, only $\simeq 0.1\%$ of the total wind kinetic power actually goes into the wind-wind interaction region of CWBs while a major portion of wind energy is transferred to the interstellar medium where it is not undergoing any such interaction. The hydrodynamic shocks are fed by this much amount of energy which is injected into the WCR. Although, the fraction of this energy is small but still it provides important insights into different physical properties of the massive systems and dynamics of their stellar winds. The different processes active in massive binaries (explained earlier) and the percentage of total wind kinetic power consumed by each of them has been illustrated in Figure 1.9.

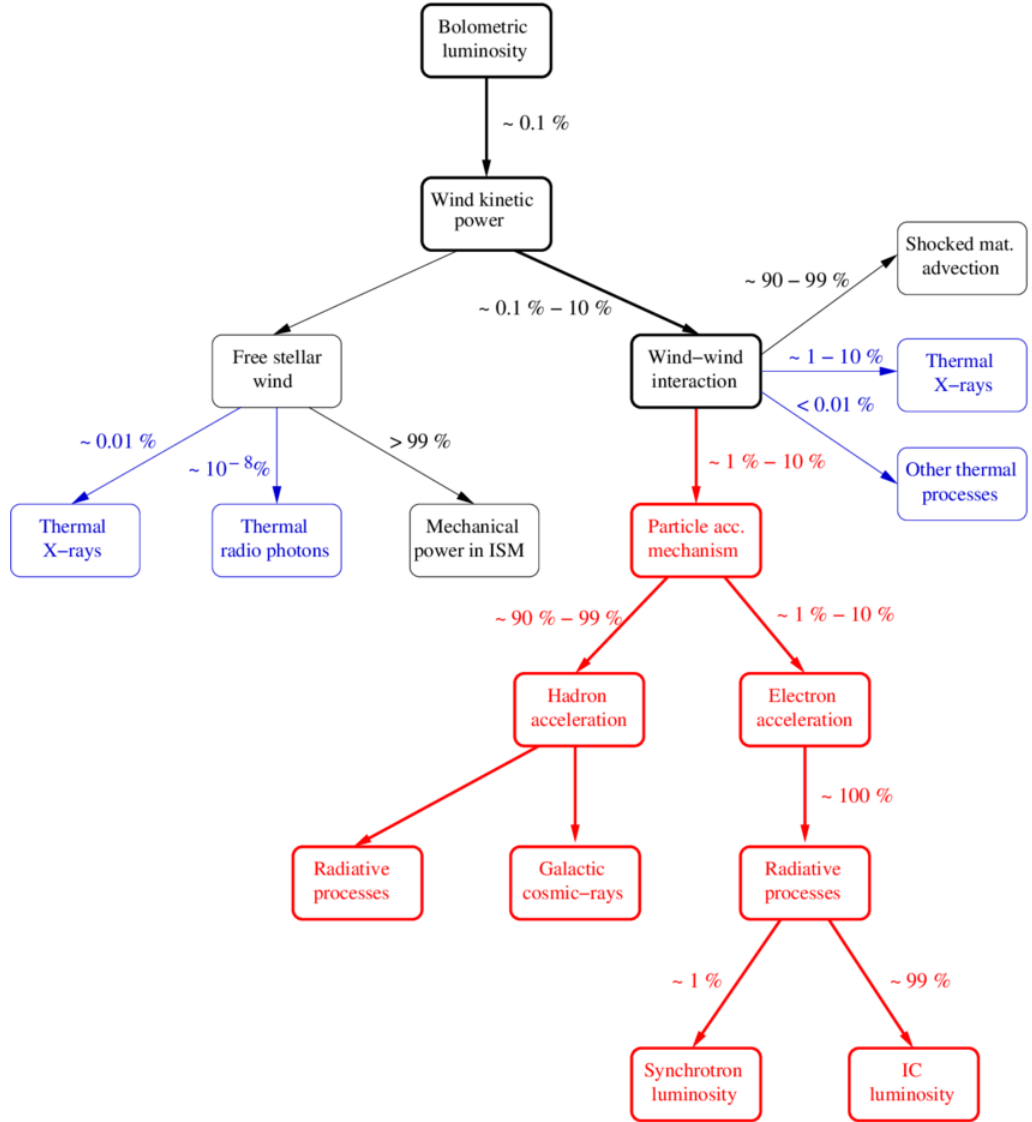


Figure 1.9: Representation of the energy budget of stellar winds in a binary hosting wind collision. Non-thermal processes are highlighted in ‘red’ color while thermal emission phenomena are mentioned in ‘blue’. The different numbers express typical percentage of energy transferred between two consecutive boxes starting from the bolometric luminosity which is the total output energy of the star. The figure is adopted from [De Becker & Raucq \(2013\)](#).

1.4 Motivation of Thesis

A deep exploration of the phenomena described above in the massive, highly energetic stars gives us a unique way to decipher different properties of stellar winds. This thesis is aimed to cover multi-wavelength studies of the O- and WR- stars and hence their associated winds. Since majority of the massive stars are a part of the

multiple stellar systems. Therefore, an observational study is needed to constrain the stellar winds properties by studying the wind collision and test the present theoretical models which provide a description of the physics of colliding winds. Because CWBs span a wide range of stellar and orbital parameters, it is important to study as many such sources as possible in detail, and consequently confront present theories to a significantly relevant sample of observational facts. This will also present some inputs to existing theoretical models to make more accurate predictions. From the observation point of view, the present study would provide a base to plan future observations of massive stars during the crucial time intervals to uncover various important aspects of stellar winds.

1.5 Outline of Thesis

There are total seven chapters in this thesis. Timing and spectral studies of massive binaries have been performed using X-ray data sets along with few infra-red photometric and optical polarimetric measurements. It has been attempted to investigate massive systems covering a large parameter space in terms of binary orbital parameters. Additionally, different spectral classes of hot stars have been considered to develop an overall view of the stellar winds of these stars. The main highlight of this thesis is that several physical phenomena related to the stellar winds have been explored and the dynamical evolution of massive stellar outflows is assessed. The outline of the thesis is given as —

Chapter 1: An introduction to massive stars is given in this chapter. Their classification as well as evolution has also been described. The concept of mass-loss through stellar winds along with its importance in deciding the evolutionary path of massive stars is explained. The different radiation mechanisms active in individual as well as multiple massive stellar systems given in this chapter forms the building block to understand various studies carried out during this thesis.

Chapter 2: In this chapter, I have explained in detail about the various telescopes, detectors, and instrumental set-ups used to obtain data-sets for the present study.

Chapter 3: Detailed long-term soft and hard X-rays timing and spectroscopic analysis of a long period CWB, WR 25, is studied in this chapter.

Chapter 4: This chapter comprises the analysis of a deeply embedded WR star, WR 121a, whose binary status was debatable.

Chapter 5: This chapter emphasizes the long-term variation of IR and X-ray flux

from a dust making as well as PACWB, WR 125. Capturing of another episode of dust formation in WR 125 is one of the highlights of this chapter.

Chapter 6: This chapter presents the investigation of massive O+O binaries using X-ray timing and spectral means as well as optical polarimetric observations.

Chapter 7: A brief summary of the problems addressed in this thesis is presented in this chapter. Timing and spectral studies of O- and WR- stars resulted in constraining the stellar wind properties. This has led to the determination of orbital elements of few massive binaries along with addressing some of the key processes associated with them like the dynamics of their stellar winds shocks, particle acceleration, dust formation, etc. in the wind interaction region.

Chapter 2

TELESCOPES, INSTRUMENTS, OBSERVATIONS, AND DATA PROCESSING

For this thesis, multiwavelength data have been obtained using different telescopes and detectors. Infra-red, optical, and X-ray data has been obtained by submitting proposals to Indian astronomical facilities. Additionally, archival data has also been used extensively in this thesis. Archival observations provide a wide temporal coverage of observations that helped to investigate the long-term variations which was otherwise difficult to obtain during the limited time period of the thesis. Infra-red imaging, optical polarimetry, and X-ray timing as well as spectroscopic studies of massive stars have been performed using these data sets. A brief description of each telescope, its back-end detectors, and the data reduction and analysis procedure have been presented in this chapter.

2.1 Charged Coupled Devices: The detector used for multiwavelength observations

Charged Coupled Devices (CCDs) are the most widely used astronomical detectors by amateur astronomers as well as professional observatories during the present times. The first astronomical CCD image was taken in 1975 of the planet Uranus at a wavelength of 8900 Å, by scientists from the Jet Propulsion Laboratory ([Janesick & Blouke, 1987](#)). CCDs have revolutionized the modern astronomy as compared to the era when photometric plates were used. High sensitivity, better response,

2. TELESCOPES, INSTRUMENTS, OBSERVATIONS, AND DATA PROCESSING

low noise as well as read-out times have recognized CCDs as one of the most useful detector now-a-days to gather light from any celestial object.

The basic working principle of a CCD is the photoelectric effect. Four tasks are performed to form an image which are generation and collection of the electron cloud, transfer of charge, and read-out in analog to digital form. Silicon is the most commonly used material in CCDs. The incoming photons hit the pixel area of the silicon chip and are absorbed if their energy is equivalent to the band gap energy of silicon. Silicon can absorb electromagnetic radiation having energy 1.1 to 4 eV as its band gap energy is 1.14 eV and cause valence band electrons to move into the conduction band. The photons of higher energy may generate multiple electron-hole pairs upon absorption. The freed electrons must be collected and confined at their place till the time read-out of each pixel takes place. Gate structures associated with each pixel help to gather the free electrons and generate a potential well to hold these electrons until the completion of exposure. During the end of the integration interval, the charge accumulated by each pixel is transferred pixel by pixel to the on-chip amplifier. The charge collected by each pixel is estimated in the form of voltage and is transformed to digital format by an Analog-to-Digital (A/D) converter. Here, it is recorded in the form of digital numbers and saved as FITS (Flexible Image Transport System) files.

2.2 X-ray telescopes and back-end detectors

2.2.1 *AstroSat*

The first Indian space-borne observatory, *AstroSat*, was launched on 2015 September 28 (Singh et al., 2014). *AstroSat* carries four co-pointed scientific instruments which provide simultaneous observations over a broad range of the electromagnetic spectrum. The optical and near as well as far-ultraviolet wavelength range is covered by the UV Imaging Telescopes (UVIT, Tandon et al. 2017). However, soft through hard X-rays are observed with Soft X-ray Telescope (SXT), Large Area Xenon Proportional Counter (LAXPC), and Cadmium-Zinc Telluride Imager (CZTI). The soft X-rays are detected with SXT in 0.3-8.0 keV energy band as described by Singh et al. (2017). LAXPC is sensitive to 3-100 keV energy band (Yadav et al., 2016) and the 25-150 keV energy band is covered by CZTI which is a coded mask imager (Bhalerao et al., 2017). There is a Scanning Sky Monitor (SSM) onboard *AstroSat* having a larger field of view (FoV) to scan the sky to discover transient X-ray sources in the

2.2 X-ray telescopes and back-end detectors

energy range 2.5-10.0 keV (Seetha et al., 2006). The three units of SSM situated on the sides of the payload rotate to cover the entire sky. A schematic of *AstroSat* payloads is shown in Figure 2.1.

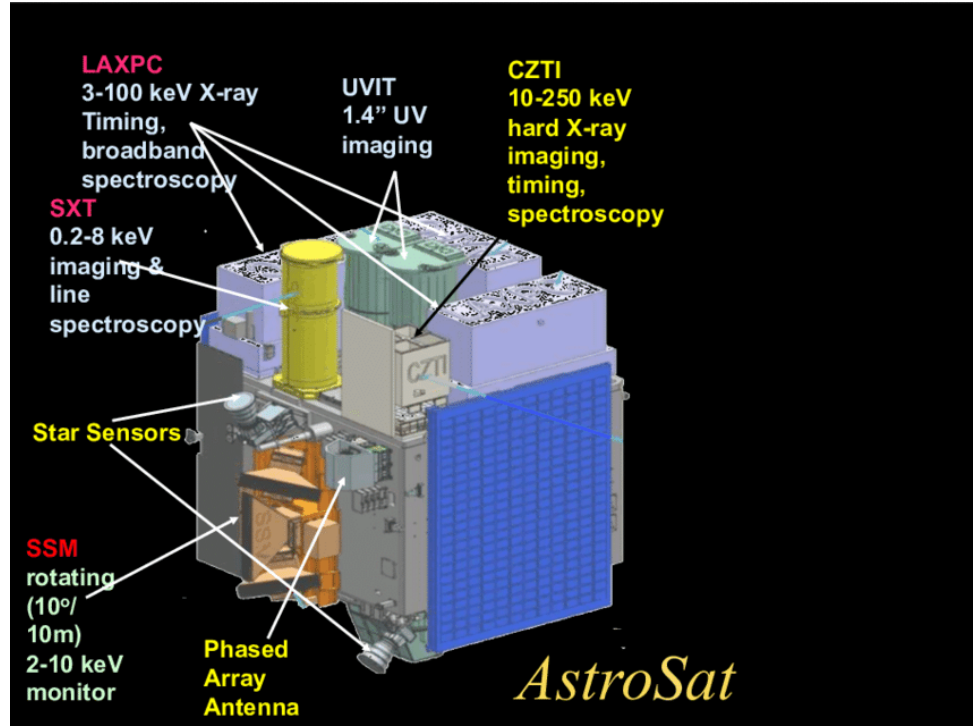


Figure 2.1: A schematic of principal instruments onboard *AstroSat* with folded solar panels. The figure is adopted from Singh (2016).

The data from SXT has been used in this thesis. SXT consists of 40 concentric Gold-coated foil-mirror grazing-incidence reflecting optics units. The effective focal length of SXT is 2 m. A 600×600 pixels image is captured by an X-ray CCD camera residing at the focus of SXT. The full width at half maximum (FWHM) of $\sim 100''$ is achieved for the on-axis point-spread function (PSF). However, half encircled-energy radius is $5.5'$. Two CCD read-out modes are available for SXT; (a) Photon Counting (PC) where the full frame is read with a time resolution of 2.4 s and (b) Fast mode (FM) mode which reads only the central 150×150 pixels with a time resolution of 0.278 s. The effective area peaks at $\sim 120 \text{ cm}^2$ in 0.8-2.0 keV energy range which decreases to $\sim 60 \text{ cm}^2$ in 2.5-5.0 keV band and it drops gradually to $\sim 7 \text{ cm}^2$ at 8.0 keV.

2.2.2 *Chandra*

The *Chandra* X-Ray Observatory is one of the “Great Observatories” of National Aeronautics and Space Administration (NASA) which was launched on 1999 July 23 (Weisskopf et al., 2000). The unprecedented capabilities of *Chandra* for sub-arcsecond and spectrometric imaging along with high-resolution dispersive spectroscopy performed over an energy range of 0.08-10.0 keV makes it unique among others. The observatory is placed into an elliptical orbit at an inclination of 28.5° with 140,000 km apogee and 10,000 km perigee distance. The highly elliptical orbit results in the lesser occultation of sky by Earth as well as smaller fraction of 63.5 hr orbital period when the observatory passes through Earth’s radiation belts leading to high backgrounds. Therefore, observing efficiency of *Chandra* is appreciable and continuous observations for greater than two days are feasible.

A high resolution mirror assembly is used to focus X-rays onto two sets of transmission gratings and two imaging detectors carried by *Chandra* spacecraft. A schematic of different components of *Chandra* is shown in Figure 2.2. One of the focal plane detectors is a High-Resolution Camera (HRC) which performs high resolution imaging or rapid timing observations or both together (Murray et al., 2000). The second instrument, Advanced CCD Imaging Spectrometer (ACIS) (Garmire et al., 2003) is an array of 10 planar 1024×1024 pixels CCDs. Simultaneous high-resolution imaging and moderate resolution spectroscopy is done by a two-dimensional array of these small detectors. Out of 10 CCDs, four are placed in a 2×2 array, named as ACIS-I, and is used for imaging. However, other six CCDs are placed in the form of a 1×6 array known as ACIS-S which is utilized both for imaging and to read-out the grating spectrum. There are two back-illuminated (BI) and eight front-illuminated (FI) CCDs. The advantage of using BI devices is that their response is better at low energies. Additionally, in terms of chip-average energy resolution, these are advantageous over FI devices. ACIS-I offers a $16.9' \times 16.9'$ FoV for high-resolution spectrometric imaging while a $8.3' \times 50.6'$ FoV is provided by ACIS-S. An important feature of ACIS is its spatial resolution. Only the physical dimension of the pixels of ACIS determines the spatial resolution which is $24.0 \mu\text{m}$ or $\sim 0.492''$. The nominal full frame read-out time is 3.24 s.

2.2 X-ray telescopes and back-end detectors

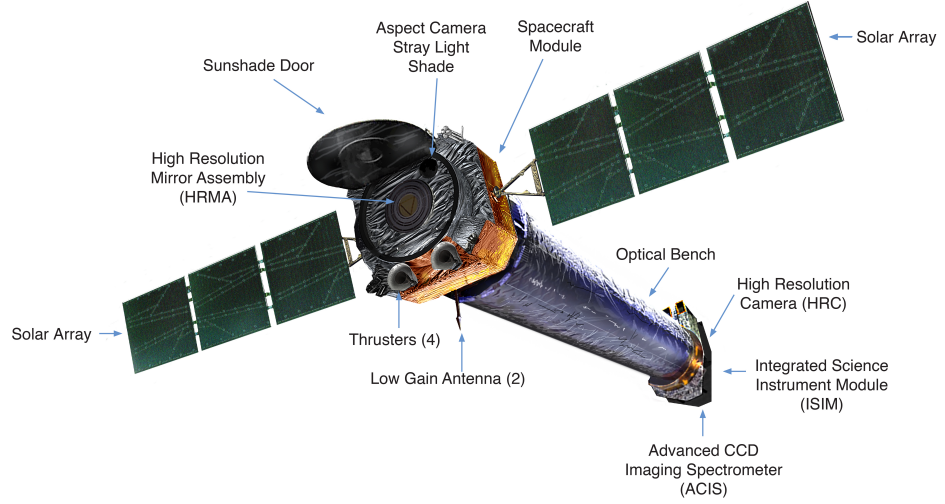


Figure 2.2: Different components of *Chandra* spacecraft. The figure is adopted from: <https://chandra.harvard.edu/about/spacecraft.html>.

2.2.3 *NuSTAR*

The first high-energy X-ray focusing telescope in orbit is the Nuclear Spectroscopic Telescope Array (*NuSTAR*, Harrison et al. 2013). It was placed into a low-Earth, near-equatorial orbit at 6° inclination on 2012 June 13. *NuSTAR* utilizes the new generation of hard X-ray optics accompanied by advanced technologies based solid-state detectors which made it the first astronomical telescope sensitive to X-ray energies significantly greater than 10 keV. The X-rays in the 3–79 keV energy range can be focused by *NuSTAR*. The core of the *NuSTAR* spacecraft is its two co-aligned telescopes where hard X-rays are grazingly incident. The telescopes consist of 133 concentric mirror shells having a conical approximation to the Wolter-I design. The mirrors are coated with multilayers of Pt/SiC and W/Si. These multilayers function like a crystal lattice and the resulting constructive interference leads to enhanced reflectivity all the way up to 79 keV. Each telescope unit has a weight of 38 kg and a focal length of 10 m.

There are two focal plane modules (FPMA and FPMB) placed next to each telescope as shown in Figure 2.3. These are the solid-state Cadmium-Zinc-Telluride (CdZnTe) 32×32 pixel detectors. A 2×2 array of these detectors, where each pixel corresponds to $12.3''$, presents a FoV of $12' \times 12'$. The FWHM energy resolution of 0.4 keV at 10 keV and 0.9 keV at 60 keV is achieved by these detectors. The

2. TELESCOPES, INSTRUMENTS, OBSERVATIONS, AND DATA PROCESSING

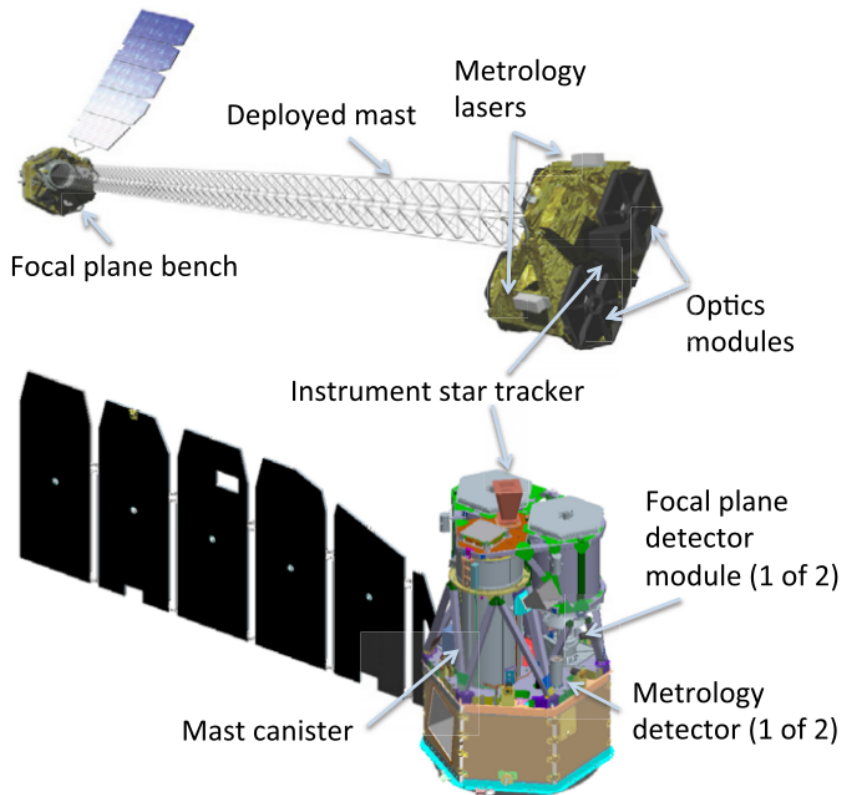


Figure 2.3: Schematic view of *NuSTAR*, the first hard X-ray focusing telescope in 3-79 keV energy range, in stowed (bottom) and deployed (top) configurations. The figure is adopted from [Harrison et al. \(2013\)](#).

detector housings are further shielded by Cesium-Iodide crystals. This prevents arrival of high energy photons and cosmic rays to the focal plane entering from off *NuSTAR* optical axis. The FWHM of *NuSTAR* PSF is $18''$ and has half-power diameter (HPD) of $58''$.

2.2.4 *Suzaku*

Suzaku ([Mitsuda et al., 2007](#)) is the fifth Japanese X-ray astronomical spacecraft developed under Japan-US international collaboration. The mission has terminated having performed its scientific operation for 10 years after being launched on 2005 July 10. The near circular orbit of *Suzaku* at 570 km altitude is inclined at 31° and has an orbital period of 96 minutes. *Suzaku* has a broad band pass from 0.2 to 600 keV. Additionally, low background and fine energy resolution make it stand out of other X-ray observatories. Upon deployment of the extensible optical bench

2.2 X-ray telescopes and back-end detectors

(EOB), the length of the space-craft is 6.5 m along the telescope axis. *Suzaku*'s scientific payload consisted of three distinct co-aligned detectors as shown in Figure 2.4. The first one is the X-ray Imaging Spectrometer (XIS) operated in 0.2-12.0 keV energy range; second is a collimated, non-imaging Hard X-ray Detector (HXD) which is sensitive to much higher energies in the range of 10-600 keV. The last detector is the X-Ray Spectrometer (XRS) which became inoperable after few days of its launch.

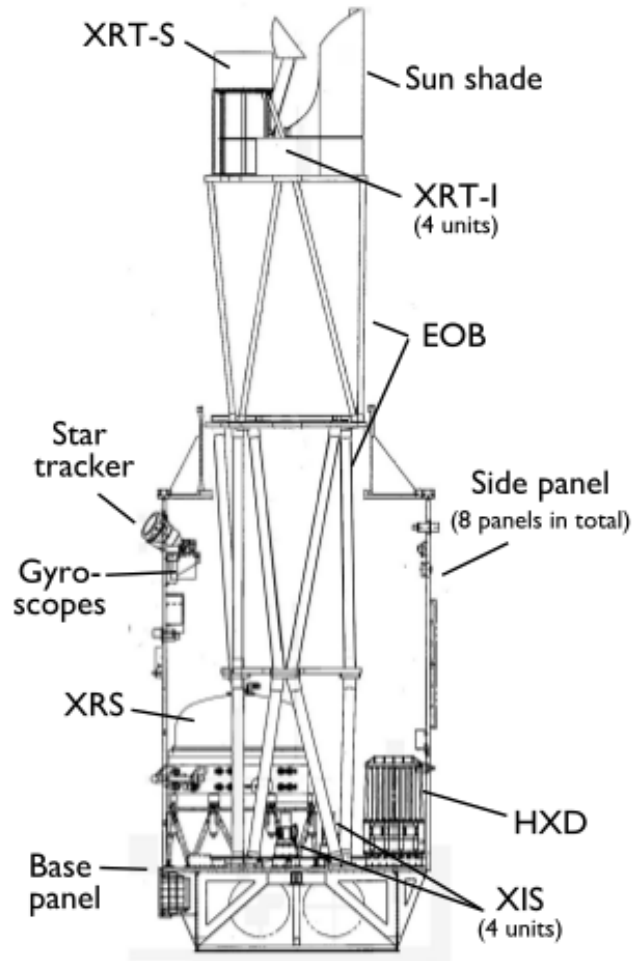


Figure 2.4: Side view of the internal structures of *Suzaku* payload upon deployment of the extensible optical bench. The figure is adopted from Mitsuda et al. (2007).

X-ray data from XIS (Koyama et al., 2007) has been used for this thesis. Silicon CCDs sensitive to X-rays are employed in XIS which are operated in PC mode. There are four sets of XIS which are designated as XIS 0, XIS 1, XIS 2, and XIS 3. Each one is a single chip CCD detector having a 1024×1024 pixels array and is

2. TELESCOPES, INSTRUMENTS, OBSERVATIONS, AND DATA PROCESSING

located at the focal plane of a dedicated X-ray Telescope (XRT). XIS 0, 2, and 3 are FI while XIS 1 is the BI CCD. The presence of a gate structure made of thin Si and SiO₂ layers in the front side of FI CCDs makes them less sensitive than BI CCDs to soft X-rays. Out of all the available CCD detectors, XIS 2 stopped working since 2006 November 9 due to charge leakage. Therefore, it could not be used for further scientific observations. The size of single pixel is 24 μm square giving a total size of CCD as 25 mm \times 25 mm. The FoV of XIS when combined with XRT is 18' \times 18'. The FWHM energy resolution of XIS is 130 eV at 5.9 keV. The normal mode of operation has a timing resolution of 8 s which can be decreased to 7.8 ms in P-sum mode which sums multiple rows of data at the bottom of imaging region.

2.2.5 *The Neil Gehrels Swift Observatory*

The Neil Gehrels Swift Observatory (hereafter *Swift*) was launched into a low-Earth orbit on 2004 November 20 (Gehrels et al., 2004). The prime aim of *Swift* was to make prompt detections of GRBs and their afterglows. This payload is comprised of three scientific instruments to identify and follow-up GRBs in the optical, ultraviolet, X-ray, and gamma-ray wavebands. A schematic view of *Swift* observatory is shown in Figure 2.5. First instrument is a Burst Alert Telescope (BAT) which detects GRBs followed by determination of their location within a few arcminutes in the sky. Second is an Ultraviolet/Optical Telescope (UVOT) which has achieved a position accuracy of 0.3'' and limiting sensitivity of 24 magnitude in 1000 s. An X-ray Telescope (XRT) is the third instrument that studies the X-ray counterparts of GRBs in the energy band of 0.2-10.0 keV (Burrows et al., 2005).

The data observed by XRT of massive binaries has been used in this thesis. XRT comprises of a Wolter-I telescope where X-rays are grazingly incident and then focused onto a CCD which is cooled thermoelectrically. The effective area of XRT is more than 120 cm² at 1.5 keV and provides 23.6' \times 23.6' FoV. However, the HPD of the telescope is 18'' at 1.5 keV for on-axis observations. The CCD is comprised of 600 \times 600 pixels array with a pixel size of 40 \times 40 μm^2 . Each pixel corresponds to 2.36'' of the sky at the *Swift* focal plane. The FWHM energy resolution of the CCD varies from \sim 190 eV at 10 keV to \sim 50 eV at 0.1 keV. The influence of charge trapping and loss to surface states becomes appreciable below \sim 0.5 keV, therefore, scientific analysis is performed in 0.5-10.0 keV range for *Swift*-XRT. Observations in four different read-out modes are possible with XRT. These are Image (IM), Photodiode (PD), Windowed Timing (WT), and Photon-Counting (PC) mode. Data observed

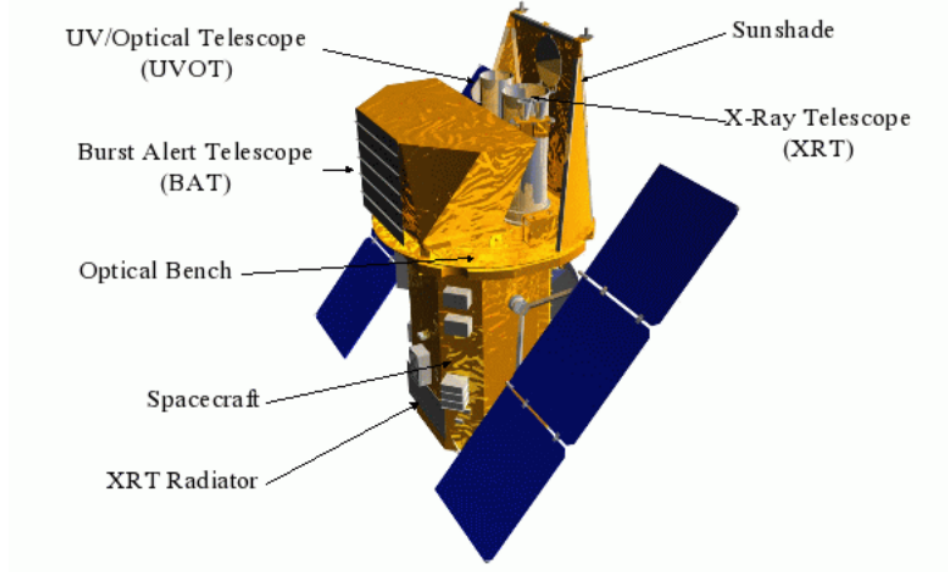


Figure 2.5: Schematic view of *Swift* observatory instruments. The figure is adopted from: <https://www.swift.ac.uk/about/instruments.php>.

in PC mode is obtained with a time resolution of 2.5 seconds and retains complete imaging and spectroscopic information and has been utilized here.

2.2.6 *XMM-Newton*

XMM-Newton observatory is a European Space Agency's (ESA) mission launched on 1999 December 10 (Jansen et al., 2001). The satellite is placed into a highly eccentric orbit of ~ 48 hour period at an inclination of -40° . The perigee and apogee distance is 7,000 and 1,14,000 km, respectively. There are three identical Wolter-I X-ray telescopes onboard *XMM-Newton* which consists of 58 coaxially and confocally nested mirrors. Their focal length is 7.5 m and grazing incidence angles belong to the $17'$ - $42'$ range. The PSF of X-ray telescopes has FWHM of $\sim 6''$ and a half energy width of $\sim 15''$ at 1.5 and 8 keV. Figure 2.6 shows the schematic view of *XMM-Newton* satellite. The focal plane of each telescope is occupied by a European Photon Imaging Camera (EPIC) that collects X-ray photons from the celestial sources. Out of the three cameras, there are two Metal-Oxide Semi-conductor detectors, referred to as EPIC-MOS (Turner et al., 2001). MOS1 and MOS2 consist of seven such FI CCDs providing a FoV of $30'$ diameter. However, the third one uses an array of twelve BI p-n-junction CCDs called EPIC-PN (Strüder et al., 2001) with the same FoV. Both EPIC-MOS and PN are most capable of performing excellent

2. TELESCOPES, INSTRUMENTS, OBSERVATIONS, AND DATA PROCESSING

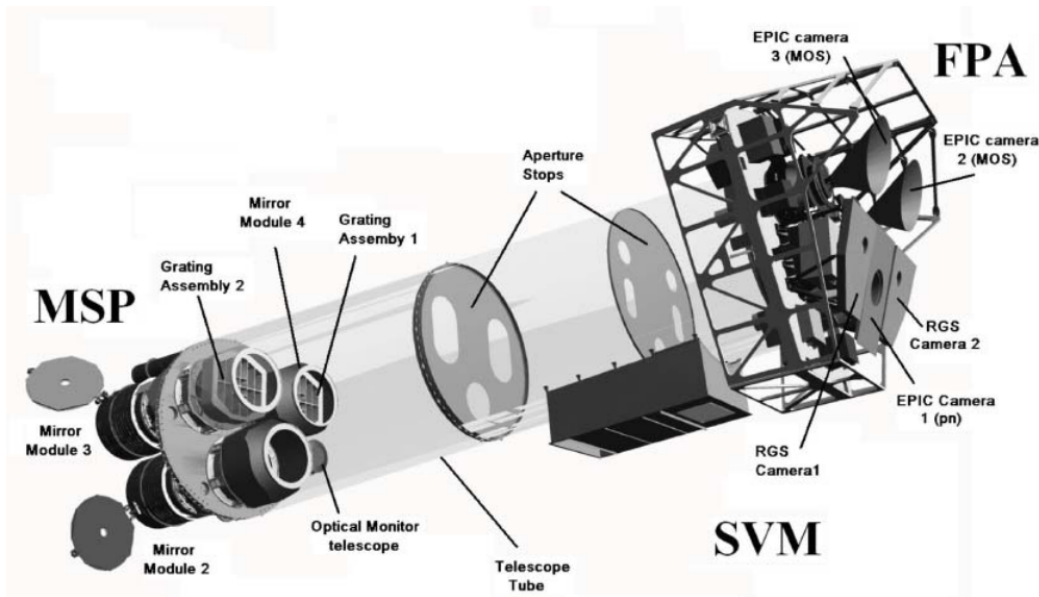


Figure 2.6: A schematic diagram of the ESA’s *XMM-Newton* observatory. This figure is adopted from [Lumb et al. \(2012\)](#).

imaging and moderate energy resolution spectroscopy ($E/\Delta E \approx 20\text{-}50$) over an energy range of $\sim 0.15\text{-}12.0$ and $\sim 0.15\text{-}15.0$ keV, respectively. Four read out modes, *viz.* full frame, large window, small window, and timing, are available to observe with MOS and PN detectors. Standard mode of operations is the full frame mode where all the pixels of the CCD are read-out. Whereas, the array of read-out pixels is shortened to achieve a high temporal resolution and prevent pile-up in other observing modes. For timing mode, the time resolution for EPIC-PN is 0.02 ms while it belongs to the 6-200 ms range for other modes. However, for EPIC-MOS, the time resolution is 0.9 s, 0.3 s, and 1.7 ms for large window, small window, and timing mode, respectively. Optical contaminations from the target source are suppressed using three types of Optical Blocking Filters (OBFs) in EPIC detectors. Based upon the V-band magnitude of the point-like sources, these are defined as thin ($V > 12$ mag), medium ($V \sim 6\text{-}9$ mag), and thick ($V \sim 1\text{-}4$ mag) filters.

A significant portion of the X-ray flux present in the telescope beams upon reaching two MOS cameras is diverted to X-ray gratings of the Reflection Grating Spectrometer (RGS, [den Herder et al. 2001](#)). Only 44% of the original flux reaches MOS1 and MOS2 because of additional structural obscuration. The observations in the 170-650 nm waveband are carried out by an Optical/UV Monitor Telescope (OM) supported on the mirror platform of *XMM-Newton* along with X-ray telescopes ([Mason et al., 2001](#)). The simultaneous ultraviolet/optical observations of

XMM X-ray targets are performed by OM which covers the central $17'$ square region of the same X-ray FoV. The auxiliary, housekeeping, and instrument science data is bundled into Observation Data File (ODF) which are essential to perform X-ray analysis. The data is further calibrated using the Current Calibration File (CCF). The complete set of tasks to process the *XMM-Newton* data is bundled together into the Science Analysis System (SAS) software.

2.3 X-ray observations and data reduction

X-ray data of massive binaries observed by satellites described above are archived by their respective science centers and can be retrieved from there. This data can also be retrieved from the High Energy Astrophysics Science Archive Research Center (HEASARC) developed by NASA. In order to bring the data observed with individual observatories to a standard format, it has to be refined first using different techniques as provided by the respective instrument teams. Data processing has been accomplished using the package High Energy Astrophysics Software (HEASoft) designed for X-ray astronomical data analysis. X-ray investigation of four massive binaries *viz.* WR 25, WR 121a, WR 125, and HD 93205 has been performed. A detailed log of X-ray observations utilized in this thesis is presented in Tables 2.1 and 2.2. Among all the sources studied, WR 25 was observed for the longest duration of ~ 16 years on 226 individual epochs by *NuSTAR*, *Suzaku*, *Swift*, and *XMM-Newton*. However, WR 121a was observed for eight times with ACIS-I onboard *Chandra*. The source was present almost at the aim-point of the detector for these data-sets. Whereas, the WR 121a was situated at a larger offset from the detector aim-point during one observation made with ACIS-S array. Also, this observation was made with a comparatively shorter exposure time. The X-ray data obtained by *XMM-Newton* of WR 121a and WR 125 for one and two epochs, respectively, is analyzed for the present work. Additionally, the X-ray data from *AstroSat* and *Swift* of WR 125 have been investigated as well. The *XMM-Newton* data used for WR 25 was also analyzed to extract X-ray products of HD 93205 also since both of them lie in the same Eta Carinae field as shown in Figure 3.1. The procedure followed for the X-ray data reduction for each X-ray observatory is summarized below.

2. TELESCOPES, INSTRUMENTS, OBSERVATIONS, AND DATA PROCESSING

Table 2.1: Log of X-ray observations of WR 25.

Obs. ID	Obs. Date	Time (UT)	Exp. (ksec.)	Offset (')	Obs. ID	Obs. Date	Time (UT)	Exp. (ksec.)	Offset (')
Instrument: <i>Suzaku</i>–XIS					00031097043	2009-06-05	06:58:00	3.4	1.595
100012010	2005-08-29	01:48:03	49.8	7.500	00031097044	2009-06-06	06:50:01	4.2	3.771
100045010	2006-02-03	09:59:30	21.4	6.521	00080760003	2014-08-19	17:40:59	2.0	6.587
402039010	2007-06-23	05:54:08	58.4	5.312	00081578001	2015-07-16	08:11:58	2.1	5.429
403035010	2008-06-10	01:51:36	35.4	5.682	00031097046	2015-07-29	00:40:58	1.4	1.466
403036010	2008-12-10	05:04:12	48.5	8.714	00031097047	2015-07-31	08:28:57	2.8	1.381
404038010	2009-06-10	19:45:43	51.2	5.708	00031097049	2015-08-21	00:48:58	9.1	2.848
404039010	2009-11-21	04:31:13	49.4	8.240	00031097050	2015-12-10	10:23:58	2.4	1.047
406039010	2011-07-24	00:47:26	42.0	6.942	00031097051	2015-12-11	16:40:57	1.8	1.429
408018010	2013-07-03	04:22:16	97.5	4.245	00031097052	2015-12-12	21:24:58	2.6	1.356
408018020	2013-07-06	01:09:11	83.9	7.473	00031097053	2015-12-13	02:14:58	2.4	1.219
Instrument: <i>Swift</i>–XRT					00031097054	2015-12-14	07:07:59	1.8	2.619
00037049001	2007-12-11	14:09:00	4.5	6.339	00031097055	2015-12-15	19:48:57	2.0	2.033
00037049002	2008-01-19	06:08:01	3.3	4.682	00031097056	2015-12-16	03:30:58	1.2	2.108
00031097001	2008-01-25	02:00:01	4.4	1.342	00031097057	2015-12-17	09:51:58	1.7	3.483
00031097002	2008-01-26	02:10:01	3.7	0.387	00031097058	2015-12-18	19:34:58	1.5	2.195
00031097003	2008-01-27	00:44:00	3.5	3.892	00031097059	2015-12-19	00:21:57	1.8	2.700
00031097004	2008-01-28	00:57:00	3.8	0.584	00031097060	2015-12-20	19:24:58	2.1	3.023
00031097006	2008-01-30	17:18:01	3.9	0.803	00031097061	2015-12-21	03:23:58	2.5	2.619
00031097007	2008-01-31	06:17:01	2.6	1.518	00031097062	2015-12-22	06:39:57	1.4	3.018
00031097008	2008-02-01	00:04:00	26.4	0.182	00031097063	2015-12-23	14:06:57	2.6	1.580
00031097009	2008-02-02	23:59:01	22.6	0.999	00031097064	2015-12-24	09:14:58	2.4	1.600
00031097010	2008-02-05	16:40:01	3.5	1.396	00031097065	2015-12-25	02:51:57	2.3	2.216
00031097011	2008-02-06	00:27:26	3.3	3.913	00031097066	2015-12-26	18:50:58	2.5	1.492
00031097012	2008-02-07	00:34:46	3.4	1.334	00031097067	2015-12-27	17:04:58	1.3	2.852
00031097013	2008-02-09	21:33:01	2.8	0.923	00031097068	2015-12-28	08:56:58	1.5	2.844
00031097016	2008-02-11	17:02:01	2.5	2.168	00031097069	2015-12-29	02:45:57	2.6	1.542
00031097017	2008-02-12	00:45:01	2.9	1.300	00031097070	2015-12-30	01:20:58	1.9	0.838
00031097018	2008-02-13	07:15:01	2.6	1.590	00031097071	2015-12-31	01:01:58	2.3	1.459
00031097019	2008-02-14	15:22:01	3.4	0.412	00031097072	2016-01-01	20:16:58	2.6	1.939
00031097020	2008-02-15	12:29:01	2.4	1.264	00031097073	2016-01-02	02:30:57	2.3	1.402
00031097022	2008-02-17	12:52:01	3.7	3.464	00031097075	2016-01-04	09:58:58	2.2	1.987
00031097023	2008-02-18	17:30:00	3.4	1.234	00031097076	2016-01-05	16:16:58	1.7	1.162
00031097025	2008-02-20	06:15:01	3.4	2.647	00031097077	2016-01-06	02:20:58	2.0	1.299
00031097026	2008-02-21	07:57:01	3.7	2.027	00031097078	2016-01-07	11:39:58	1.2	1.818
00031097028	2008-02-23	14:33:01	2.9	1.415	00031097079	2016-01-08	00:22:57	2.2	1.308
00031097029	2008-02-24	16:14:00	2.4	0.638	00031097080	2016-01-09	01:58:57	2.6	1.633
00031097030	2008-02-25	11:35:01	2.4	0.816	00031097081	2016-01-10	00:19:58	2.5	3.433
00031097031	2008-02-26	05:10:01	3.8	2.159	00031097082	2016-01-10	20:46:57	2.7	1.613
00031097034	2008-03-16	08:35:01	9.2	1.688	00031097083	2016-01-12	07:46:57	2.9	1.859
00031308001	2008-12-14	03:17:01	6.8	6.929	00031097085	2016-01-14	18:57:58	1.7	1.435
00090033001	2009-03-18	08:44:01	14.4	6.457	00031097086	2016-01-15	17:34:58	2.4	1.381
00031097035	2009-04-01	12:10:22	9.2	1.270	00031097087	2016-01-16	09:07:58	2.9	1.628
00031097036	2009-04-02	08:59:01	12.5	1.741	00031097089	2016-01-18	07:32:39	1.7	4.277
00031097037	2009-04-03	09:10:01	10.2	1.064	00031097091	2016-01-20	13:52:58	2.1	1.109
00031097038	2009-04-07	09:24:01	8.7	0.911	00031097092	2016-01-21	07:08:58	1.1	1.401
00031097039	2009-04-08	07:53:01	8.3	1.191	00031097093	2016-01-24	02:13:58	1.5	1.365
00031097040	2009-04-09	13:04:00	9.9	1.465	00031097094	2016-01-24	05:25:58	1.4	1.562
00031097041	2009-06-03	01:46:01	3.8	0.348	00031097095	2016-01-24	08:37:58	1.4	1.895
00031097042	2009-06-04	06:51:00	3.9	1.858	00031097098	2016-01-24	21:30:58	1.5	0.719

2.3 X-ray observations and data reduction

Continued: Log of X-ray observations of WR 25.

Obs. ID	Obs. Date	Time (UT)	Exp. (ksec.)	Offset (')	Obs. ID	Obs. Date	Time (UT)	Exp. (ksec.)	Offset (')
00031097099	2016-01-25	02:13:58	1.3	1.529	00031097175	2016-02-23	04:57:58	2.5	2.188
00031097100	2016-01-25	05:25:57	1.2	1.343	00031097176	2016-02-25	12:46:58	1.2	3.272
00031097101	2016-01-25	08:37:58	1.3	1.547	00031097177	2016-02-26	04:50:58	1.0	1.165
00031097102	2016-01-25	13:25:58	1.5	3.258	00031097178	2016-02-27	12:36:57	2.4	2.837
00031097107	2016-01-26	08:39:58	1.1	1.068	00031097179	2016-02-28	06:09:58	1.9	2.487
00031097110	2016-01-30	00:34:58	1.1	4.812	00031097184	2016-03-04	05:44:58	1.6	2.160
00031097111	2016-01-30	05:21:58	1.1	5.312	00031097185	2016-03-05	00:53:58	1.1	2.178
00031097112	2016-01-30	10:12:58	1.3	2.953	00031097187	2016-03-08	02:16:58	2.7	1.377
00031097113	2016-01-30	13:20:58	1.5	1.911	00031097189	2016-03-12	13:14:58	1.9	1.849
00031097114	2016-01-30	18:10:57	1.5	4.683	00031097190	2016-03-13	09:53:58	1.0	0.464
00031097119	2016-01-31	14:54:58	1.1	4.862	00031097195	2016-03-18	00:13:58	2.3	1.378
00031097120	2016-01-31	18:04:01	1.2	1.541	00031097197	2016-03-20	16:13:58	2.1	1.520
00031097121	2016-01-31	22:51:11	1.3	2.550	00031097196	2016-03-21	16:16:58	2.1	3.483
00031097122	2016-02-01	02:02:38	1.3	2.013	00031097199	2016-03-23	01:45:58	2.3	1.727
00031097123	2016-02-01	06:52:00	1.2	2.212	00031097200	2016-03-24	03:20:58	1.9	6.596
00031097124	2016-02-01	11:36:59	1.1	1.672	00031097201	2016-03-25	18:59:58	2.2	4.631
00031097125	2016-02-01	14:50:58	1.2	2.260	00031097202	2016-03-26	17:16:58	1.3	4.102
00031097126	2016-02-01	16:24:09	1.3	2.112	00031097203	2016-03-27	20:44:41	1.0	5.428
00031097127	2016-02-01	19:35:35	1.3	1.950	00031097204	2016-03-28	18:41:58	2.1	4.475
00031097128	2016-02-02	00:19:58	1.5	4.091	00031097205	2016-03-31	16:59:58	2.1	5.803
00031097129	2016-02-02	05:06:57	1.4	2.740	00031097206	2016-04-03	02:13:58	2.5	1.858
00031097130	2016-02-02	08:17:58	1.4	4.764	00031097208	2016-04-09	12:55:57	2.1	1.689
00031097131	2016-02-02	13:04:57	1.5	3.064	00031097210	2016-04-15	01:14:58	2.4	2.035
00031097132	2016-02-02	17:51:58	1.5	1.861	00031097211	2016-04-18	02:49:59	1.3	2.165
00031097133	2016-02-02	22:38:58	1.5	1.526	00031097213	2016-04-24	20:11:52	1.8	1.908
00031097137	2016-02-03	13:01:58	1.4	6.598	00031097214	2016-04-27	00:25:57	1.4	2.681
00031097143	2016-02-04	14:30:57	1.0	2.631	00031097215	2016-04-30	00:18:58	2.1	2.326
00031097144	2016-02-04	16:09:58	1.5	3.099	00031097216	2016-05-03	07:57:58	2.3	2.905
00031097148	2016-02-05	09:46:58	1.5	3.359	00031097217	2016-05-06	07:44:58	2.0	2.744
00031097152	2016-02-10	20:23:58	1.6	4.873	00031097218	2016-05-08	01:13:57	2.1	2.521
00031097154	2016-02-11	12:32:58	2.5	2.487	00031097219	2016-05-12	13:53:58	1.3	3.624
00031097155	2016-02-12	03:06:57	2.1	2.947	00031097220	2016-05-15	04:03:58	2.4	2.901
00031097156	2016-02-12	18:54:47	1.5	5.326	00031097222	2016-05-24	00:05:57	2.4	2.799
00031097157	2016-02-13	01:13:57	2.3	1.049	00031097225	2016-06-05	02:30:58	2.2	2.250
00031097158	2016-02-13	13:45:58	2.3	1.976	00031097226	2016-06-08	07:01:26	2.4	2.150
00031097159	2016-02-14	01:12:57	2.2	0.977	00081901001	2016-06-14	23:58:58	1.7	4.799
00031097160	2016-02-14	12:06:58	2.4	1.561	00031097228	2016-06-15	01:40:57	2.3	1.875
00031097161	2016-02-15	08:48:58	2.3	1.423	00031097230	2016-06-20	04:19:58	2.3	3.231
00031097162	2016-02-15	13:38:58	2.3	1.686	00031097231	2016-06-23	05:36:58	2.6	2.868
00031097163	2016-02-16	01:17:57	2.4	2.267	00031097233	2016-07-05	11:25:58	2.3	0.472
00031097164	2016-02-16	18:24:57	2.5	1.401	00031097234	2016-07-09	15:51:58	2.3	3.512
00031097165	2016-02-17	07:02:58	1.6	8.381	00031097239	2016-07-30	05:58:58	1.3	0.857
00031097166	2016-02-17	13:25:58	1.9	2.525	00031097240	2016-08-05	05:27:58	2.6	1.101
00031097167	2016-02-18	00:59:57	2.3	1.995	00031097241	2016-08-13	20:47:58	2.0	2.541
00031097168	2016-02-18	14:56:58	2.5	1.765	Instrument: XMM-Newton-EPIC				
00031097169	2016-02-19	05:21:00	1.7	2.533	0112580601	2000-07-26	04:59:20	33.6	6.935
00031097170	2016-02-19	12:07:58	1.9	4.399	0112580701	2000-07-27	23:49:25	10.9	6.935
00031097171	2016-02-20	04:16:30	1.7	3.368	0112560101	2001-06-25	06:51:26	34.2	0.002
00031097173	2016-02-21	08:18:57	2.8	1.665	0112560201	2001-06-28	07:22:56	35.9	0.002
00031097174	2016-02-22	11:25:58	2.3	1.418	0112560301	2001-06-30	04:39:01	37.1	0.002

2. TELESCOPES, INSTRUMENTS, OBSERVATIONS, AND DATA PROCESSING

Continued: Log of X-ray observations of WR 25.

Obs. ID	Obs. Date	Time (UT)	Exp. (ksec.)	Offset (')
0145740101	2003-01-25	12:57:37	6.80	7.085
0145740201	2003-01-27	01:02:55	6.90	7.085
0145740301	2003-01-27	20:36:23	6.80	7.085
0145740401	2003-01-29	01:39:47	8.30	7.085
0145740501	2003-01-29	23:54:24	6.80	7.085
0160160101	2003-06-08	13:29:39	28.4	7.085
0160160901	2003-06-13	23:51:15	22.2	7.085
0145780101	2003-07-22	01:50:45	8.30	7.085
0160560101	2003-08-02	21:00:17	17.6	7.085
0160560201	2003-08-09	01:43:21	12.7	7.085
0160560301	2003-08-18	15:22:43	18.9	7.085
0311990101	2006-01-31	18:03:33	63.0	6.935
0560580101	2009-01-05	10:22:08	14.6	7.036
0560580201	2009-01-09	14:27:16	11.6	7.036
0560580301	2009-01-15	11:22:01	26.6	7.036
0560580401	2009-02-02	04:45:24	23.9	7.036
0742850301	2014-06-06	19:13:05	9.07	7.036
0742850401	2014-07-28	15:32:43	23.8	7.036
0762910401	2015-07-16	01:18:44	8.20	7.029
Instrument: <i>NuSTAR</i>–FPMA & B				
30002010002	2014-03-31	06:56:07	28.8	6.672
30002010005	2014-05-26	11:21:07	79.4	5.383
30002040002	2014-06-06	10:31:07	32.9	5.338
30002040004	2014-07-28	10:31:07	61.4	5.454
30002010007	2014-08-11	05:36:07	31.0	5.919
30002010008	2014-08-11	23:01:07	56.9	5.182
30002010010	2014-08-19	16:41:07	54.5	5.552
30002010012	2014-09-26	00:41:07	81.5	7.454
30101005002	2015-07-16	01:31:08	23.6	5.749
30201030002	2016-06-15	02:36:08	73.8	5.245

Notes.: (i) Time refers to the start time of the exposure (Exp.) in hh:mm:ss format.
(ii) Since WR 25 and HD 93205 lie within the same field of view of *XMM-Newton*, therefore, the same X-ray data of *XMM-Newton* is analyzed to extract X-ray products for both.

2.3.1 *AstroSat*

The X-ray data for a WR binary WR 125 was obtained using *AstroSat* through submission of proposals during the observing cycle A0-4 and Target of Opportunity program TO-3 (Observation IDs: 9000002152 and 9000002816). Both observations were made with a time gap of ~ 9 months using SXT as the prime instrument in PC mode. The Level-1 data files were collected from *AstroSat* data archive¹. The

¹https://astrobrowse.issdc.gov.in/astro_archive/archive/Home.jsp

2.3 X-ray observations and data reduction

Table 2.2: Log of X-ray observations of WR 121a and WR 125.

Satellite	Obs. ID	Detector	Obs. Date	Time (UT)	Eff. Exp. (ksec)	Offset ^a (')
Object–WR 121a						
<i>XMM-Newton</i>	0203850101	PN	2004-10-22	05:48:23	21.8	0.136
		MOS1			25.3	
		MOS2			25.3	
<i>Chandra</i>	9612	ACIS-S	2008-05-27	16:58:20	1.6	0.489
<i>Chandra</i>	18868	ACIS-I	2016-06-13	16:27:05	13.9	0.008
<i>Chandra</i>	17716	ACIS-I	2016-06-14	03:33:28	43.5	0.008
<i>Chandra</i>	18870	ACIS-I	2016-06-16	02:09:55	32.7	0.008
<i>Chandra</i>	18867	ACIS-I	2016-06-16	19:28:17	47.4	0.008
<i>Chandra</i>	18869	ACIS-I	2016-06-19	07:33:11	39.5	0.008
<i>Chandra</i>	18887	ACIS-I	2016-07-28	09:05:55	77.5	0.008
<i>Chandra</i>	17717	ACIS-I	2016-07-29	15:25:49	45.5	0.008
<i>Chandra</i>	18888	ACIS-I	2016-07-31	09:47:19	45.0	0.008
Object–WR 125						
<i>Astrosat</i>	9000002152	SXT	2018-06-11	05:58:14	14.8	0.00
<i>Astrosat</i>	9000002816	SXT	2019-03-24	11:46:34	22.6	0.00
<i>Swift</i>	00034826001	XRT	2016-11-28	01:50:58	4.8	3.595
<i>Swift</i>	00034826002	XRT	2016-12-17	13:26:57	4.7	3.845
<i>Swift</i>	00034826003	XRT	2017-03-16	06:18:57	2.3	1.034
<i>Swift</i>	00034826004	XRT	2019-07-28	05:00:35	4.3	4.047
<i>Swift</i>	00034826005	XRT	2019-09-29	06:36:35	4.3	1.791
<i>Swift</i>	00034826007	XRT	2019-11-27	10:43:35	4.6	1.193
<i>Swift</i>	00034826008	XRT	2020-02-16	01:18:35	4.3	1.450
<i>Swift</i>	00034826009	XRT	2020-04-09	08:52:36	4.5	1.974
<i>Swift</i>	00034826010	XRT	2020-06-04	00:08:36	3.4	2.461
<i>Swift</i>	00034826011	XRT	2020-06-09	08:57:36	1.4	1.492
<i>Swift</i>	00034826012	XRT	2020-07-30	01:00:18	2.4	3.936
<i>Swift</i>	00034826013	XRT	2020-08-05	01:45:35	2.5	4.076
<i>Swift</i>	00034826014	XRT	2020-09-30	02:37:34	3.6	3.032
<i>Swift</i>	00034826015	XRT	2020-10-05	11:54:35	1.2	3.877
<i>Swift</i>	00034826016	XRT	2020-11-25	00:13:34	4.8	3.877
<i>XMM-Newton</i>	0794581101	PN	2017-05-11	08:25:51	1.3	0.004
		MOS1			14.4	
		MOS2			14.9	
<i>XMM-Newton</i>	0853980101	PN	2019-10-23	07:09:02	11.5	0.004
		MOS1			19.8	
		MOS			18.1	

Notes.: (a) Offset between target source position and the telescope pointing.

2. TELESCOPES, INSTRUMENTS, OBSERVATIONS, AND DATA PROCESSING

task `SXTPIPELINE` (`AS1SXTLevel2`, v1.4b)¹ was used to process the Level-1 SXT data. Any contamination caused by the charged particles during the passage of the instrument through the South Atlantic Anomaly region or occultation by the Earth was filtered out. Only the grade 0–12 events (single-quadrupal pixel events) were selected during the cleaning process which eliminates effects of any charged particles incident on the CCD. Hence, the calibration of the source events along with the extraction of Level-2 cleaned event files for every single orbit is performed by this pipeline. A Julia based merger tool was utilized to merge the cleaned event files of the individual orbits to make a single cleaned event file. Finally, the source spectra were extracted using this Level-2 merged cleaned event file in the `XSELECT` (v2.4d) package.

For the extraction of the source spectrum, a circular region of radius of 13' centered at the source co-ordinates was chosen. The selection of the source size has been made based upon the fact that the PSF of SXT is large (HPD of 11') due to the scattering by the mirrors and attitude control of the satellite (Singh et al., 2017). Therefore, it has been suggested to carry out the extraction for a radius of 10'-14' which further depends upon the brightness of the source. The time bin was set at 2.3775 s (equal to the timing resolution of SXT in PC mode). An unusual high count rate was noticed during the initial 6029 s interval in the observation ID 9000002152. Therefore, this time interval was discarded while extracting the source products leaving the total effective exposure time of 14814 s for this data-set. However, other observation ID was seen to be free from such instances. For the background estimation, the composite background spectrum (`SkyBkg_comb_EL3p5_Cl_Rd16p0_v01.pha`) obtained after a deep blank sky observation is used. However, the ancillary response file (ARF) “`sxt_pc_excl00_v04_20190608.arf`” and the response matrix file (RMF) “`sxt_pc_mat_g0to12.rmf`” provided by the instrument team² has been used for the spectral analysis.

2.3.2 *Chandra*

Only the source WR 121a was observed with *Chandra* which is studied in this thesis. The standard reduction techniques mentioned in *Chandra* data reduction threads³ were employed to process the data with the CIAO v4.11 which is the dedicated

¹https://www.tifr.res.in/~astrosat_sxt/sxtpipeline.html

²https://www.tifr.res.in/~astrosat_sxt/dataanalysis.html

³<http://cxc.harvard.edu/ciao/threads/>

2.3 X-ray observations and data reduction

software for this purpose. However, the data was calibrated using the *Chandra* CALDB v4.8.2 as suggested by the instrument designers. The CHANDRA_REPRO reprocessed the level=1 event files. The reprocessed, level=2 event files were further rectified by the CIAO task AXBARY to apply the barycentric correction. The purpose of this task is to correct the arrival time of the X-ray photons to the detector which is modified because of the Earth's rotation around the Sun. The high background rate was checked in the background light curves obtained for each data-set. However, none was found to be affected with unusually high background intervals. A circular region with its center lying at the detected position of WR 121a and radius 1.72'' was selected to generate the source light curves and spectra. Similarly, another circular region of radius 4.92'' was adopted to on the same ACIS-CCD chip to determine the background. The background region lied in the area surrounding the target source and void of any other X-ray source. The background subtracted X-ray light curves were obtained in three different energy bands *viz.* 0.5-8.0 keV, 0.5-2.0 keV, and 2.0-8.0 keV using the task DMEXTRACT. However, for the extraction of the spectra and the associated response matrices (ARF and RMF), the task SPECEXTRACT was utilized. It was ensured that each bin in the spectra has minimum 15 counts while its grouping.

2.3.3 *NuSTAR*

The X-ray data observed by FPMA and FPMB on-board *NuSTAR* of WR 25 has been reduced using data analysis software NuSTARDAS (v1.5.1) distributed by HEASARC within HEASoft 6.18. The task NUPIPELINE (v0.4.4) was used to generate calibrated, cleaned, and screened event files by considering the calibration files released on 2016-08-30 (v20160824). The source and background counts were extracted from circular regions of 30'' radius at a source and nearby surrounding source-free regions, respectively. Both the regions were selected on the same detector. The source region size is equivalent to the detector HPD ($\sim 1'$). The NUPRODUCTS package built within NuSTARDAS was used to extract the source and background light curves in 3–79 keV energy range. The same task was also utilized for the extraction of the source and background spectra along with the essential response files. The time binning was set to 10 s. In order to correct the arrival times of the X-ray photons, the barycentric correction was applied to the background subtracted light curves using the task BARYCORR. Individual spectra were grouped using the task GRPPHA to have 10 counts per spectral bin.

2. TELESCOPES, INSTRUMENTS, OBSERVATIONS, AND DATA PROCESSING

2.3.4 *Suzaku*

The *Suzaku* satellite observed WR 25 several times taking Eta Carinae at the center of XIS-0, 1, and 3 FoV. Reprocessing of the individual observation ID was performed using the latest calibration database by the task AEBPIPELINE (v1.1.0). The standard screening criteria was adopted for the data reduction. This included selecting Grade 0, 2, 3, 4, and 6 events only. Additionally, the events registered during the passage of South Atlantic Anomaly, Earth day-time elevation angle below 20° , and Earth elevation angle below 5° were rejected. Hot and flickering pixels were also removed. Application of the barycentric correction to the clean event files was executed using the task AEBARYCEN. A circular region centered at source location with radius $90''$ was selected to extract the source products. The size of the chosen source region is more than HPD of XIS ($=2'$). However, other circular regions of radius $45''$ near the source free region were selected as background regions. Both the 3×3 and 5×5 observation mode event files were used collectively to obtain the light curves, spectra, and response files. This was done by XSELECT (v2.4c) package. The addition of the background subtracted light curves and spectra obtained from two FI XIS chips (XIS-0 and 3) was done with the tasks LCMATH and ADDASCASPEC, respectively. Finally, GRPPHA was used to group the spectra to have minimum 20 counts per energy bin for further spectral analysis.

2.3.5 *Swift*

Swift-XRT data has been used for WR 25 as well as WR 125 investigation. The data were processed with *Swift* XRTPipeline (v0.13.3) using the updated calibration files. The resulted cleaned event lists are free from the hot pixels effects and bright Earth. The calibrated event files were used for the extraction of image, light curve, and spectrum for every observation. This was done by selecting standard event grades of 0–12 in the XSELECT (v2.4d) package. In order to extract the source products, a circular region at the source position with $30''$ radius was chosen. However, background X-ray emission was estimated using an annular region around the source position. The inner radius of the annular region was $69''$ whereas $127''$ was the outer radius. The RMF provided by the *Swift* team (swxpc0to12s6_20130101v014.rmf) was used. The task XRTMKARF was used to calculate an ARF for each data set individually by considering the associated exposure maps which took care of the bad columns.

2.3.6 *XMM-Newton*

The X-ray data observed by EPIC on-board *XMM-Newton* has been used for all the massive binaries studied in this thesis. The data has been obtained using different configurations of three EPIC instruments *viz.* MOS1, MOS2, and PN. The data reduction was performed by using the latest calibration files with SAS v17.0.0 and above.

The raw ODFs were pipeline processed using the tasks EPCHAIN and EMCHAIN for the PN and MOS data, respectively. This allows both the energy and astrometric calibration of the events recorded by each CCD. The SAS task EVSELECT generated the list of event files by considering the good events having patterns 0–4 for PN and 0–12 for MOS data. The data was checked for the effects of pile-up and was found to be unaffected after examining with the task EPATPLOT for each source. In order to check the presence of high background intervals in the data, the light curves were generated considering the single-event (PATTERN = 0) in >10 keV energy range for MOS and that in the 10-12 keV band for PN. Selection of the good time intervals was made by removing the high-background intervals where the count rate was higher than 0.35 counts s⁻¹ for MOS and 0.4 counts s⁻¹ for PN in these light curves.

A circular region of radius of 30'', 15'', and 22'' centered at the source co-ordinates was selected to extract the EPIC light curves and spectra of WR 25, WR 121a, and WR 125, respectively. Background estimation was done from circular region of the same size at source-free regions surrounding the source. For HD 93205, the source region was chosen as an ellipse having semi-major and minor axis of 17'' and 10'', respectively. However, a circular region of radius 15'' was selected for background determination. The task EPICLCCORR corrected the obtained light curves by selecting good time intervals and discarding the dead time events. Additionally, the light curves were also corrected for the exposure and PSF improvements while subtracting background from the source light curves. The source as well as the background spectra were generated by the task EVSELECT. The dedicated ARF and RMF response matrices required for calibrating the energy and flux axes were calculated by the tasks ARFGEN and RMFGEN, respectively. Back scaling of the extracted spectra was done using the task BACKSCALE. Further temporal and spectral analyses were performed using HEASoft v6.21 and above.

2.4 X-ray analysis techniques

X-ray observations of celestial sources obtained by operating CCDs in PC mode can be utilized in three ways. The total number of incoming photons from a particular sky region can be counted and an image is made out of it. Secondly, the information about arrival time of the photons can be used to obtain the light curves (time versus counts or counts s^{-1}) that show how bright a source is over time. Lastly, the measured energies of the X-ray photons provide spectrum of the source of interest. The different techniques involved in analyzing X-ray light curves and spectra are explained below.

2.4.1 Timing analysis

The initial step to carry out the detailed timing analysis of any source is to obtain a light curve over a sufficiently long time baseline with appropriate resolution. In order to generate the light curve of the object of interest, a circular region having radius of a few arcsecond to a few arcminute (depending upon the detector specifications) is chosen around the source position in the extracted X-ray image. An elliptical source region has also been selected in the case of HD 93205. Similarly, background light curve is obtained from a region surrounding the source on the same detector. Further, the task LCMATH is used to subtract the background light curve from the source light curve by taking proper care of the scaling of the two regions of extraction. Lastly, plotting and re-binning of the source light curve can be performed using the task LCURVE. Both LCMATH and LCURVE are the packages built in FTOOLS.

2.4.2 Spectral analysis

X-ray spectral fitting is performed in XSPEC ([Arnaud, 1996](#)). XSPEC is built inside HEASoft and is an interactive and command-driven program. It can be used for the X-ray spectrum observed by any spectrometer. An X-ray observed source spectrum is a distribution of X-ray photon counts (C) in a given instrument channel (I). It is obtained by using two files in XSPEC, a source spectrum file and another is the background spectrum file. Firstly, the total counts recorded by the detector in a particular channel for both the files are estimated. Ultimately, the source spectra $C(I)$ after background subtraction (in counts/seconds) is obtained as

$$C(I) = \frac{D(I)}{t_D} - \frac{a_{D(t)}}{a_{B(t)}} \times \frac{B(I)}{t_B} \quad (2.1)$$

where $D(I)$ and $B(I)$ express the counts whereas t_D and t_B are the exposure times of the data and background files, respectively. However, $a_{D(t)}$ and $a_{B(t)}$ denote the BACKSCAL keyword values in the source and background spectral files, respectively, which is the ratio of the area from which the spectrum is extracted to the total detector area. The actual source spectrum ($f(E)$) may be obtained from the observed spectrum by the relation

$$C(I) = \int f(E)R(I, E)dE \quad (2.2)$$

where the response of the instrument is considered by the term $R(I, E)$. It includes the contribution from (a) effective area of the telescope as well as the scientific instrument, $ARF(E)$, where both are energy-dependent, and (b) the probability of detecting an incoming photon of energy E in the channel I , $RMF(I, E)$. The most common approach to perform low- or moderate-resolution X-ray spectral analysis is the forward fitting. This begins by specifying a possible model spectrum $f(E)$ which depends upon a set of parameters. The chosen model should be based upon the physical nature of the source. The spectrum is convolved with the detector response. Further, the predicted count spectrum, $C_p(I)$, is calculated which is compared to the observed spectrum, $C(I)$ using some statistical measure. The parameters of the initial spectral model $f(E)$ are then modified until the best value of the statistics chosen is found. These model parameters are referred to as the best-fit parameters and the corresponding model, $f_b(E)$, is considered as the best-fit model.

The fit statistic commonly used for estimating the “best-fit” model is the χ^2 statistics. It is defined as

$$\chi^2 = \sum \frac{(C(I) - C_p(I))^2}{(\sigma(I))^2} \quad (2.3)$$

where $\sigma(I)$ is the error associated with counts of the specified channel and is given as $\sqrt{C(I)}$. Goodness of fit is provided by χ^2 statistic for a given number of degrees of freedom (dof) (=number of channels–number of model parameters). Generally, “reduced χ^2 ” ($=\chi^2/(dof)$) is expected to be close to one. If the value of reduced χ^2 is $\gg 1$ then it indicates a poor fit of the model. However, a value $\ll 1$ signifies over-estimation of the error on the data.

2. TELESCOPES, INSTRUMENTS, OBSERVATIONS, AND DATA PROCESSING

The χ^2 statistic is also used for estimating the “confidence interval” for the best-fit parameter. It is computed by varying the value of the concerned parameter around its “best-fit” number. It is varied until χ^2 increases by a particular amount from the minimum value achieved ($\Delta\chi^2$). Here, $\Delta\chi^2$ is dependent upon the required confidence level and the number of concerned parameters. For example, $\Delta\chi^2$ is 2.706 for 90% confidence level for a single parameter of interest.

There are a few additive, multiplicative, and convolution models used for the X-ray spectral fitting of massive stars. A brief description of each model used is given below.

2.4.2.1 Astrophysical Plasma Emission Code (APEC)

There are several plasma emission models that can be used to analyze data from the high resolution X-ray spectrometers on-board various X-ray satellites. There are mainly three emission processes giving rise to the X-ray continuum from a hot thermal gas having cosmic abundances in ionization equilibrium. These are thermal bremsstrahlung (free-free emission), recombination (free-bound emission), and two-photon decay of metastable states. However, the characteristic X-ray lines result from the collision between hot ions and electrons. X-ray emission lines originate from the valence or inner-shell electrons excitation from collisions, radiative and di-electronic recombination, inner-shell collisional ionization, and radiative cascades following any of these processes. The information about the abundances, charge state, density, temperature, thermal motion, and the bulk motion of the emitting plasma can be obtained from the emission lines as well as the line ratios.

The X-ray emission from the interaction region of massive multiple systems is thermal. Thus, the chemical abundances, emission measure, and temperature of the hot plasma determine its main characteristics. This is true for the case of plasma under the conditions of collisional ionization equilibrium. An optically thin plasma model, APEC, is included in XSPEC to model the observed X-ray spectrum which can later be compared with the X-ray emission predicted by the colliding stellar wind models. APEC is the Astrophysical Plasma Emission Code (Smith et al., 2001) evolved from the original Raymond & Smith (1977) code. The temperature of the emitting plasma constitutes the main parameter of APEC model along with the normalization of the emission. Normalization constant is the emission measure ($= \int n_e n_H dV$ where n_e and n_H denote the electron and hydrogen densities) of the

emitting plasma scaled down by the distance to the emitting source. The third important parameter is the abundances of different elements that determine the line emission spectrum as well as continuum emission. Several components of APEC having multiple temperatures can be considered simultaneously to model an observed X-ray spectrum.

In order to calculate the hot plasma spectral models, APEC uses atomic data provided by Astrophysical Plasma Emission Database (APED¹). The APED contains the all the necessary atomic information such as recombination cross-sections, collisional and radiative rates, satellite line wavelengths, and dielectronic recombination rates, etc. Atomic data for over a million lines is present in APED in spite of the fact that several of them are very weak to observe individually. Both the line and continuum emissivities are calculated by APEC for a hot, optically-thin plasma that is in collisional ionization equilibrium. The APED line and continuum outputs are applied to the optically-thin thermal plasma with astronomical abundances as those of [Anders & Grevesse \(1989\)](#). Therefore, an X-ray spectrum is calculated by taking information of the atomic transition rates and energies of the ions involved from APED and a code, APEC calculates the interplay between the different rates.

2.4.2.2 Photo-electric absorption model

A photoelectric absorption (PHABS) model is used for measuring the effects of interstellar absorption and the local stellar wind absorption of the X-rays from the target source. It is a multiplicative model used with the plasma emission model. The functional form of PHABS is given as:

$$M(E) = \exp[-N_H\sigma(E)] \quad (2.4)$$

where the cross-section for the photo-electric interaction is given by $\sigma(E)$ and doesn't include Thomson scattering. The equivalent hydrogen column density is denoted with N_H in 10^{22} atoms cm^{-2} unit. Here, the elemental abundances are set according to [Anders & Grevesse \(1989\)](#).

2.4.2.3 X-ray flux

CFLUX is the model used for determining the X-ray flux and the corresponding error from other model components. It is implemented as a convolution model in XSPEC.

¹<http://www.atomdb.org/index.php>

Three parameters are required for the working of this model. These are lower and higher energies over which the flux has to be determined and third is the $\log_{10}(\text{flux})$ which calculates the flux in units of $\text{erg cm}^{-2} \text{s}^{-1}$. However, an online X-ray tool called WebPIMMS¹ is used to convert X-ray count rate to flux when the spectra has the low counts to fit it properly in XSPEC.

2.5 Near Infra-Red (NIR) observations

2.5.1 Telescope

The NIR data analyzed in this thesis has been obtained from 3.6 m Devasthal Optical Telescope (DOT) (Kumar et al. 2018, Omar et al. 2017). The telescope is situated at Devasthal having longitude=79.69° E, latitude=29.36° N, and altitude = 2426 m. It is the largest optical telescope in India currently with its 3.6 m diameter of the primary mirror. The telescope is equipped with Ritchey-Chretien optics having an effective f-ratio as f/9 with a plate scale of $6.366'' \text{mm}^{-1}$. The primary mirror is 165 mm thick with an optical diameter of 3.6 m and is characterized with f/2 focal ratio. However, the secondary mirror has 120 mm thickness, an optical diameter of 953 mm and f/4 focal ratio. The telescope is supported on an altitude-azimuth mount and is operational in 350-5000 nm waveband.

The quality of the telescope image is affected adversely because of the aberrations caused by temperature fluctuations or mechanical flexure of the telescope tube. Therefore, an active optics system (AOS) has been equipped with 3.6 m DOT to compensate for the effects of distorting forces which vary over timescales of few seconds. A total of 69 actuators actively control the primary mirror and maintain its appropriate shape as well as position for every elevation. Whereas, a hexapod system actively controls the position and orientation of the secondary mirror of the telescope to counter the optical aberrations effects. The wavefront incoming to the telescope is measured and analyzed by a wave front sensor (WFS) giving output to upgrade the image quality. AOS helps to keep the proper alignment of the primary and secondary mirrors. Further, Shack-Hartmann wavefront sensing system can also be operated in a closed-loop to implement the mirror adjustments.

There are three Cassegrain ports available with DOT at 2.5 m back focal distance. The science FoV of the main axial port is 30' diameter while each of the

¹<https://heasarc.gsfc.nasa.gov/cgi-bin/Tools/w3pimms/w3pimms.pl>

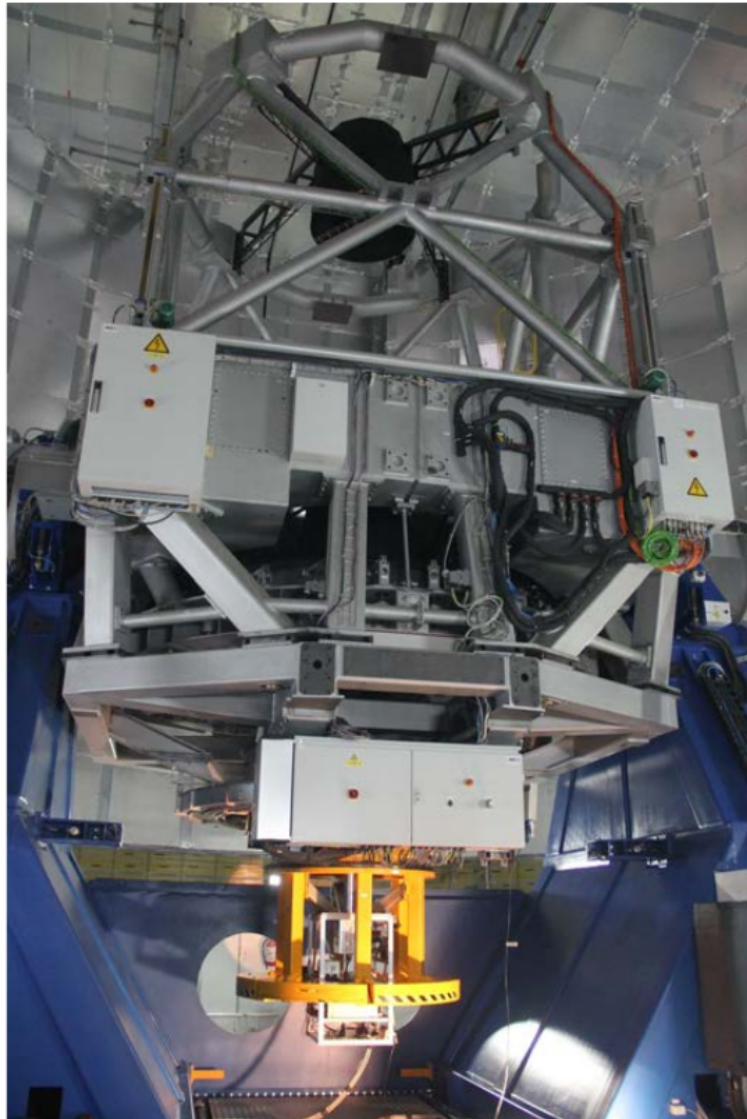


Figure 2.7: TIRCAM2 mounted on the axial port of 3.6 m DOT. The figure is adopted from [Baug et al. \(2018\)](#).

two side ports present 10' diameter FoV. Presently, four scientific instruments are operational to observe with DOT. In the optical waveband, there is a 4K×4K IMAGER and spectroscopic data is observed with ARIES-Devasthal Faint Object Spectrograph and Camera (ADFOSC). Whereas photometric and spectroscopic observations in the NIR waveband are performed with TIFR NIR Imaging Camera-II (TIRCAM2) and TIFR-ARIES NIR Spectrometer (TANSPEC). Data from TIRCAM2 has been collected for few carbon-rich WR stars to study their dust emission properties.

2.5.2 Instrument

TIRCAM2 is a Raytheon 512×512 pixels InSb Aladdin III Quadrant focal plane array (Ojha et al. 2018, Baug et al. 2018). It works at an operating temperature of 35 K maintained through a closed-cycle Helium cryo-cooler. Sensitivity of TIRCAM2 lies in 1-5 μm wavelength band but the telescope optics limits the working wavelength range to less than 3.8 μm . The camera pixel scale is $0.169'' \pm 0.002''$ when mounted with the telescope and has a small FoV of $86.5'' \times 86.5''$. TIRCAM2 has three broad-band ($\Delta\lambda \sim 0.3\text{-}0.4 \mu\text{m}$) photometric filters which are J (1.2 μm), H (1.65 μm), and K (2.19 μm). However, the narrow-band ($\Delta\lambda \sim 0.03\text{-}0.07 \mu\text{m}$) filters include Br- γ (2.16 μm), K-cont (2.17 μm), Polycyclic aromatic hydrocarbon (PAH, 3.29 μm), and narrow band L (nbL, 3.59 μm). The dark current, readout noise, and median gain of the detector has been found to be $\sim 12 \text{ e}^- \text{ s}^{-1}$, $\sim 30 \text{ e}^-$ (single readout), and $\sim 10 \text{ e}^- \text{ ADU}^{-1}$, respectively. The sampling time of TIRCAM2 is ~ 256 ms for the full frame mode and for observing a window of 32×32 square pixels, it is ~ 16 ms. TIRCAM2 plays a significant role in observing bright nbL and PAH sources up to 3.59 μm wavelength which are otherwise saturated in Spitzer-Infrared Array Camera observations.

2.5.3 Observations and data reduction

The NIR imaging of WR 125 was performed on the nights of 2017 October 17, 2020 October 09, and 2021 March 01 using TIRCAM2. Observations were carried out in J, H, and K filters. The FWHM of the source PSF was seen to be sub-arcsecond in all JHK bands throughout the observations. The standard strategy for the NIR imaging was adopted which included (a) dark frame acquisition and (b) flat frames observations in each filter during the twilights. The science frames were taken by dithering the source position to three different locations on the CCD. For WR 125, eleven frames of 1 s exposure were obtained in J band in each of the three dithered positions. However, the same number of frames with 0.5 s exposure time were obtained in both H and K bands. For the photometric reduction, the Image Reduction and Analysis Facility (IRAF) software¹ was used. A similar strategy was followed for all the filters which included the following pre-processing steps to transform the raw images into useful science frames.

¹<http://iraf.net/>

1. **Dark current correction:** The additional charge is generated in the electronic detector due to the thermal fluctuations. This charge is measured through the dark frames taken with closed shutter of the CCD for the same exposure time as given to the source frames. To apply the dark correction, a master dark frame was obtained by average combining all the corresponding dark frames using the “IMCOMBINE” task of the IRAF package. Later, the master dark frame was subtracted from each scientific frame using the task “IMARITH”.
2. **Flat fielding:** All the pixels of a CCD do not have the same response to the incoming light. Further, the telescope optics also creates potential distortions. These result in addition of spatial noise to the frames because of different reactions of the neighboring pixels for similar input conditions. An image of uniform background is used to make corrections for the non-uniform sensitivity of pixels called flat frames. Flat frames were observed either during morning or evening twilight time when the illumination of the sky is uniform. To apply flat correction, a median flat frame was obtained using the “FLATCOMBINE” task of the IRAF package. Further, “CCDPROC” was utilized to get the science frames free from non-uniform pixel variations.
3. **Sky subtraction:** The presence of OH emission lines, zodiacal emission, water vapor, moonlight, and thermal emission from the atmosphere and the telescope illuminates the NIR night sky. Therefore, the NIR sky is many times brighter as compared to the sky in optical bands and its elimination from the target source frames is a necessary step in the data reduction procedure. Here, we have constructed the master sky frame in each of the filters by median combining the science frames with dithered source positions of the corresponding NIR band using the task “IMCOMBINE”. This was possible because the acquired target field was not crowded. Further, the master sky frame was subtracted from each science frame using the task “IMARITH”.

The sky subtracted science frames were finally aligned and combined to yield a good signal to noise ratio image of the source. This completes the pre-processing of the data. Further, the aperture photometry was performed in all the JHK bands as WR 125 was isolated in all the science frames. The aperture photometry collects and adds up the observed counts in a specified circular geometric region called “aperture”. This does not depend upon the original shape of the source PSF. The

2. TELESCOPES, INSTRUMENTS, OBSERVATIONS, AND DATA PROCESSING

total photons are estimated within an aperture having its center at the source coordinates. Generally, the aperture corresponding to three times the FWHM of the PSF is chosen which contains >99% of the source light. Additionally, background sky photons are also measured from a star free area in the frame. The difference between these two counts is computed. The IRAF task “PHOT” is used to convert the resulting counts of a particular star into magnitude scale. “PHOT” allows specifying a series of increasing concentric apertures for the target source and a sky annulus for the background estimation.

To calibrate the instrumental magnitude of the target source to the standard system, the following two sets of transformation equations were used for the observations made in the year 2017, 2020, and 2021, respectively.

$$(J - H) = (0.50 \pm 0.12) \times (j - h) + (0.79 \pm 0.08) \quad (2.5)$$

$$(J - K) = (0.98 \pm 0.08) \times (j - k) + (1.34 \pm 0.03) \quad (2.6)$$

$$(J - j) = (0.33 \pm 0.07) \times (J - H) + (-4.05 \pm 0.07) \quad (2.7)$$

and

$$(J - H) = (0.81 \pm 0.13) \times (j - h) + (0.91 \pm 0.07) \quad (2.8)$$

$$(J - K) = (0.79 \pm 0.11) \times (j - k) + (1.43 \pm 0.07) \quad (2.9)$$

$$(J - j) = (0.28 \pm 0.09) \times (J - H) + (-4.14 \pm 0.08) \quad (2.10)$$

and

$$(J - H) = (0.87 \pm 0.12) \times (j - h) + (1.35 \pm 0.06) \quad (2.11)$$

$$(J - K) = (1.24 \pm 0.19) \times (j - k) + (2.64 \pm 0.20) \quad (2.12)$$

$$(J - j) = (0.33 \pm 0.13) \times (J - H) + (-4.51 \pm 0.12) \quad (2.13)$$

where the capital JHK denote the standard magnitudes of the stars taken from the 2MASS catalog while the small jhk represents the current instrumental magnitudes of the same stars present in the FoV. The absolute JHK magnitudes obtained for WR 125 are given in Table 2.3.

Table 2.3: NIR observations of WR 125 with TIRCAM2

Date	J	H (mag)	K
2017-10-17	8.95 ± 0.09	8.14 ± 0.09	8.07 ± 0.11
2020-10-09	9.16 ± 0.12	8.29 ± 0.14	7.59 ± 0.14
2021-03-01	8.90 ± 0.14	8.31 ± 0.08	7.50 ± 0.12

2.6 Optical polarimetric observations

2.6.1 Aries IMaging POLarimeter (AIMPOL)

The polarimetric observations in optical waveband have been made using 1.04-m Sampurnanand Telescope (ST; [Sinvhal et al. 1972](#)) located at Manora Peak, Nainital with AIMPOL as the back-end instrument. The telescope with a diameter of 1.04-m (f/13, plate scale of $15.5''/\text{mm}$) is a Ritchey-Chrétien reflector with a Cassegrain focus and equatorial 2-pier mounting. The tracking accuracy of ST is around $7''/\text{hr}$ ($0.1''/\text{min}$) without guider. AIMPOL is further coupled to TK 1024×1024 CCD camera in which each pixel corresponds to $1.73''$ on the sky. The central 325×325 pixels of the CCD imaging area are used for the observations. The CCD offers a gain of $11.98 \text{ e}^-/\text{ADU}$, however, has read-out noise as 7.0 e^- . The CCD is operated at a temperature of -110° C and read-out at 40 kHz rate.

The optical design of AIMPOL is shown in Figure 2.8 (taken from [Rautela et al. 2004](#)). AIMPOL is consisted of an achromatic half-wave plate (HWP) and beam-splitter Wollaston prism acting as a modulator and analyzer, respectively. A f/13 beam from the telescope falls on the field lens that makes an image on the CCD chip after passing through the camera lens. The HWP and the analyzer are present in between the field lens and camera lens. HWP is rotated through 0° to 67.5° in 22.5° steps. It gives two orthogonal components of polarized electric vector with variable intensities upon emerging out of the Wollaston prism. The north-south axis of the telescope is considered as a reference to align the axis of the Wollaston prism. Further, the fast axis of HWP axis is made to be aligned with the prism axis by adjusting the position of the plate. The system optical axis is normal to the prism axis as well as HWP fast axis. When light passes through the Wollaston prism, it splits into two orthogonal polarization components, parallel and perpendicular to the axis of Wollaston prism. Both components travel slightly in different directions resulting in to two images being produced on the CCD, ordinary

2. TELESCOPES, INSTRUMENTS, OBSERVATIONS, AND DATA PROCESSING

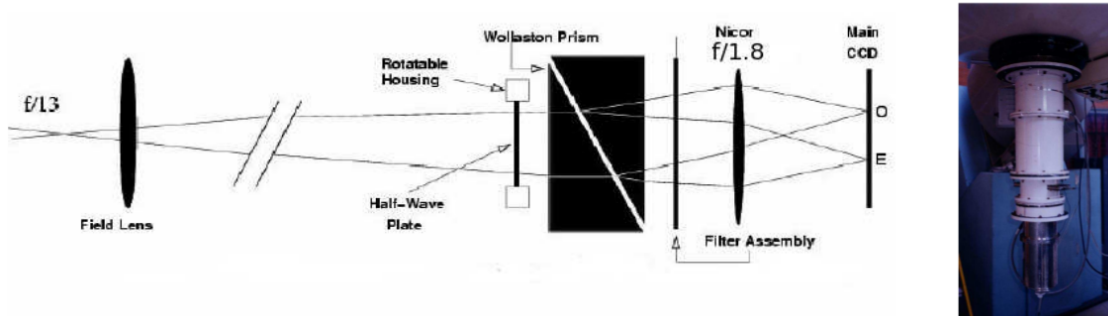


Figure 2.8: Optical design of AIMPOL from [Rautela et al. \(2004\)](#) (*left*) and AIMPOL mounted at the base of ST along with 1024×1024 CCD camera (*right*).

(O) and extraordinary (E), separated by 27 pixels for each source in the 8' diameter FoV of AIMPOL.

2.6.2 Observations and data processing

We have initiated a polarimetric observation campaign of a sample of 12 massive binaries consisting of WR+O as well as O+O systems during the years 2016-2020. The observations obtained for DH Cep are presented in this thesis. DH Cep was observed in the B, V, R, and I photometric bands having $\lambda_{eff} = 0.44, 0.55, 0.66,$ and $0.80 \mu\text{m}$, respectively, on the nights of 2017 October 15, 16, and November 12, 20, 21 as well as December 14. The typical exposure time of 30 s, 10 s, 5 s, and 10 s was used in B, V, R, and I filters, respectively. The same exposure time was set to observe the source at each of the four positions of the HWP which comprises a single data point. Polarized and unpolarized standard stars from [Schmidt et al. \(1992\)](#) were also observed to perform the zero point calibration of the estimated polarization angles of the target and the correction for instrumental polarization, respectively.

The processing of the polarimetric data was also performed using the IRAF software. The cleaning of the polarimetric data includes subtraction of bias frame from the individual science frames. The bias frames are observed by simply reading out the pixels with closed CCD shutter. It provides information about the noise level produced by CCD electronics. Several bias frames were acquired in each observing run and then a master bias frame was obtained by combining them using median statistics using the “ZEROCOMBINE” task in IRAF. The master bias was then subtracted from all the raw images. The FWHM of the stellar images varies from 2-3

2.7 Data taken from surveys and other literature

pixels during the observations. The standard aperture photometry technique, as employed in case of NIR data, has been performed to estimate the ordinary and extraordinary fluxes for the program star. A quantity called $R(\alpha)$ is defined as following by [Rautela et al. \(2004\)](#):

$$R(\alpha) = \frac{\frac{I_e(\alpha)}{I_o(\alpha)} - 1}{\frac{I_e(\alpha)}{I_o(\alpha)} + 1} = p \cos(2\psi - 4\alpha) \quad (2.14)$$

where p is the degree of polarization and ψ is the polarization angle. I_e and I_o are the estimated fluxes of extra-ordinary and ordinary images of a single source, respectively. The α denotes the position of the fast axis of HWP at 0° , 22.5° , 45° , and 67.5° with the north-south direction. The values of $R(\alpha)$ at the four positions of the HWP define the four normalized Stokes parameters as $R(0^\circ) = q$, $R(22.5^\circ) = u$, $R(45^\circ) = q_1$, and $R(67.5^\circ) = u_1$. The error associated with $R(\alpha)$ is given as

$$\sigma_R(\alpha) = \frac{\sqrt{I_e + I_o + 2I_b}}{I_e + I_o} \quad (2.15)$$

where I_b is the average background counts around the E-ray and O-ray images. The response of the CCD to the two orthogonal polarization components may be different as it is a function of the position on the CCD surface. Therefore, the genuine signal may deviate from the measured signal by a factor F_o/F_e given as

$$\frac{F_o}{F_e} = \left[\frac{I_o(0^\circ)}{I_e(45^\circ)} \times \frac{I_o(45^\circ)}{I_e(0^\circ)} \times \frac{I_o(22.5^\circ)}{I_e(67.5^\circ)} \times \frac{I_o(67.5^\circ)}{I_e(22.5^\circ)} \right]^{1/4} \quad (2.16)$$

so that the accurate normalized fluxes of E-ray (I'_e) and O-ray (I'_o) can be represented as below:

$$\frac{I'_e(\alpha)}{I'_o(\alpha)} = \frac{I_e(\alpha)}{I_o(\alpha)} \times \frac{F_o}{F_e} \quad (2.17)$$

By fitting the equation 2.14 using the estimated four normalized stokes parameters, the values of p and ψ can be derived.

2.7 Data taken from surveys and other literature

Apart from the telescopes and observations described above, the infra-red and X-ray data from some other telescopes have also been used for this study. This data has

2. TELESCOPES, INSTRUMENTS, OBSERVATIONS, AND DATA PROCESSING

not been reduced but used directly by taking their output either from the previous papers or the survey results.

1. ***Einstein***: The count rate for WR 125 estimated by Imaging Proportional Counter (IPC) on-board *Einstein* (Giacconi et al., 1979) has been utilized in this work. 1978 November 13 marks the date of *Einstein* launch and it was working till April 1981. *Einstein* utilized X-ray focusing optics with imaging detectors for the first time and few arcseconds of angular resolution was provided. The *Einstein* payload consisted of a high resolution X-ray telescope which is a Wolter Type I grazing incidence telescope. It was sensitive to X-rays with energies 0.1-4.0 keV. A full focal plane coverage was provided by IPC which is a position sensitive proportional counter. Two units of such counters were carried by *Einstein* which differ only because of the window material at the front. The FoV of IPC was $75' \times 75'$, and had a spatial resolution of $\sim 1'$. The data was obtained with a time resolution of 63 msec in 0.4-4.0 keV energy range. The detector offered an effective area of $\sim 100 \text{ cm}^2$ and the background count rate was estimated to be $\sim 10^{-2} \text{ counts sec}^{-1}$.
2. ***ROSAT***: Similar to *Einstein*, count rate of WR 125 has also been obtained from the ROentgen SATellite (*ROSAT*) observatory launched on 1990 June 1 (Truemper, 1982). The *ROSAT* payload consisted of two co-aligned scientific experiments, an X-Ray Telescope and the Wide Field Camera (WFC). The X-ray telescope is used in conjunction with one of the two detectors, Position Sensitive Proportional Counter (PSPC) and High Resolution Imager (HRI), at its focal plane in energy range of 0.1-2.5 keV. There are two units of PSPC, detector B is used for the pointed observations while survey mode is operated by detector C. PSPC have 2° diameter FoV and 240 cm^2 effective area at 1 keV. These detectors provide relative time resolution down to $130 \mu\text{s}$.
3. ***NEOWISE-R survey***: The Near-Earth Object Wide-field Infrared Survey Explorer Reactivation mission (NEOWISE-R; Mainzer et al. 2011, Mainzer et al. 2014) is a NASA survey program for the asteroids and comets discovery and characterization. The Wide-Field Infrared Explorer (WISE; Wright et al. 2010) spacecraft is utilized by NEOWISE-R survey. WISE has surveyed the entire sky using a 40 cm telescope and four 1024×1024 array detectors sensitive to mid-infrared 3.4, 4.6, 12, and $22 \mu\text{m}$ wavelengths named as W1, W2, W3, and W4 bands, respectively. Similar kind of survey strategy has been adopted

2.7 Data taken from surveys and other literature

by NEOWISE-R survey as that of the prime mission. Every six months, twelve or more completely independent Single-exposures of each point on the sky are taken. The scan is made uninterruptedly along the great circles having nearly same ecliptic longitude. The sky is frozen on the focal planes for a duration of 9.9 s and 1.1 s later, it returns to the starting position. With the help of the beam splitters, W1 and W2 bands simultaneously capture the frozen sky portion with 7.7 s of effective exposure time every 11 s. Each frame is taken at 92.5° solar elongation angle and covers $47' \times 47'$ FoV. There is a 10% overlap in the scanned portions of the sky for two back to back exposures. As the Earth orbits around the Sun, there is a progress of 1° in a day in the scan path. The NEOWISE-R survey images and the extracted source data can be accessed publicly from the NASA/IPAC Infrared Science Archive (IRSA¹).

4. **2MASS survey:** The data from Two Micron All Sky Survey (2MASS, [Skrutskie et al. 2006](#)) has been utilized to standardize the instrumental magnitude of WR 125 obtained from TIRCAM2 to the absolute magnitudes (see Section 2.5.3). 2MASS survey has been performed using two 1.3 m telescopes, located at Mount Hopkins, Arizona, and Cerro Tololo, Chile. The instrument used for the survey is a three-channel camera. A 256×256 array of HgCdTe detectors is equipped in each channel. Observations were obtained at three wavelengths namely J ($1.25 \mu\text{m}$), H ($1.65 \mu\text{m}$), and Ks ($2.17 \mu\text{m}$) bands simultaneously with an integration time of 7.8 s.

¹<https://irsa.ipac.caltech.edu/>

Chapter 3

X-RAY INVESTIGATION OF THE COLLIDING WIND BINARY WR 25

3.1 WR 25: An Introduction

WR 25 (HD 93162) is a bright ($V \sim 8.03$ mag) WR binary system located in the Carina Nebula region. The spectral classification of WR 25 has always been a matter of debate because it displays dilute WN6-7 emission line spectrum (Walborn et al., 1985) combined with strong absorption features (Moffat, 1978). Later on WR 25 was classified as WN6ha by Smith et al. (1996). Looking at various spectral features of WR 25 as observed by many authors, van der Hucht (2001) categorized it as WN6h+O4f. More recently, it has been moved to the class of the “hot slash” objects by Crowther & Walborn (2011) on the basis of its P-Cygni $H\beta$ profile and was given O2.5If*/WN6 spectral type. Sota et al. (2014) detected a visual companion in WR 25 with a separation of 790 mas and V-band magnitude difference of 5.8 mag using the *Hubble Space Telescope* observations. Therefore, the latest spectral classification of WR 25 is O2.5If*/WN6+OB, with no detailed information about the spectral and luminosity class of companion star. WR 25 was seen in X-ray energy range for the first time by Seward et al. (1979) using *Einstein* X-ray observations (0.2-4.0 keV) of the Trumpler 16 open cluster and its surroundings. Later observations of *Einstein* of the same region revealed the ratio of X-ray to bolometric luminosity of $\sim 2 \times 10^{-6}$ for WR 25 is an order of magnitude higher than observed for other WR stars in same region (Seward & Chlebowski, 1982). In the X-ray survey of WR stars by Pollock (1987) and Pollock et al. (1995), WR 25 was again found to be the brightest X-ray

The results of this chapter are published in Arora et al. 2019a.

3. X-RAY INVESTIGATION OF THE COLLIDING WIND BINARY WR 25

source. Significant variability in the optical polarization was noticed by [Drissen et al. \(1992\)](#) and it was suggested that these modulations were caused by the binary motion of the stars in WR 25. [Raassen et al. \(2003\)](#) attempted to investigate the X-ray emission of WR 25 and could not notice any variability in the emission over a period of 10 yrs. But the presence of the Fe xxv emission line in *XMM-Newton* spectrum of WR 25 pointed towards wind collision occurring in the system. [Pollock & Corcoran \(2006\)](#) recognized the variations in the X-ray emission of WR 25 for the first time and suggested that it is a CWB system with a period of about 4 yrs. Later in the same year, [Gamen et al. \(2006\)](#) provided the radial velocity solutions for WR 25 and it was found to be a long period (~ 208 d) and eccentric ($e=0.5$) binary system. Orbital parameters of WR 25 are given in Table 3.1.

Table 3.1: Orbital parameters of WR 25.

Parameter	Value	Reference
Period (d)	207.85 ± 0.02	1
V_o (km s $^{-1}$)	-34.6 ± 0.5	1
K (km s $^{-1}$)	44 ± 2	1
eccentricity	0.50 ± 0.02	1
ω (degrees)	215 ± 3	1
$T_{periastron}$ (HJD)	2451598 ± 1	1
T_{RVmax} (HJD)	2451654 ± 1	1
$a \sin i$ (R_{\odot})	156 ± 8	1
$M_{pri} \sin^3 i$ (M_{\odot})	75 ± 7	2
$M_{sec} \sin^3 i$ (M_{\odot})	27 ± 3	2

Notes: Here, V_o is the radial velocity, K is the radial velocity amplitude, ω is the longitude of periastron, $T_{periastron}$ is the time of periastron passage, T_{RVmax} is the time of maximum radial velocity, $a \sin i$ is the projected semi-major axis, $M_{pri} \sin^3 i$ and $M_{sec} \sin^3 i$ are the minimum masses of primary and secondary binary components, respectively.

Reference: (1) [Gamen et al. \(2006\)](#); (2) [Gamen et al. \(2008\)](#)

A more detailed X-ray study of WR 25 was performed by [Pandey et al. \(2014\)](#) using *Swift* and *XMM-Newton* observations spanning over ~ 10 yrs. Looking at enhanced X-ray luminosity accompanied with the phase locked modulations, they concluded that WR 25 is a CWB where the X-ray emission is significantly coming from the hot plasma heated by the colliding winds. Their analysis also pointed towards the hints for a $1/D$ (D is the binary separation) variation of the X-ray luminosity, at least at higher energies (i.e. above 2 keV), while the variations in the softer energy bands were seen to be modulated by absorption effects. In order

to investigate these variations, a detailed monitoring of the X-ray emission as a function of the orbital phase must be conducted. To date, there are only a few massive binaries with longer periods (longer than ~ 100 d) which were observed with a good phase coverage. In this context, we have executed a deep X-ray study of WR 25 using the long-term archival X-ray data from modern X-ray observatories.

To this aim, we used X-ray observations of WR 25 made by *Suzaku*, *Swift*, *XMM-Newton*, and *NuSTAR* from 2000 July to 2016 August for a total of 226 epochs and investigated both the thermal and non-thermal X-ray emission. A detailed log of these observations is given in Table 2.1. The orbital phase (ϕ) of each observation was derived by using ephemeris $\text{HJD}=2,451,598.0+207.85\text{E}$ (Gamen et al., 2006). We have also included the *Swift* and *XMM-Newton* data-sets that were studied by Pandey et al. (2014). For homogeneity and application of latest calibration, these X-ray data were processed again. An X-ray image of Eta-Carinae region in 0.3-10.0 keV energy range is shown in Figure 3.1 as observed by *XMM-Newton*. The position of WR 25 and other massive stars present in this region has also been highlighted.

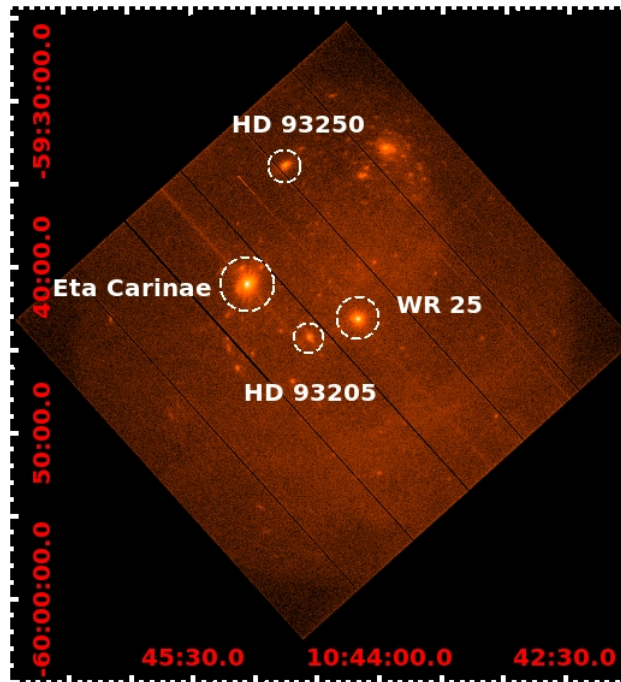


Figure 3.1: *XMM-Newton*–PN false-color image of η -Carinae field in 0.3-10.0 keV energy range from observation ID 0112560201. X- and Y- axes correspond to R.A. (J2000) and Dec. (J2000), respectively.

This chapter is organized as follows. Section 3.2 describes the X-ray spectral properties of WR 25. The X-ray light curve analysis is given in Section 3.3. The

thermal X-ray emission as well as non-thermal high energy emission from WR 25 are discussed in detail in Section 3.4, and Section 3.5 gives the conclusions.

3.2 The Spectra

3.2.1 Look at the X-ray spectra of WR 25

The X-ray spectrum of WR 25 below 10.0 keV presents the typical features of an optically thin thermal plasma emission at high temperature (above 10^6 K), as expected for a colliding wind massive binary (see e.g. Pandey et al., 2014).

The FI *Suzaku*–XIS spectrum of WR 25 at different orbital phases (but at almost same binary separation) are shown in Figures 3.2a, 3.2b, and 3.2c. The two spectra in each of the figure show the difference in the source flux when the two components of the binary system move towards and away from each other. Figure 3.2a shows the source spectra before ($\phi = 0.88$, black in colour) and after ($\phi = 0.12$, red in colour) the periastron passage. The system is brighter in X-rays just before periastron passage than after it at all the energies. Similarly, the *XMM-Newton*–MOS2 spectra of WR 25, as shown in Figure 3.2d, display the same behavior. However, as the two components move towards apastron this difference keeps on decreasing (Figure 3.2b) and vanishes close to apastron (Figure 3.2c).

The *NuSTAR*–FPMA spectrum of WR 25 without background subtraction (black in colour) as well as the background spectrum (red in colour) in 3.0–79.0 keV energy range are shown in Figure 3.3. It is evident that after 10.0 keV, both spectra are almost identical which confirms that the source counts are significant only in 3.0–10.0 keV energy range. Background photons are dominating in the extracted spectrum beyond 10.0 keV. The lack of hard X-ray emission is discussed in Sect. 3.4.2. Therefore, the *NuSTAR* spectrum of WR 25 was considered in 3.0–10.0 keV energy range only for further spectral analysis.

3.2.2 X-ray spectral analysis

The fitting of X-ray spectra in 0.3–10.0 keV energy range was done using the thermal plasma emission model APEC in XSPEC. The form of the model used was PHABS(ISM)*PHABS(LOCAL)*(VAPEC+VAPEC). The component PHABS was used to model the interstellar as well as local absorption effects. A similar model was also used by Pandey et al. (2014) for the spectral analysis of WR 25. However, Pandey et al. (2014) used WABS instead of PHABS. Since the X-ray spectra from

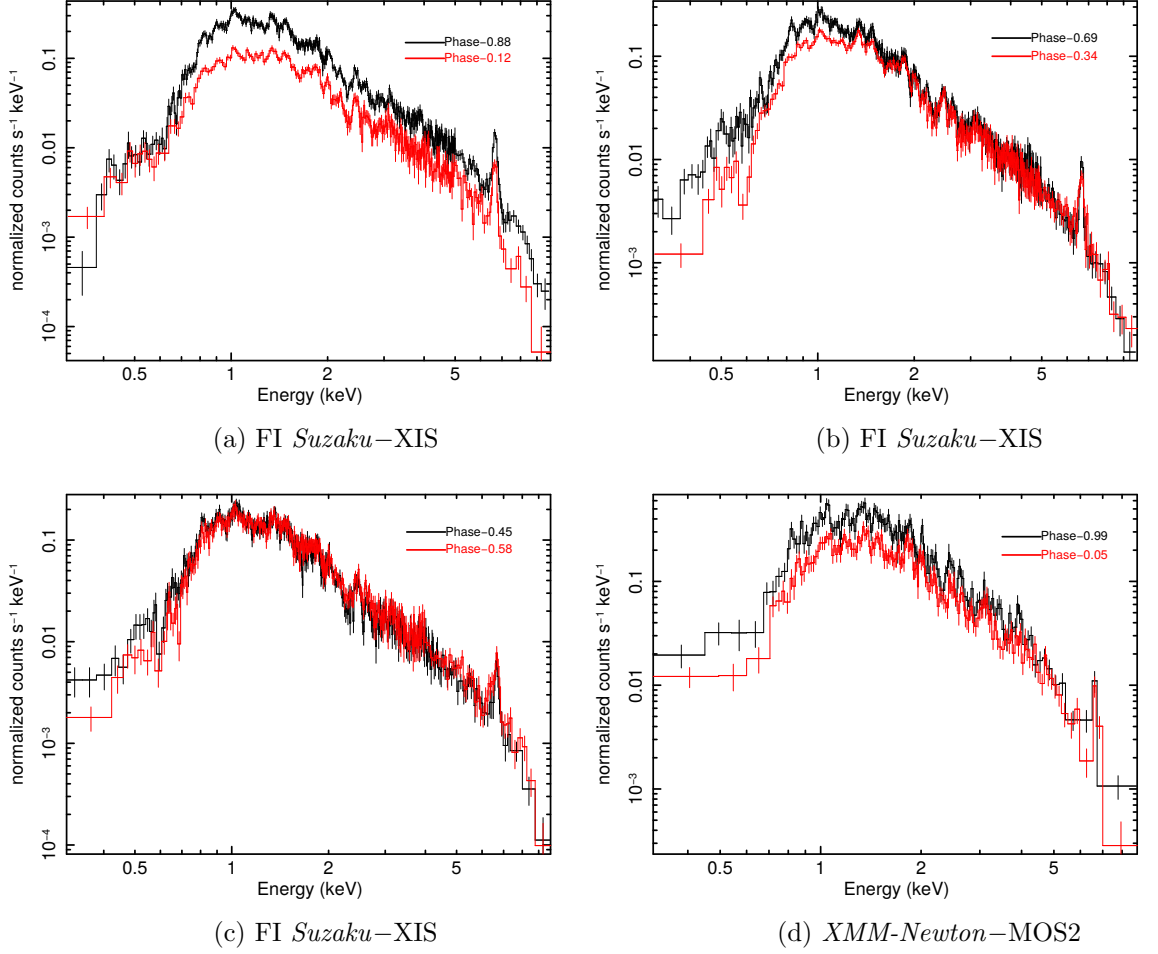


Figure 3.2: FI *Suzaku*–XIS and *XMM-Newton*–MOS2 spectra of WR 25 at different orbital phases. In each panel the stars are at (almost) identical binary separation but either receding (phase < 0.5) or approaching each other (phase > 0.5).

XMM-Newton have best photon statistics than the others, therefore, firstly, all the parameters excluding interstellar equivalent H-column density (N_H^{ISM}) were free in the spectral fitting. Temperature corresponding to cool component was found to be constant around its mean value of 0.628 keV. Phased variation of temperatures corresponding to hot component (kT_2) is shown in Figure 3.4, which is also found to be constant within 1σ level around the mean value of 2.75 keV. The model parameters derived from the current spectral fitting which are based on the latest calibration, software, and larger data sets are found to be similar to that found by Pandey et al. (2014). Therefore, the values of N_H^{ISM} , as well as the temperature and abundances for the two thermal components, were kept fixed at those obtained by

3. X-RAY INVESTIGATION OF THE COLLIDING WIND BINARY WR 25

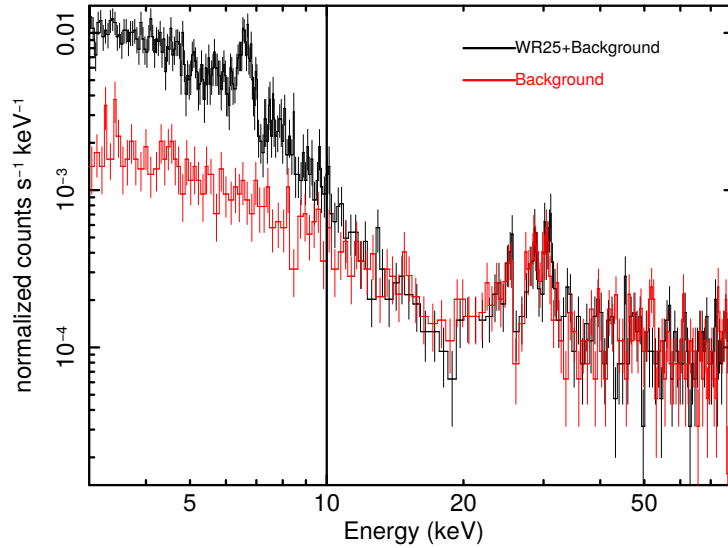


Figure 3.3: *NuSTAR*–*FPMA* spectra of WR 25 without background correction (black line) and only background (red line) of observation ID 30002010005.

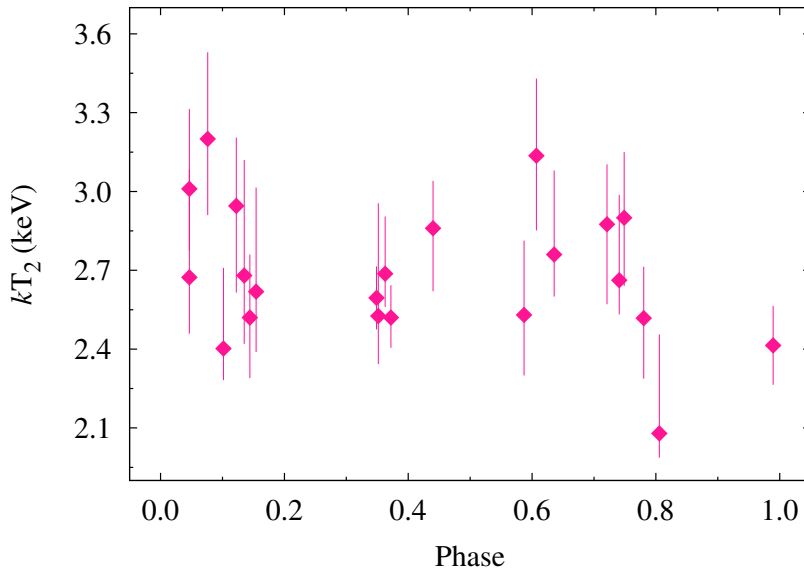


Figure 3.4: Variation of plasma temperature corresponding to hot component (kT_2) with orbital phase of WR 25 derived from *XMM-Newton*–*EPIC* data.

Pandey et al. (2014). Only the local equivalent H-column density (N_H^{local}), as well as the normalization constants for the two temperature components, were kept free. χ^2 minimization method was used to best fit the model to the data. The observed (not corrected for any absorption effects, F^{obs}), ISM corrected (F^{ism}), and intrinsic (corrected for both ISM and local wind absorption, F^{int}) X-ray fluxes of WR 25 in

soft (0.3–2.0 keV, F_S), hard (2.0–10.0 keV, F_H), and 3.0–10.0 keV (F_X) energy bands were derived. The normalization constants, $norm_1$ and $norm_2$, corresponding to the cool and hot plasma components, respectively, were also derived. The method used for fitting of the spectra from each satellite, with this model, is explained as follows:

3.2.2.1 *Suzaku*

The BI and FI *Suzaku*–XIS spectra of WR 25 were fitted jointly in 0.7–10.0 keV energy range due to poor signal-to-noise ratio (SNR) of data below 0.7 keV. The spectra obtained from each data-set were fitted individually. The spectral parameters obtained after the spectral fitting (*viz.* $norm_1$, $norm_2$, N_H^{local} , F_S^{obs} , F_H^{obs} , F_S^{ism} , F_H^{ism} , F_S^{int} , and F_H^{int}) are given in Table 3.2 and are plotted as a function of orbital phase in Figure 3.5a.

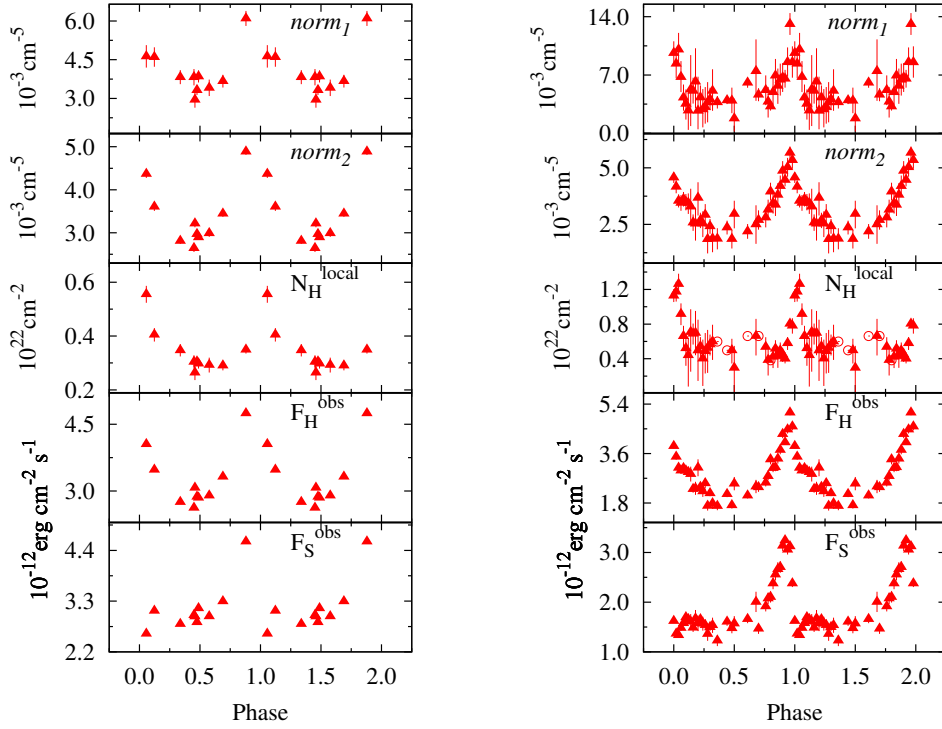
3.2.2.2 *Swift*

The fitting of the *Swift*–XRT spectra was done in the 0.5–10.0 keV energy range. Since the SNR of individual *Swift* spectra is very low, we decided to jointly fit the spectra lying within a phase interval of ≤ 0.02 . But still, we were not able to fit certain phase bins spectra due to very poor SNR. To solve this problem, we had to jointly fit those spectra with those of nearby phase bins. In addition, some orbital phase bins were not covered by observations. As a result, we defined phase bins 1 to 36 (introduced in the Table 3.2) and a joint fitting of the spectra taken in the same phase bin was performed. The values of the different spectral parameters obtained are given in Table 3.2 and their variation with orbital phase is shown in Figure 3.5b. For the five phase bins, *viz.* 32, 33, 34, 35, and 36, we had to fix the N_H^{local} values to those obtained by the spectral fitting of the nearby phase bins. The open circles in the middle panel of Figure 3.5b mark these values.

3.2.2.3 *XMM-Newton*

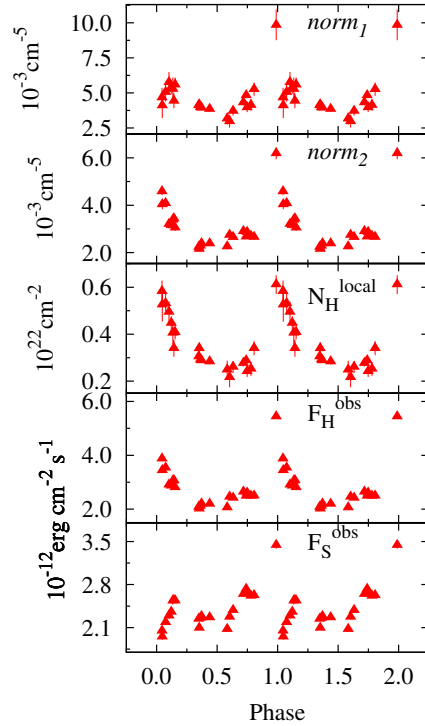
The spectra obtained from MOS1, MOS2, and PN detectors of the same data-set were fitted jointly in the 0.3–10.0 keV energy range. The spectra obtained from observation IDs 0145740201 and 0145740301 were added since these were observed on the same day. Similarly, spectra from IDs 0145740401 and 0145740501 were also added. Other spectra from different data-sets were fitted individually. The spectral

3. X-RAY INVESTIGATION OF THE COLLIDING WIND BINARY WR 25



(a) *Suzaku*–XIS

(b) *Swift*–XRT



(c) *XMM-Newton*–EPIC

Figure 3.5: Spectral parameters as a function of orbital phase as observed by (a) *Suzaku*–XIS, (b) *Swift*–XRT, and (c) *XMM-Newton*–EPIC.

parameters obtained after fitting of EPIC spectra are given in Table 3.2. These parameters are plotted as a function of orbital phase in Figure 3.5c.

3.2.2.4 *NuSTAR*

The *NuSTAR* spectrum was fitted in the 3.0–10.0 keV energy range only for the reasons mentioned earlier. Since the *NuSTAR* spectrum does not include the soft energy range, it was fitted using the single temperature component with $kT = 2.75$ keV. The form of the model used was PHABS(ISM)*PHABS(LOCAL)*VAPEC. The spectrum obtained by the detectors FPMA and FPMB of the same observation dataset were fitted jointly. Additionally, the spectrum observed within a phase difference of ≤ 0.02 were fitted jointly. Since the soft energy range is missing in *NuSTAR* spectra, N_H^{local} could not be determined through the standard fitting procedure. We had to freeze the N_H^{local} values, for *NuSTAR* spectra, to those obtained by the fitting of the very close-by phases spectra from other satellites data. The normalization constant ($norm$), and the resulting observed (F_X^{obs}), ISM corrected (F_X^{ism}) as well as intrinsic (F_X^{int}) X-ray fluxes were determined and are given in Table 3.3. The variation of $norm$ and F_X^{obs} with orbital phase is shown in Figure 3.6.

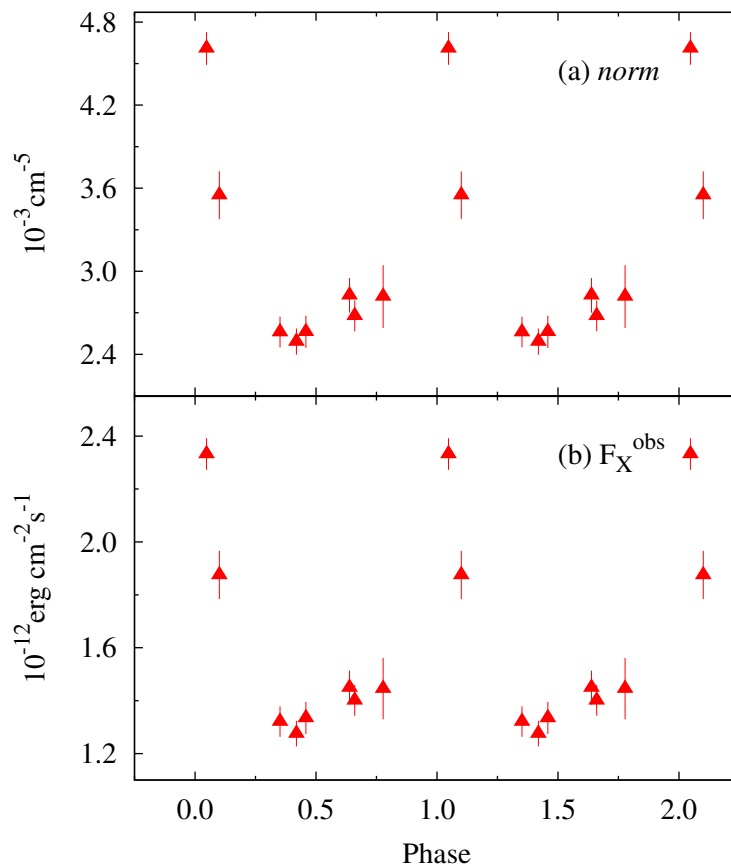


Figure 3.6: Normalization constant ($norm$) and observed X-ray flux (F_X^{obs}) as a function of orbital phase for *NuSTAR*–FPMs data.

3. X-RAY INVESTIGATION OF THE COLLIDING WIND BINARY WR 25

Table 3.2: Best fit parameters obtained from spectral fitting of WR 25 as observed from *Suzaku*, *Swift*, and *XMM-Newton*.

Obs. ID / Phase bin	ϕ	N_H^{local} (10^{22} cm $^{-2}$)	$norm_1$ (10^{-3} cm $^{-5}$)	$norm_2$ (10^{-5} cm $^{-5}$)	F_S^{obs}	F_H^{obs}	F_S^{ism} (10^{-12} erg cm $^{-2}$ s $^{-1}$)	F_H^{ism}	F_S^{int}	F_H^{int}	$\chi^2(dof)$
<i>Suzaku</i>											
100012010	0.689	0.29 $^{+0.02}$ -0.02	3.67 $^{+0.25}$ -0.25	3.45 $^{+0.07}$ -0.07	3.29 $^{+0.03}$ -0.03	3.32 $^{+0.03}$ -0.03	4.68 $^{+0.04}$ -0.04	3.39 $^{+0.03}$ -0.03	12.23 $^{+0.11}$ -0.11	3.55 $^{+0.03}$ -0.03	1.32 (775)
100045010	0.450	0.30 $^{+0.02}$ -0.02	3.82 $^{+0.32}$ -0.32	2.64 $^{+0.09}$ -0.09	2.99 $^{+0.04}$ -0.04	2.62 $^{+0.03}$ -0.04	4.27 $^{+0.06}$ -0.06	2.69 $^{+0.04}$ -0.04	11.72 $^{+0.16}$ -0.16	2.81 $^{+0.04}$ -0.04	1.39 (753)
402039010	0.879	0.35 $^{+0.01}$ -0.01	6.09 $^{+0.29}$ -0.29	4.89 $^{+0.08}$ -0.08	4.59 $^{+0.03}$ -0.03	4.74 $^{+0.03}$ -0.03	6.39 $^{+0.05}$ -0.05	4.85 $^{+0.03}$ -0.03	19.42 $^{+0.14}$ -0.14	5.12 $^{+0.04}$ -0.04	1.46 (730)
403035010	0.577	0.29 $^{+0.03}$ -0.03	3.41 $^{+0.32}$ -0.32	2.99 $^{+0.08}$ -0.08	2.97 $^{+0.04}$ -0.04	2.89 $^{+0.04}$ -0.04	4.22 $^{+0.05}$ -0.05	2.97 $^{+0.04}$ -0.04	11.13 $^{+0.14}$ -0.14	3.09 $^{+0.04}$ -0.04	1.11 (634)
403036010	0.458	0.26 $^{+0.03}$ -0.03	2.95 $^{+0.31}$ -0.31	3.22 $^{+0.09}$ -0.09	2.97 $^{+0.04}$ -0.04	3.07 $^{+0.04}$ -0.04	4.24 $^{+0.05}$ -0.05	3.14 $^{+0.04}$ -0.04	10.31 $^{+0.13}$ -0.13	3.27 $^{+0.04}$ -0.04	1.29 (632)
404038010	0.337	0.35 $^{+0.02}$ -0.02	3.82 $^{+0.27}$ -0.27	2.81 $^{+0.07}$ -0.07	2.80 $^{+0.03}$ -0.03	2.75 $^{+0.03}$ -0.03	3.92 $^{+0.04}$ -0.04	2.82 $^{+0.03}$ -0.03	11.90 $^{+0.13}$ -0.13	2.97 $^{+0.03}$ -0.03	1.08 (575)
404039010	0.123	0.40 $^{+0.02}$ -0.02	4.60 $^{+0.38}$ -0.37	3.61 $^{+0.09}$ -0.09	3.09 $^{+0.04}$ -0.04	3.48 $^{+0.04}$ -0.04	4.23 $^{+0.05}$ -0.05	3.56 $^{+0.04}$ -0.04	14.56 $^{+0.17}$ -0.17	3.78 $^{+0.04}$ -0.04	1.36 (575)
406039010	0.057	0.56 $^{+0.03}$ -0.03	4.63 $^{+0.44}$ -0.43	4.37 $^{+0.09}$ -0.09	2.59 $^{+0.03}$ -0.03	4.05 $^{+0.05}$ -0.05	3.38 $^{+0.04}$ -0.04	4.14 $^{+0.05}$ -0.05	15.45 $^{+0.18}$ -0.18	4.49 $^{+0.05}$ -0.05	1.23 (575)
408018010	0.475	0.30 $^{+0.02}$ -0.02	3.32 $^{+0.19}$ -0.19	2.97 $^{+0.05}$ -0.05	2.84 $^{+0.02}$ -0.02	2.87 $^{+0.02}$ -0.02	4.02 $^{+0.03}$ -0.03	2.94 $^{+0.02}$ -0.02	10.90 $^{+0.08}$ -0.08	3.08 $^{+0.02}$ -0.02	1.22 (575)
408018020	0.488	0.29 $^{+0.02}$ -0.02	3.85 $^{+0.23}$ -0.23	2.89 $^{+0.06}$ -0.06	3.14 $^{+0.03}$ -0.03	2.85 $^{+0.03}$ -0.03	4.48 $^{+0.04}$ -0.04	2.92 $^{+0.03}$ -0.03	12.06 $^{+0.11}$ -0.11	3.05 $^{+0.03}$ -0.03	1.84 (575)
<i>Swift</i>											
1	0.00	1.13 $^{+0.07}$ -0.07	9.63 $^{+1.42}$ -1.36	4.57 $^{+0.23}$ -0.24	1.62 $^{+0.04}$ -0.04	3.87 $^{+0.09}$ -0.09	2.50 $^{+0.06}$ -0.06	4.08 $^{+0.09}$ -0.09	31.76 $^{+0.72}$ -0.72	4.84 $^{+0.11}$ -0.11	1.33 (635)
2	0.02	1.17 $^{+0.11}$ -0.11	8.35 $^{+1.89}$ -1.76	4.16 $^{+0.28}$ -0.29	1.36 $^{+0.04}$ -0.04	3.48 $^{+0.10}$ -0.10	2.08 $^{+0.06}$ -0.06	3.66 $^{+0.11}$ -0.11	27.77 $^{+0.82}$ -0.82	4.38 $^{+0.13}$ -0.13	1.27 (393)
3	0.04	1.26 $^{+0.12}$ -0.12	10.05 $^{+1.99}$ -1.84	3.54 $^{+0.29}$ -0.29	1.34 $^{+0.05}$ -0.05	3.08 $^{+0.11}$ -0.11	2.02 $^{+0.07}$ -0.07	3.25 $^{+0.11}$ -0.11	31.75 $^{+1.09}$ -1.09	3.96 $^{+0.14}$ -0.14	1.47 (332)
4	0.06	0.92 $^{+0.12}$ -0.12	6.74 $^{+1.92}$ -1.79	3.45 $^{+0.34}$ -0.35	1.48 $^{+0.06}$ -0.06	2.98 $^{+0.12}$ -0.12	2.42 $^{+0.09}$ -0.09	3.14 $^{+0.13}$ -0.13	22.52 $^{+0.91}$ -0.91	3.62 $^{+0.15}$ -0.15	1.08 (210)
5	0.08	0.66 $^{+0.12}$ -0.12	4.28 $^{+1.58}$ -1.57	3.62 $^{+0.31}$ -0.32	1.58 $^{+0.06}$ -0.06	3.07 $^{+0.12}$ -0.12	2.77 $^{+0.11}$ -0.11	3.23 $^{+0.12}$ -0.12	15.92 $^{+0.61}$ -0.61	3.56 $^{+0.18}$ -0.18	1.09 (224)
6	0.10	0.52 $^{+0.14}$ -0.14	3.54 $^{+1.73}$ -1.89	3.49 $^{+0.35}$ -0.37	1.69 $^{+0.07}$ -0.08	2.98 $^{+0.13}$ -0.13	3.15 $^{+0.10}$ -0.10	3.14 $^{+0.14}$ -0.14	13.73 $^{+0.60}$ -0.61	3.39 $^{+0.15}$ -0.15	0.98 (149)
7	0.12	0.44 $^{+0.19}$ -0.19	2.73 $^{+2.28}$ -2.33	3.44 $^{+0.42}$ -0.48	1.66 $^{+0.09}$ -0.09	2.92 $^{+0.16}$ -0.16	3.16 $^{+0.17}$ -0.17	3.08 $^{+0.17}$ -0.17	11.41 $^{+0.63}$ -0.63	3.28 $^{+0.18}$ -0.18	1.19 (97)
8	0.14	0.71 $^{+0.26}$ -0.26	5.26 $^{+4.13}$ -4.39	3.29 $^{+0.79}$ -0.83	1.61 $^{+0.15}$ -0.15	2.85 $^{+0.27}$ -0.27	2.81 $^{+0.27}$ -0.27	3.01 $^{+0.28}$ -0.28	18.26 $^{+1.72}$ -1.73	3.35 $^{+0.32}$ -0.32	0.97 (31)
9	0.16	0.69 $^{+0.12}$ -0.12	5.09 $^{+1.59}$ -1.53	2.58 $^{+0.36}$ -0.37	1.48 $^{+0.08}$ -0.08	2.31 $^{+0.13}$ -0.13	2.65 $^{+0.15}$ -0.15	2.43 $^{+0.14}$ -0.14	16.98 $^{+0.94}$ -0.95	2.71 $^{+0.15}$ -0.15	1.36 (115)
10	0.18	0.69 $^{+0.25}$ -0.25	6.21 $^{+4.01}$ -3.23	2.53 $^{+0.71}$ -0.75	1.67 $^{+0.17}$ -0.17	2.33 $^{+0.24}$ -0.24	2.99 $^{+0.31}$ -0.31	2.47 $^{+0.25}$ -0.25	19.99 $^{+2.05}$ -2.05	2.76 $^{+0.28}$ -0.28	0.95 (25)
11	0.20	0.49 $^{+0.35}$ -0.35	2.69 $^{+4.09}$ -2.22	3.67 $^{+0.69}$ -0.78	1.57 $^{+0.16}$ -0.16	3.08 $^{+0.31}$ -0.31	2.89 $^{+0.29}$ -0.29	3.24 $^{+0.32}$ -0.32	11.49 $^{+1.15}$ -1.15	3.48 $^{+0.35}$ -0.35	1.10 (27)
12	0.22	0.54 $^{+0.11}$ -0.11	4.29 $^{+1.45}$ -1.44	2.68 $^{+0.36}$ -0.36	1.66 $^{+0.08}$ -0.08	2.38 $^{+0.12}$ -0.12	3.13 $^{+0.15}$ -0.15	2.51 $^{+0.12}$ -0.12	14.89 $^{+0.73}$ -0.73	2.73 $^{+0.13}$ -0.13	1.07 (105)
13	0.24	0.40 $^{+0.22}$ -0.22	2.86 $^{+2.45}$ -2.16	2.54 $^{+0.54}$ -0.60	1.57 $^{+0.14}$ -0.14	2.22 $^{+0.19}$ -0.19	3.14 $^{+0.28}$ -0.28	2.34 $^{+0.21}$ -0.21	10.79 $^{+0.97}$ -0.96	2.49 $^{+0.22}$ -0.22	0.94 (34)

Continued: Best fit parameters obtained from spectral fitting of WR 25 as observed from *Suzaku*, *Swift*, and *XMM-Newton*.

Obs. ID / Phase bin	ϕ	N_H^{local} (10^{22} cm $^{-2}$)	$norm_1$ (10^{-3} cm $^{-5}$)	$norm_2$	F_S^{obs}	F_H^{obs}	F_S^{ism} (10^{-12} erg cm $^{-2}$ s $^{-1}$)	F_H^{ism}	F_S^{int}	F_H^{int}	$\chi_\nu^2(dof)$
14	0.26	0.49 $^{+0.21}$ -0.26	3.15 $^{+2.40}$ -1.99	2.92 $^{+0.48}$ -0.53	1.54 $^{+0.11}$ -0.11	2.51 $^{+0.18}$ -0.18	2.92 $^{+0.21}$ -0.21	2.65 $^{+0.19}$ -0.19	12.00 $^{+0.88}$ -0.88	2.85 $^{+0.21}$ -0.21	0.75 (52)
15	0.28	0.52 $^{+0.21}$ -0.29	3.70 $^{+2.44}$ -2.39	1.85 $^{+0.60}$ -0.63	1.36 $^{+0.14}$ -0.14	1.69 $^{+0.17}$ -0.17	2.64 $^{+0.27}$ -0.27	1.79 $^{+0.18}$ -0.18	12.32 $^{+1.24}$ -1.25	1.95 $^{+0.19}$ -0.19	0.99 (28)
16	0.30	0.56 $^{+0.11}$ -0.13	4.09 $^{+1.37}$ -1.32	2.42 $^{+0.32}$ -0.33	1.49 $^{+0.07}$ -0.07	2.15 $^{+0.11}$ -0.11	2.81 $^{+0.14}$ -0.14	2.27 $^{+0.11}$ -0.11	14.04 $^{+0.69}$ -0.69	2.48 $^{+0.12}$ -0.12	1.14 (166)
17	0.32	0.59 $^{+0.19}$ -0.21	5.09 $^{+2.59}$ -2.39	1.88 $^{+0.59}$ -0.60	1.58 $^{+0.15}$ -0.15	1.78 $^{+0.18}$ -0.18	2.90 $^{+0.29}$ -0.29	1.89 $^{+0.19}$ -0.19	16.17 $^{+1.62}$ -1.62	2.08 $^{+0.21}$ -0.21	0.85 (41)
18	0.48	0.49 $^{+0.13}$ -0.15	3.91 $^{+1.56}$ -1.50	1.85 $^{+0.41}$ -0.42	1.48 $^{+0.10}$ -0.10	1.72 $^{+0.12}$ -0.12	2.92 $^{+0.20}$ -0.20	1.82 $^{+0.13}$ -0.13	12.90 $^{+0.90}$ -0.89	1.97 $^{+0.14}$ -0.14	1.21 (79)
19	0.50	0.29 $^{+0.25}$ -0.31	1.77 $^{+2.38}$ -1.57	2.97 $^{+0.58}$ -0.64	1.57 $^{+0.15}$ -0.15	2.50 $^{+0.24}$ -0.24	3.19 $^{+0.31}$ -0.31	2.64 $^{+0.25}$ -0.25	8.74 $^{+0.84}$ -0.84	2.76 $^{+0.27}$ -0.27	0.76 (29)
20	0.68	0.66 $^{+0.19}$ -0.22	7.46 $^{+3.82}$ -3.56	2.50 $^{+0.84}$ -0.86	2.01 $^{+0.20}$ -0.20	2.39 $^{+0.24}$ -0.24	3.69 $^{+0.37}$ -0.37	2.54 $^{+0.26}$ -0.26	23.44 $^{+2.38}$ -2.38	2.83 $^{+0.29}$ -0.29	0.76 (29)
21	0.76	0.54 $^{+0.11}$ -0.13	5.17 $^{+1.77}$ -1.79	2.80 $^{+0.43}$ -0.43	1.92 $^{+0.10}$ -0.10	2.54 $^{+0.13}$ -0.13	3.67 $^{+0.19}$ -0.19	2.68 $^{+0.14}$ -0.14	17.45 $^{+0.92}$ -0.92	2.91 $^{+0.15}$ -0.15	0.89 (25)
22	0.78	0.39 $^{+0.13}$ -0.18	3.79 $^{+1.77}$ -1.89	3.15 $^{+0.44}$ -0.46	2.08 $^{+0.11}$ -0.11	2.78 $^{+0.15}$ -0.15	4.24 $^{+0.23}$ -0.23	2.93 $^{+0.16}$ -0.16	14.04 $^{+0.76}$ -0.76	3.11 $^{+0.17}$ -0.17	1.12 (106)
23	0.82	0.42 $^{+0.11}$ -0.13	4.93 $^{+1.79}$ -1.82	3.44 $^{+0.45}$ -0.46	2.38 $^{+0.13}$ -0.12	3.07 $^{+0.15}$ -0.15	4.79 $^{+0.24}$ -0.24	3.24 $^{+0.16}$ -0.16	17.52 $^{+0.86}$ -0.86	3.46 $^{+0.17}$ -0.17	1.36 (103)
24	0.84	0.52 $^{+0.09}$ -0.11	6.92 $^{+2.01}$ -2.01	3.37 $^{+0.49}$ -0.49	2.56 $^{+0.12}$ -0.12	3.10 $^{+0.14}$ -0.14	4.99 $^{+0.23}$ -0.23	3.28 $^{+0.15}$ -0.15	22.91 $^{+1.07}$ -1.07	3.56 $^{+0.17}$ -0.17	0.83 (116)
25	0.86	0.43 $^{+0.11}$ -0.14	5.69 $^{+2.08}$ -2.16	3.81 $^{+0.52}$ -0.52	2.67 $^{+0.14}$ -0.14	3.41 $^{+0.18}$ -0.18	5.36 $^{+0.28}$ -0.28	3.59 $^{+0.19}$ -0.19	20.04 $^{+1.05}$ -1.05	3.85 $^{+0.20}$ -0.20	1.13 (133)
26	0.88	0.49 $^{+0.09}$ -0.11	6.43 $^{+1.92}$ -1.90	4.19 $^{+0.47}$ -0.47	2.71 $^{+0.11}$ -0.11	3.73 $^{+0.16}$ -0.16	5.25 $^{+0.22}$ -0.22	3.94 $^{+0.17}$ -0.17	22.52 $^{+0.96}$ -0.96	4.25 $^{+0.18}$ -0.18	1.05 (103)
27	0.90	0.45 $^{+0.08}$ -0.09	6.69 $^{+1.73}$ -1.74	4.87 $^{+0.43}$ -0.43	3.14 $^{+0.11}$ -0.11	4.31 $^{+0.15}$ -0.15	6.19 $^{+0.21}$ -0.21	4.55 $^{+0.16}$ -0.16	24.01 $^{+0.83}$ -0.83	4.87 $^{+0.17}$ -0.17	1.02 (169)
28	0.92	0.40 $^{+0.05}$ -0.05	6.54 $^{+1.07}$ -1.05	4.46 $^{+0.28}$ -0.28	3.24 $^{+0.08}$ -0.08	4.01 $^{+0.09}$ -0.09	6.65 $^{+0.16}$ -0.16	4.23 $^{+0.10}$ -0.10	23.12 $^{+0.55}$ -0.55	4.49 $^{+0.11}$ -0.11	1.08 (237)
29	0.94	0.58 $^{+0.07}$ -0.08	8.53 $^{+1.75}$ -1.75	5.03 $^{+0.41}$ -0.42	3.06 $^{+0.09}$ -0.09	4.47 $^{+0.14}$ -0.14	5.69 $^{+0.18}$ -0.18	4.72 $^{+0.15}$ -0.15	29.26 $^{+0.94}$ -0.94	5.16 $^{+0.17}$ -0.17	1.17 (517)
30	0.96	0.80 $^{+0.04}$ -0.04	13.10 $^{+1.33}$ -1.29	5.66 $^{+0.28}$ -0.28	3.12 $^{+0.06}$ -0.06	5.09 $^{+0.09}$ -0.09	5.35 $^{+0.10}$ -0.10	5.38 $^{+0.10}$ -0.10	42.59 $^{+0.83}$ -0.83	6.09 $^{+0.12}$ -0.12	1.00 (317)
31	0.98	0.78 $^{+0.09}$ -0.09	8.52 $^{+1.92}$ -1.85	5.34 $^{+0.38}$ -0.38	2.38 $^{+0.07}$ -0.07	4.58 $^{+0.14}$ -0.14	4.03 $^{+0.12}$ -0.12	4.83 $^{+0.15}$ -0.15	29.59 $^{+0.89}$ -0.89	5.44 $^{+0.17}$ -0.17	1.62 (570)
32	0.36	0.59	3.72 $^{+0.75}$ -0.75	1.87 $^{+0.47}$ -0.47	1.23 $^{+0.11}$ -0.11	1.69 $^{+0.15}$ -0.15	2.28 $^{+0.21}$ -0.21	1.79 $^{+0.16}$ -0.16	12.39 $^{+1.12}$ -1.12	1.96 $^{+0.18}$ -0.18	1.17 (37)
33	0.44	0.49	3.96 $^{+0.45}$ -0.45	2.36 $^{+0.30}$ -0.30	1.61 $^{+0.08}$ -0.08	2.12 $^{+0.11}$ -0.11	3.13 $^{+0.16}$ -0.16	2.24 $^{+0.12}$ -0.12	13.61 $^{+0.70}$ -0.70	2.42 $^{+0.13}$ -0.13	1.15 (112)
34	0.61	0.66	6.06 $^{+0.60}$ -0.60	2.19 $^{+0.32}$ -0.32	1.66 $^{+0.08}$ -0.08	2.07 $^{+0.11}$ -0.11	3.04 $^{+0.15}$ -0.15	2.19 $^{+0.11}$ -0.11	19.22 $^{+0.98}$ -0.97	2.44 $^{+0.12}$ -0.12	1.26 (117)
35	0.70	0.66	4.63 $^{+0.78}$ -0.78	2.69 $^{+0.43}$ -0.43	1.47 $^{+0.10}$ -0.10	2.37 $^{+0.17}$ -0.17	2.62 $^{+0.18}$ -0.18	2.50 $^{+0.18}$ -0.18	15.84 $^{+1.12}$ -1.12	2.77 $^{+0.19}$ -0.19	1.22 (73)
36	0.80	0.38	3.21 $^{+0.48}$ -0.48	3.95 $^{+0.39}$ -0.39	2.10 $^{+0.11}$ -0.11	3.38 $^{+0.18}$ -0.18	4.17 $^{+0.22}$ -0.22	3.56 $^{+0.19}$ -0.19	13.35 $^{+0.71}$ -0.71	3.77 $^{+0.20}$ -0.19	1.18 (106)
<i>XMM-Newton</i>											
0112580601	0.741	0.29 $^{+0.01}$ -0.01	4.83 $^{+0.19}$ -0.19	2.68 $^{+0.06}$ -0.06	2.73 $^{+0.02}$ -0.02	2.49 $^{+0.02}$ -0.02	6.16 $^{+0.04}$ -0.04	2.64 $^{+0.02}$ -0.02	16.38 $^{+0.12}$ -0.12	2.76 $^{+0.02}$ -0.02	1.28 (961)
0112580701	0.748	0.24 $^{+0.02}$ -0.02	3.98 $^{+0.35}$ -0.34	2.87 $^{+0.09}$ -0.10	2.66 $^{+0.04}$ -0.03	2.61 $^{+0.03}$ -0.03	6.12 $^{+0.08}$ -0.08	2.75 $^{+0.04}$ -0.04	14.24 $^{+0.19}$ -0.19	2.86 $^{+0.04}$ -0.04	1.15 (564)

3. X-RAY INVESTIGATION OF THE COLLIDING WIND BINARY WR 25

Continued: Best fit parameters obtained from spectral fitting of WR 25 as observed from *Suzaku*, *Swift*, and *XMM-Newton*.

Obs. ID / Phase bin	ϕ	N_H^{local} (10^{22} cm $^{-2}$)	$norm_1$ (10^{-3} cm $^{-5}$)	$norm_2$ (10^{-5} cm $^{-5}$)	F_S^{obs}	F_H^{obs}	F_S^{ism} (10^{-12} erg cm $^{-2}$ s $^{-1}$)	F_H^{ism}	F_S^{int}	F_H^{int}	$\chi_b^2(dof)$
0112560101	0.348	$0.31^{+0.01}_{-0.01}$	$4.12^{+0.17}_{-0.17}$	$2.24^{+0.05}_{-0.05}$	$2.24^{+0.02}_{-0.02}$	$2.09^{+0.02}_{-0.02}$	$5.00^{+0.04}_{-0.04}$	$2.21^{+0.02}_{-0.02}$	$13.93^{+0.10}_{-0.10}$	$2.31^{+0.02}_{-0.02}$	1.19 (954)
0112560201	0.363	$0.29^{+0.01}_{-0.01}$	$3.98^{+0.16}_{-0.16}$	$2.29^{+0.05}_{-0.05}$	$2.26^{+0.02}_{-0.02}$	$2.12^{+0.01}_{-0.01}$	$5.07^{+0.04}_{-0.03}$	$2.24^{+0.02}_{-0.02}$	$13.59^{+0.09}_{-0.09}$	$2.35^{+0.02}_{-0.02}$	1.29 (1014)
0112560301	0.372	$0.29^{+0.01}_{-0.01}$	$3.94^{+0.15}_{-0.15}$	$2.39^{+0.04}_{-0.04}$	$2.26^{+0.01}_{-0.01}$	$2.20^{+0.01}_{-0.01}$	$5.13^{+0.03}_{-0.03}$	$2.33^{+0.01}_{-0.01}$	$13.59^{+0.09}_{-0.09}$	$2.43^{+0.02}_{-0.02}$	1.27 (1075)
0145740101	0.134	$0.41^{+0.05}_{-0.05}$	$5.28^{+0.82}_{-0.79}$	$3.38^{+0.21}_{-0.21}$	$2.54^{+0.06}_{-0.06}$	$3.06^{+0.08}_{-0.08}$	$5.21^{+0.13}_{-0.13}$	$3.23^{+0.08}_{-0.08}$	$18.43^{+0.46}_{-0.46}$	$3.44^{+0.06}_{-0.06}$	0.98 (178)
0145740201		$0.34^{+0.04}_{-0.04}$	$4.44^{+0.54}_{-0.53}$	$3.44^{+0.14}_{-0.14}$	$2.55^{+0.04}_{-0.04}$	$3.07^{+0.05}_{-0.05}$	$5.39^{+0.09}_{-0.09}$	$3.24^{+0.06}_{-0.06}$	$16.15^{+0.28}_{-0.28}$	$3.42^{+0.06}_{-0.06}$	1.11 (285)
0145740301											
0145740401	0.153	$0.41^{+0.03}_{-0.03}$	$5.59^{+0.51}_{-0.50}$	$3.06^{+0.14}_{-0.14}$	$2.54^{+0.04}_{-0.04}$	$2.81^{+0.05}_{-0.05}$	$5.26^{+0.09}_{-0.09}$	$2.97^{+0.05}_{-0.05}$	$18.89^{+0.32}_{-0.31}$	$3.17^{+0.05}_{-0.05}$	0.98 (284)
0145740501											
0160160101	0.779	$0.25^{+0.03}_{-0.03}$	$4.13^{+0.42}_{-0.41}$	$2.71^{+0.12}_{-0.12}$	$2.62^{+0.04}_{-0.04}$	$2.49^{+0.04}_{-0.04}$	$6.03^{+0.10}_{-0.10}$	$2.64^{+0.04}_{-0.04}$	$14.48^{+0.25}_{-0.24}$	$2.74^{+0.05}_{-0.05}$	1.51 (273)
0145780101	0.988	$0.61^{+0.04}_{-0.04}$	$9.85^{+1.10}_{-1.09}$	$6.19^{+0.25}_{-0.25}$	$3.44^{+0.06}_{-0.06}$	$5.44^{+0.09}_{-0.09}$	$6.28^{+0.11}_{-0.11}$	$5.74^{+0.10}_{-0.09}$	$34.21^{+0.59}_{-0.60}$	$6.31^{+0.11}_{-0.11}$	1.29 (285)
0160560101	0.045	$0.58^{+0.04}_{-0.05}$	$4.68^{+0.68}_{-0.66}$	$4.59^{+0.15}_{-0.15}$	$2.05^{+0.03}_{-0.03}$	$3.88^{+0.06}_{-0.06}$	$3.68^{+0.06}_{-0.06}$	$4.09^{+0.07}_{-0.07}$	$18.12^{+0.30}_{-0.29}$	$4.45^{+0.07}_{-0.07}$	1.21 (322)
0160560201	0.075	$0.53^{+0.04}_{-0.04}$	$5.06^{+0.69}_{-0.68}$	$4.09^{+0.16}_{-0.16}$	$2.19^{+0.04}_{-0.04}$	$3.54^{+0.06}_{-0.06}$	$4.09^{+0.07}_{-0.07}$	$3.73^{+0.07}_{-0.07}$	$18.62^{+0.34}_{-0.34}$	$4.04^{+0.07}_{-0.07}$	1.06 (281)
0160560301	0.121	$0.45^{+0.03}_{-0.03}$	$5.41^{+0.48}_{-0.47}$	$3.16^{+0.12}_{-0.12}$	$2.36^{+0.04}_{-0.04}$	$2.87^{+0.04}_{-0.04}$	$4.73^{+0.07}_{-0.07}$	$3.03^{+0.05}_{-0.05}$	$18.51^{+0.28}_{-0.28}$	$3.25^{+0.05}_{-0.05}$	1.05 (308)
0311990101	0.439	$0.28^{+0.01}_{-0.01}$	$3.85^{+0.16}_{-0.16}$	$2.39^{+0.04}_{-0.04}$	$2.27^{+0.02}_{-0.02}$	$2.19^{+0.01}_{-0.01}$	$5.10^{+0.03}_{-0.03}$	$2.32^{+0.02}_{-0.02}$	$13.34^{+0.09}_{-0.09}$	$2.43^{+0.02}_{-0.02}$	1.32 (990)
0560580101	0.583	$0.25^{+0.04}_{-0.04}$	$3.17^{+0.42}_{-0.41}$	$2.26^{+0.12}_{-0.12}$	$2.08^{+0.04}_{-0.04}$	$2.06^{+0.04}_{-0.04}$	$4.77^{+0.09}_{-0.09}$	$2.18^{+0.04}_{-0.04}$	$11.31^{+0.23}_{-0.23}$	$2.27^{+0.04}_{-0.04}$	1.70 (228)
0560580201	0.603	$0.22^{+0.04}_{-0.04}$	$2.98^{+0.47}_{-0.45}$	$2.75^{+0.13}_{-0.13}$	$2.28^{+0.05}_{-0.05}$	$2.46^{+0.05}_{-0.05}$	$5.28^{+0.11}_{-0.11}$	$2.59^{+0.05}_{-0.05}$	$11.34^{+0.23}_{-0.23}$	$2.68^{+0.05}_{-0.05}$	1.04 (229)
0560580301	0.632	$0.26^{+0.03}_{-0.03}$	$3.72^{+0.33}_{-0.32}$	$2.66^{+0.09}_{-0.09}$	$2.39^{+0.03}_{-0.03}$	$2.42^{+0.03}_{-0.03}$	$5.42^{+0.07}_{-0.07}$	$2.56^{+0.03}_{-0.03}$	$13.27^{+0.18}_{-0.18}$	$2.66^{+0.04}_{-0.04}$	1.15 (332)
0560580401	0.717	$0.27^{+0.01}_{-0.01}$	$4.33^{+0.22}_{-0.22}$	$2.90^{+0.06}_{-0.06}$	$2.65^{+0.02}_{-0.02}$	$2.65^{+0.02}_{-0.02}$	$5.95^{+0.05}_{-0.05}$	$2.79^{+0.02}_{-0.02}$	$15.25^{+0.13}_{-0.13}$	$2.92^{+0.02}_{-0.02}$	1.37 (863)
0160160901	0.806	$0.34^{+0.03}_{-0.03}$	$5.26^{+0.47}_{-0.47}$	$2.66^{+0.13}_{-0.13}$	$2.63^{+0.05}_{-0.05}$	$2.50^{+0.04}_{-0.04}$	$5.74^{+0.09}_{-0.09}$	$2.65^{+0.05}_{-0.05}$	$17.55^{+0.31}_{-0.30}$	$2.79^{+0.05}_{-0.05}$	1.41 (197)
0742850301	0.102	$0.49^{+0.04}_{-0.04}$	$5.77^{+0.73}_{-0.72}$	$3.21^{+0.19}_{-0.19}$	$2.29^{+0.05}_{-0.05}$	$2.91^{+0.07}_{-0.07}$	$4.49^{+0.10}_{-0.10}$	$3.07^{+0.07}_{-0.07}$	$19.56^{+0.45}_{-0.45}$	$3.32^{+0.08}_{-0.08}$	1.39 (159)
0742850401	0.352	$0.34^{+0.03}_{-0.03}$	$4.17^{+0.32}_{-0.32}$	$2.15^{+0.09}_{-0.09}$	$2.09^{+0.03}_{-0.03}$	$2.02^{+0.03}_{-0.03}$	$4.58^{+0.07}_{-0.07}$	$2.13^{+0.03}_{-0.03}$	$13.95^{+0.21}_{-0.21}$	$2.25^{+0.03}_{-0.03}$	1.59 (208)
0762910401	0.047	$0.52^{+0.07}_{-0.07}$	$4.11^{+0.92}_{-0.90}$	$4.04^{+0.20}_{-0.21}$	$1.95^{+0.05}_{-0.05}$	$3.44^{+0.09}_{-0.09}$	$3.61^{+0.09}_{-0.09}$	$3.63^{+0.09}_{-0.09}$	$15.93^{+0.40}_{-0.39}$	$3.92^{+0.09}_{-0.09}$	1.07 (152)

Notes: The fitted model has the form PHABS(ISM)*PHABS(LOCAL)*(VAPEC+VAPEC), with N_H^{ISM} fixed to 3.7×10^{21} cm $^{-2}$ and the temperatures fixed to 0.628 and 2.75 keV. Abundances are given in Table 4 of Pandey et al. (2014). χ_b^2 is the reduced χ^2 and dof is degrees of freedom. Errors quoted on different parameters refer to 90% confidence level. The N_H^{local} values for 32 to 36 phase bins of *Swift* were fixed to those of the nearby phase bins. The *XMM-Newton* spectra obtained from observation IDs 0145740201 and 0145740301 as well as 0145740401 add 0145740501 were added.

Table 3.3: Best fit parameters obtained from spectral fitting of WR 25 as observed from *NuSTAR*.

Obs. ID	ϕ	N_H^{local} (10^{22} cm $^{-2}$)	$norm$ (10^{-3} cm $^{-5}$)	F_X^{obs} (10^{-12} erg cm $^{-2}$ s $^{-1}$)	F_X^{ism} (10^{-12} erg cm $^{-2}$ s $^{-1}$)	F_X^{int}	$\chi^2(dof)$
30002010002	0.777	0.29	$2.82^{+0.23}_{-0.23}$	$1.45^{+0.12}_{-0.12}$	$1.48^{+0.12}_{-0.12}$	$1.50^{+0.12}_{-0.12}$	1.26 (31)
30002010005	0.048	0.99	$4.61^{+0.12}_{-0.12}$	$2.33^{+0.06}_{-0.06}$	$2.38^{+0.06}_{-0.06}$	$2.52^{+0.06}_{-0.06}$	1.34 (63)
30101005002							
30002040004	0.351	0.34	$2.56^{+0.11}_{-0.11}$	$1.32^{+0.06}_{-0.06}$	$1.35^{+0.06}_{-0.06}$	$1.38^{+0.06}_{-0.06}$	1.04 (31)
30002010007	0.419	0.32	$2.49^{+0.09}_{-0.09}$	$1.28^{+0.05}_{-0.05}$	$1.30^{+0.05}_{-0.05}$	$1.33^{+0.05}_{-0.05}$	1.35 (63)
30002010008							
30002010010	0.458	0.26	$2.56^{+0.12}_{-0.12}$	$1.33^{+0.06}_{-0.06}$	$1.36^{+0.06}_{-0.06}$	$1.39^{+0.06}_{-0.06}$	1.03 (31)
30002010012	0.639	0.28	$2.83^{+0.12}_{-0.12}$	$1.45^{+0.06}_{-0.06}$	$1.48^{+0.07}_{-0.07}$	$1.51^{+0.07}_{-0.07}$	1.69 (31)
30002040002	0.101	0.45	$3.55^{+0.17}_{-0.17}$	$1.87^{+0.09}_{-0.09}$	$1.92^{+0.09}_{-0.09}$	$1.97^{+0.09}_{-0.09}$	0.82 (31)
30201030002	0.660	0.32	$2.68^{+0.11}_{-0.11}$	$1.40^{+0.06}_{-0.06}$	$1.43^{+0.06}_{-0.06}$	$1.46^{+0.06}_{-0.06}$	1.49 (31)

Notes: The fitted model has the form PHABS(ISM)*PHABS(LOCAL)*VAPEC, with N_H^{ISM} fixed to 3.7×10^{21} cm $^{-2}$ and the temperature fixed to 2.75 keV. Abundances are given in Table 4 of Pandey et al. (2014). χ^2_{ν} is the reduced χ^2 and dof is degrees of freedom. Errors quoted on different parameters refer to 90% confidence level. The spectra obtained from observation IDs 30002010005 and 30101005002 as well as 30002010007 and 30002010008 were fitted jointly. The N_H^{local} values for *NuSTAR* spectra were fixed to those obtained by the spectral fitting of the very close-by phases spectra from other observatories data.

3.3 X-ray light curves analysis

The background subtracted X-ray light curves as observed by *Swift*-XRT in broad (0.3–10.0 keV), soft (0.3–2.0 keV), and hard (2.0–10.0 keV) energy bands are shown in Figure 3.7, where each data point represents an average count rate of the corresponding observation. Blue triangles mark the data observed during 2007 December to 2009 June which was studied by Pandey et al. (2014). However, red filled circles corresponds to the data observed continuously from 2014 August to 2016 August. A time span of 250 d is covered between JD 2457370.0 and 2457620.0. The time period of this binary system is estimated to be 207.85 ± 0.02 d by Gamen et al. (2006) from radial velocity measurements of WR 25 using N IV $\lambda 4058$ emission line. Pandey et al. (2014) also found a period of 207.5 ± 3.4 d on the basis of X-ray light curves. The present 250 d continuous monitoring of WR 25 covers more than one orbital cycle in Figure 3.7. Therefore, count rate initially increased (at around JD = 2457370.0) to the maximum and then decreased (at around JD = 2457495.0) to the minimum and then again increased towards the end of the light curve in all the energy bands mentioned here. However, the change in the hard energy band is not as steep as that in the soft energy band.

The long-term observation of WR 25 also enabled us to determine its orbital period more accurately than the previous studies. Lomb-Scargle periodogram (Lomb, 1976; Scargle, 1982) was used to perform the period analysis from *Swift* light curves. The peak with the highest power lies at frequency 0.00481 ± 0.00005 cycles d^{-1} in broad energy band. This corresponds to 207.8 ± 3.4 d orbital period which is consistent with the previous findings also. The power spectra of *XMM-Newton* light curves also showed a similar orbital period of 208.3 ± 2.2 d.

The light curves from other observatories (*NuSTAR*, *Suzaku*, and *XMM-Newton*) data are not shown here because none of them presents a continuous monitoring of the source. Only a few observations of WR 25 were made at random orbital phases and hence no regular pattern was visible in their light curves.

3.3.1 Folded X-ray light curves

The background subtracted light curves as observed by FPMA and FPMB onboard *NuSTAR* were obtained in 3.0–10.0 keV and 10.0–78.0 keV energy bands. The median of the ratio of the count rate to the corresponding error in 3.0–10.0 keV energy range was estimated to be 3.51 while it was 2.00 in 10.0–78.0 keV energy band. Therefore, we have considered *NuSTAR* light curves only in 3.0–10.0 keV

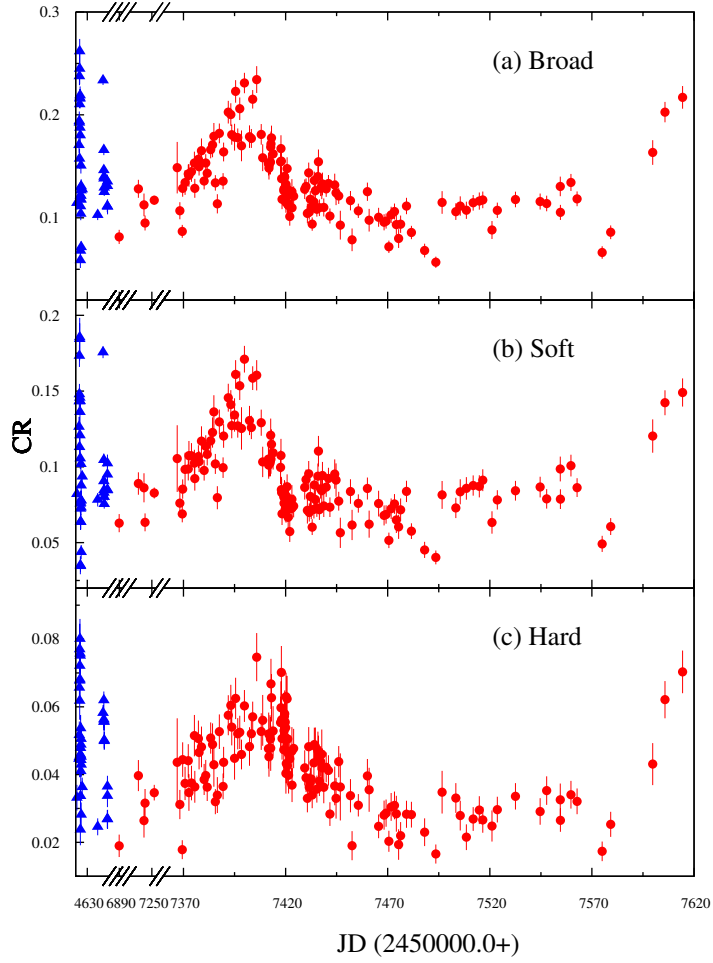
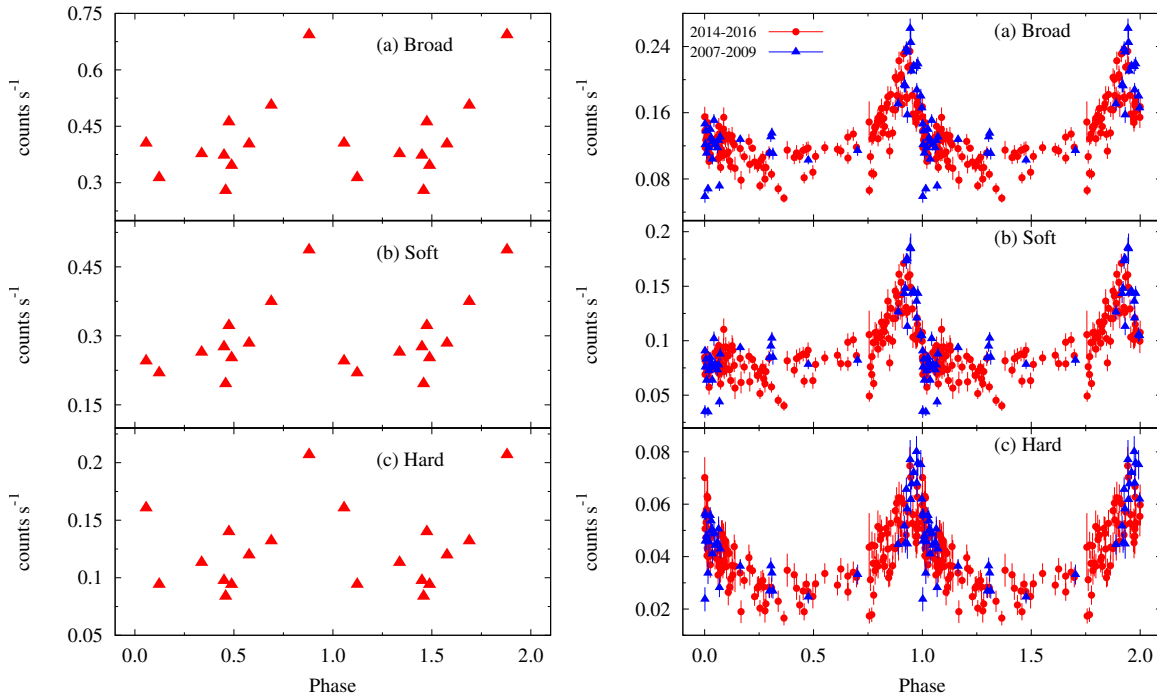


Figure 3.7: X-ray light curves in broad (0.3–10.0 keV), soft (0.3–2.0 keV), and hard (2.0–10.0 keV) energy bands as observed by *Swift*–XRT. Blue triangles mark the data observed during 2007 December to 2009 June and the red filled circles correspond to 2014 August to 2016 August observations.

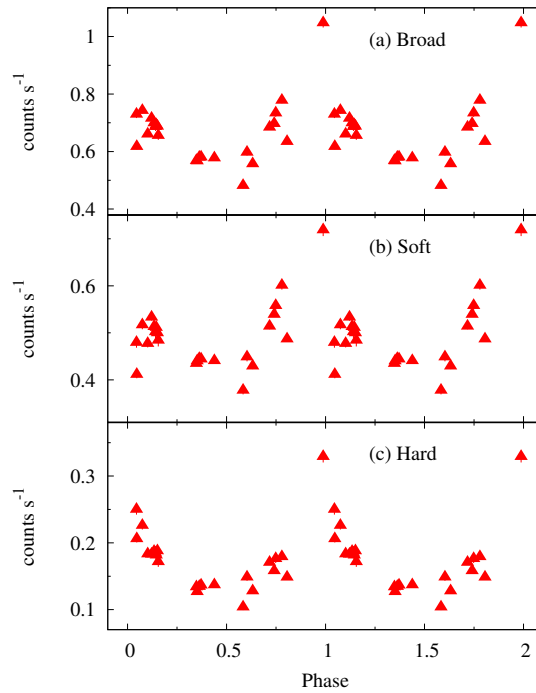
energy band for further analysis (see also Sect. 3.2.1). The background subtracted X-ray light curves were folded using the ephemeris $\text{HJD}=2,451,598.0+207.85\text{E}$ given by [Gamen et al. \(2006\)](#). The zero phase in the folded light curves corresponds to the time of the periastron passage. The X-ray light curves observed by FI *Suzaku*–XIS, *Swift*–XRT, and *XMM-Newton*–MOS2 were folded in (a) broad, (b) soft, and (c) hard energy ranges and are shown in Figures 3.8a, 3.8b, and 3.8c, respectively. Each point in the folded light curves corresponds to the average count rate of an observation ID. In Figure 3.8b, the folded X-ray light curve of *Swift*–XRT, red filled circles and blue triangles mark the observations made with a time gap of ~ 7 yrs as in Figure 3.7. It is evident that the count rates before and after this gap overlap fairly well, suggesting a reasonably stable behaviour of the phase-dependent X-ray emis-

3. X-RAY INVESTIGATION OF THE COLLIDING WIND BINARY WR 25



(a) FI *Suzaku*–XIS

(b) *Swift*–XRT



(c) *XMM-Newton*–MOS2

Figure 3.8: Folded X-ray light curves in broad, soft, and hard energy bands as observed by (a) FI *Suzaku* – XIS, (b) *Swift*–XRT, and (c) *XMM-Newton*–MOS2.

3.3 X-ray light curves analysis

sion over several orbits. Moreover, it also points towards the absence of any third component on a wider orbit, which would have been a potential cause of longer-term modulations (on top of that of the 208-d binary) in the X-ray light curve. Phase locked variations were seen in all the folded X-ray light curves and a similar kind of trend is observed. In the folded light curves of FI *Suzaku*–XIS, *Swift*–XRT, and *XMM-Newton*–MOS2, initially the count rate increases around the periastron passage followed by a very sharp decrease in broad and soft energy bands just after the periastron and then it recovers to an average value around the apastron. On the other hand, the folded light curves as observed by *NuSTAR*–FPMA and FPMB in 3.0–10.0 keV energy band are as shown in Figure 3.9. Here again, the count rate decreases gradually while moving from periastron to apastron. The ratio of the maximum to the minimum count rate in broad, soft, and hard energy bands were found to be 2.48, 2.48, and 2.47 for FI *Suzaku*–XIS, 4.46, 5.37, and 4.83 for *Swift*–XRT, and 2.2, 1.9, and 3.2 for *XMM-Newton*–MOS2 observations, respectively. However, for *NuSTAR*–FPMA and FPMB observations in 3.0–10.0 keV energy range, this ratio is 2.1 and 2.5, respectively.

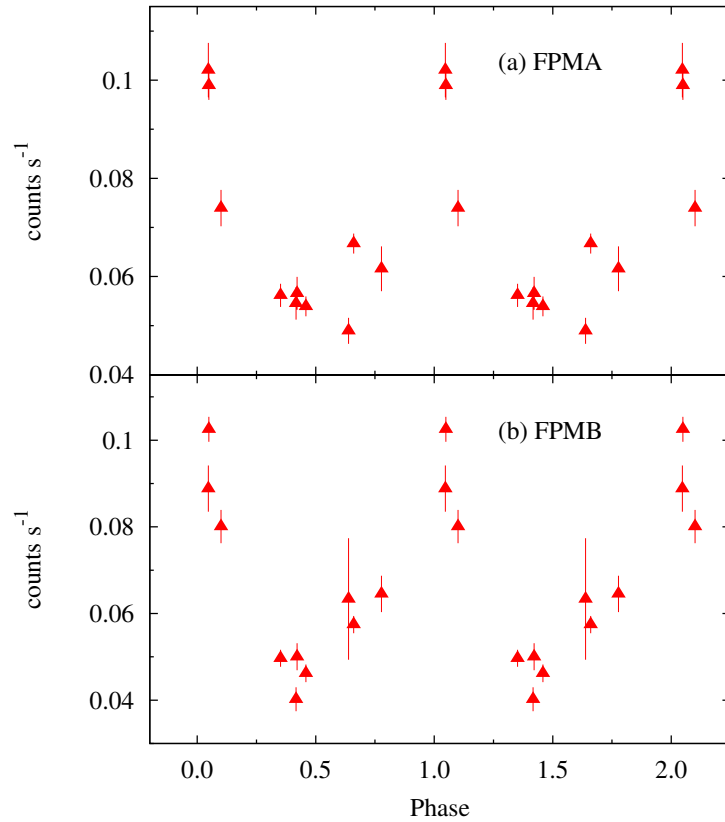


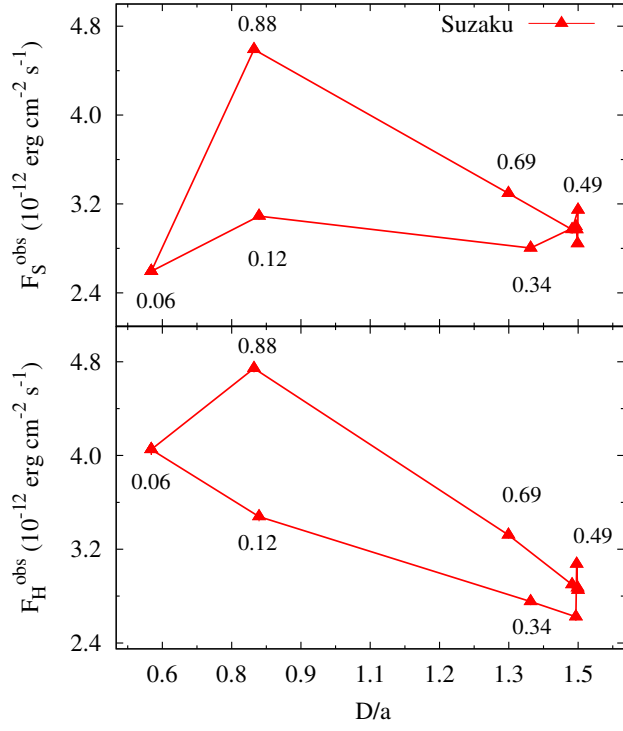
Figure 3.9: Folded X-ray light curves in 3.0–10.0 keV energy range as observed by *NuSTAR* – FPMA (upper panel) and FPMB (lower panel).

3.3.2 Flux vs. binary separation

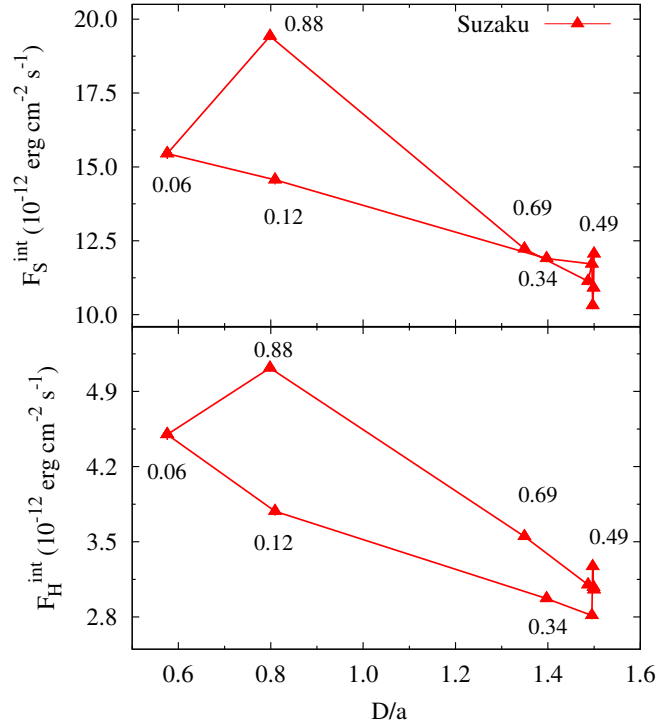
The variation of observed and intrinsic X-ray fluxes in soft (F_S) and hard (F_H) energy bands with binary separation (D/a , i.e. the binary separation normalized to the semi-major axis a) as observed by *Suzaku*, *Swift*, and *XMM-Newton* is shown in Figures 3.10, 3.11, and 3.12, respectively. The orbital phases corresponding to a few observations are also mentioned in the figures. It is evident from these plots that the intensity of the X-ray emission varies as the two components of this binary system move towards and away from each other. These variations were found to be deviated from the linear trend. In order to find the significance of deviations from the linear trend a chi-square test was performed on the best fit straight line. We found that deviation was more than 99.9% confidence level from linear trend for all the observations in both soft and hard energy bands. F_S seems to be more affected as compared to F_H . The most pronounced variation in the emission occurs close to periastron passage, however, around the apastron, there is not much difference. *Swift* observations has the dense coverage of the orbital period of WR 25 than other satellites' observations. Therefore, it will be more appropriate to discuss the *Swift* observations. For *Swift*, the maximum value of F_S^{obs} occurred at phase 0.92 and dropped sharply to the phase 0.04. However, for F_H^{obs} , the maximum and minimum values were measured at phases 0.96 and 0.48 (Figure 3.11a), respectively. Both F_S^{int} and F_H^{int} were highest at phase 0.96 (Figure 3.11b) i.e. before the periastron passage but these were lowest at phases 0.50 and 0.48, respectively. The plots for *Suzaku* (Figures 3.10a and 3.10b) and *XMM-Newton* (Figures 3.12a and 3.12b) also express a similar variation pattern but the poorer orbital sampling (especially close to periastron) prevents any accurate determination of the position of F_S and F_H extrema. We do not show the variation of F_S and F_H with D for all satellites data together since there are some differences between the individual satellite results, probably because of noise and cross-calibration effects, but a similar trend is followed by each.

The variation of F_X^{obs} and F_X^{int} as a function of normalized D as observed by *NuSTAR* is shown Figures 3.13a and 3.13b, respectively, and there is not much difference in both values at all the orbital phases. It appears that F_X varied with D almost linearly and there is not any significant deviation in X-ray emission as two components of WR 25 move around the periastron. But a careful inspection of plots reveals that *NuSTAR* observations did not cover much of the orbit around the periastron passage. After the phase 0.78, *NuSTAR* observed WR 25 at phase 0.05 and then at phase 0.1. Therefore, the flux information in between the orbital

3.3 X-ray light curves analysis



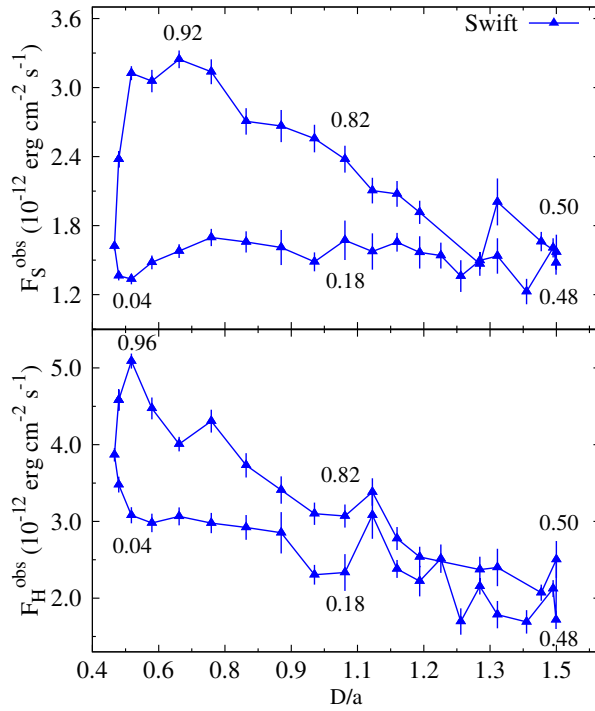
(a) Observed X-ray flux variation



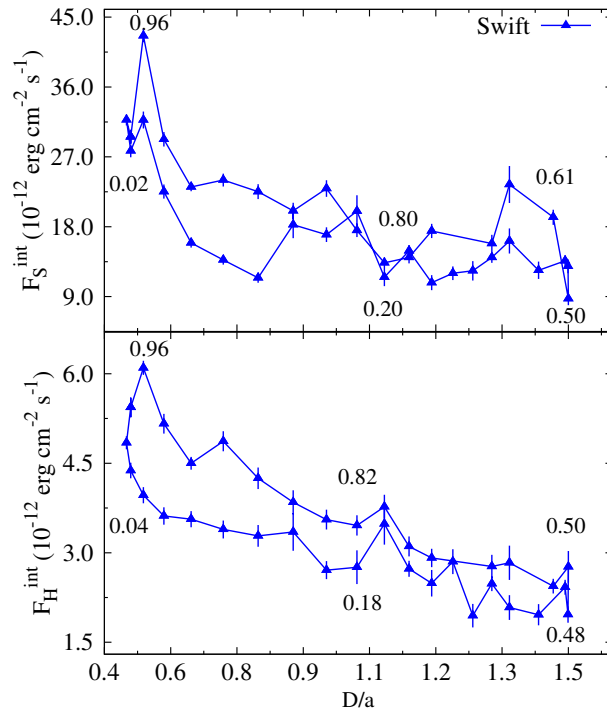
(b) Intrinsic X-ray flux variation

Figure 3.10: Observed (top) and intrinsic (bottom) X-ray flux of WR 25 as a function of binary separation in soft (F_S) and hard (F_H) energy bands as observed by *Suzaku*–XIS. The orbital phases corresponding to a few data points have also been mentioned in the figures.

3. X-RAY INVESTIGATION OF THE COLLIDING WIND BINARY WR 25

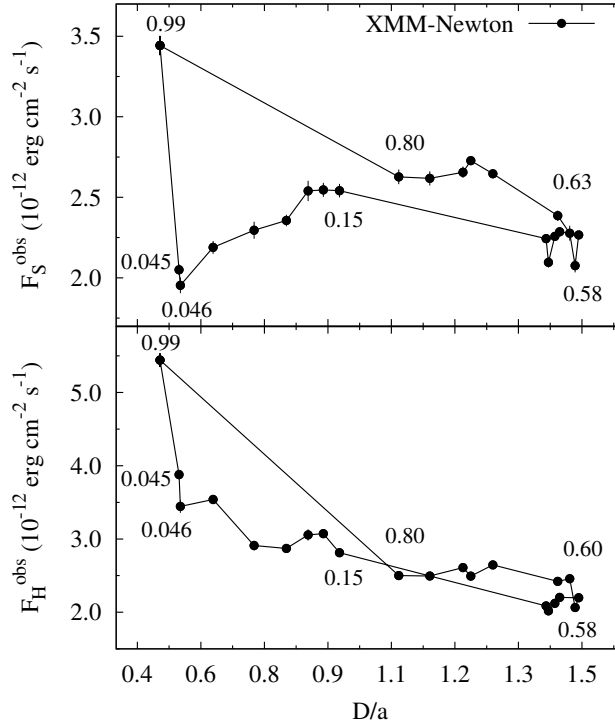


(a) Observed X-ray flux variation

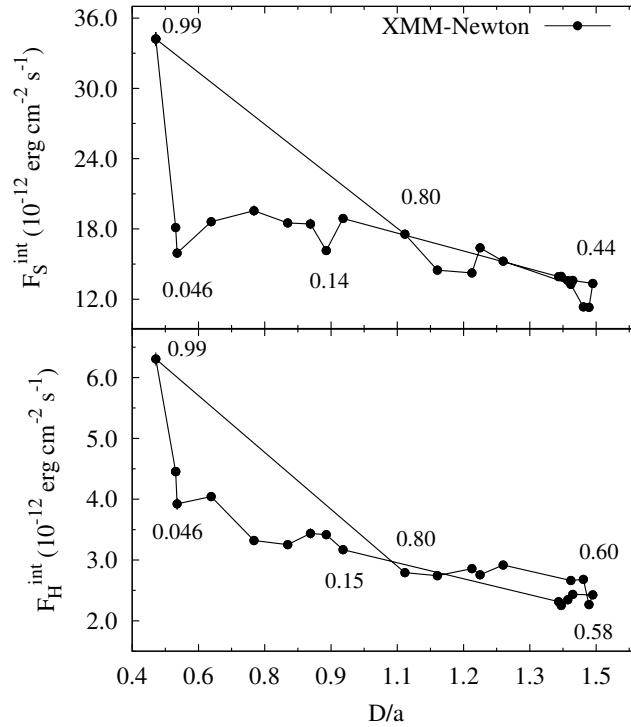


(b) Intrinsic X-ray flux variation

Figure 3.11: Observed (top) and intrinsic (bottom) X-ray flux of WR 25 as a function of binary separation in soft (F_S) and hard (F_H) energy bands as observed by *Swift*-XRT. The orbital phases corresponding to a few data points have also been mentioned in the figures.



(a) Observed X-ray flux variation

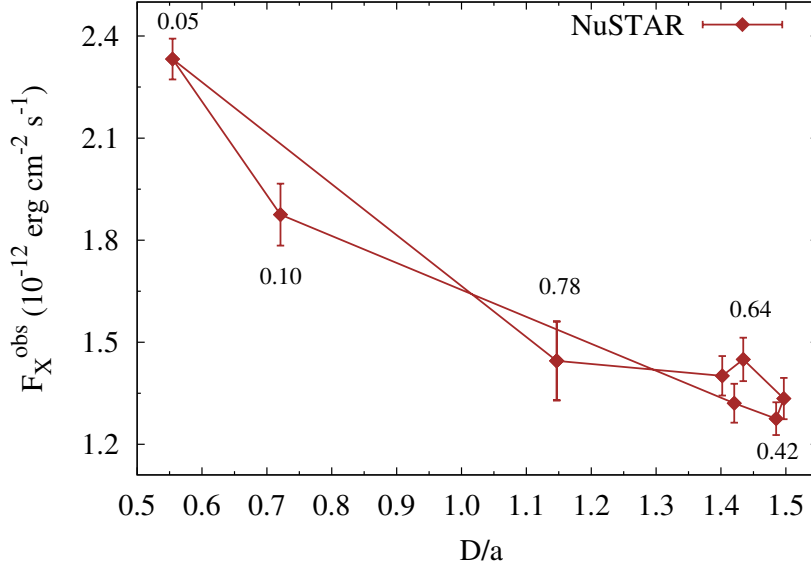


(b) Intrinsic X-ray flux variation

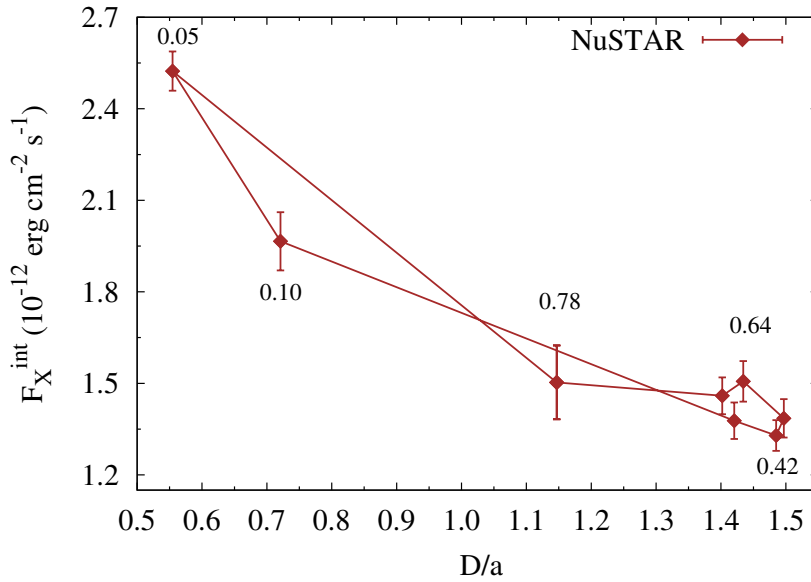
Figure 3.12: Observed (top) and intrinsic (bottom) X-ray flux of WR 25 as a function of binary separation in soft (F_S) and hard (F_H) energy bands as observed by *XMM-Newton*–EPIC. The orbital phases corresponding to a few data points have also been mentioned in the figures.

3. X-RAY INVESTIGATION OF THE COLLIDING WIND BINARY WR 25

phases 0.78 to 0.05 is missing in the part of the orbit where the most pronounced changes in the X-ray emission are expected.



(a) Observed X-ray flux variation



(b) Intrinsic X-ray flux variation

Figure 3.13: (a) Observed and (b) intrinsic X-ray flux as a function of binary separation in 3.0–10.0 keV (F_X) energy band as observed by *NuSTAR*–FPMs. The orbital phases corresponding to a few data points have also been mentioned in the figures.

3.4 Discussion

3.4.1 Variability of the thermal X-ray emission

The folded X-ray light curve of *Swift*-XRT measurements (which offers the best orbital sampling) presents a peaked maximum close to the periastron passage, followed by a decrease of the emission on the way to apastron, suggesting an X-ray emission dependent on the stellar separation. This maximum is observed at orbital phases 0.943, 0.943, and 0.973, respectively in the broad, soft, and hard energy bands. The investigation of the separation-dependent variations must be based on quantities independent of the ISM as well as local absorption by the stellar wind (see below). A first indicator should be the X-ray flux measured in the hard band, weakly affected by photoelectric absorption. It is clear that the hardest emission is produced by the WCR and therefore should be affected by the varying separation, while the soft emission is produced by both the individual stellar winds and the wind-wind interaction region. The evolution of the hard X-ray flux as a function of distance is shown in the lower panels of Figures 3.10a to 3.12a, and in Figure 3.13a. An alternative way would consist in plotting the intrinsic values (i.e. corrected for both local and interstellar absorptions) as a function of distance as shown in Figures 3.10b to 3.12b and in Figure 3.13b. A third approach is to follow the evolution of the normalization constant corresponding to the hard component ($norm_2$, relevant for the colliding winds emission) as a function of distance. The general trends shown by these three indicators, especially when only hard X-ray fluxes are considered, are indeed very similar as expected.

Hydrodynamic models of wind interactions in massive binaries predict that WCR can behave either adiabatically or radiatively (Stevens et al., 1992). In shorter period systems, instabilities arise in the interaction region which leads to a quite turbulent wind collision and the X-ray luminosity then follows a relation of the form $L_X \propto f\dot{M}v^2$, where f is the fraction of the wind involved in the collision, \dot{M} is the mass loss rate, and v is the pre-shock wind velocity. However, in the adiabatic regime, the interaction appears smoother and the X-ray luminosity scales as $L_X \propto \dot{M}^2v^{-3.2}D^{-1}$, where D is the binary separation (Luo et al., 1990). This behaviour is expected for binaries with orbital periods longer than a few days. Since WR 25 has the orbital period of ~ 208 d, therefore, it should follow the latter X-ray luminosity relation and hence the intrinsic flux is expected to be maximum at periastron, where the plasma density is higher. Based on the limited data set, Gosset (2007) found that the hard X-ray flux of WR 25 increases linearly with the

inverse of the relative binary separation using *XMM-Newton* data, in full agreement with the expected behavior for an adiabatic case.

Light curves shown in Figure 3.11 present a behaviour reminiscent of a hysteresis, even though this is not well supported by Figure 3.13 characterized by a poorer orbital phase sampling. Pittard & Parkin (2010) predicted hysteresis behaviour in the variation of the X-ray luminosity from colliding winds as a function of the binary separation for eccentric systems. Though the model of Pittard & Parkin (2010) is designed for eccentric O+O binaries with period less than 10 d and weaker stellar winds, we find the similar features in the X-ray emission of WR 25. The origin of this effect is an asymmetry in the WCR about the line of centres, especially close to periastron passage. In the specific case of WR 25, the orbital velocity close to periastron reaches its maximum, while radiative effects (such as radiative inhibition and sudden radiative breaking, see below in this section) can reduce substantially the pre-shock wind velocity. The combination of these two effects is expected to result in an increase of the ratio between the orbital and wind velocities at periastron, which favors a distortion of the WCR. Such a distortion is expected to lead to a significant departure with respect to pure symmetry about the line of centers, causing the hysteresis. If the trends shown in Figure 3.11 are real, one may thus tentatively transpose the case described by Pittard & Parkin (2010) to provide a likely interpretation context to our observations, provided we remember the basic idea behind this effect has to be slightly adapted to take into account some specificities of the system. The emission is brighter when the two components move towards each other than when they separate again. It may happen because of a higher pre-shock wind velocities when stars are getting closer, favoring a brighter hard X-ray component. As the two stars come close to each other, their winds collide with lower terminal velocities. The lower pre-shock velocity is less favorable to the hard X-ray emission that appears thus weaker. Therefore, the maximum X-ray luminosity is observed before the periastron passage. When the two components move away from each other after periastron, less hard X-ray emission is observed which reflects the smaller pre-shock wind velocities attained at earlier orbital phases, reducing the emission measure of the plasma that is warm enough to produce radiation significantly above 2 keV. We have, however, to caution that this interpretation relies notably on a significant phase-locked variation of the pre-shock velocity, which is not fully supported by our measurements of the post-shock plasma temperature, as detailed in the discussion below in this section.

Our analysis shows that the X-ray emission deviates from the linear $1/D$ trend close to periastron, suggesting a departure from the adiabatic regime when the

stellar separation is shorter. It is worth checking the evolution along the orbit of the cooling parameter (χ) defined by [Stevens et al. \(1992\)](#) as the ratio of the cooling time of the post-shock gas to the typical escape time from the shock region. It is expressed as $\chi = v^4 r / \dot{M}$, where v is the pre-shock wind velocity in 1000 km s^{-1} units, r is the distance from the star to the shock in 10^7 km and \dot{M} is the mass loss rate in $10^{-7} \text{ M}_{\odot} \text{ yr}^{-1}$ ([Stevens et al., 1992](#)). For $\chi \ll 1$, the gas cools rapidly and the collision is considered to be radiative while for the adiabatic case, $\chi \geq 1$. The switch of χ down to radiative values can be further enhanced by radiative effects such as radiative inhibition and sudden radiative braking. These are related to the presence of the radiation field of the companion star and it has been shown that they may reduce the pre-shock velocity of colliding winds. Radiative inhibition involves the reduction in the initial acceleration of the stellar wind by the radiation field of its companion ([Stevens & Pollock, 1994](#)). It is more suitable for close O + O binaries with comparably strong optically thin winds. However, sudden radiative braking is more favoured in WR + O binaries where the wind of the primary star is suddenly decelerated by the radiative momentum flux of its companion as it approaches the surface of that star ([Gayley et al., 1997](#)). It constitutes a more severe interaction that can significantly alter the bow shock geometry close to periastron passage. Since the cooling parameter is proportional to v^4 , the lowering of the pre-shock velocity through this effect can have a significant impact on the shock regime, leading to a reinforcement of the radiative regime around periastron.

We estimated v and χ for both components of WR 25 at the position of the WCR by using the standard β -velocity law (thus without any influence by radiative effects mentioned in the previous paragraph). To achieve this, the typical values of the various stellar parameters for the WN6ha (primary) and O4 (secondary) stars were considered as given in [Table 3.4](#). χ is expected to change as a function of the orbital phase because (i) the stellar separation changes and (ii) the pre-shock velocity is likely to change if the winds collide before they reach their terminal velocity. Our estimates show that within a 0.10 phase interval around periastron, both shocked winds should become slightly radiative with a χ value slightly lower than 1, especially if the O4 star is assumed to be a supergiant. χ remains higher than 1 during the remaining parts of the orbit for both winds. The evolution of v and χ with the orbital phase for both components of WR 25 are shown in [Figure 3.14](#) assuming secondary star as an O4 supergiant. Here, we see that v decreases by 25% and 34% for WN- and O- star, respectively, from apastron to periastron. One should however caution that the above discussion is valid for expectations based on simple principles, but one has to note a clear discrepancy between the expected

3. X-RAY INVESTIGATION OF THE COLLIDING WIND BINARY WR 25

Table 3.4: List of the stellar parameters adopted for the estimation of cooling parameter (χ) at the WCR of WR 25.

Parameter	WN6ha	O4 (secondary)		
	(primary)	Dwarf	Giant	Supergiant
Mass (M_{\odot})	-	46.16	48.80	58.03
Radius (R_{\odot})	20	12.31	15.83	18.91
Mass-loss rate ($M_{\odot} \text{ yr}^{-1}$)	10^{-5}	$10^{-5.836}$	$10^{-5.540}$	$10^{-5.387}$
Terminal wind velocity (km s^{-1})	2500	3599	2945	2877
β -velocity law	1.00	0.90	0.90	0.92

Notes: The radius of the primary component was derived using the values of luminosity ($10^{6.18} L_{\odot}$) and temperature (45000 K) for WN6ha star from Crowther (2007) assuming the black body emission. **References:** (1) Crowther (2007); (2) Muijres et al. (2012)

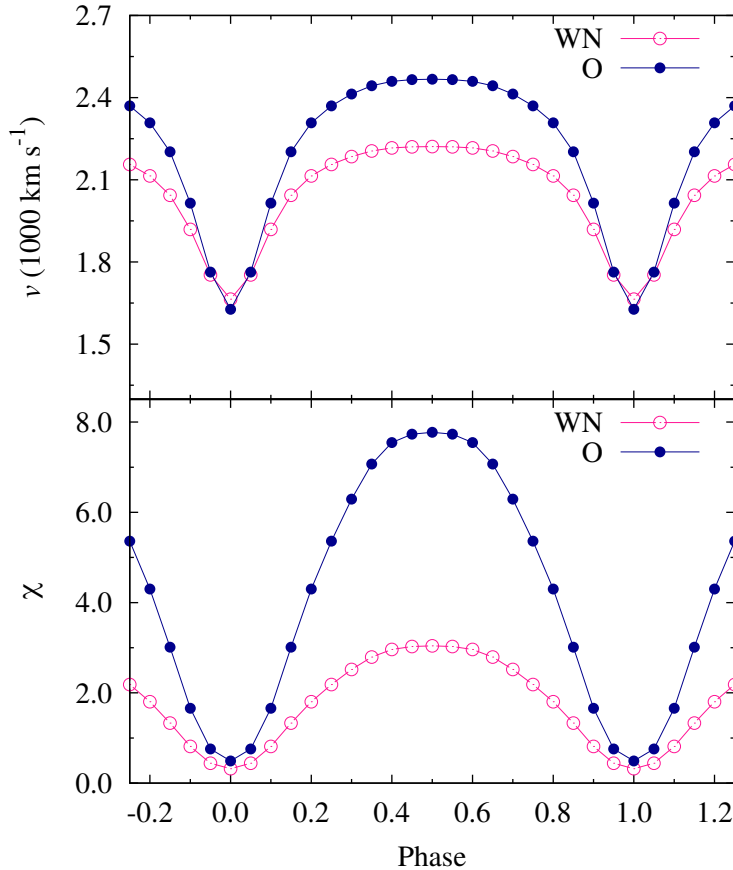


Figure 3.14: Expected evolution of the pre-shock wind velocity (v) and cooling parameter (χ) with the orbital phase for both components of WR 25. Here, secondary component of WR 25 is an O4 supergiant.

trend of the pre-shock velocity illustrated in Figure 3.14 and the measurements of the post-shock plasma temperature reported on in Figure 3.4. As the post-shock plasma temperature should scale with the square of the pre-shock velocity, a significant and smooth phase-locked evolution of the plasma temperature should be measured, but this is not observed. Provided the measured plasma temperature is an adequate proxy of the pre-shock velocity in the wind-wind interaction region, the simple interpretation context described here fails to explain all the emission properties described in this study. In order to achieve a more appropriate interpretation of the X-ray emission of WR 25 and its variability, the support of more sophisticated modelling is strongly required. In particular, the pre-shock velocity along the colliding-wind region appears as a critical physical quantity strongly influencing the overall X-ray emission of the system. An adequate dynamical modelling is needed to reconcile the apparent contradiction between the trends shown by Figure 3.14 and Figure 3.4.

Besides the trend discussed above related to the change of stellar separation, local absorption by the stellar winds material is also important to interpret X-ray light curves. The impact of this local absorption is clearly measured as a sudden and sharp drop in the X-ray flux that occurs shortly after periastron passage, in the broad and soft energy bands. According to the radial velocity curve of WR 25, presented by [Gamen et al. \(2006\)](#), primary component of this binary remains towards the observer from phase ~ 0.95 to 0.27 . A sharp minimum is observed in F_S^{ism} at orbital phase 0.04 ± 0.01 of WR 25. Therefore, this drop is the resultant of the strong local absorption faced when the WN wind is in front of the colliding-wind region, around this phase, from the observer's point of view. This feature was not so obvious in the results presented in the previous studies ([Gosset, 2007](#); [Pandey et al., 2014](#)) because of a sparser orbital sampling. This post-periastron minimum is not observed in the hard energy band, which is basically unaffected by photoelectric absorption.

We want to caution that the results obtained from the present study represent a very approximate picture of the actual physical condition of the system. In particular, one knows that the plasma temperature derived from our modelling approach consists of a rough average. Actually, the X-ray emitting region is made of the distribution of cells spreading over wide ranges of density and temperature. The post-shock temperature distribution is expected to peak along the line of centres where the pre-shock velocity of the colliding winds is the highest, with lower typical temperatures away from the apex of the shocks. Such a more realistic representation would be much too detailed considering the accuracy of the data used in this study.

Our approach focuses thus on average and typical values, easily represented by the models and the modelling tools we used in this study. On the other hand, one also has to clarify that freezing the post-shock plasma temperature across the full spectral time series is at first sight at odd with the expectation of a varying pre-shock velocity in an eccentric system. In particular, the hardest component significantly accounting for the X-ray emission close to the line of centres should in principle be affected. However, the change in pre-shock velocity is not high enough to completely lead to dramatic changes in plasma temperatures, at least in a large part of the orbit and at the level of accuracy of the measurements allowed by the data (see Figure 3.4). As a result, this approximation does not compromise the validity of our general interpretation. Concerning the element abundances, one should also keep in mind that the emitting plasma is coming from both stellar winds, and this is not straight forward to anticipate in which proportion, especially as a function of the orbital phase. In addition, the abundances of the absorbing plasma are also expected to vary depending on which stellar wind is in front. The required improvements in the spectral analysis to account for such effects are far beyond the information content of our data series and out of reach of our modelling tools. Our approach offers thus the advantage to provide a relevant description with a reasonably low number of free parameters, which constitutes a convenient requirement to perform the variability analysis described in this study.

Finally, the long time basis of the data series investigated in this chapter (about 16 yrs) suggests a fairly good consistency of the phase-folded X-ray emission even when observations distant by several years are considered. This indicates that the binary system scenario is fully satisfactory to explain the temporal behavior of WR 25, rejecting the idea that it might be a higher multiplicity system with an additional WCR (on a wider orbit) contributing to the overall thermal X-ray emission.

3.4.2 Lack of non-thermal X-ray emission

It has been noticed that some CWBs also act as sources of particle acceleration in their WCR through the DSA mechanism (see Section 1.3) which leads to the production of relativistic particles (De Becker & Raucq, 2013). Relativistic electrons travelling in the magnetic field may give rise to synchrotron radio emission or they may also inverse comptonize the photospheric stellar light to X-rays or even soft γ -rays. This opens up the possibility that some non-thermal X-ray emission may be measured in CWBs. As emphasized in this paper, and the same holds for other CWBs, the soft X-ray emission (below 10 keV) is dominated by thermal emission

from the wind-wind interaction region. As a result, attempts to measure such a non-thermal X-ray emission should focus on hard X-rays, above 10 keV (see e.g. De Becker, 2007). However, the lack of significant X-ray emission revealed by *NuSTAR* between 10 and 78 keV provides evidence that no IC scattering emission is produced by WR 25 above the background level.

The availability of hard X-ray data allows, however, to derive upper limits on the count rate of the putative non-thermal X-ray emission between 10 and 78 keV for FPMA and FPMB instruments. We applied the procedure applied by De Becker et al. (2014) to *NuSTAR* data-sets obtained at two extreme orbital phases, respectively close to periastron ($\phi = 0.049$) and apastron ($\phi = 0.458$). We filtered event lists using a circular spatial filter with a radius of $30''$ to measure the associated number of counts (C). This radius was selected because it corresponds to the half the HPD given by Harrison et al. (2013). This extraction region is large enough to collect a count number still significant for Poisson statistics, and it is small enough to avoid any significant contamination by adjacent imaging resolution elements. This count number was then corrected for the encircled energy fraction corresponding to the extraction radius (50%, as we adopted an extraction radius corresponding to that fraction), and it was further corrected for the position dependent effective area of the FPMs. For the latter correction, we considered a median energy, i.e. 40 keV. According to Harrison et al. (2013), at a distance of about $5.5'$ from the on-axis position (see the observation log in Table 2.1) the effective area is about 45% of its maximum (on-axis) value. We thus obtain a corrected count number (C_{cor}). We then determined a count threshold (C_{max}) corresponding to a logarithmic likelihood (L) of 12, translating into a probability (P) to find a count number in excess of C_{max} of about 6×10^{-6} ($L = -\ln P$), under the null hypothesis of pure background Poisson fluctuations. This criterion is frequently adopted as a threshold for statistical fluctuations. In practice, we iteratively estimated the logarithmic likelihood assuming Poisson statistics on the basis of the corrected count number and adopting a first guess for C_{max} . At every iteration, C_{max} was adapted to converge to a logarithmic likelihood of 12, for a fixed C_{cor} value. The difference between these two quantities (C_{max} at $L = 12$ and C_{cor}) gives the maximum expected count excess. The division of the latter quantity by the effective exposure time gives the count rate (CR) upper limit on the putative emission, as shown in Table 3.5. This approach has the benefit to estimate a count excess on a statistically relevant basis.

The upper limits on the count rate for a hypothetical IC scattering X-ray emission can be converted into physical flux units assuming an adequate emission model. The non-thermal spectrum should be a power law, slightly affected by interstellar

3. X-RAY INVESTIGATION OF THE COLLIDING WIND BINARY WR 25

Table 3.5: Estimates of the upper limits on the count rate for *NuSTAR* instruments at the position of WR 25.

	FPMA	FPMB
$\phi = 0.049$		
C (cnt)	189	194
C_{cor} (cnt)	839	861
C_{max} (cnt)	969	993
$C_{max} - C_{cor}$ (cnt)	130	132
Eff. exp. time (s)	79400	79400
CR (cnt s $^{-1}$)	1.6×10^{-3}	1.6×10^{-3}
$\phi = 0.458$		
C (cnt)	144	126
C_{cor} (cnt)	639	559
C_{max} (cnt)	753	666
$C_{max} - C_{cor}$ (cnt)	114	107
Eff. exp. time (s)	54500	54500
CR (cnt s $^{-1}$)	2.0×10^{-3}	2.0×10^{-3}

and local absorption in the softer energy band. Even though our upper limits on the count rate relies on the 10–78 keV range, the IC process should contribute over the full X-ray range, and we estimated the flux between 0.1 and 100 keV. We used the WebPIMMS on-line tool assuming two different values of the photon index: 1.5 (the standard value for DSA in strong shocks, e.g. [De Becker 2007](#)) and 1.7 (valid for the likely leptonic component in Eta Car’s soft γ -ray spectrum, [Farnier et al. 2011](#)). Depending on the orbital phase, on the instrument, and on the assumed photon index, we obtain intrinsic non-thermal X-ray fluxes in the range $7\text{--}9 \times 10^{-13}$ erg cm $^{-2}$ s $^{-1}$. For a distance of 2.1 kpc ([Gaia DR2; Lindegren et al., 2018](#)), this converts into upper limits on the intrinsic luminosities in the range $3.6\text{--}4.7 \times 10^{32}$ erg s $^{-1}$.

These numbers deserve to be discussed in the context of the energy budget of colliding-wind massive binaries, and of their participation in non-thermal processes. The IC process (over the full X-ray domain) and the thermal X-ray emission (measured below 10 keV) share the same energy reservoir, i.e. the fraction of the wind kinetic power that is injected in the colliding winds. On the basis of previous measurements on CWBs, the fraction of that energy that is converted into thermal X-rays emerging from the winds is of the order of 1-10%. A similar fraction is

expected to apply for the energy injection into non-thermal particles, on the basis of theoretical considerations and of a comparison with the case of supernova remnants which share the same physics. However, IC scattering comes only from the energy injected into electrons, which constitutes only a fraction of the energy of the non-thermal particles, i.e. likely a few percent of the energy injected in relativistic particles (see [De Becker & Raucq, 2013](#), for a discussion of the energy budget of PACWBs). Considering the high radiative energy density in the particle acceleration region, the energy injected in relativistic electrons should be dominantly radiated through IC scattering. The amount of energy injected into the IC process should thus, roughly, be at most equivalent to a few percent of the energy radiated in thermal X-rays and escaping from the winds. However, our upper limits on the non-thermal X-ray emission are only a few percent of the intrinsic thermal X-ray fluxes reported in this paper, and about a factor 10 lower than the thermal X-ray fluxes corrected for ISM absorption only (see [Table 3.2](#)). These upper limits do not, therefore, provide better constraints than the anticipated educated guesses proposed by previous studies. Consequently, the limitations due to the sensitivity of *NuSTAR* lead to quite loose upper limits, which do not provide stringent constraints on the non-thermal physics. Only systems with higher kinetic power, hence with a more abundant mechanical energy reservoir, would have a chance to be detected as non-thermal emitters in hard X-rays with *NuSTAR*. As a result, present day non-detection constitute by no means a severe drawback for the scenario of non-thermal high energy emission from massive binaries.

On the other hand, the most active indicator for particle acceleration in massive binaries is synchrotron radio emission. Previous radio continuum observations of Southern massive stars allowed to measure a flux density of 0.90 ± 0.15 mJy at a wavelength of 3 cm for WR 25 ([Chapman et al., 1999](#); [Leitherer et al., 1995](#)). Only upper limits to the flux density could be obtained at longer wavelengths. No formal determination of the nature (thermal or non-thermal) of the radio emission from WR 25 could be achieved as it was detected at only one frequency, preventing therefore any spectral index determination ([Leitherer et al., 1997](#)). However, by combining all the measurements, [Dougherty & Williams \(2000\)](#) gave a lower limit of $j = -1.26$ to the radio spectral index of WR 25 (for a flux density dependence on the frequency defined as $S_\nu \propto \nu^j$). [Leitherer et al. \(1995\)](#) argued that the observed 3 cm emission from WR 25 is of thermal nature by comparing the mass loss rate of WR 25 using models given by [Wright & Barlow \(1975\)](#) and [Panagia & Felli \(1975\)](#) to those obtained by some independent techniques which assumed thermal nature of the emission. We calculated the expected thermal free-free radio emission from

the WN wind following the [Wright & Barlow \(1975\)](#) approach, adopting the stellar parameters for a WN star wind quoted in [Table 3.4](#). We also adopted an electron temperature equal to 50% of the effective temperature ([Drew, 1990](#)), for an effective temperature of 45000 K (for a WN6h classification, [Crowther 2007](#)). Our estimate of the flux density was corrected to take into account wind clumping, following the same approach as [De Becker \(2018\)](#). As noted by [Puls et al. \(2008\)](#), mass loss determinations on the basis of radio flux density measurements should be reduced by a factor \sqrt{f} to account for clumping (where f is the clumping factor). Accordingly, a clumped stellar wind characterized by a given mass loss rate will generate thermal radio emission with a flux density a factor $f^{2/3}$ greater than for a smooth, unclumped configuration. We assumed a clumping factor of 4, valid for the outer parts of the wind where the thermal radio emission is produced ([Runacres & Owocki, 2002](#)). The same procedure was followed to estimate the contribution from the O-star wind, using the wind parameters given in [Table 3.4](#) and an effective temperature of about 40000 K ([Muijres et al., 2012](#)). As a result, we estimate that the observed cumulative flux density at 3 cm for both components winds, at a distance of 2.1 kpc, should be of the order of 0.60 mJy (about 0.50 and 0.10 mJy for the WN and the O components, respectively), in fair agreement (within uncertainties) with the measurement at that wavelength. This provides some significant support to the idea that the radio measurement of WR 25 is more likely made of thermal emission only, without the need to call upon any additional non-thermal contribution to interpret the measurements. The lack of non-thermal radio emission associated to WR 25 may be attributed either to an inefficient acceleration process or to a strong free-free absorption by the WN (and to some extent O) stellar wind material. The latter process constitutes indeed a very likely turn-over process for synchrotron spectra produced by massive binaries (see e.g. [De Becker et al., 2017](#)). At this stage, no hint for particle acceleration has been revealed for WR 25.

3.4.3 Comparison with other systems

CygOB2#9 is another wind interacting source (O5–5.5I+O3–4III, $e=0.71$, orbital period (P)=858.4 d) which shows a very clear $1/D$ variation of the X-ray flux as expected for very long period binary systems ([Nazé et al., 2012](#)). A small deviation with respect to the $1/D$ trend was observed for the hard X-ray flux at periastron. [Nazé et al. \(2012\)](#) suggested that this might be a consequence of the collision becoming slightly radiative around the periastron due to increased wind density. They also found that the emission was somewhat softer near periastron and suggested that

radiative inhibition and/or braking became efficient when the two binary components were closest. [Parkin et al. \(2014\)](#) confirmed this assertion for CygOB2#9 and showed that wind acceleration is inhibited at all phases by the radiation field of the companion star. 9 Sgr (O3.5 V((f*))+O5-5.5 V((f)), $e=0.71$, $P=9.1$ yr, [Rauw et al. 2016](#)) is another long period CWB with a significant deviation from the expected $1/D$ behaviour close to periastron. Among shorter period systems, some massive binaries display a clear hysteresis effect in the dependence of the X-ray emission as a function of stellar separation ([Pittard & Parkin, 2010](#)). These systems include CygOB2#8a (O6If+O5.5III(f), $e=0.21$, $P=21.9$ d, [Cazorla et al. 2014](#); [De Becker et al. 2006](#)); HD 152248 (O7.5(f)III+O7(f)III, $e=0.13$, $P=5.816$ d, [Rauw & Nazé 2016](#); [Sana et al. 2004](#)); HD 152218 (O9IV+O9.7V, $e=0.26$, $P=5.60$ d, [Rauw & Nazé 2016](#); [Sana et al. 2008](#)); WR 21a (WN5h+O3V, $e=0.69$, $P=31.680$ d, [Gosset & Nazé 2016](#)); HD 166734 (O7.5If+O9I(f), $e=0.618$, $P=34.53$ d, [Nazé et al. 2017](#)). All of these systems, with shorter orbital periods, show larger X-ray flux values around apastron than periastron with a maximum value in between apastron and periastron. But in the case of CygOB2#9 and WR 25, lower X-ray fluxes are observed at apastron than periastron with a maximum close to periastron only. This is expected as shorter period systems undergo stronger deviations from the expected $1/D$ behaviour as compared to longer period binary systems: on the one hand shorter period systems are more prone to be radiative, and on the other hand the dynamics of the shocks is more sensitive to the distortion produced by the higher orbital velocity in short period binaries ([Pittard & Parkin, 2010](#)).

From the point of view of non-thermal X-ray emission, our results are in line with previous non-detection already reported for massive binaries in the Cygnus region on the basis of *INTEGRAL* observations ([De Becker et al., 2007](#)). However, our upper limits are more constraining than those derived with *INTEGRAL* by about two orders of magnitude, thanks to the better sensitivity of *NuSTAR*. The only massive binary system with a reported non-thermal high energy emission is Eta Car, with a hard X-ray luminosity of about 7×10^{33} erg s⁻¹ ([Leyder et al., 2008](#), on the basis of *INTEGRAL* observations), thus significantly brighter than the upper limit we derived for WR 25. More recently, [Hamaguchi et al. \(2018\)](#) reported even on phase-locked non-thermal hard X-ray emission from Eta Car using *NuSTAR* data. This lends support to the idea already mentioned in Sect. 3.4.2 that only systems with a significantly high wind kinetic power (such as Eta Car) may reveal their non-thermal high energy emission, given the sensitivity of current instruments.

3.5 Conclusions

A deep X-ray study of WR 25 using the archival X-ray data from *Suzaku*, *Swift*, *XMM-Newton*, and *NuSTAR* has been carried out. The time basis of the observations we investigated is more than 16 yrs, thus much longer than previous studies on this object.

In the soft X-ray domain below 10 keV, WR 25 is an over-luminous X-ray source as a result of the colliding stellar winds of the two components of the binary system. The system is brighter before periastron passage and becomes fainter when the line of sight passes through the dense wind of the WR star in front. Since harder X-rays are less affected by the enhanced column density, this atmospheric eclipse-like effect is not observed above 2 keV. The analysis of the present data shows the wind collision is more or less adiabatic but with a significant deviation with respect to the expected $1/D$ dependence of the X-ray luminosity around periastron passage. This deviation may tentatively be explained by a lower pre-shock velocity close to periastron favoring a brief switch to the radiative regime, especially if the velocity drop is enhanced by sudden radiative braking. However, this interpretation is not supported by our measurements of post-shock plasma temperatures as a function of the orbital phase, which do not present any measurable drop close to periastron. Our long-term monitoring suggests the thermal X-ray emission overlaps fairly well when orbits distant in time are compared. This indicates that WR 25 is unlikely a triple system where an additional WCR in a wider orbit may contribute to the overall thermal X-ray emission.

Above 10 keV, *NuSTAR* data do not reveal any X-ray emission attributable to a non-thermal high energy component due to IC scattering. The upper limits we derived on the putative non-thermal X-ray flux are in the range of $7-9 \times 10^{-13} \text{ erg cm}^{-2} \text{ s}^{-1}$ (between 0.1 and 100.0 keV), which is about a factor 10 lower than the ISM corrected thermal X-ray flux we measure below 10.0 keV. Considering one may expect the non-thermal energy injection into relativistic electrons (responsible for IC scattering) is at most a few percent of the energy radiated in thermal X-rays, the presently accessible upper limits provide only loose constraints on the non-thermal high energy emission. A measurable IC emission could, however, be envisaged from systems characterized by quite large wind kinetic power, as in the case of Eta Car for instance. Non-thermal energy budget consideration for CWBs show that even a significant energy injection would lead to a putative non-thermal emission below the sensitivity of *NuSTAR* for most known systems. A sensitivity improvement of at least one order of magnitude is needed to access more stringent limits on the IC

emission, or even have a chance to detect it for massive star systems with the most powerful winds.

Chapter 4

WR 121a: A SHORT PERIOD COLLIDING WIND BINARY

4.1 Overview

Massive stars in our galaxy are born pre-dominantly within the dense cores of giant molecular clouds. They start affecting their environment very soon after a star has formed through their intense ionizing radiation fields as well as strong stellar winds. W43 (=G30.8–0.2) is one such star forming complex, which was first discovered in radio domain by [Westerhout \(1958\)](#). It lies in the first galactic quadrant with galactic longitude of 30.8° and latitude of -0.2° along the connecting point of the Scutum-Centaurus arm and the Galactic bar. The distance estimated for the W43 complex is ~ 6 kpc from the Sun and it contains a total mass of $\sim 7.1 \times 10^6 M_\odot$ ([Nguyen Luong et al., 2011](#)). The core of W43 hosts a well-known giant HII region powered by an open cluster of young and luminous stars embedded in it (named in the SIMBAD database as [BDC99] W43 cluster). The detailed study of this region was performed in infra-red wavelength by [Blum et al. \(1999\)](#) and they pointed out that W43 cluster is totally obscured in optical band with an estimated value of A_V of ~ 34 mag, which is equivalent to a hydrogen column density of about $6.5 \times 10^{22} \text{ cm}^{-2}$ ([Luque-Escamilla et al., 2011](#)). [Blum et al. \(1999\)](#) also showed that the three brightest members of this cluster are massive stars, one of those is a WR star (named as W43 #1 = WR 121a) and other two belong to the category of O-type giants/supergiants (named as W43 #2 and #3). Using these spectral classifications, the dust extinction (A_K) to the individual object could be estimated as close to 3.5 mag for all of them.

The results of this chapter are published in [Arora & Pandey 2020](#).

¹<https://simbad.u-strasbg.fr/simbad/>

4. WR 121A: A SHORT PERIOD COLLIDING WIND BINARY

WR 121a was classified as WN7+abs owing to the similarity of its K -band spectrum with that of WR 131 (Blum et al., 1999). The “abs” component was added to the spectral type of this object because of the presence of the diluted emission lines in its spectrum which might be originating from the unseen companion of this star. In the 7th catalogue of galactic WR stars, WR 121a was placed in the category of probable binary systems and was specified with WN7+a/OB? spectral type (van der Hucht, 2001). WR 121a was seen in X-rays for the first time by Sugizaki et al. (2001) during the *ASCA* Galactic Plane Survey (AGPS). They detected this source (AX J184738–0156) in 0.7–10.0 keV energy band with $>5\sigma$ significance level and it was unidentified at that time. Grave & Kumar (2007) also pointed hints towards the binary nature of WR 121a using the spectro-astrometric technique. Anderson et al. (2011) investigated the previously unidentified X-ray sources during AGPS with *Chandra X-ray Observatory* data. They pointed out that the source AX J184738–0156 is co-incident with WR 121a discovered by Blum et al. (1999). Based upon the *Chandra* and *XMM–Newton* spectral features of WR 121a, Anderson et al. (2011) suggested that this object belongs to a class of CWBs. However, they did not find any hint of variability in the data. Later, in the same year, Luque-Escamilla et al. (2011) studied the infra-red and radio properties of the W43 cluster. They reported that two components (W43 #1a and W43 #1b) of WR 121a has been resolved with a separation of 598 ± 3 mas and a position angle of $255^\circ \pm 1^\circ$ using J -band observations from ESO Very Large Telescope (VLT). Based upon the position of W43 #1b which was found to be exactly coincident with the position of an X-ray source CXO J184736.6-015633, they have also speculated that W43 #1a is likely the WR member of the system, while W43 #1b is the O-type companion since the X-ray emitting region generally lies close to the star with relatively weaker wind in a CWB. Non-thermal synchrotron radiation was also found to emerge from an extended region of the cluster but with a peak offset from the position of WR 121a by $\sim 3''$ (much closer to W43 #3). As suggested by Luque-Escamilla et al. (2011), this non-thermal radio emission is originating due to the cumulative effect of stellar outflows from the WR and O stars in the cluster. There are several other pieces of evidence as well which associate very high energy sources (MeV to TeV) to the surrounding star formation region of WR 121a (see Acero et al., 2013; Bulgarelli et al., 2019; Chaves et al., 2008; de Wilt et al., 2017; H. E. S. S. Collaboration et al., 2018; Rappoldi et al., 2016).

Our motivation to carry out the study of WR 121a is to explain the underlying mechanism of the X-ray emission from it. Many times speculations were made for this object to be a massive binary system but a systematic confirmation is

required. If it is a CWB then it should reveal some hints of variability in its long-term observations. This information will help us to classify this source among the category of other massive binaries. The previous studies, carried out to constrain the stellar winds interaction features of massive binaries, have enriched us with valuable information (e.g. [Arora et al., 2019a](#); [De Becker et al., 2006](#); [Lomax et al., 2015](#); [Oskinova & Hamann, 2008](#); [Pandey et al., 2014](#); [Skinner et al., 2015](#); [Zhekov, 2012](#), etc.). Also, WR 121a lies in a rich complex of star-forming region towards the galactic center, therefore, it is important to know about the nature of massive stars present in that region to quantify their contribution towards different dynamical processes occurring there.

This chapter is organized as follows. Section 4.2 presents the analysis of *Chandra* X-ray images of WR 121a to measure its accurate position as well as to look for the close companion detected in other wavelengths. The X-ray timing analysis is given in Section 4.3. In Section 4.4, we present the X-ray spectral analysis of WR 121a. Our main results are discussed in Section 4.5 and Section 4.6 presents the conclusions.

4.2 X-ray image analysis of WR 121a

W43–Main cluster was observed with *Chandra* for several times during 2016 June–July with different configurations of ACIS-I as detailed in Table 2.2. WR 121a was present almost at the aim-point of the detector for these data-sets. The exposure times of these observations were in the range of 13.9 to 77.5 ksec. The pointing Right Ascension (R.A.) and Declination (Dec.) of the telescope was almost the same for all of these observations but the satellite roll pointing angle was different for the data observed in 2016 June than those of 2016 July data-sets. WR 121a was also observed by *Chandra*–ACIS-S in 2008 May with relatively shorter exposure time and at a position with a larger offset from the detector aim-point.

To determine the position of WR 121a accurately in the observed X-ray frames, we have merged different *Chandra* observations. Another aim of merging different data-sets is to increase the signal to noise ratio and search for the binary companion in WR 121a, which was shown in ESO-VLT *J*-band images by [Luque-Escamilla et al. \(2011\)](#), so that even if it is X-ray faint it could be detected. The data-sets with different pointing roll angles were merged separately. The first set is made of observation IDs 18868, 17716, 18870, 18867, and 18869 (set 1) and another set 2 was made with IDs 18887, 17717, and 18888. Next, we ran WAVDETECT on each

4. WR 121A: A SHORT PERIOD COLLIDING WIND BINARY

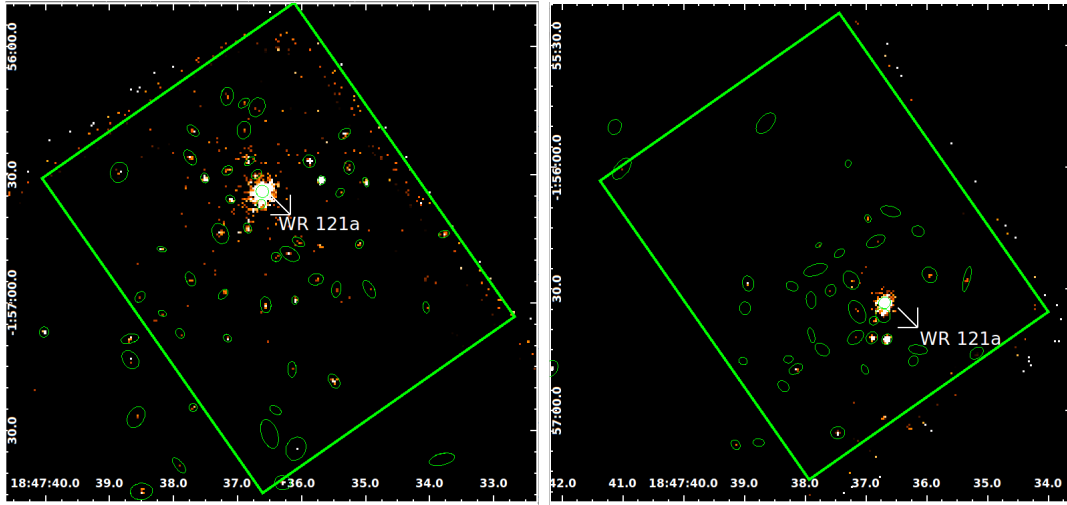


Figure 4.1: Merged and exposure corrected images of W43-Main from the observation IDs 18868, 17716, 18870, 18867, and 18869 (*left*) and 18887, 17717, and 18888 (*right*) of *Chandra*– ACIS-I observations in the 0.5–7.0 keV energy band. The images are binned into $\sim 0.5'' \times 0.5''$ pixels (1×1 binning). The $1.5' \times 1.2'$ region of the W43-Main around its center has been marked by a rectangle. The X- and Y- axes correspond to R.A. (J2000) and Dec. (J2000), respectively. The position of WR 121a as well as various other sources detected in the field has also been marked in the figures.

exposure independently to determine the position of various sources for matching between different exposures. The IDs 18867 and 18887 were chosen as references to align the different images of the set 1 and 2, respectively, due to their maximum exposure time among others in their respective sets. We then ran `WCS_MATCH` between all other exposures of each set with their respective reference image using sources returned from `WAVDETECT`. Subsequently, the aspect solutions as well as event files were updated with `WCS_UPDATE` for each observation to align them with their respective reference image.

Finally, we produced two merged, exposure-corrected images for these two sets in 0.5–7.0 keV energy band and are shown in Figure 4.1. The individual exposures of a set were first reprojected onto the frame of their respective reference image and then merged using CIAO task `REPROJECT_OBS`. The merged images were then exposure corrected and binned into $\sim 0.5'' \times 0.5''$ pixels (1×1 binning) using the task `FLUX_OBS`. Further, the source detection algorithm `WAVDETECT` was run onto the merged data and the position of the various sources detected has been shown with green ellipses in the Figure 4.1.

WR 121a was detected at an average position of R.A. (J2000) = 18:47:36.643

and Dec (J2000) = -01:56:33.77. The detected position of this X-ray source is closest to the position of WR 121a as given in the 2MASS All-Sky Catalog of Point Sources (Cutri et al., 2003). No nearby X-ray source was detected towards the North-East direction of the position of WR 121a in the merged images as shown by Luque-Escamilla et al. (2011) in the *J*-band image. The co-ordinates (R.A., Dec.) of W43 #1a and #1b as provided by Luque-Escamilla et al. (2011) are 18:47:36.691, -01:56:33.06 and 18:47:36.653, -01:56:33.22, respectively. The detected position of WR 121a lies closer to W43 #1b toward its south. Further, we have also checked the possible structure of the X-ray source WR 121a. A simulated *Chandra* PSF image using the MARX¹ software tool was generated following the CIAO science thread procedure as instructed. The CIAO task SRCEXTENT was used to determine the structure of the source using this simulated PSF. The X-ray source centered at the position of WR 121a was found to be point-like with 90% confidence level. The average position of the source detected nearest to WR 121a has the co-ordinates (R.A., Dec.) as 18:47:36.677, -01:56:36.72. It is at a distance of $\sim 3.0''$ towards the south of the detected position of WR 121a. The observed position of this closest source suggests that it is probably W43 #3 which is an O+O binary system (Luque-Escamilla et al., 2011). A detailed investigation is required to find the exact identity of this object.

In the case of *XMM-Newton* data, the X-ray light curves and spectra of WR 121a from EPIC instruments were generated from a circular region centered at the source position with a radius of $15''$ (equal to the HPD). In order to ascertain that no nearby sources contaminate the X-ray products generated for WR 121a, we have also identified sources present in the field using the task EDETECT_CHAIN. The source detected closest to the position of WR 121a lied outside the selected source region of $15''$ radius at a distance of $\sim 26''$. However, *Chandra* detected 3 sources using the observation ID 18869 (at the nearest phase) under the selected $15''$ radius of WR 121a. These sources contribute only 3.5% to the total count rate of WR 121a in $15''$ source radius of *Chandra* observation. Further, we have converted count rates of all of these 3 *Chandra* detected sources to the EPIC–PN of *XMM-Newton* using the WebPIMMS. The corresponding count rates from EPIC–PN instrument for each source are equivalent or less than to the background count rate of the EPIC–PN for the present observation of 21.8 ks. This could be a probable reason that these sources were not detected by *XMM-Newton*. Under these circumstances, there is a low probability of contamination by neighboring sources to WR 121a in

¹http://cxc.harvard.edu/ciao/threads/marx_sim/

its 15'' source radius in this *XMM-Newton* observation. Nevertheless, we caution the readers to take the results obtained from *XMM-Newton* with care against the possible contamination (if any) from neighboring sources.

4.3 X-ray timing analysis

The background subtracted X-ray light curves as observed by *XMM-Newton*–EPIC and *Chandra*–ACIS were produced in the three energy bands and have been shown in Figure 4.2. The *XMM-Newton* light curves were binned with 200 s while *Chandra* light curves were binned with 1000 s. The smaller number of count rate in the 0.5–2.0 keV energy band is indicative of the high absorption towards the source. However, the count rate in the other two energy bands follows a similar pattern. As shown in Figure 4.2b, a hint of variability is clearly seen in 0.5–8.0 and 2.0–8.0 keV energy bands.

4.3.1 Search for variability

We have examined the collective *Chandra*–ACIS light curve of WR 121a in the 0.5–8.0 keV energy range using the χ^2 -test of variability defined as

$$\chi^2 = \sum_{i=1}^N \frac{(C_i - \bar{C})^2}{\sigma_i^2} \quad (4.1)$$

where \bar{C} is the average count rate, C_i is the count rate of i^{th} observation and σ_i is the error corresponding to C_i . The value of χ^2 obtained for the *Chandra*–ACIS light curve in the 0.5–8.0 keV energy band is 1346 for 379 degrees of freedom. The χ^2 statistic was compared against a critical value (χ^2_{ν}) for 0.1 % significance level, obtained from χ^2 probability distribution function. The χ^2 value obtained is very large as compared to the χ^2_{ν} of 470 for 379 degrees of freedom. This confirms that WR 121a was essentially variable with a 99.9% confidence level during these observations. Light curves of the individual epoch of observations were also examined for the presence of variability using the χ^2 -test. None of them was found to be significantly variable.

Further, we have performed a Fourier Transform (FT) of the *Chandra*–ACIS light curve in the 0.5–8.0 keV energy band using the Lomb-Scargle periodogram (Horne & Baliunas, 1986; Lomb, 1976; Scargle, 1982) to find any periodic signal. This is particularly effective in determining periodicities in those time series which are obtained over unequally spaced intervals of time. The top panel of Figure 4.3

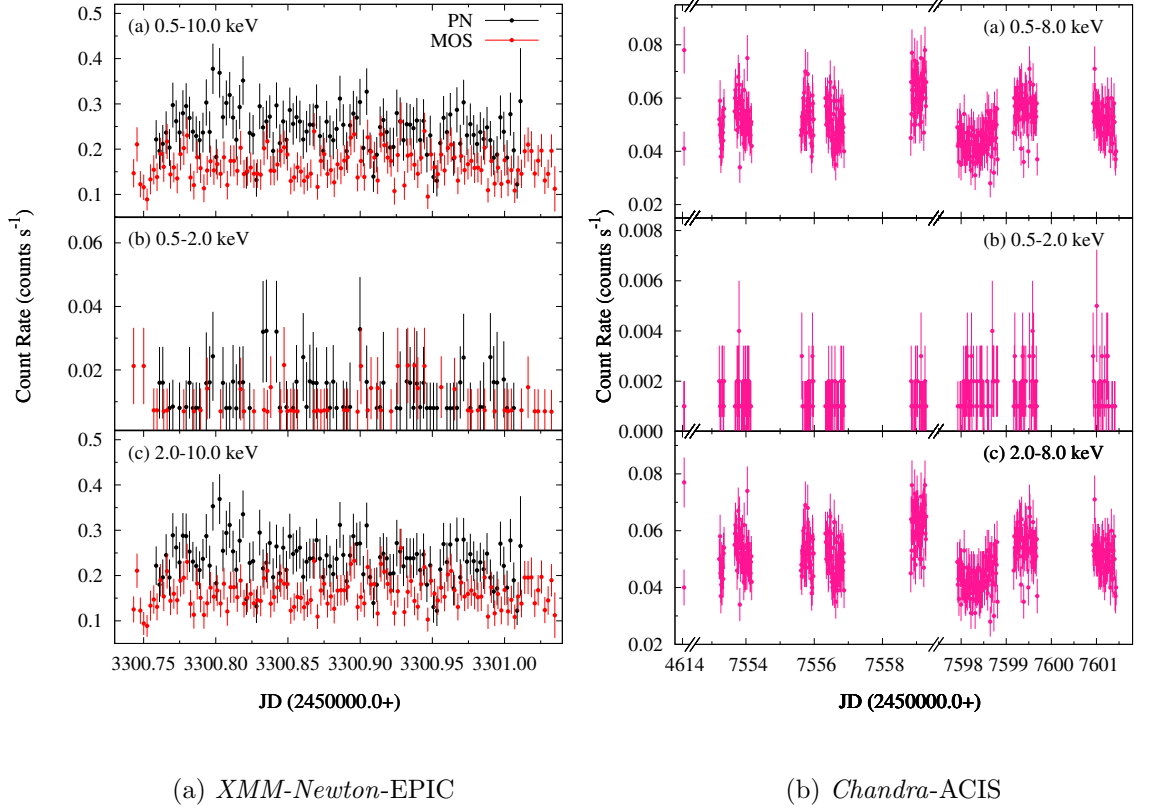


Figure 4.2: X-ray light curves of WR 121a in different energy bands as observed by (a) *XMM-Newton-EPIC*, and (b) *Chandra-ACIS*.

shows the Lomb-Scargle power spectra of the *Chandra* light curve in the 0.5-8.0 keV energy band, where a peak power corresponding to a period of 4.1 ± 0.1 d was noticed. We have also calculated a false alarm probability (see [Horne & Baliunas 1986](#)) to check the significance of detected peaks. It is shown by the horizontal line in the top panel of Figure 4.3. Several other peaks were also present in the Lomb-Scargle power spectra, which may be due to the aliasing. To verify whether the identified peak in the periodograms is caused by the purely periodic signal or by the sampling, we have obtained the periodogram called the data window as shown in the middle panel of Figure 4.3. It has been determined by setting all the data values as well as its variance to unity which were used to estimate the Lomb-Scargle periodogram of the light curve. Therefore, it simply depends upon how the sampling of the signal was performed and does not depend upon the signal itself. The identified peak in the Lomb-Scargle power spectra did not fall under the window function indicating

4. WR 121A: A SHORT PERIOD COLLIDING WIND BINARY

that the derived periodicity is real. We have also performed a periodogram analysis of the data using the CLEAN algorithm (Roberts et al., 1987). The CLEAN power spectrum was obtained by using a loop-gain of 0.1 and the number of iteration of 100. Similar to the Lomb-Scargle periodogram, a peak corresponding to a period of 4.1 ± 0.1 d was also found in the CLEAN power spectra (see bottom panel of Figure 4.3).

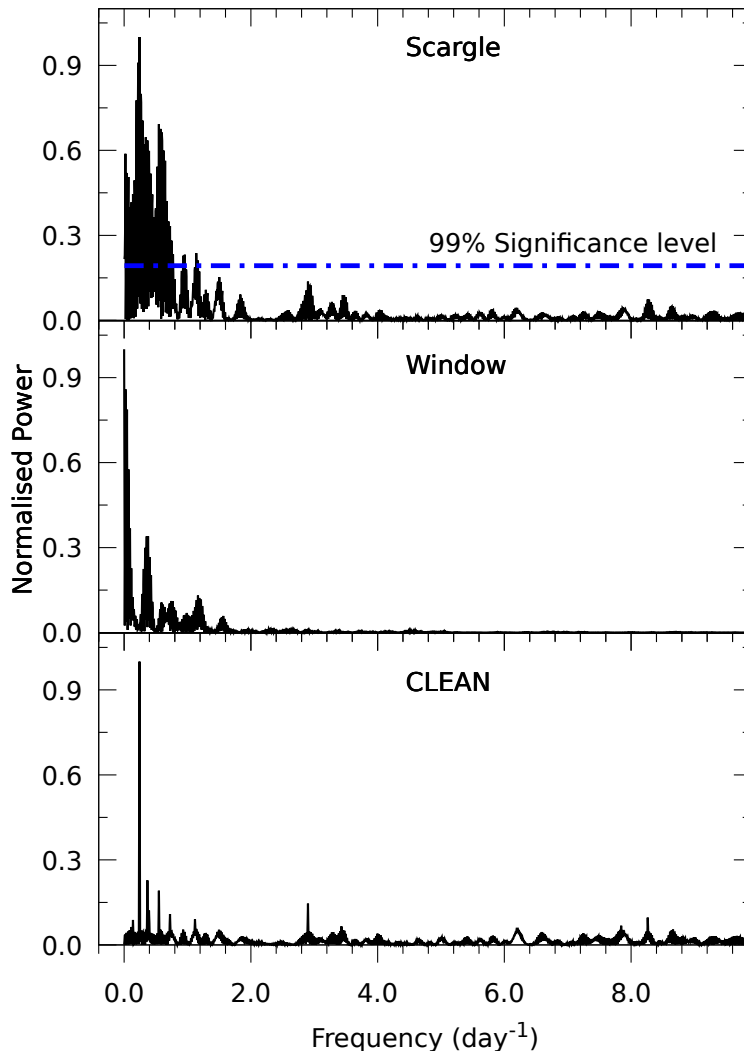


Figure 4.3: Lomb-Scargle (*top*), data window (*middle*), and CLEAN (*bottom*) power spectra of WR 121a in 0.5-8.0 keV energy range using data from *Chandra*-ACIS. The dashed-dotted line in the top panel shows the false alarm probability corresponding to 99% significance level.

4.3.2 Folded X-ray light curves

X-ray light curves of WR 121a were folded using the ephemeris $\text{HJD}=2457553.27+4.1\text{E}$, where zero phase corresponds to a minimum X-ray count rate as observed for the Obs. ID 18868 and are shown in Figure 4.4. The average count rate of an individual observation was taken as a single data point in the folded light curve as light curve of individual observation was non-variable. In the energy band 0.5-2.0 keV, the average count rate belonging to the Obs. ID 9612 was found to be significant with 1.4σ level, whereas average count rates for other Obs. IDs were significant by more than 3σ level. The light curves in the individual bands show phase-locked variability. X-ray light curves in 0.5-8.0 keV and 2.0-8.0 keV energy bands show similar behavior. In both of these energy bands, the count rate increased from the the phase ~ 0.0 to a phase ~ 0.4 and then decreased up to the phase ~ 1.0 . However, in the 0.5-2.0 keV energy band, initially, the count rates were increased from phase 0.0 to a phase ~ 0.23 . Then, it dropped in the later phase and became constant up to a phase ~ 1.0 within a 1σ level. The ratio of the maximum to the minimum count rates in 0.5–8.0 keV, 0.5–2.0 keV, and 2.0–8.0 keV energy bands was found to be 1.60 ± 0.15 , 1.51 ± 0.38 , and 1.61 ± 0.15 , respectively.

The hardness ratio (HR), which is defined as the ratio of count rates in 2.0-8.0 keV and 0.5-2.0 keV energy bands, can reveal information about the spectral variations. The HR curve as shown in panel (d) of Figure 4.4 displays similar behavior to that of the light curve in the 2.0–8.0 keV energy band. The maximum value of the HR near the orbital phase ~ 0.4 indicates a harder spectrum relative to other orbital phases.

4.4 X-ray spectral analysis

The *Chandra*–ACIS-I spectra of WR 121a at different orbital phases have been shown in Figure 4.5. Several emission lines are visible in the X-ray spectrum of WR 121a. The two spectra in the Figure 4.5 display the difference in the source flux when the two components of the binary system were ~ 0.5 phase apart. The soft energy part is highly absorbed as predicted for this deeply embedded object. But the system appears to be slightly brighter around phase 0.41 than phase 0.97 while this difference vanishes below ~ 4 keV. The HR curve as shown in the bottom panel of Figure 4.4 also imparts a similar feature.

The best fit model to fit the X-ray spectrum of WR 121a has been obtained using *XMM-Newton* data since the X-ray spectra from EPIC instruments have the

4. WR 121A: A SHORT PERIOD COLLIDING WIND BINARY

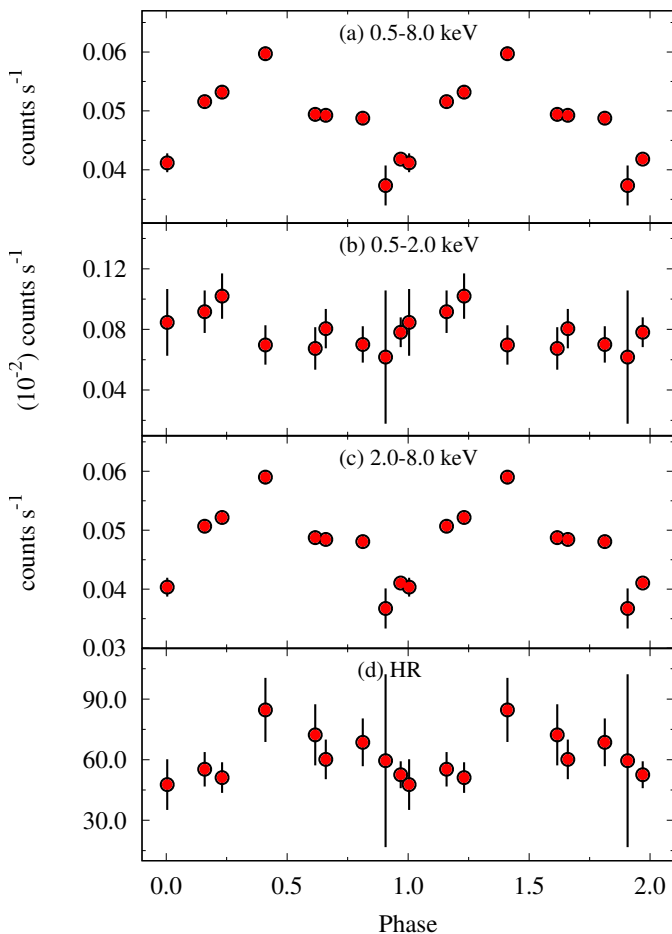


Figure 4.4: Folded X-ray light curves of WR 121a in different energy bands as observed by *Chandra*–ACIS.

better photon statistics than those of *Chandra* data. We have even attempted to fit combined spectra from all the 9 data-sets of *Chandra* to obtain the best-fit parameters. But it returned some bizarre values after spectral fitting. Therefore, we began with the fitting of MOS and PN spectra of WR 121a jointly in 0.5–10.0 keV energy range using the thermal plasma models.

We could not derive the abundances of individual elements using the *XMM-Newton* spectra of WR 121a by using the model “VAPEC” in XSPEC as the best fit model returned to unphysical values of abundances. Therefore, instead of using variable abundances plasma model, as used for WR 25, we have used an average abundanced plasma model “APEC” for the spectral fitting of WR 121a. The model was used in the form PHABS(ISM)*PHABS(LOCAL)*(APEC+APEC). The component PHABS(ISM) and PHABS(LOCAL) were used to model the interstellar absorption and the local wind absorption effects, respectively. The parameter N_H^{ISM} corresponding

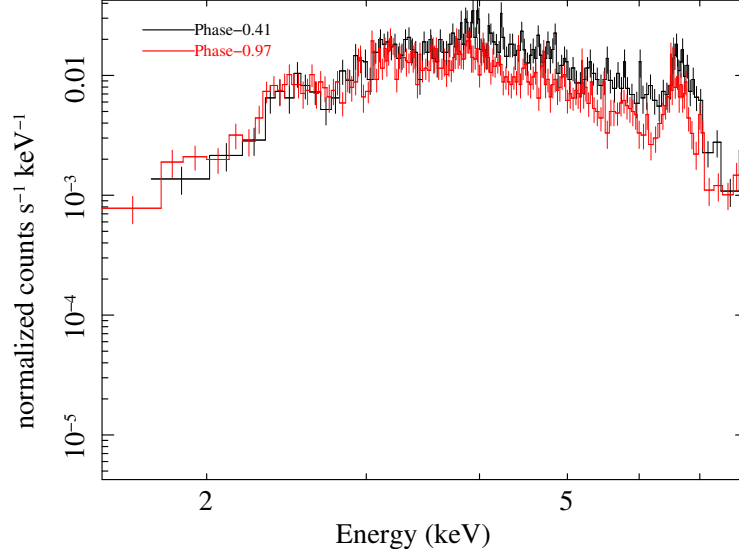


Figure 4.5: Comparison of *Chandra*–ACIS spectra of WR 121a at two different orbital phases. Black points correspond to an orbital phase ~ 0.41 and red points refer to a phase ~ 0.97 .

to the model component “PHABS(ISM)” was frozen at the value of $6.5 \times 10^{22} \text{ cm}^{-2}$ (Luque-Escamilla et al., 2011). The abundances (Z) were tied for both components of “APEC” model. All other parameters along with Z were kept free in the fitting. A χ^2 statistics was used for the spectral fitting. The best fit model on *XMM-Newton*–EPIC spectra returned the values of two temperatures (*i.e.* kT_1 and kT_2) as $0.98 \pm 0.34 \text{ keV}$ and $3.55 \pm 0.69 \text{ keV}$, respectively. However, Z was found to be 0.8 ± 0.1 times of solar photospheric abundances. The blending of various emission lines in the low resolution X-ray spectrum of WR 121a as well as non-detection of few lines below 2.5 keV due to heavy absorption leads to sub-solar global abundances in the spectral fitting. Therefore, high resolution grating spectra are needed for precise abundance determinations. The X-ray spectra of WR 121a as observed by MOS and PN along with the best fit model has been shown in Figure 4.6. Various spectral lines along with the continuum have been fitted properly with a reduced χ^2 of 0.99 for 351 degrees of freedom. The strong emission line has been detected between 6 and 7 keV. The centroid of the line has been estimated by fitting a Gaussian profile and found to be at $6.66 \pm 0.01 \text{ keV}$ with an equivalent width of $1.38 \pm 0.15 \text{ keV}$, which is similar to that found by Anderson et al. (2011). This line has been identified as Fe XXV and remains unresolved in the *XMM-Newton* spectrum of WR 121a since *XMM-Newton* possess energy resolution of $\sim 135\text{--}140 \text{ eV}$ (FWHM) around 7 keV.

4. WR 121A: A SHORT PERIOD COLLIDING WIND BINARY

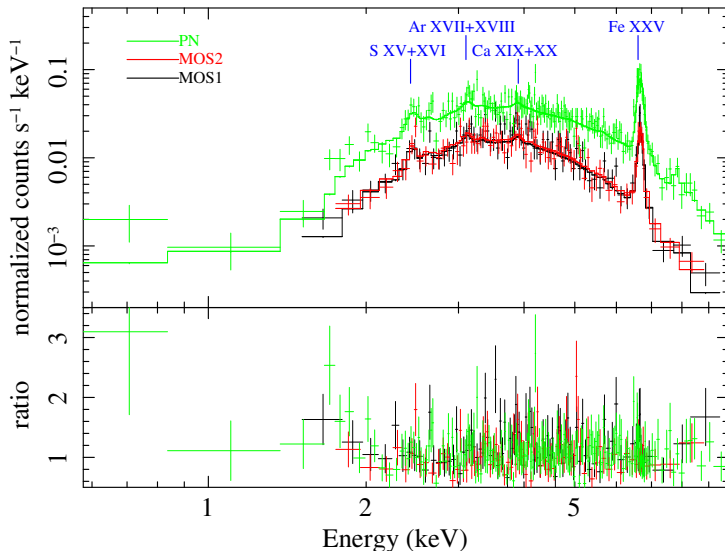


Figure 4.6: X-ray spectra of WR 121a as observed from MOS and PN detectors onboard *XMM-Newton* along with the best fit folded two-temperature plasma emission model (2T APEC). The lower panel shows the residual in terms of the ratio of the data and model.

While fitting the *Chandra* spectrum from individual observations, initially we have followed the same procedure as applied to fit the EPIC spectra. But the temperature of both components over all phases were found to be consistent. Thus, *Chandra* spectra of WR 121a at different epochs of observations were fitted by keeping fixed the parameters N_H^{ISM} , kT_1 , kT_2 , and Z to the best fit values obtained from the EPIC spectra. Whereas the local equivalent H-column density (N_H^{local}) along with the normalization constants of both temperature components ($norm_1$ and $norm_2$) were free parameters. Each spectrum from *Chandra*-ACIS was fitted individually except one from Obs. ID 9612 due to its poor photon counts. Therefore, it was fitted jointly with the spectrum of Obs. ID 18887 which lies at its closest phase. The ISM corrected X-ray fluxes of WR 121a in broad (0.3–10.0 keV, F_B^{ism}), soft (0.3–2.0 keV, F_S^{ism}), and hard (2.0–10.0 keV, F_H^{ism}) energy bands were derived using the model CFLUX in XSPEC. The intrinsic X-ray flux (*i.e.* corrected for both the galactic as well as local absorption) has also been estimated in broad (F_B^{int}) energy band. The values of the best-fit parameters are given in Table 4.1. The variation of spectral parameters with orbital phase has been shown in Figure 4.7, where the red filled circles and green filled triangles correspond to *Chandra*-ACIS and *XMM-Newton*-EPIC data, respectively. The parameters $norm_1$ and N_H^{local} were

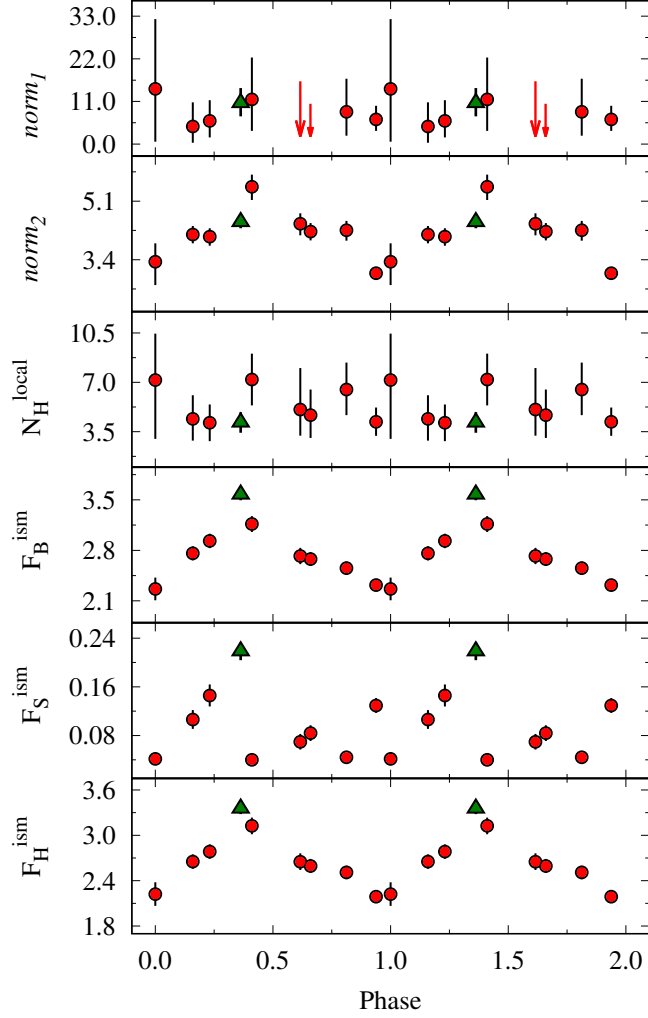


Figure 4.7: Spectral parameters as a function of the orbital phase of WR 121a obtained from *Chandra*–ACIS (red filled circles) and *XMM-Newton*–EPIC data (green filled triangles). Here, $norm_1$ and $norm_2$ are in the units of 10^{-3} cm^{-5} , N_H^{local} in 10^{22} cm^{-2} , and F_B^{ism} , F_S^{ism} as well as F_H^{ism} are in the units of $10^{-12} \text{ erg cm}^{-2} \text{ s}^{-1}$. The downward arrows in the top panel mark the upper limits of $norm_1$ for two *Chandra* Obs. IDs (see Table 4.1).

found to vary along with the orbital phase within 1σ level. Whereas the parameters $norm_2$, F_B^{ism} and F_H^{ism} were varied in a similar fashion. A secular variation in these parameters was noticed, they increased from phase 0.0 to a phase near ~ 0.4 and then decreased up to a phase 1.0. However, the variation in F_S^{ism} was found different than that seen in F_H^{ism} . At first, F_S^{ism} increased from phase 0.0 to a phase near 0.36 then suddenly dropped to a phase 0.41, after this phase F_S^{ism} increased again to a phase ~ 0.6 then showed a decreasing trend afterward.

Table 4.1: Best fit parameters obtained from spectral fitting of WR 121a as observed from *Chandra*–ACIS and *XMM-Newton*–EPIC.

Obs.	Orbital phase	$norm_1$ (10^{-3} cm^{-5})	$norm_2$ (10^{22} cm^{-2})	N_H^{local} (10^{22} cm^{-2})	F_B^{ism}	F_S^{ism}	F_H^{ism}	F_B^{int}	$\chi^2(dof)$
0203850101	0.36	$10.60^{+3.86}_{-3.44}$	$4.49^{+0.18}_{-0.18}$	$4.15^{+0.73}_{-0.73}$	$3.57^{+0.08}_{-0.08}$	$0.22^{+0.01}_{-0.01}$	$3.35^{+0.07}_{-0.07}$	$32.74^{+2.5}_{-2.5}$	0.99 (351)
18868	0.00	$14.26^{+17.99}_{-13.66}$	$3.34^{+0.54}_{-0.68}$	$7.17^{+3.29}_{-4.18}$	$2.26^{+0.16}_{-0.16}$	$0.04^{+0.01}_{-0.01}$	$2.22^{+0.16}_{-0.16}$	$39.53^{+8.74}_{-8.77}$	1.61 (36)
17716	0.16	$4.54^{+6.23}_{-4.20}$	$4.13^{+0.25}_{-0.26}$	$4.41^{+1.67}_{-1.54}$	$2.76^{+0.09}_{-0.09}$	$0.11^{+0.02}_{-0.02}$	$2.65^{+0.09}_{-0.09}$	$17.62^{+3.24}_{-3.25}$	1.25 (120)
18870	0.62	16.22^a	$4.44^{+0.30}_{-0.34}$	$5.07^{+2.94}_{-1.86}$	$2.72^{+0.11}_{-0.11}$	$0.07^{+0.01}_{-0.01}$	$2.65^{+0.11}_{-0.11}$	$17.10^{+4.08}_{-4.08}$	0.99 (93)
18867	0.81	$8.32^{+8.55}_{-6.14}$	$4.25^{+0.27}_{-0.29}$	$6.49^{+1.91}_{-1.82}$	$2.55^{+0.09}_{-0.09}$	$0.04^{+0.01}_{-0.01}$	$2.51^{+0.09}_{-0.09}$	$26.89^{+4.25}_{-4.25}$	1.16 (121)
18869	0.41	$11.53^{+10.81}_{-8.12}$	$5.52^{+0.35}_{-0.38}$	$7.19^{+1.84}_{-1.83}$	$3.16^{+0.11}_{-0.11}$	$0.04^{+0.01}_{-0.01}$	$3.12^{+0.11}_{-0.11}$	$36.66^{+5.75}_{-5.76}$	1.03 (127)
17717	0.23	$5.97^{+5.36}_{-4.26}$	$4.07^{+0.25}_{-0.26}$	$4.13^{+1.29}_{-1.31}$	$2.93^{+0.10}_{-0.09}$	$0.15^{+0.02}_{-0.02}$	$2.79^{+0.09}_{-0.09}$	$20.97^{+3.19}_{-3.19}$	0.99 (130)
18888	0.66	10.42^a	$4.21^{+0.25}_{-0.25}$	$4.68^{+1.81}_{-1.63}$	$2.68^{+0.09}_{-0.09}$	$0.08^{+0.01}_{-0.01}$	$2.59^{+0.09}_{-0.09}$	$16.27^{+3.25}_{-3.25}$	1.00 (119)
18887	0.97	$6.37^{+3.51}_{-2.96}$	$3.01^{+0.17}_{-0.18}$	$4.20^{+1.01}_{-0.99}$	$2.32^{+0.07}_{-0.07}$	$0.13^{+0.01}_{-0.01}$	$2.19^{+0.06}_{-0.06}$	$20.19^{+2.25}_{-2.26}$	1.25 (175)
9612	0.91								

Notes: Fit parameters are based on a two-temperature APEC model with two absorption components N_H^{ISM} (for galactic absorption) and N_H^{local} (for local wind absorption). The fitted model has the form PHABS(ISM)*PHABS(LOCAL)*(APEC+APEC) with $N_H^{ISM} = 6.5 \times 10^{22} \text{ cm}^{-2}$, the two temperatures $kT_1 = 0.98 \pm 0.34 \text{ keV}$ and $kT_2 = 3.55 \pm 0.69 \text{ keV}$, and abundances $Z = 0.8$ fixed to values derived from fitting of *XMM-Newton*–EPIC spectra of WR 121a. $norm_1$ and $norm_2$ are the normalization constants for two temperature components. F_B^{ism} , F_S^{ism} , and F_H^{ism} are the ISM corrected X-ray fluxes of WR 121a in broad, soft and hard energy bands, respectively. F_B^{int} is the intrinsic X-ray flux corrected for both N_H^{ISM} as well as N_H^{local} in broad energy band. χ^2 is the reduced χ^2 and dof is degrees of freedom. Errors quoted on different parameters refer to 90% confidence level. The spectra obtained from Obs. IDs 18887 and 9612 has been fitted jointly.

^a Mentioned values correspond to the upper limits of the specified parameter.

4.5 Discussion

A detailed investigation of WR 121a using a long-term X-ray data from *Chandra* and *XMM-Newton* satellites have been carried out for the first time. The X-ray spectrum of WR 121a below 10.0 keV represents the typical characteristics of an X-ray emission from an optically thin thermal plasma at temperature $>10^6$ K (see Figure 4.6). These features are expected to arise from plasma heated in the WCR of a colliding wind massive binary where supersonic winds from the two massive stars produce shock-heated gas (Stevens et al., 1992). This results in the production of thermal hard X-ray emission. Anderson et al. (2011) fitted *XMM-Newton* spectra of WR 121a with a simpler one-temperature Raymond & Smith (1977) model attributed to the presence of a likely thermal component to the X-ray emission. The values of temperature and abundances derived by them are consistent with our estimates. Analyzing the X-ray spectrum of WR 121a, Anderson et al. (2011) has also suggested that it belongs to the category of CWBs. The current study verifies this fact by looking at the following details:

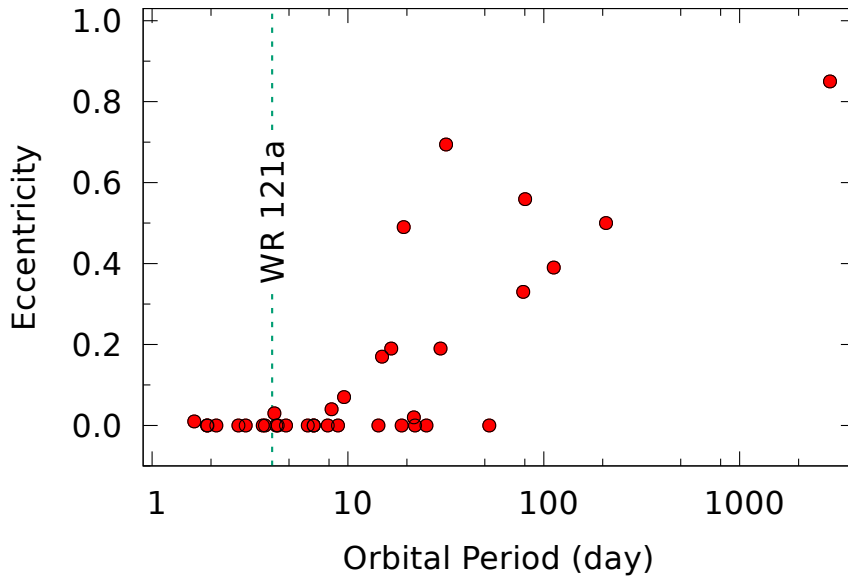
1. The maximum ISM corrected X-ray luminosity (L_X^{ism}) of WR 121a in 0.3-10.0 keV energy band is estimated to be 1.54×10^{34} erg s $^{-1}$ (corresponding to a distance of 6 kpc). While the ISM and local wind absorption corrected X-ray luminosity (L_X^{int}) has been estimated to 1.70×10^{35} erg s $^{-1}$. This belongs to the typical X-ray luminosity range of $\sim 10^{32}$ to 10^{35} erg s $^{-1}$ for WR + O binary systems (e.g. Gagné et al., 2012). The derived X-ray luminosity for WR 121a is also found to be more than the typical X-ray luminosity of several single WN stars (Skinner et al., 2010, 2012).
2. The presence of a strong 6.7 keV Fe xxv emission line further supports this fact since its generation requires the high temperature plasma (approximately 10^7 K) which is present in the WCR as pointed out by Raassen et al. (2003) .
3. The present theoretical models about CWBs suggests that a substantial amount of X-rays originate from the collisions of dense and highly supersonic stellar winds of binary components (Cherepashchuk, 1976; Prilutskii & Usov, 1976). However, the individual stars may also have a considerable intrinsic soft X-ray emission due to the relatively less stronger shocks that develop as an outcome of the line driven instabilities (Lucy, 1982; Owocki et al., 1988). Therefore, the fitting of X-ray spectra of bright WR + O binaries requires at least two thermal components, which is also seen in the case of WR 121a (see section

4. WR 121A: A SHORT PERIOD COLLIDING WIND BINARY

4.4). The two temperatures derived from the spectral fitting of WR 121a are well within a range typically found for massive binaries, e.g. ≤ 1 keV for cool and 2.0-4.0 keV for hot temperature component (Feldmeier et al., 1997; Rauw & Nazé, 2016).

4. Another important aspect of CWBs is the phase-locked variability of the flux and/or the hardness of the X-ray emission. This depends upon the amount of absorption suffered by the X-rays through the orbit. Since soft X-rays are more strongly absorbed, therefore, increasing absorption reduces observed flux but increases the hardness. Figs. 4.4, 4.5, and 4.7 display clear signatures of variability along the orbit and hence supports CWB status of WR 121a.

The X-ray light curves of WR 121a in the 0.5-8.0 keV energy band shows periodicity corresponding to 4.1 ± 0.1 d period. For the WR+O binaries, Cherepashchuk & Karetnikov (2003) suggested that the orbits of WR+O binaries are circular if their orbital periods are less than ~ 14 d. Figure 4.8 shows the plot between eccentricity and the orbital period of WR+O binaries. Location WR 121a is shown by a dashed line. From this figure, it appears that circularization occurs in the orbital period between 10 - 20 d. Thus, the orbit of WR 121a can be considered as a circular. Further, it appears that the circular orbit implies a phase independent wind collision in between the stars.



If we consider a circular orbit, the phase variation in X-ray flux could be due to the change in absorption by the variable wind density along the line of sight and/or occultation of the X-ray emitting region. Since hard X-rays are mainly generated in the WCR, therefore, the minimum F_H^{ism} at phase 0.0, as shown in Figure 4.7, could be due to the eclipsing of WCR behind the O-type companion. We suggest that the WCR is eclipsed by O-star as the location of WCR is close to the O-star (as explained later in this section) and the size of O-star is larger than its companion WN star. After the maximum flux at ~ 0.36 , F_H^{ism} decreases gradually till the orbital phase ~ 1.0 . This is also evident from the larger HR ratio as well as the harder *Chandra* X-ray spectrum of WR 121a near phase ~ 0.4 as seen in Figures 4.4 and 4.5, respectively. The F_S^{ism} also follows a similar trend as that of F_H^{ism} during the orbital phase 0.0 to 0.36. But it shows instances of increased/decreased values around other orbital phases which is exactly opposite to the trend followed by N_H^{local} . Although it is difficult to anticipate anything from the variation of N_H^{local} , owing to its large error bars, still it presents hints about our line of sight passing through stellar winds of different densities. Since N_H^{local} mostly affects the soft X-rays, therefore, this might be giving rise to orbital variations in F_S^{ism} . The estimation of N_H^{local} with large uncertainty along with the sparse orbital sampling do not allow us to accurately determine the geometry of the binary components as well as of the WCR during the orbital period. Therefore, further observations of WR 121a with dense orbital sampling in different wavebands are urgently required to understand its binary nature more deeply.

Luque-Escamilla et al. (2011) has suggested that the separation between the two components of WR 121a is $\sim 0.598''$. Using this separation, we have estimated the orbital period (P) of WR121a system by using the Kepler's third law as

$$P^2 = \frac{4\pi^2 a^3}{G(M + m)} \quad (4.2)$$

where a is the linear separation corresponding to $0.598''$ angular separation at a distance of 6 kpc, G is the universal Gravitational Constant, M and m represent the masses of the primary and secondary star of the binary, respectively. Because of the similarity of the K -band spectra of WR 121a and WR 131, as noted by Blum et al. (1999), the value of M is taken same as that for the WN7 star of WR 131 *i.e.* equal to $44 M_\odot$ (Hamann et al., 2019). Using the several values of m for typical O-type dwarf/giant/supergiant star from Muijres et al. (2012), the value of P is found to be more than 2700 yrs. Further, it is very unlikely for the faraway companions to give rise to a strong wind-wind collision to emit significant

4. WR 121A: A SHORT PERIOD COLLIDING WIND BINARY

X-rays. Till now, the massive binaries having an orbital period only up to a few years have been seen to harbor X-ray bright wind-wind collision (e.g. 9 Sgr with an orbital period of 9.1 yr; [Rauw et al. 2016](#)). Therefore, either the companion of WN7 star in WR 121a as described by [Luque-Escamilla et al. \(2011\)](#) may not be correct or this may be a triple system where X-ray modulations of 4.1 d observed in this study are originating from the shorter orbital components. The radius of WN7 star has been estimated to be $7.85 R_{\odot}$ by using its typical values of luminosity as $10^{5.54} L_{\odot}$, temperature as 50 000 K ([Crowther, 2007](#)), and assuming a black body emission. Whereas, there is a large spread in the mass of WN7-type star in the range of 7–49 M_{\odot} ([Hamann et al., 2019](#)). The mass, as well as the radius of O-type companion, has been noted to lie in a range of 16.46–66.89 M_{\odot} and 7.39–23.11 R_{\odot} , respectively, by considering all the possible cases of dwarf/giant/supergiant star ([Muijres et al., 2012](#)). Assuming a circular orbit scenario and the above mentioned mass estimations, the linear separation from center of WN7 star to the center of O-type star of WR 121a system is found to lie in the range of 30.90–52.75 R_{\odot} which translates to an angular separation of 0.024–0.041 mas at a distance of 6 kpc. The WR 121a system appears to be either detached or semi-detached where O-type star is filling its Roche-lobe especially when it is in supergiant state.

To explore the nature of wind collision in WR 121a, the value of the cooling parameter (χ) at the position of wind collision in between two stars has also been estimated in a similar way as done for WR 25. Since the spectral features of WR 121a are similar to that of WR 131, the mass of WN7 star has been adopted as 44 M_{\odot} for the rest of the analysis. However, a range of masses as mentioned above for the O-type star has been considered. Additionally, by assuming the typical values of mass-loss rate, radius, and terminal-wind velocity for a WN7 and O-type dwarf/giant/supergiant star ([Crowther, 2007](#); [Hamann et al., 2019](#); [Muijres et al., 2012](#)), the position of WCR was estimated and correspondingly the wind speeds of two stars was calculated at the WCR using the standard β -velocity law. It was seen that the stellar winds of both the components of WR 121a interact at sub-terminal speeds and the value of χ for a circular orbit of period 4.1 d is estimated to be $\ll 1$ for both the winds of WN- and O-star at the position of WCR as shown in [Figure 4.9](#). This is as expected since the shocked-wind has not enough time to escape the WCR and cool-down via adiabatic expansion in a short period massive binary, therefore, it cools rapidly through radiation emission.

The plasma temperature derived from the spectral fitting of WR 121a can also be used to estimate the pre-shock velocity by using the relation from [Luo et al. \(1990\)](#) as

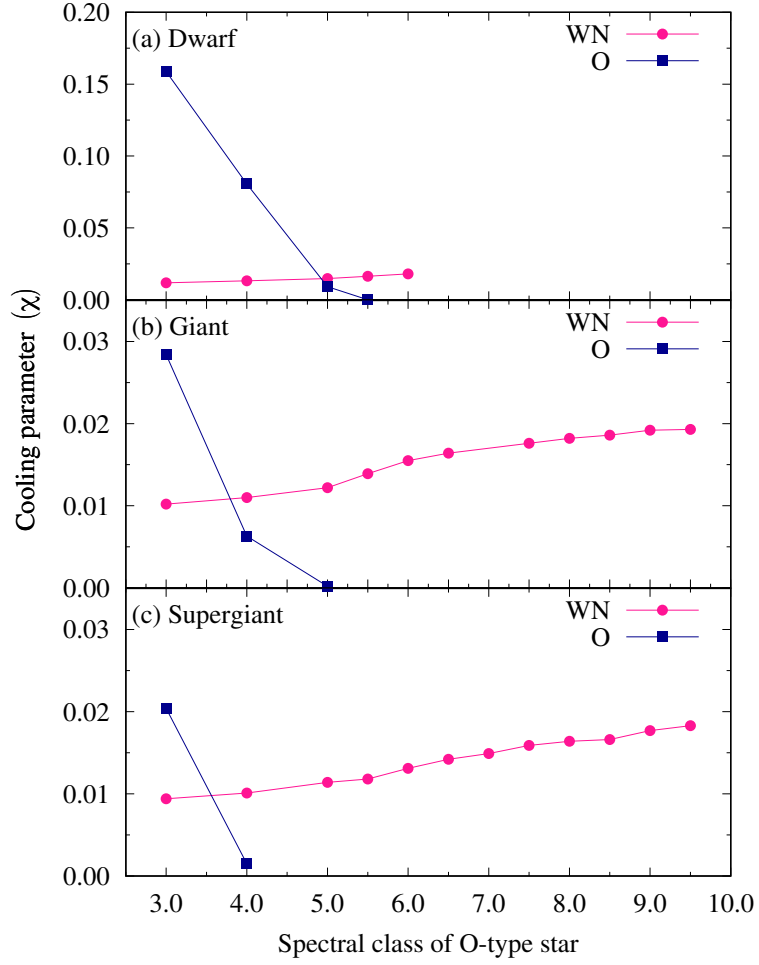


Figure 4.9: Variation of cooling parameter (χ) as a function of the orbital phase for WR 121a by assuming primary as a WN7 star and an O-type dwarf/giant/supergiant star as secondary.

$$kT_{sh,max} = 1.95\mu v_{\perp,1000}^2 \text{ keV} \quad (4.3)$$

where μ is mean mass per particle in units of the proton's rest mass, which is 1.16 for a WN star (Skinner et al., 2007) and 0.62 for an O-type star (Cassinelli et al., 2008), and $v_{\perp,1000}$ is the wind velocity component perpendicular to the shock front in units of 1000 km s^{-1} . This is the same relation as derived in Equation 1.17 where plasma temperature behind the shock is derived by RH conditions. The average values of pre-shock velocities corresponding to the cool temperature (which is mostly generated due to the radiation driven wind shock of individual component of binary) for the WN and O components of WR 121a are found to be ~ 658 and $\sim 900 \text{ km s}^{-1}$, respectively. Whereas the pre-shock velocities in the WCR corresponding to

4. WR 121A: A SHORT PERIOD COLLIDING WIND BINARY

the hot temperature are estimated to be as 1253 and 1714 km s⁻¹ for WN and O-type components of WR 121a system, respectively. These values are lower than the typical terminal velocity observed for the single WN and O-type stars. This may be happening because of two reasons. One is that a wide range of temperatures is covered by the shocked plasma in WCR. The hottest plasma is expected to lie near the stagnation point while the cooler plasma is present along the wings of the shock front. But the X-ray spectral fitting gives the average temperature prevailing in the WCR which will be less than the maximum shock temperature mentioned in the relation 4.3. Another probable reason could be that if the winds of individual binary stars have not reached terminal speeds before colliding, as it is likely for short-period binaries, then the maximum shock temperature will further be decreased.

In addition to the presence of hydrodynamic shocks in the CWBs, some other effects have to be considered as well. These include alterations of the characteristics of pre-shock flow along with the microscopic phenomena prevailing in post-shock plasma. For massive binaries, the interaction of the stellar wind with the strong radiation fields of the component stars inhibits the acceleration of one star's wind and prohibits it to reach v_∞ (Stevens & Pollock, 1994). On the other hand, another outcome of the radiation pressure of the companion star called radiative braking was examined by Gayley et al. (1997). This effect is most favorable for those binary configurations in which the wind momenta of the component stars are highly imbalanced e.g. WR + O binaries. For those systems, as the dominant star wind approaches close to the surface of companion star, the radiative momentum flux of the companion star suddenly decelerates it. This process leads to significant modification of the bow shock geometry and the wider opening angle of the shock cone. In some situations, it is impossible for the companion wind to sustain the momentum of the dominant wind. Radiative braking prevents the collision of incoming wind onto the surface of companion star for those scenarios. For example, consider the case of V444 Cyg (WR 139). It is a massive binary where the primary is a WN5 star whereas secondary is an O6 star. They move around an orbit which is almost circular (eccentricity=0.03) with an orbital period of ~ 4.2 d (Marchenko et al., 1994; Münch, 1950). Owing to the shorter period and strong stellar winds of its components, it was suggested that both the radiative braking and inhibition are required to explain the X-ray light curves of V444 Cyg by Lomax et al. (2015). They have also estimated the shock opening angle for wind collision in V444 Cyg and it was found to be approximately 75°. The large value of shock opening angle confirmed that these two mechanisms play an important role in the stellar wind interaction of two components of this binary. Our analysis reveals that WR 121a is also similar to

V444 Cyg in terms of its orbit. Their periods are almost same. We have also noticed that while calculating χ , the position of the WCR was found to coincide with the position of the secondary star in the orbit for the O-type star later than O6.0, O5.5 and O5.0 for dwarfs, giants, and supergiant, respectively. This indicates that the WCR might be just collapsing onto the surface of the secondary star of WR 121a. The ratio of the companion star radius to the binary separation is found to lie in the range of 0.22–0.51, where the WR wind is shocking onto the companion surface. To explore this scenario further, we have estimated the shock opening angle (θ) for various combinations of WN7 and O-type star in a 4.1 d circular orbit according to [Eichler & Usov \(1993\)](#) as

$$\theta \simeq 2.1 \left(1 - \frac{\eta^{\frac{2}{5}}}{4} \right) \eta^{\frac{1}{3}} \quad \text{for } 10^{-4} \leq \eta \leq 1 \quad (4.4)$$

where $\eta = (\dot{M}v_\infty)_O / (\dot{M}v_\infty)_{WN}$ is the wind momentum ratio. It has been seen that η varies from 0.018 to 0.73 for all combinations of WN7 primary with different O-type secondaries and correspondingly θ was found to lie in the range of $\sim 30^\circ$ to 84° as displayed in [Figure 4.10](#). The larger value of η and hence θ observed for early O-type companions indicates that the radiative braking is playing an important role in the WCR of WR 121a as early O-type stars carry sufficient wind momentum to reduce the effect of the WN wind momentum. However, as the secondary star moves to the later O-type stars, the decreasing shock opening angle points towards the scenario of either no or low radiative braking and hence WN star wind overpowers the O-star wind and the shock forms at or very near the O-star surface as inferred from χ calculations also.

As mentioned in the beginning of this section, WR 121a lies towards the high end of the L_X range observed for massive binaries. Therefore, it is one of the brightest WR+O binary in X-rays. It was noted by [Gagné et al. \(2012\)](#) that generally all of the binary systems with WR stars having supergiant early O-type secondaries have $L_X > 10^{33}$ erg s $^{-1}$. However, the systems with supergiant late O-type star as a companion of WR star have $L_X^{int} \sim 10^{33}$ erg s $^{-1}$ e.g. CQ Cep (WN6+O9II-Ib; [Skinner et al. 2015](#)) and WR 133 (WN5+O9I; [Oskinova 2005](#)). Since L_X^{int} of $\sim 10^{35}$ erg s $^{-1}$ for WR 121a is much higher than the WR systems with late-type supergiant companion, therefore, we anticipate that WR 121a system may have an early O-type supergiant companion with WN7 primary. If it is so, then the radiative braking, as well as inhibition, would certainly be playing an important role in the WCR of WR 121a system. The denser wind of WN7 star may hide the spectral features specific

4. WR 121A: A SHORT PERIOD COLLIDING WIND BINARY

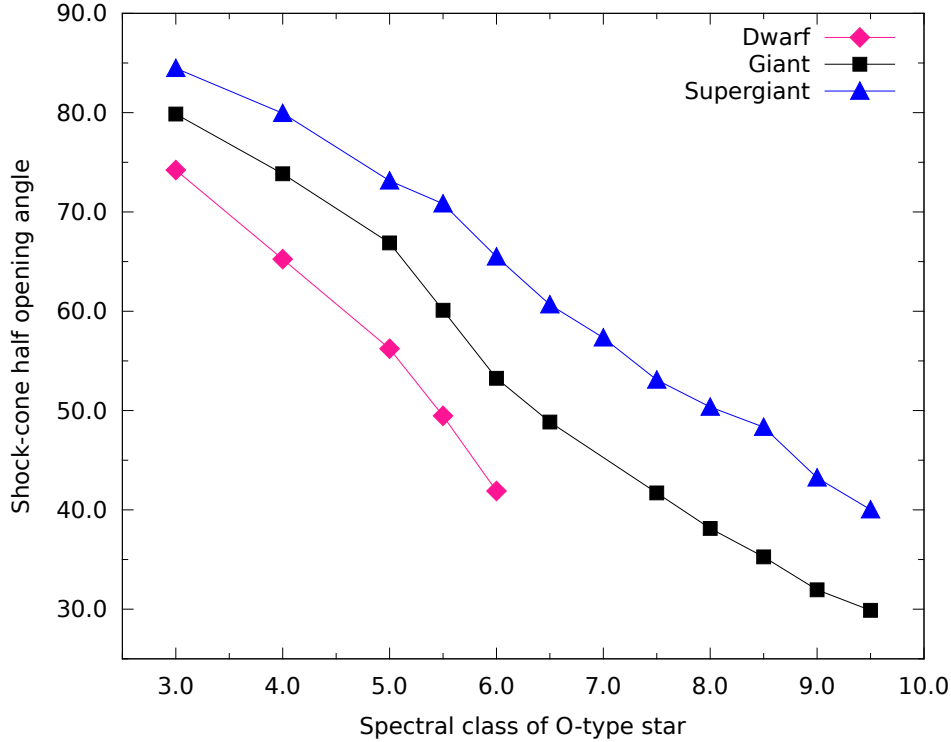


Figure 4.10: Variation of half opening angle of the shock-cone formed due to collision between stellar winds of a WN7 star and an O-type dwarf/giant/supergiant star in a circular binary orbit of period 4.1 d.

to an O-type companion as the bolometric luminosity of a O-type star is almost similar to that of WN7 star (Crowther, 2007; Muijres et al., 2012). The K -band spectrum of WR 121a also provides a hint about the presence of a companion, in spite of the large extinction towards the source direction (Blum et al., 1999), which suggest that the companion may be a bright object. However, detailed investigation into the matter is necessary.

An estimate of the intrinsic luminosity from the wind collision in a binary system containing WN7 and O-type dwarf/giant/supergiant star has been made using the theoretical relations given by Usov (1992). It has already been mentioned that for all the combinations of WN7 and O-type star, the stellar winds of two binary components interact at sub-terminal speeds either in between the stars or on the surface of the secondary star. Therefore, WR 121a with an orbital period of ~ 4.1 d can be regarded as one of the very close or close binary systems according to Usov (1992). However, the predicted intrinsic X-ray luminosity (L_X) is estimated from the equation (81) of Usov (1992), where the WR wind is shocking onto the

companion surfaces, as

$$L_X \simeq 5.8 \times 10^{32} \left(\frac{\dot{M}_{WR}}{10^{-5} M_\odot \text{ yr}^{-1}} \right)^2 \left(\frac{R_{OB}}{10^{12} \text{ cm}} \right)^3 \left(\frac{D}{10^{13} \text{ cm}} \right)^{-4} \left(\frac{V_{WR}^\infty}{10^3 \text{ km s}^{-1}} \right)^{-1} \quad (4.5)$$

where \dot{M}_{WR} denotes the mass-loss rate of the WR star in the system, R_{OB} is the radius of the O-type star and D is the binary separation. The terminal wind velocity of the WR star is mentioned by V_{WR}^∞ . L_X , in this case, is found to lie in the range of $\sim 0.5\text{--}6.0 \times 10^{35} \text{ erg s}^{-1}$. On the other hand, when the stellar winds interact in between the stars at sub-terminal speeds, then L_X is given by the sum of the X-ray luminosity from the external (L_{ext}) and internal (L_{int}) shock layers as

$$L_{ext} \simeq 8 \times 10^{34} \left(\frac{\dot{M}_{WR}}{10^{-5} M_\odot \text{ yr}^{-1}} \right)^{1/2} \left(\frac{\dot{M}_{OB}}{10^{-6} M_\odot \text{ yr}^{-1}} \right)^{3/2} \left(\frac{V_{WR}^*}{10^3 \text{ km s}^{-1}} \right)^{-5/2} \left(\frac{V_{OB}^*}{10^3 \text{ km s}^{-1}} \right)^{3/2} \left(\frac{D}{10^{13} \text{ cm}} \right)^{-1} \quad (4.6)$$

$$L_{int} \simeq 1.3 \times 10^{35} \left(\frac{\dot{M}_{WR}}{10^{-5} M_\odot \text{ yr}^{-1}} \right)^{1/2} \left(\frac{\dot{M}_{OB}}{10^{-6} M_\odot \text{ yr}^{-1}} \right)^{3/2} \left(\frac{V_{WR}^*}{10^3 \text{ km s}^{-1}} \right)^{1/2} \left(\frac{V_{OB}^*}{10^3 \text{ km s}^{-1}} \right)^{-3/2} \left(\frac{D}{10^{13} \text{ cm}} \right)^{-1} \quad (4.7)$$

$$L_X = L_{ext} + L_{int} \quad (4.8)$$

where V_{WR}^* and V_{OB}^* denote the wind velocity of WR and O-star, respectively at the WCR. Here, the predicted X-ray luminosity belongs to $\sim 14\text{--}152 \times 10^{35} \text{ erg s}^{-1}$ range, which is one to two orders of magnitude larger than typically seen for CWBs and the value determined here for WR 121a. However, the value of L_X^{int} for WR 121a derived from observations is subjected to uncertainties in the distance to the source and the hydrogen column density used to correct for X-ray absorption. The imprecise estimation of mass-loss rate rates, as well as clumped winds, might also be possible explanations for this discrepancy (Cherepashchuk, 1990).

4.6 Conclusions

A deep exploration of the X-ray emission from a WR star WR 121a using the long-term archival data is presented in this paper. WR 121a is found to be a periodic

4. WR 121A: A SHORT PERIOD COLLIDING WIND BINARY

variable in X-rays with a period of ~ 4.1 d, where the significant amount of X-rays are originating from the hot plasma heated by the colliding winds. This periodic variation is also found both in soft and hard energy bands where X-ray flux was increased by $\sim 53\%$ of minimum flux in hard X-rays. These variations are explained due to the eclipsing of WCR by the companion star in WR 121a system. The two binary components of WR 121a could not be resolved by *Chandra* and it was detected as a point-like source close to the position of W43 #1b. The X-ray spectra of WR 121a below 2.5 keV is heavily absorbed and have been well modelled with two-temperature plasma emission models with the temperature of cool and hot components as 0.98 ± 0.34 and 3.55 ± 0.69 keV, respectively. The stellar winds from binary components of WR 121a interact at sub-terminal speeds and the wind collision is found to be radiative. The derived values of opening angles for WR 121a suggest that the processes like radiative braking and inhibition must be significantly affecting the wind collision if the companion is an early O-type star. We encourage more multi-wavelength observations of WR 121a to identify the accurate spectral types of the binary components and to explain the dynamics of winds more precisely in its WCR.

Chapter 5

QUEST FOR THE UPCOMING PERIASTRON PASSAGE IN WR 125

5.1 Overview

A direct consequence of the enhanced surface metallicity of WC stars is the production of strong and dense stellar winds. Several decades ago, it appeared that some of these WC stars displayed a significant infrared excess, attributed to the presence of circumstellar dust (Allen et al., 1972). The exact circumstances for the formation of dust in WC star environments are still far from being completely elucidated. Many WCs often undergo variable dust production, some periodic, and others random. The class of episodic dust makers (EDMs) shows recurrent infrared bursts that fade away with time (Williams, 1995, 2008). The standard interpretation framework for EDMs is dust formation in the WCR of a binary systems made of a WC star and another massive companion. The episodic nature of the dust emission is reasonably well explained as a result of colliding stellar winds in a wide, massive binary system with highly elliptical orbit (Williams et al., 1990).

It is well established that physics of WCRs can also be investigated at other wavelengths. Massive binary systems produce thermal X-ray emission that originates from the interaction region of the winds of the massive binary components, in addition to some contributions from the individual stellar winds (Cherepashchuk, 1976; Pittard & Parkin, 2010; Prilutskii & Usov, 1976; Stevens et al., 1992). As it is noticed in case of WR 25, the X-ray contribution from the WCR is expected to vary periodically, especially if the stars move in an elliptic orbit. The binary separation, D , varies so that the WCR moves periodically in and out of deeper regions of the

The results of this chapter are under review in *The Astronomical Journal* (Arora et al., 2021, *AJ*, under review).

stellar winds. In particular, in the case of adiabatic shocks, the X-ray emission from the WCR is expected to vary as $1/D$, i.e. stronger emission close to periastron (Stevens et al., 1992). In addition, depending on the inclination of the system, our line of sight to the WCR passes through varying amounts of stellar wind as the orbit progresses, causing variations in the photoelectric absorption by the stellar wind material. Given the high density of WC star winds, the emission measure of the X-ray emitting plasma is expected to be rather high, such as in the case of WR 140 (e.g. Williams et al. 1990).

Massive binaries are also radio emitters. Besides the steady thermal free-free emission produced by individual stellar winds (e.g. Panagia & Felli 1975; Wright & Barlow 1975), in a binary system the WCR is likely to produce some non-thermal, synchrotron radiation. The latter component is expected to vary as a function of the orbital phase (especially in eccentric orbits) and is characterized by a negative spectral index j , defined as $S_\nu \propto \nu^j$ (recall from Section 1.3.1). A requirement is the existence of a population of relativistic electrons, hence the so-called class of PACWBs, (De Becker & Raucq, 2013). The intrinsic synchrotron emission is expected to peak close to the periastron, even though free-free absorption (FFA) will modulate the measured flux densities depending on the orientation of the line-of-sight in the system. The brightness of the synchrotron emission arises downstream of a series of energy conversion processes, including energy injection in particle acceleration, that is fed by the kinetic power of the stellar winds. This criterion is especially in favor of CWBs including a WC component, characterized by the strongest stellar winds (De Becker et al. 2017; De Becker & Raucq 2013). Very good examples are once again WR 140 (Dougherty et al. 2005; Williams et al. 1990), or more recently the extreme Apep system made of two WR stars (Marcote et al., 2021).

It is thus clear that valuable indicators of binarity can be investigated across the electromagnetic spectrum, especially when a WC-type star is involved. These indicators are notably relevant to establish the occurrence of successive periastron passages, and therefore achieve the first determination of their orbital period. The period determination through standard methods (spectroscopy or astrometry) is highly time consuming, and especially proves difficult for orbital periods of several years or a few decades. Searching for indications of orbital modulations through processes related to the WCR on the basis of archived and new data is therefore quite valuable to characterize these objects. In return, the knowledge of their orbital period is crucial to establish future observation strategies and determine the physical dimensions of these systems, which is required for further modeling of such systems.

The present study is dedicated to one of the most studied, still poorly characterized WC system WR 125. This is expected to be a long period WC + O system with unknown orbital parameters. This interesting system already benefited of plenty of observations and would greatly benefit of a multiwavelength investigation to complete the already existing data. The objective of this study is to provide updated constraints on the occurrence of its upcoming periastron passage, and to check how updated time series may help to clarify its orbital period. To this aim, we have observed WR 125 using SXT onboard *AstroSat* and TIRCAM2 mounted at the focal plane of the 3.6 m DOT. We have also used archival *Swift* and *XMM–Newton* X-ray data. Mid-infrared investigations were performed using archival data from NEOWISE-R survey. In addition, we also considered radio measurements published over the past decades in our discussion. Details of these observations are provided in Chapter 2 of this thesis.

This chapter is organized as follows. Section 5.2 describes the target and summarizes the outcome of previous works relevant for our purpose. The X-ray light curve and spectral analysis are detailed in Section 5.3. Finally, Section 5.4 includes the discussion of our main results, while conclusions are drawn in Section 5.5.

5.2 The colliding wind binary WR 125

WR 125 (MR 93) is a galactic WR binary system classified as WC7ed+O9 III with period >6600 d (van der Hucht, 2001). It undergoes mass loss at $6 \times 10^{-5} M_{\odot} \text{ yr}^{-1}$ with a terminal velocity of 2900 km s^{-1} (Williams et al., 1992).

Infrared photometry during 1981-91 showed a 10-fold rise in 3-4 μm flux during 1990-91 (Williams et al., 1992). This was interpreted in terms of condensation of dust in its wind close to the periastron passage, *i.e.*, when the density of the shocked gas in the WCR is the highest. Further characterization of this IR excess revealed that it started in 1990 and lasted for ~ 3 yrs being maximum during 1992-93. In addition, absorption lines were seen in its spectrum supporting its CWB status (Williams et al., 1994). No recurrence of the 1990-93 dust formation episode was noticed till 2014 in 2MASS, *Spitzer* GLIMPSE, and *WISE* surveys according to Williams (2014). Few hints regarding infrared brightening in the beginning of 2018 have been provided by Williams (2019), suggesting an orbital period of about 28.3 yr.

The first X-ray observation of WR 125 was performed by *Einstein* observatory in 1981. It was found to be a bright X-ray source with an ISM corrected X-ray

luminosity of $1.4 \times 10^{33} \text{ ergs}^{-1}$ in 0.2–4.0 keV energy range (Pollock, 1987). *ROSAT* also made a pointed observation of WR 125 during 2141 s exposure time where it was only marginally detected with an X-ray luminosity of $\sim 9.1 \times 10^{32} \text{ erg s}^{-1}$ in 0.2–2.4 keV energy band (Pollock et al., 1995). However, no variation in the X-ray emission from four observations in 2016–17 was found by Midooka et al. (2019). We note that, at higher energies, Werner et al. (2013) searched gamma-ray emission from WR 125 using 24 months *Fermi-LAT* data. Gamma-ray emission was not detected in the analyzed data-set but could only provide upper limits to the high energy photon flux.

In the radio domain, WR 125 is a strong, variable source which showed signatures of both thermal and non-thermal emission with a spectral index varying from -0.5 to +0.7 during its observation from 1982 to 1989 (Abbott et al. 1986; Williams et al. 1992). The non-thermal radio emission from WR 125 faded between 1985 and 1988, very likely due to a more pronounced free-free absorption as the system approached periastron passage shortly before its dust-formation episode occurring in 1991. Cappa et al. (2004) reported on an additional measurement obtained in 2001 but at one wavelength only, therefore preventing any conclusion on nature (thermal or non-thermal) of the radio emission at that epoch.

X-ray data of WR 125 obtained with *AstroSat*, *Swift*, and *XMM-Newton* from 2016 November to 2020 November have been analyzed. Table 2.2 presents the detailed log of these data sets, covering a total of 21 epochs of X-ray observations including the *Einstein* and *ROSAT* data (see section 5.3). For *AstroSat* data, the total count rate in the source region is ~ 1.5 times larger than the background count rate for both the data-sets. Therefore, the count rate obtained for WR 125 has been considered as an upper limit for both the available observation IDs. The X-ray observations of WR 125 from *Swift* and *XMM-Newton* which were investigated by Midooka et al. (2019) have also been considered in the present study. The processing of those X-ray data sets has been performed again in order to maintain the homogeneity and application of the latest calibration. The *XMM-Newton*-PN image of WR 125 in 0.2–15.0 keV energy range is shown in Figure 5.1.

5.3 X-ray spectral and light curve analysis

In order to obtain the best-fit model which explains the X-ray spectrum of WR 125, we have made use of *XMM-Newton* data as the X-ray spectra from EPIC instruments have better photon statistics than data from other observatories. Therefore,

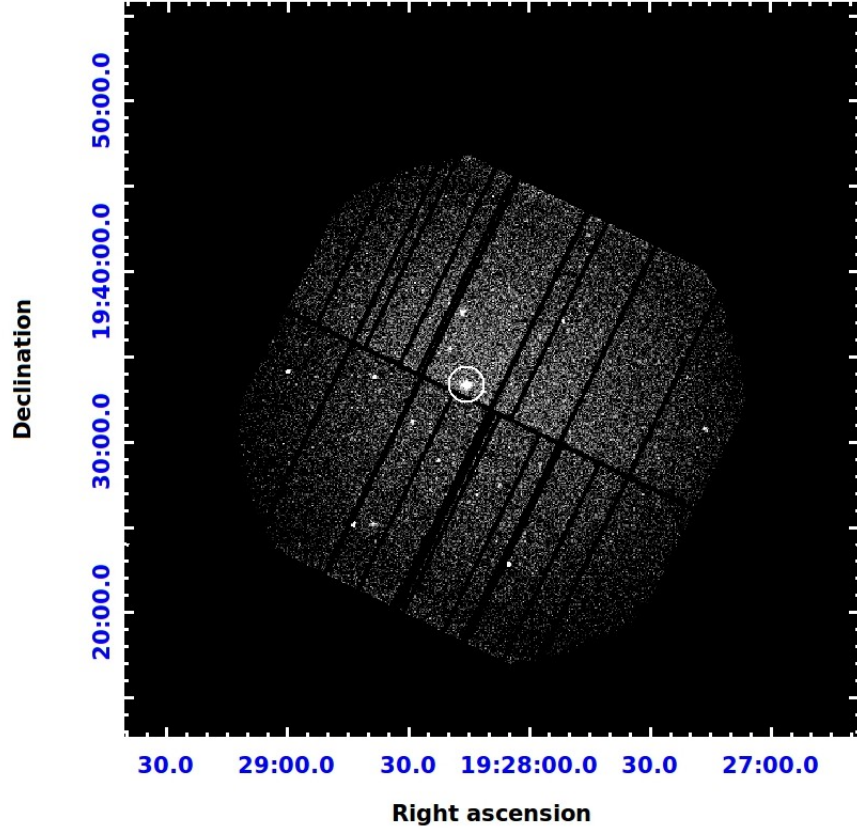


Figure 5.1: *XMM-Newton*–PN image from the observation ID 0794581101 in 0.2–15.0 keV energy band. The position of WR 125 has been highlighted with a circle.

we initially decided to jointly fit the MOS1, MOS2, and PN spectra of WR 125 in 0.5–10.0 keV energy range using the thermal plasma model “APEC”. Such an optically thin thermal emission model is adequate to reproduce the soft X-ray emission from plasmas heated in CWBs (see e.g. Chapters 3, 4, De Becker 2015; Midooka et al. 2019). The composite model used for spectral fitting has a form similar to that for WR 121a. The interstellar and the circumstellar wind absorption effects were taken into consideration by the model components PHABS(ISM) and PHABS(LOCAL), respectively. The value of N_H^{ISM} , which is the parameter corresponding to the model component PHABS(ISM), was frozen at $0.94 \times 10^{22} \text{ cm}^{-2}$ (Midooka et al., 2019). This value is similar to the galactic N_H along the direction of WR 125. The other parameters were kept free in the spectral fitting, including the tied abundances (Z) for both components of APEC model. The best-fit parameters obtained separately for the two observation IDs of *XMM-Newton* have been given in Table 5.1 (referred

to as Model 1a and Model 1b) while the X-ray spectra of WR 125 with the best-fit model are shown in Figure 5.2.

Since the photon counts are very less in the *Swift* spectra, we decided to fit this by fixing the model parameters to the values as obtained for *XMM-Newton* spectra. The spectrum from each observation ID was fitted individually. For the low count *Swift* spectra, Cash-statistic was used with the spectral binning such that each bin contains at least one count. The *Swift* data obtained closer to the *XMM-Newton* observation ID 0794581101 was fitted with Model 1a. However, the spectra observed in 2019 and later were fitted with Model 1b obtained for *XMM-Newton* ID 0853980101. In spite of this, four *Swift* spectra could not be fitted well even with the fixed parameters of this model due to very poor net counts. For that, we have made use of the X-ray analysis tool WebPIMMS to convert their count rate to flux. For this, we have fitted the *XMM-Newton* spectra with the single temperature model as PHABS*APEC as well, to get an average value of N_H^{total} and temperature to be used in WebPIMMS. The values of parameters obtained using this model are mentioned in Table 5.2 and are referred to as Model 2a and 2b for the *XMM-Newton* IDs 0794581101 and 0853980101, respectively. Since the *Swift* spectra which could not be fitted well with two temperature plasma components were observed in 2020, therefore, those were fitted with Model 2b.

Table 5.1: Best-fit parameters obtained from joint fitting of *XMM-Newton*–EPIC spectra of WR 125 using the model PHABS*PHABS(APEC+APEC).

Parameter	XMM1 ^a (Model 1a)	XMM2 ^b (Model 1b)
N_H^{ism} (10^{22} cm ⁻²)	0.94 [†]	0.94 [†]
N_H^{local} (10^{22} cm ⁻²)	0.71 ^{+0.14} _{-0.15}	1.99 ^{+0.78} _{-0.49}
kT_1 (keV)	0.98 ^{+0.14} _{-0.14}	0.11 ^{+0.06} _{-0.03}
Abundances (Z_{\odot})	0.56 ^{+0.53} _{-0.29}	0.17 ^{+0.12} _{-0.11}
kT_2 (keV)	>2.93	3.44 ^{+0.91} _{-0.57}
χ^2_{ν} (dof)	0.99 (123)	0.99 (116)

Notes: (a) XMM1: ID–0794581101 (b) XMM2: ID–0853980101

[†]Reference: [Midooka et al. \(2019\)](#)

Here, N_H^{ism} and N_H^{local} refer to the galactic and circumstellar H-column density. kT_1 and kT_2 represent the temperatures of the two components of the plasma model. χ^2_{ν} is the reduced χ^2 and *dof* is the number of degrees of freedom. Errors quoted on different parameters refer to the 90% confidence level.

Further, *Einstein* also observed WR 125 with a count rate of 0.0122 ± 0.0028 counts/s in the 0.4–4.0 keV energy band on 1981 April 9 using IPC ([Midooka et al.](#),

5.3 X-ray spectral and light curve analysis

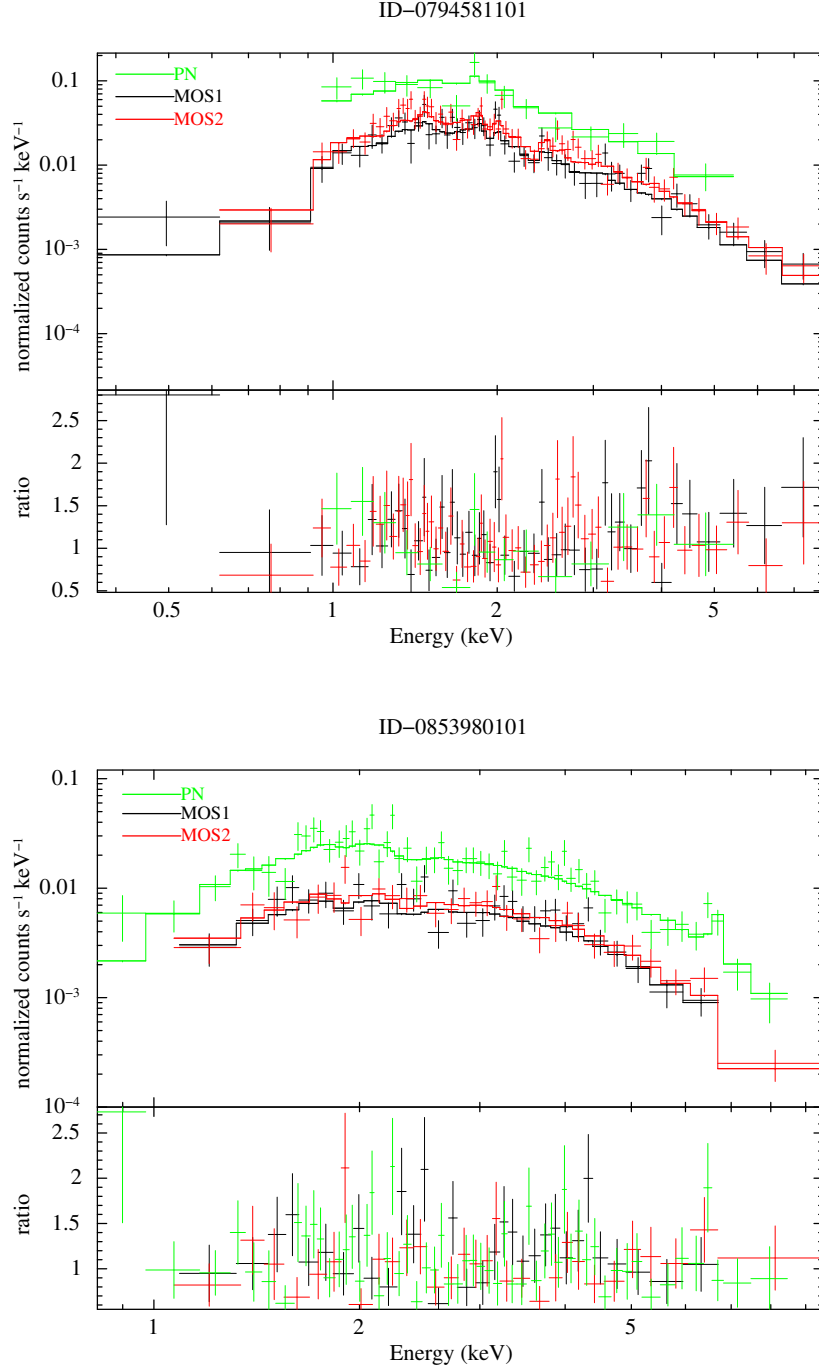


Figure 5.2: *XMM-Newton*–EPIC spectra of WR 125 from the observation IDs (a) 0794581101 (*top*) and (b) 0853980101 (*bottom*). The EPIC spectra have been fitted jointly using the model $\text{PHABS}^*\text{PHABS}(\text{APEC}+\text{APEC})$ with parameters given in Table 5.1 for both the IDs. The lower panels show the ratio of the data to the model.

5. QUEST FOR THE UPCOMING PERIASTRON PASSAGE IN WR 125

Table 5.2: Best-fit parameters obtained from joint fitting of *XMM-Newton*–EPIC spectra of WR 125 using the model PHABS*APEC.

Parameter	XMM1 ^a (Model 2a)	XMM2 ^b (Model 2b)
N_H^{total} (10^{22} cm ⁻²)	$0.97^{+0.14}_{-0.13}$	$2.26^{+0.28}_{-0.26}$
kT (keV)	$2.57^{+0.47}_{-0.33}$	$4.35^{+1.12}_{-0.73}$
Abundances (Z_{\odot})	$0.23^{+0.22}_{-0.17}$	$0.16^{+0.13}_{-0.13}$
$norm$ (10^{-3} cm ⁻⁵)	$1.63^{+0.27}_{-0.24}$	$0.877^{+0.16}_{-0.13}$
χ^2_{ν} (dof)	1.20 (125)	1.08 (118)

Notes: (a) XMM1: ID–0794581101 (b) XMM2: ID–0853980101

2019). However, *ROSAT* only marginally detected WR 125 by making use of PSPC in 0.1-2.0 keV energy range on 1991 October 28. The upper limit of the WR 125 count rate by *ROSAT*-PSPC is 5.0×10^{-3} counts/s (Midooka et al., 2019). Also, the *AstroSat*-SXT spectra of WR 125 were also very poor to be fitted properly in XSPEC. Therefore, the *Einstein*-IPC, *ROSAT*-PSPC, and *AstroSat*-SXT count rates were converted to flux using Model 2a with WebPIMMS only. Finally, the observed X-ray flux (F^{obs}) and the ISM corrected X-ray flux (F^{ism}) of WR 125 in three energy bands viz. broad (0.5-10.0 keV, F_B), soft (0.5-2.0 keV, F_S) and hard (2.0-10.0 keV, F_H) have been estimated for each of the available spectra and are plotted with date of observation in Figure 5.3. Table 5.3 gives the details of the spectral fitting of each of the spectra and also includes the spectral fitting parameters as well as the flux values.

The background subtracted X-ray light curve of WR 125 as observed by *AstroSat*-SXT, *Swift*-XRT and *XMM-Newton*-PN in the 0.3-10.0 keV energy band is shown in Figure 5.4. The average count rate of an individual observation was taken as a single data point in the light curve as the light curve of individual observations was non-variable. Here, the *AstroSat*-SXT count rate in the 0.5-7.0 keV band has been converted to that of *Swift*-XRT in the 0.3-10.0 keV band using WebPIMMS with Model 2a. However, *XMM-Newton*-PN count rate from observation ID 0794581101 and 0853980101 was converted to *Swift*-XRT using Model 2a and 2b, respectively. As seen in the light curve, the X-ray flux switches from a higher emission state in 2017 to a lower emission state in 2020. The ratio of the maximum to the minimum count rate was found to be 15.33 ± 11.70 .

5.3 X-ray spectral and light curve analysis

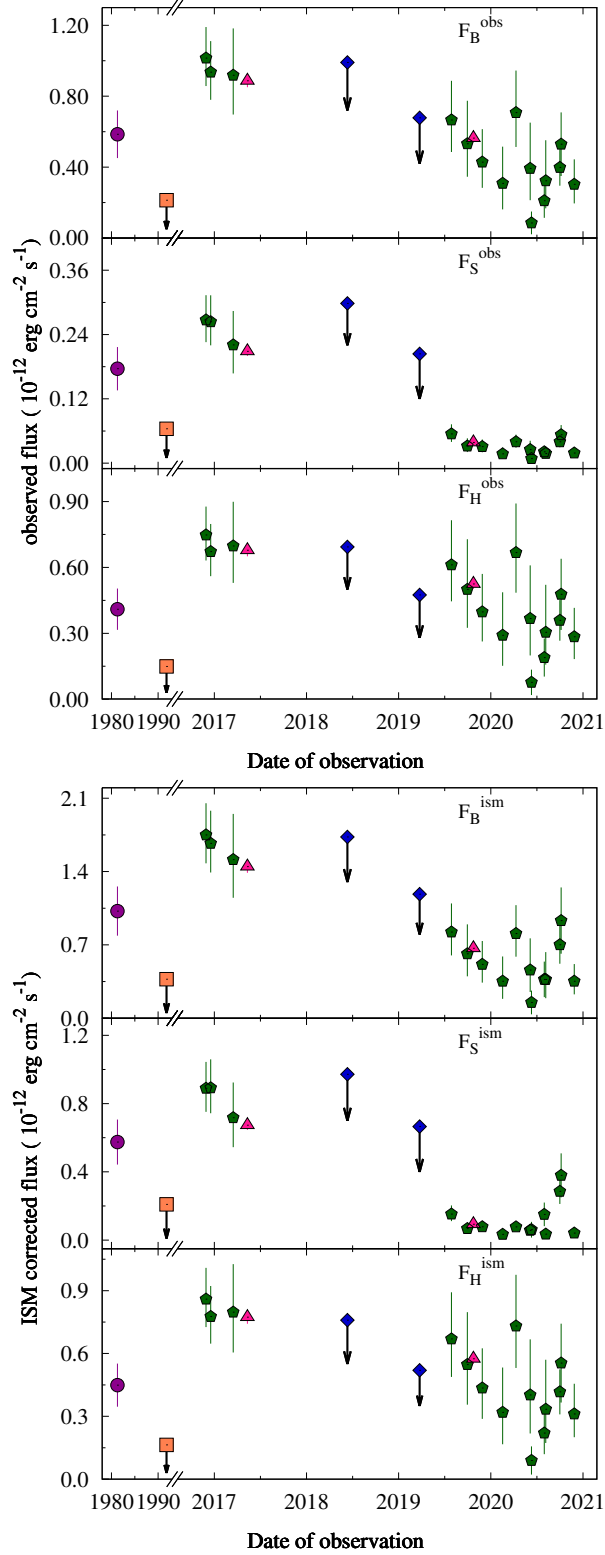


Figure 5.3: Observed (F^{obs} , top) and ISM corrected (F^{ism} , bottom) flux from WR 125 *viz.* F_B , F_S , and F_H in broad (0.5-10.0 keV), soft (0.5-2.0 keV), and hard (2.0-10.0 keV) energy bands, respectively. The purple circle marks the *Einstein*–IPC data point, the orange square is the *ROSAT*–PSPC flux, green pentagons are the *Swift*–XRT flux measurements while pink triangles correspond to the *XMM-Newton*–EPIC observations and blue diamonds show the *Astrosat*–SXT flux values.

Table 5.3: Best-fit parameters obtained from spectral fitting of WR 125 using different models as observed from *AstroSat*, *Einstein*, *Rosat*, *Swift*, and *XMM-Newton*.

Satellite/ Detector	Obs. ID/ Sequence No.	Fitting Model [†]	$norm_1$ (10^{-3} cm^{-5})	$norm_2$	$\chi^2(dof)$	F_B^{obs}	F_S^{obs}	F_H^{obs}	F_B^{ism}	F_S^{ism}	F_H^{ism}
						(10 ⁻¹² erg cm ⁻² s ⁻¹)					
<i>Einstein</i> /IPC	8680 [†]	2a	-	-	-	0.59 ^{+0.13} _{-0.13}	0.18 ^{+0.04} _{-0.04}	0.41 ^{+0.09} _{-0.09}	1.02 ^{+0.24} _{-0.23}	0.57 ^{+0.13} _{-0.13}	0.45 ^{+0.10} _{-0.10}
<i>ROSAT</i> /PSPC	RP170260N00 [†]	2a	-	-	-	< 0.21	< 0.06	< 0.15	< 0.37	< 0.21	< 0.16
<i>Swift</i> /XRT	00034826001	1a	2.42 ^{+0.96} _{-0.90}	0.96 ^{+0.56} _{-0.48}	0.91 (85)	1.02 ^{+0.18} _{-0.16}	0.27 ^{+0.05} _{-0.05}	0.75 ^{+0.13} _{-0.12}	1.75 ^{+0.30} _{-0.27}	0.89 ^{+0.15} _{-0.14}	0.86 ^{+0.15} _{-0.13}
<i>Swift</i> /XRT	00034826002	1a	2.54 ^{+1.21} _{-1.14}	0.79 ^{+0.76} _{-0.66}	0.81 (73)	0.94 ^{+0.18} _{-0.16}	0.26 ^{+0.05} _{-0.04}	0.67 ^{+0.13} _{-0.11}	1.67 ^{+0.31} _{-0.28}	0.89 ^{+0.15} _{-0.15}	0.78 ^{+0.13} _{-0.13}
<i>Swift</i> /XRT	00034826003	1a	1.82 ^{+1.48} _{-1.38}	0.98 ^{+0.99} _{-0.77}	0.88 (34)	0.92 ^{+0.26} _{-0.22}	0.22 ^{+0.06} _{-0.05}	0.69 ^{+0.20} _{-0.17}	1.51 ^{+0.44} _{-0.37}	0.72 ^{+0.21} _{-0.17}	0.79 ^{+0.23} _{-0.19}
<i>XMM-Newton</i> /EPIC	0794581101	1a	1.67 ^{+0.19} _{-0.19}	0.97 ^{+0.11} _{-0.11}	0.99 (127)	0.89 ^{+0.04} _{-0.04}	0.21 ^{+0.01} _{-0.01}	0.68 ^{+0.03} _{-0.03}	1.45 ^{+0.06} _{-0.06}	0.67 ^{+0.03} _{-0.03}	0.77 ^{+0.03} _{-0.03}
<i>Astrosat</i> /SXT	9000002152 [†]	2a	-	-	-	< 0.99	< 0.29	< 0.69	< 1.73	< 0.97	< 0.76
<i>Astrosat</i> /SXT	9000002816 [†]	2a	-	-	-	< 0.68	< 0.20	< 0.47	< 1.18	< 0.67	< 0.52
<i>Swift</i> /XRT	00034826004	1b	< 29.79 × 10 ³	1.34 ^{+0.47} _{-0.38}	1.10 (25)	0.67 ^{+0.22} _{-0.18}	0.05 ^{+0.02} _{-0.01}	0.61 ^{+0.20} _{-0.17}	0.82 ^{+0.27} _{-0.22}	0.15 ^{+0.05} _{-0.04}	0.67 ^{+0.22} _{-0.18}
<i>Swift</i> /XRT	00034826005	1b	< 09.54 × 10 ³	1.09 ^{+0.52} _{-0.39}	0.89 (15)	0.53 ^{+0.24} _{-0.19}	0.03 ^{+0.01} _{-0.01}	0.49 ^{+0.18} _{-0.18}	0.61 ^{+0.22} _{-0.22}	0.07 ^{+0.02} _{-0.02}	0.55 ^{+0.25} _{-0.19}
<i>XMM-Newton</i> /EPIC	0853980101	1b	< 04.09 × 10 ³	1.15 ^{+0.05} _{-0.05}	0.96 (120)	0.56 ^{+0.02} _{-0.02}	0.04 ^{+0.001} _{-0.001}	0.52 ^{+0.02} _{-0.02}	0.67 ^{+0.03} _{-0.03}	0.09 ^{+0.003} _{-0.003}	0.57 ^{+0.02} _{-0.02}
<i>Swift</i> /XRT	00034826007	1b	< 12.03 × 10 ³	0.87 ^{+0.42} _{-0.32}	0.22 (17)	0.43 ^{+0.16} _{-0.14}	0.03 ^{+0.01} _{-0.01}	0.39 ^{+0.17} _{-0.13}	0.51 ^{+0.22} _{-0.17}	0.08 ^{+0.03} _{-0.03}	0.44 ^{+0.19} _{-0.15}
<i>Swift</i> /XRT	00034826008	1b	< 10.48 × 10 ³	0.64 ^{+0.43} _{-0.30}	0.68 (07)	0.31 ^{+0.21} _{-0.15}	0.02 ^{+0.01} _{-0.01}	0.29 ^{+0.19} _{-0.14}	0.35 ^{+0.24} _{-0.17}	0.03 ^{+0.02} _{-0.02}	0.32 ^{+0.21} _{-0.15}
<i>Swift</i> /XRT	00034826009	1b	< 03.79 × 10 ³	1.45 ^{+0.49} _{-0.39}	1.86 (23)	0.71 ^{+0.24} _{-0.19}	0.04 ^{+0.01} _{-0.01}	0.67 ^{+0.22} _{-0.22}	0.81 ^{+0.27} _{-0.22}	0.08 ^{+0.03} _{-0.02}	0.73 ^{+0.24} _{-0.20}
<i>Swift</i> /XRT	00034826010	1b	< 11.43 × 10 ³	0.80 ^{+0.58} _{-0.39}	0.61 (07)	0.39 ^{+0.26} _{-0.18}	0.03 ^{+0.02} _{-0.01}	0.37 ^{+0.24} _{-0.17}	0.46 ^{+0.36} _{-0.21}	0.06 ^{+0.04} _{-0.03}	0.40 ^{+0.27} _{-0.18}
<i>Swift</i> /XRT	00034826011 [†]	2b	-	-	-	0.09 ^{+0.06} _{-0.06}	0.008 ^{+0.006} _{-0.006}	0.08 ^{+0.06} _{-0.06}	0.15 ^{+0.11} _{-0.11}	0.06 ^{+0.05} _{-0.05}	0.09 ^{+0.07} _{-0.07}
<i>Swift</i> /XRT	00034826012 [†]	2b	-	-	-	0.21 ^{+0.09} _{-0.09}	0.02 ^{+0.01} _{-0.01}	0.19 ^{+0.09} _{-0.09}	0.37 ^{+0.17} _{-0.17}	0.15 ^{+0.07} _{-0.07}	0.22 ^{+0.10} _{-0.10}
<i>Swift</i> /XRT	00034826013	1b	< 17.20 × 10 ³	0.67 ^{+0.47} _{-0.34}	1.34 (06)	0.32 ^{+0.23} _{-0.16}	0.02 ^{+0.01} _{-0.01}	0.30 ^{+0.22} _{-0.30}	0.37 ^{+0.26} _{-0.37}	0.04 ^{+0.03} _{-0.03}	0.33 ^{+0.24} _{-0.33}
<i>Swift</i> /XRT	00034826014 [†]	2b	-	-	-	0.39 ^{+0.10} _{-0.10}	0.04 ^{+0.01} _{-0.01}	0.36 ^{+0.09} _{-0.36}	0.70 ^{+0.18} _{-0.18}	0.29 ^{+0.07} _{-0.07}	0.42 ^{+0.11} _{-0.11}
<i>Swift</i> /XRT	00034826015 [†]	2b	-	-	-	0.53 ^{60.18} _{-0.18}	0.05 ^{+0.02} _{-0.02}	0.48 ^{+0.16} _{-0.48}	0.93 ^{+0.32} _{-0.93}	0.38 ^{+0.13} _{-0.13}	0.55 ^{+0.19} _{-0.55}
<i>Swift</i> /XRT	00034826016	1b	< 20.57 × 10 ³	0.62 ^{+0.29} _{-0.23}	2.77 (16)	0.30 ^{+0.14} _{-0.11}	0.02 ^{+0.01} _{-0.01}	0.28 ^{+0.13} _{-0.10}	0.35 ^{+0.16} _{-0.13}	0.04 ^{+0.02} _{-0.01}	0.31 ^{+0.14} _{-0.11}

Notes. Here, $norm_1$ and $norm_2$ are the normalization constants for two temperature components. χ^2_ν is the reduced χ^2 and dof is the number of degrees of freedom. F_B^{ism} , F_S^{ism} , and F_H^{ism} are the ISM corrected fluxes while F_B^{obs} , F_S^{obs} , and F_H^{obs} are the observed X-ray fluxes of WR 125 in broad, soft, and hard energy bands, respectively. Errors quoted on different parameters refer to the 90% confidence level.

[†] The online X-ray analysis tool WebPIMMS has been used to convert the average count rate to fluxes in different energy bands with the specified fitting model.

[‡] See Tables 5.1 and 5.2.

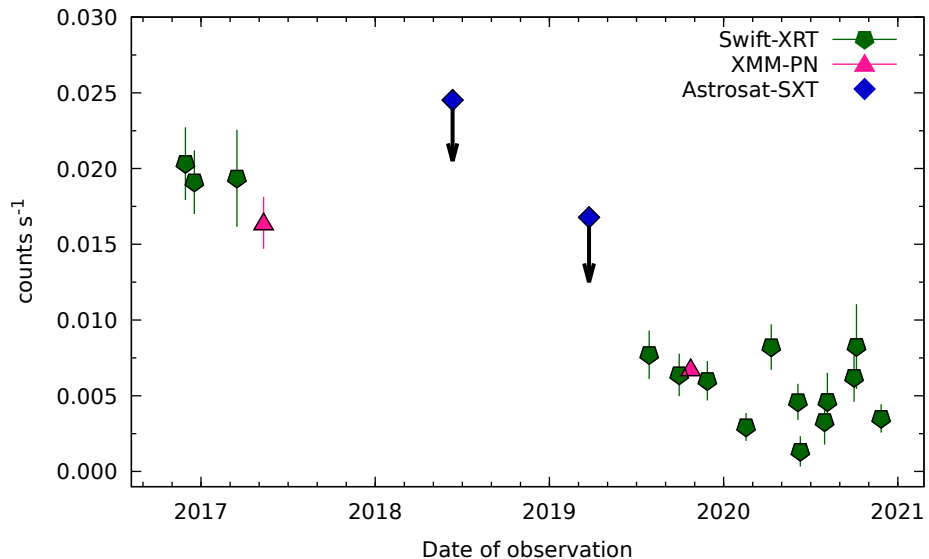


Figure 5.4: X-ray light curve of WR 125 in 0.3–10.0 keV energy band as observed by *Swift*–XRT (green pentagons), *XMM-Newton*–PN (pink triangles), and *Astrosat*–SXT (blue diamonds). The PN and SXT count rate has been converted to that of the *Swift*–XRT using WebPIMMS.

5.4 Discussion

5.4.1 Dust emission

The dust emission is efficiently revealed at wavelengths longer than J- and H-bands (Williams et al., 1992, 1994). Therefore, a comparison of K -band magnitude of WR 125 obtained from TIRCAM2 in present the study has been made with the estimations provided in literature as well as in the 2MASS survey in Figure 5.5. It is clear that during the episode of dust formation in the early 1990’s, the K -magnitude varied from 8.26 (continuum level) to 7.42 (during outburst) over the years \sim 1992–1993 (Williams et al., 1994). Additionally, the K -band magnitude obtained from this study shows enhanced emission indicating that the recent measurements were also made during another episode of dust formation.

Two time scales deserve to be considered when investigating episodic dust production episodes: one is the time required for the dimming of the IR emission to the pre-outburst level and the other is the time interval between two such consecutive incidences. The dimming of the IR emission is caused by the fading of the dust when being taken away by the stellar wind and is not replenished further. This

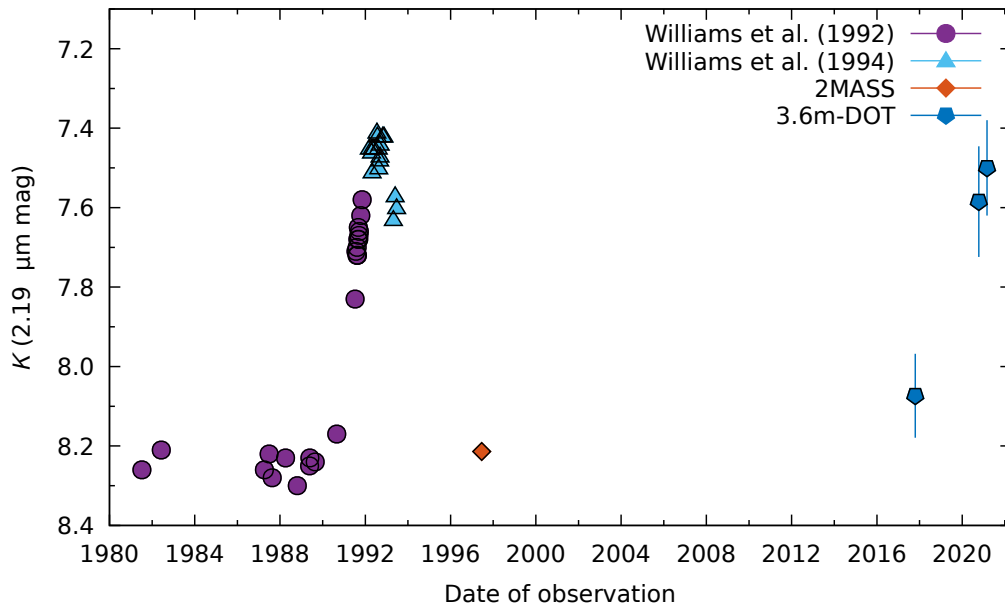


Figure 5.5: K -band light curve of WR 125 by combining data from the literature, 2MASS survey and the present study. The accuracy of data from Williams et al. (1992, 1994) is 0.05 mag.

duration depends upon the terminal velocity of the winds and the amplitude of the dust emission. On the other side, the orbital period of the binary system governs the interval between the two episodes. As the previous dust formation episode was associated to the time of periastron passage of this eccentric CWB system, the enhanced IR emission from the source during our new observations suggests that the next periastron passage of WR 125 has been captured. The previous episode of enhanced emission by dust followed by fading lasted for about 3-4 yrs which is also reflected in the present three epochs of IR observations performed with a time interval of ~ 3 yrs. Due to the absence of data in between the latest epochs, the time sampling of this outburst is rather poor. Our assertions are supported by Williams (2019) which also gave an indication of IR brightening of WR 125 in the beginning of 2018 using NEOWISE-R observations. We have also retrieved NEOWISE-R Single Exposure Source observations of WR 125 made in 2019 from NASA/IPAC Infrared Science Archive (IRSA¹). A comparison of $W1$ ($3.4 \mu\text{m}$) and $W2$ ($4.6 \mu\text{m}$) bands magnitudes given in Williams (2019) and those obtained in 2019 are shown in Figure 5.6. It is clear that the source showed signatures of IR brightening in 2018 which further enhanced in the year 2019.

¹<https://irsa.ipac.caltech.edu/>

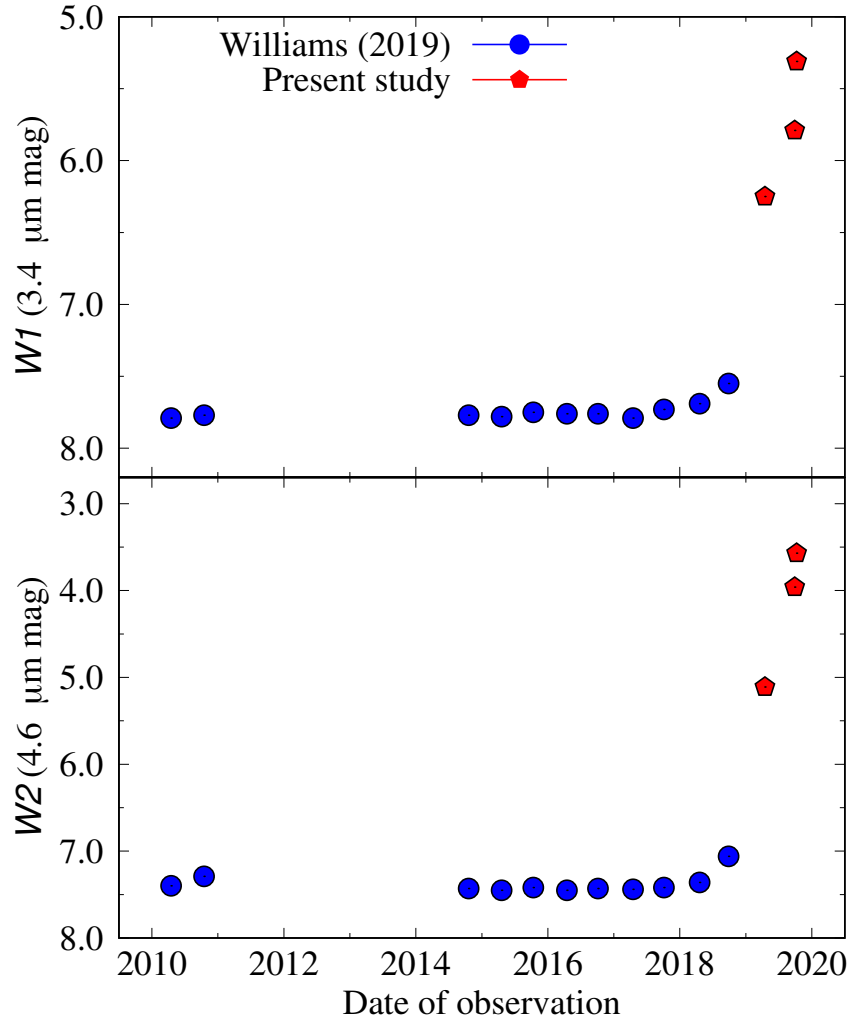


Figure 5.6: NEOWISE-R $W1$ and $W2$ bands light curve of WR 125 by combining data from Williams (2019) and the recent observations.

In summary,

- under the reasonable assumption that dust production is enhanced at periastron, the recent rise of the infrared emission very likely indicates WR 125 underwent periastron passage close to 2019-2021.
- the previous infrared peak occurred in the early 1990's. A time interval of about 28-29 yrs can thus be considered as a candidate for the orbital period. However, we caution that the lack of infrared data close to 2004 doesn't allow us to completely rule out an orbit twice as short, i.e. 14-15 yrs.

5.4.2 X-ray emission

The main features arising from the long term X-ray monitoring are summarized below:

- the observed as well as ISM corrected X-ray flux from WR 125 present long term variations.
- the X-ray emission switches from some kind of high state in 2016-2017, to a low state at the end of 2019 and in 2020.
- the low state is clearly noticed in the soft band, but the hard band is much less conclusive. In addition, best-fit models for *XMM-Newton* data show a stronger absorption column N_H^{local} during the low state at the end of 2019, as compared to the high state in 2017.
- if one relies on the *ROSAT* measurement in 1991 showing a quite low emission state, it suggests a recurrence in the occurrence of the low emission state.
- a brief rise of the X-ray emission is measured in the second half of 2020, followed by a drop of the emission down to the low state plateau. The current time series thus does not reveal any trend leading to a return to a high state as measured in 2016-2017.

In their recent study, [Midooka et al. \(2019\)](#) speculate on the occurrence of the minimum emission close to periastron passage. A minimum X-ray emission is tentatively attributed to a more pronounced absorption of X-rays produced in the WCR by the dense and thick WC wind. This interpretation may be compatible with the rather broad low state essentially measured in the soft band, where photoelectric absorption is active. Such an enhanced absorption is expected to happen close to periastron, where the WCR is more deeply surrounded by the WC wind material. We note that the expected dependence of the 1/D trend for adiabatic colliding winds is not revealed in our data set. This would require high quality data over a significant part of the orbit, especially in a part of the orbit that is not that much modulated by a strong absorption. In other words, during the low state, the effect of absorption completely dominates the effect of the reduced separation on the intrinsic X-ray emission in the WCR. Such a situation is similar to what has been observed for WR 140 ([Williams et al., 1990](#)). The start and duration of a low state due to enhanced absorption by the wind depend on the exact geometric configuration of the system (separation, inclination, ...). As a result, even though the low state is likely related

to periastron, the exact time of periastron passage cannot be determined with accuracy, given the available information on the system. We also clarify that in such a long period system, we can certainly reject the hypothesis of an eclipse of the WCR by one of the stars as observed in the short period massive binary WR 121a (Arora & Pandey, 2020).

Based on the features summarized above, one may speculate on the recurrence of the minimum emission. Given the duration of the recent low state, it is not possible to provide any accurate estimate of the time interval between two minima. The order of magnitude is 28-29 yrs. In a scenario where these low states are associated to periastron passages, this time interval is a candidate for the orbital period of WR 125. However, we caution that the time sampling of the X-ray emission over such a long period is very sparse. On the basis of the available X-ray data alone, one cannot reject the idea that such a low state event happened just in between, reducing the estimate of the orbital period by a factor 2.

5.4.3 Synchrotron radio emission

Only a few measurements have been published, and the radio time series is too sparse to lead to any firm conclusion. The only important result so far is that WR 125 presents significant variations in its behavior, switching between a pure thermal spectrum and a spectrum showing strong indications for non-thermal emission (Abbott et al., 1986; Cappa et al., 2004; Williams et al., 1992). The thermal emission components from the individual stellar winds are steady, and thus do not contribute to the measured variations. In the context of PACWBs, besides the obvious change of physical conditions in the synchrotron emitting region as the separation changes in an eccentric orbit, such a behavior is frequently interpreted in terms of changing FFA. This can happen (i) in an eccentric orbit when the synchrotron emitting region moves in and out the radio photosphere, or (ii) when the WCR is partly hidden behind the thick stellar wind of one of the two stars in the binary system at some orbital phases (line of sight effect). In both cases, this is not the synchrotron radiation process that is inhibited at some epochs, but the disappearance of the non-thermal emission is attributed to FFA. Both aspects are illustrated in Figure 5.7. The blue spheres illustrate the different sizes for radio photospheres of the WC and O-star winds, respectively. Typical sizes for the photosphere can range between tens and thousands of solar radii, depending on the nature of the wind and on the photon frequency (see e.g. Benaglia et al. 2020; De Becker et al. 2019). For a WC wind, the photosphere radius can be of the order of 1000-1500 solar radii at the

frequencies of the observations reported by [Abbott et al. \(1986\)](#); [Williams et al. \(1992\)](#) and [Cappa et al. \(2004\)](#). Depending on the orbital phase along the eccentric orbit, the WCR can be out of the radio photosphere at apastron, or fully hidden within it at periastron. At intermediate orbital phases, the synchrotron emitting region (coincident with the WCR) may be only partially buried in the photosphere, therefore displaying a spectrum deviating from the pure thermal emission, without any strong non-thermal signature (case (b) in Figure 5.7). However, depending on the orientation of the line of sight, even a not completely buried WCR can be located behind the strong wind of the WC star, and the synchrotron source will thus be significantly absorbed. Let's consider an observer in the orbital plane in Figure 5.7. When observing from the left part, no synchrotron radiation would be measured, but when observing from the bottom some synchrotron radiation could be detected. This orientation effect is more likely to happen not too far from periastron. Otherwise, the alignment between the observer, the WCR, and the densest part of the WC wind would not be good enough to lead to a complete absorption of the synchrotron radiation.

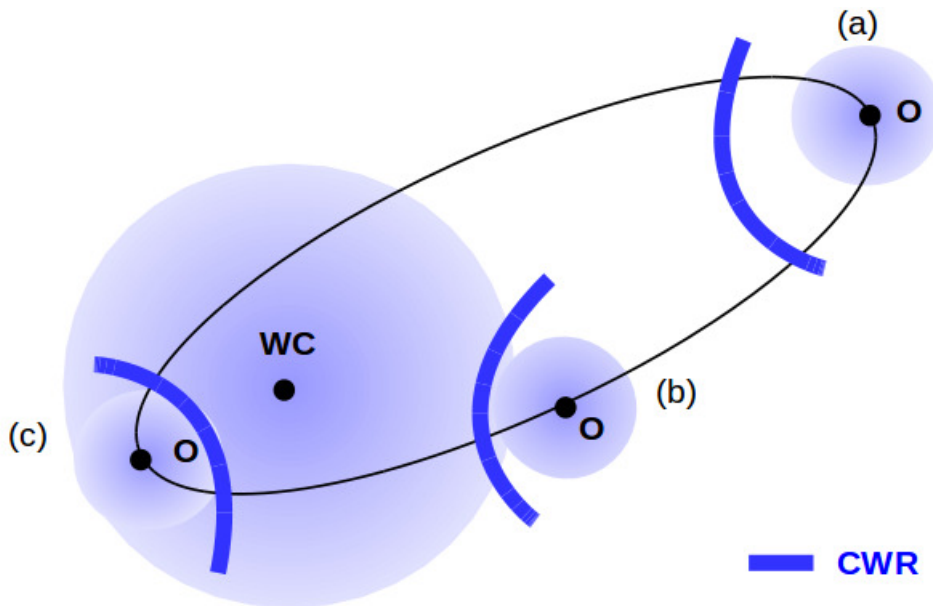


Figure 5.7: Sketch of the likely eccentric orbit of WR 125, illustrating three specific orbital phases: (a) close to apastron, (b) intermediate phase, and (c) close to periastron. Blue spheres represent the (not to scale) radio photospheres.

With the above picture in mind, the radio measurements allow us to notice that,

- the clear non-thermal radiation identified in 1985 was certainly produced at

an orbital phase sufficiently far from periastron.

- the drop by about a factor 6 of the flux density at 6 cm measured in 1988 (compared to that measured in 1985) is likely pointing to an orbital phase closer to periastron.

5.4.4 Toward a more complete picture

We can now summarize the outcomes of Section 5.4.1, Section 5.4.2, and Section 5.4.3,

- a strong indication for periastron passage is provided by the dust emission in the infrared. It seems it is occurring close to 2020-2021, in agreement with some complementary elements gathered in X-rays.
- a previous periastron passage likely occurred at the beginning of the 1990's. This is indicated by a peak in dust production, and by a drop in the soft X-ray emission at the same epoch. In addition, radio measurements at the end of the 1980's suggest an approaching periastron passage. At the scale of a long period orbit, this is compatible with a likely periastron passage at the beginning of the 1990's.
- the tentative period suggested by the infrared and X-ray data sets is about 28-29 yrs. The existing time series in these spectral bands are not enough to rule out a period of 14-15 yrs. However, if the constraint on the orbital period published by [van der Hucht \(2001\)](#) is robust ($P > 6600$ d), this would favor the long period hypothesis.

Our results provide helpful guidelines for future observations, that we can summarize as follows:

- a follow-up study of this system in the infrared (and in X-rays) close to year 2034 would be adequate, at it would either be another periastron passage (for the 14-15 yr period hypothesis) or a more quiet apastron passage (for 28-29 yr period hypothesis). The lack of any episode of dust formation (and of low X-ray emission state) would point to an apastron passage, in favor of the longest period hypothesis.
- despite its high interest for the investigation of non-thermal processes in CWBs, WR 125 was the target of only a few radio observations. It's orbital motion away from periastron would constitute a relevant opportunity to

measure the rise of the radio emission (as FFA would decrease), followed by a likely fade out of the emission while approaching apastron (as the separation increases). This would constitute an alternative test to check what is the most realistic orbital period hypothesis.

- with an orbital period of several years, WR 125 is a valid target for long baseline interferometric measurements aimed at following its orbit and derive orbital parameters. At a distance of about 2 kpc, an orbital period of several years translates into a projected separation of several (tens of) milli-arcseconds, thus easily resolved with current long baseline interferometers operating at the milli-arcsecond scale. In addition, the combination with spectroscopic measurements would allow to deriving a three-dimensional orbit (see e.g. [Le Bouquin et al. 2017](#)).

5.5 Conclusions

We have conducted a long term monitoring of the episodic dust maker WR 125 using archive and new data in X-rays and in the (near and mid) infrared. In X-rays, we confirm the switch of the emission to a low state in 2020 (especially in the soft band), that may indicate a recent periastron passage. The drop in the soft X-ray emission could be attributed to a significant photoelectric absorption close to periastron, when the X-ray emission from the WCR may be more quantitatively absorbed by the dense WC wind. The occurrence of a previous low emission state in 1991 suggests a previous periastron passage occurred about 28-29 yrs before. The infrared emission attributed to dust formation presents a clear rise in 2019-2021, that is confirmed by our very recent measurements. The infrared outburst measured in 2019-2021 is reminiscent of a previous one measured at the beginning of the 1990's, both reasonably coincident with periastron passage in an eccentric long period orbit. Once again, the time interval between these two events is about 28-29 yrs. We also note that the careful inspection of the radio measurements tends to confirm that the beginning of the 1990's is a very likely epoch of periastron passage. However, the lack of recent radio data prevents any further conclusion to be drawn.

Even though the data analysis reported in this paper seems to confirm that a periastron passage occurred in 2019-2021, one has to be more careful about the orbital period of WR 125. Both the X-ray emission and the dust production suggest a recurrence of about 28-29 yrs, but the lack of data in both time series prevents us to completely rule out a period twice as short. The available X-ray and infrared

data do not cover the 2004-2005 epoch, where another un-noticed periastron passage could have occurred. Future observations, especially close to year 2034 would allow us to definitely lift the uncertainty on the period of this system. At that epoch, the system will undergo either a periastron passage (shorter period hypothesis) or an apastron passage (long period hypothesis).

Chapter 6

X-RAY INVESTIGATION AND OPTICAL POLARIMETRY OF MASSIVE O+O BINARIES

The O+O binaries having orbital period of a few days have also been investigated in the present work using different techniques. This chapter consists of two parts. Part one includes the detailed X-ray study of a massive O+O binary HD 93205 lying in Carina nebula region while optical polarimetric study of another such system, DH Cep, is presented in the second part.

6.1 Part I: Characteristics of X-ray emission from HD 93205

The Carina nebula region is an interesting star-forming region of the galaxy containing some of the youngest and most massive O-type stars. The open clusters Trumpler 14, Trumpler 16, and Collinder 228 present in this region harbor significant fraction of the known O-type stars in the nearby Milky Way. HD 93205 is an O-type member of Trumpler 16 and it also holds the position of the only O3 V star present in the galaxy having double-lined spectroscopic binary nature (Walborn, 1971, 1973). The binary components of HD 93205 are classified as O3 V+O8 V by Conti & Walborn (1976). They also estimated the first radial velocity solution for the binary orbit of this system and derived an orbital period of 6.0810

The results of the Part I of this chapter are to be submitted to MNRAS. However, Part II is published in Arora et al. (2019b).

6. X-RAY INVESTIGATION AND OPTICAL POLARIMETRY OF MASSIVE O+O BINARIES

Table 6.1: Orbital parameters of HD 93205.

Parameter	Value
Period (d)	6.08102 ± 0.00066
Primary:	
V_o (km s ⁻¹)	3.6 ± 2.5
K_1 (km s ⁻¹)	139.1 ± 6.0
$a \sin i$ (km)	$(1.015 \pm 0.047) \times 10^7$
eccentricity	0.49 ± 0.03
ω (degrees)	12 ± 3
$T_{periastron}$ (JD)	2442532.784 ± 0.060
$M_{pri} \sin^3 i$ (M_\odot)	39
Secondary:	
K_2 (km s ⁻¹)	360 ± 53
$M_{sec} \sin^3 i$ (M_\odot)	15

Notes: Here, γ is the systemic velocity or radial velocity of the center of mass of the system, K is the radial velocity semi-amplitude, ω is the longitude of periastron, $T_{periastron}$ is the time of periastron passage, $a \sin i$ is the projected semi-major axis, $M_{pri} \sin^3 i$ and $M_{sec} \sin^3 i$ are the minimum masses of primary and secondary binary components, respectively. All the parameters are taken from [Conti & Walborn \(1976\)](#).

± 0.0007 d, along with minimum masses of primary and secondary stars as 39 and 15 M_\odot respectively. The highly elliptical orbit of HD 93205 with an eccentricity of 0.5 pointed towards very young evolutionary status of both the components lying near the zero-age main sequence. Additionally, HD 93205 has been identified as the earliest type star in the galaxy having a well constrained orbital solution. This makes this system especially valuable to study its stellar wind properties. The main orbital parameters of HD 93205 have been given in [Table 6.1](#)

[Sota et al. \(2014\)](#) has modified the spectral type of primary star in HD 93205 as O3.5 V((f)). They have also detected visual companion in the system at a separation of $3.68''$, position angle of 272° , and with visual magnitude difference of (ΔV) of 9.3 mag. Many previous studies are available where HD 93205 has been detected in X-ray with moderate X-ray luminosity of 10^{32} erg s⁻¹, (see e.g. [Corcoran et al. 1995](#); [Seward & Chlebowski 1982](#); [Seward et al. 1979](#) etc.). But a few have discussed about variable X-ray emission from the source. For example, [Chlebowski & Garmany \(1991\)](#) did not notice any significant sign of variability in the *Einstein* observed X-ray data of HD 93205 which was investigated by [Seward & Chlebowski \(1982\)](#). However, clear phase-locked X-ray modulations have been noticed by [Corcoran \(1996\)](#) where X-ray flux is suggested to be maximum close

to the periastron passage than other positions in the binary orbit. [Morrell et al. \(2001\)](#) provided only a marginal support to this idea. Using five X-ray observations from *XMM-Newton*, [Antokhin et al. \(2003\)](#) have shown that X-ray flux changes in accordance to the distance between two binary components and found no significant change in spectral shape at different orbital phases. A few hints of X-ray variability have also been provided by [Albacete Colombo et al. \(2003\)](#) and [Albacete-Colombo et al. \(2008\)](#), where colliding winds have been suspected to be the reason behind its behavior. [Antokhin et al. \(2008\)](#) has also suggested that X-ray flux varies with orbital motion of HD 93205 which is one of the best X-ray covered source. Further, [Gagné et al. \(2011\)](#) noticed a decline in the X-ray count rate of HD 93205 over one day of observation where most of the emission is observed from the cooler temperature component as suggested by [Nazé et al. \(2011\)](#) also. Their analysis aid the periodicity results obtained by [Morrell et al. \(2001\)](#). Detailed modeling of the colliding winds is clearly necessary to understand its behavior. With this aim, we have explored X-ray observations of HD 93205 over a considerably long time baseline.

6.1.1 X-ray light curve analysis

HD 93205 lies in the vicinity of WR 25 in the Carina region as shown in Figure 3.1 of this thesis. Therefore, same archival X-ray data observed by *XMM-Newton* for a total of 24 epochs has been used for HD 93205. The data span over a period of ~ 15 years from 2000 to 2015. The background subtracted X-ray light curves as observed by MOS1, MOS2, and PN on-board *XMM-Newton* are shown Figure 6.1. The light curves were extracted in broad₁ (0.3-5.0 keV), soft (0.3-2.0 keV), and hard₁ (2.0-5.0 keV) energy bands and binned with 1000 sec intervals. Light curves were extracted up to 5.0 keV energy band as beyond this the source count rates were similar to background count rates. The source was present in the FoV of MOS2 for most of the times. The X-ray variability is clearly seen in the broad₁ and soft energy bands light curves with less ambiguous trend displayed in the hard band. We have also attempted to split a single exposure to multiple intervals of the order of 10 ksec each to look for the short-term variability in this short period binary system. However, no such variability over the small time intervals was noticed.

In order to see the variation of count rate with the orbital phase, the light curves were folded using the ephemeris $JD = 2442532.784 + 6.08102E$ ([Conti & Walborn, 1976](#)). Here, the zero orbital phase is represented by the time of periastron passage. The folded light curves were also obtained in the same three energy bands

6. X-RAY INVESTIGATION AND OPTICAL POLARIMETRY OF MASSIVE O+O BINARIES

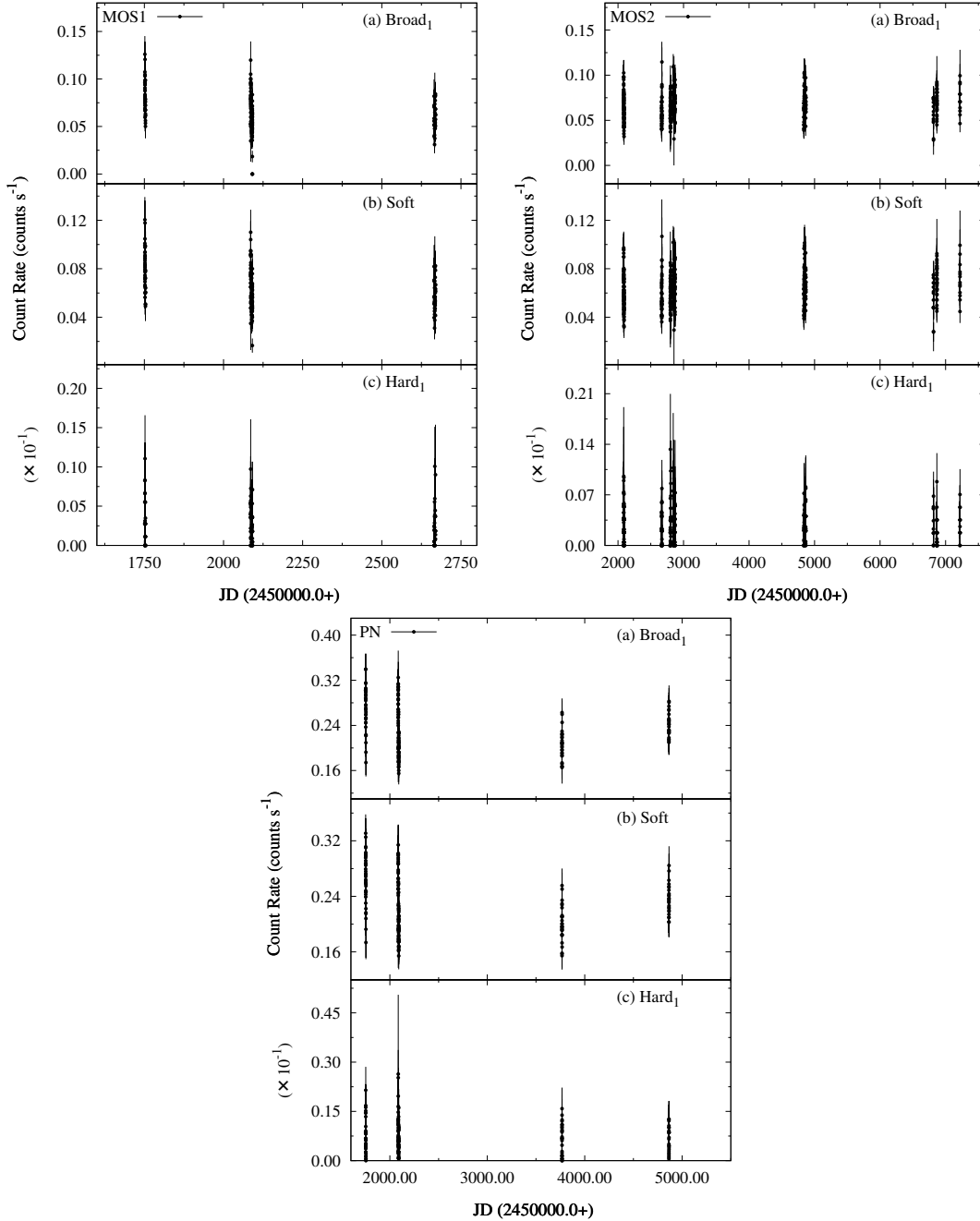


Figure 6.1: X-ray light curves of HD 93205 as observed by *XMM-Newton* using (a) MOS1, (b) MOS2, and (c) PN in broad₁ (0.3-5.0 keV), soft (0.3-2.0 keV), and hard₁ (2.0-5.0 keV) energy bands.

to investigate behavior of soft and hard₁ bands photons individually. The average count rate of an observation ID is represented by each point in the folded X-ray light curves observed by MOS1, MOS2, and PN as shown in Figure 6.2. Phase locked modulations are observed in the folded X-ray light curves of HD 93205 where the

6.1 Part I: Characteristics of X-ray emission from HD 93205

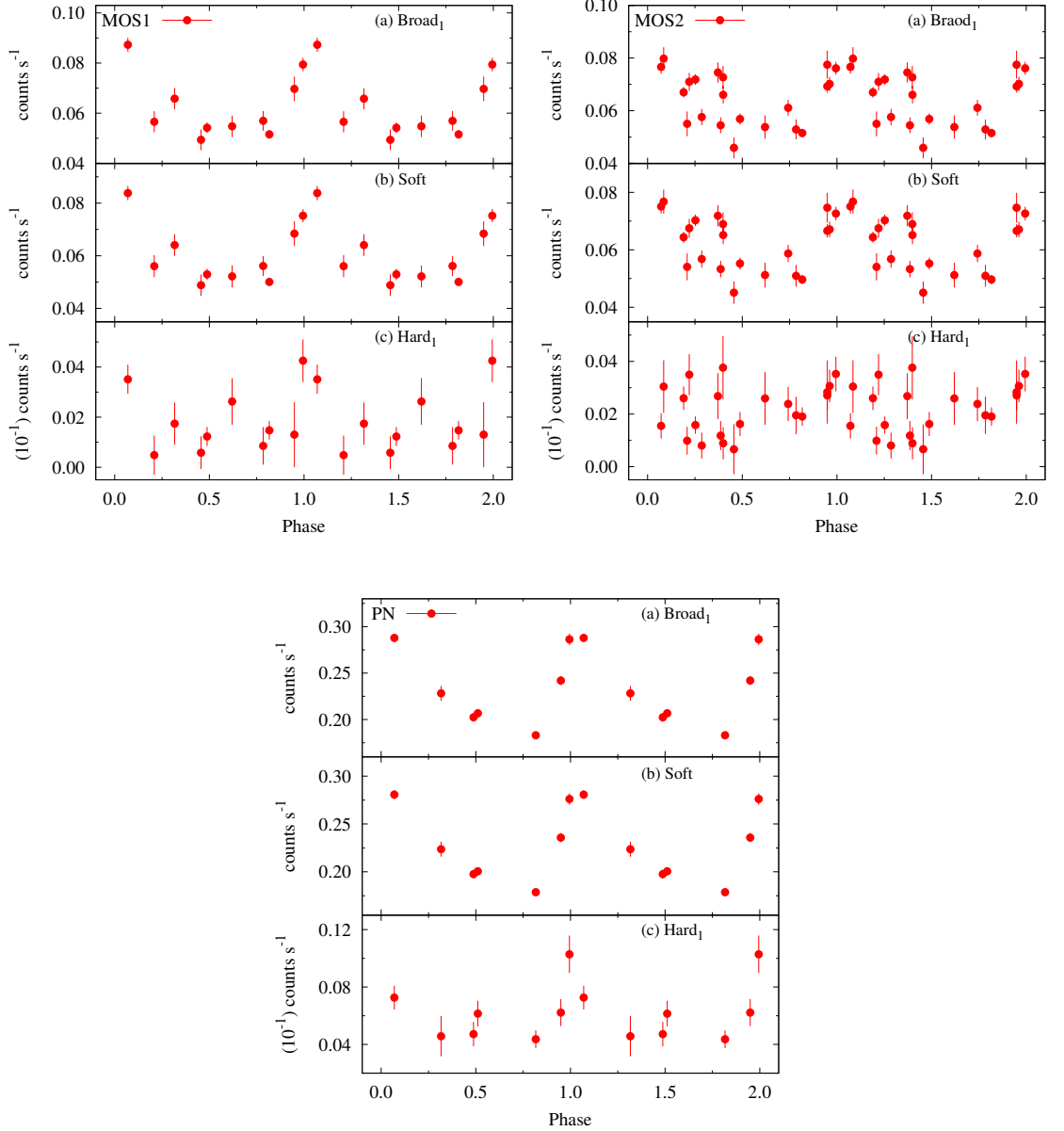


Figure 6.2: Folded X-ray light curves of HD 93205 as observed by *XMM-Newton* using (a) MOS1, (b) MOS2, and (c) PN in broad₁ (0.3-5.0 keV), soft (0.3-2.0 keV), and hard₁ (2.0-5.0 keV) energy bands.

count rate is maximum around the periastron passage and it decreases gradually as the system moves away to the apastron. Similar kind of behavior is there in all the energy bands but MOS1 and PN light curves showcase the count rate variations more clearly as compared to the crowded light curves of MOS2. The maximum to the minimum count rate ratio in broad₁ and soft energy bands is 1.77 ± 0.16

6. X-RAY INVESTIGATION AND OPTICAL POLARIMETRY OF MASSIVE O+O BINARIES

and 1.72 ± 0.13 for MOS1, 1.73 ± 0.18 and 1.70 ± 0.17 for MOS2, and 1.57 ± 0.04 and 1.57 ± 0.04 for PN observations, respectively. However, the lesser number of hard₁ X-ray photons observed in the light curve of HD 93205 limits us to draw any firm conclusion about the high energy emission from the source. Therefore, the spectral analysis is required to understand various physical processes at work in this massive binary system.

6.1.2 X-ray spectral analysis

The X-ray spectrum of HD 93205 is similar to the hot stars' spectra displaying optically thin thermal plasma emission at high temperature where the soft band is populated by several emission lines from C, N, O, and Ne, whereas, the 2.0-4.5 keV energy region is dominated by continuum radiation and > 4.5 keV range includes the Fe xxvi 6.4 keV line. Since the HD 93205 spectrum appears much softer with negligible counts above 5 keV, hence, the spectral fitting was performed in 0.3-5.0 keV energy band. Still, the single temperature model was seen to be insufficient to reproduce the observed spectra. Ultimately, individual spectra obtained from a single observation ID were fitted using the similar model as used for WR 121a by fixing N_H^{ISM} to $0.24 \times 10^{22} \text{ cm}^{-2}$ (Jenkins, 2019) and varying all other parameters of the model. The abundances for the two thermal APEC models were tied together. It was found that kT_1 was almost constant with an average value of 0.20 ± 0.07 keV. Therefore, further spectral fitting was performed by fixing kT_1 to the average value. Since the quality of the EPIC spectrum of HD 93205 was not good enough to fit the spectrum obtained from a single observation ID individually and properly constrain the spectral parameters. Therefore, all the spectra available from MOS1, MOS2 and PN within very close by orbital phases were fitted jointly. All of this lead to definition of total eight bins (1-8) having phase ranges from 0.069–0.085, 0.190–0.221, 0.250–0.320, 0.370–0.400, 0.450–0.511, 0.620–0.621, 0.740–0.820, and 0.948–0.995 (see Table 6.2). So, further spectral fitting was performed by varying the values of N_H^{local} , abundance (Z), kT_2 , $norm_1$, and $norm_2$. The modeled X-ray spectra of HD 93205 are shown in Figure 6.3 for all of the eight phase bins. The different spectral parameters estimated are plotted with orbital phase in Figure 6.4 and are mentioned in Table 6.2. The ISM corrected X-ray flux was also estimated for HD 93205 in broad₁ ($F_{B_1}^{ism}$), soft (F_S^{ism}), and hard₁ ($F_{H_1}^{ism}$) energy bands. The variation of X-ray flux as a function of orbital phase and binary separation has been shown in Figure 6.5 in different energy bands. The phase locked X-ray flux variations are clearly displayed in this figure where it is maximum around periastron

6.1 Part I: Characteristics of X-ray emission from HD 93205

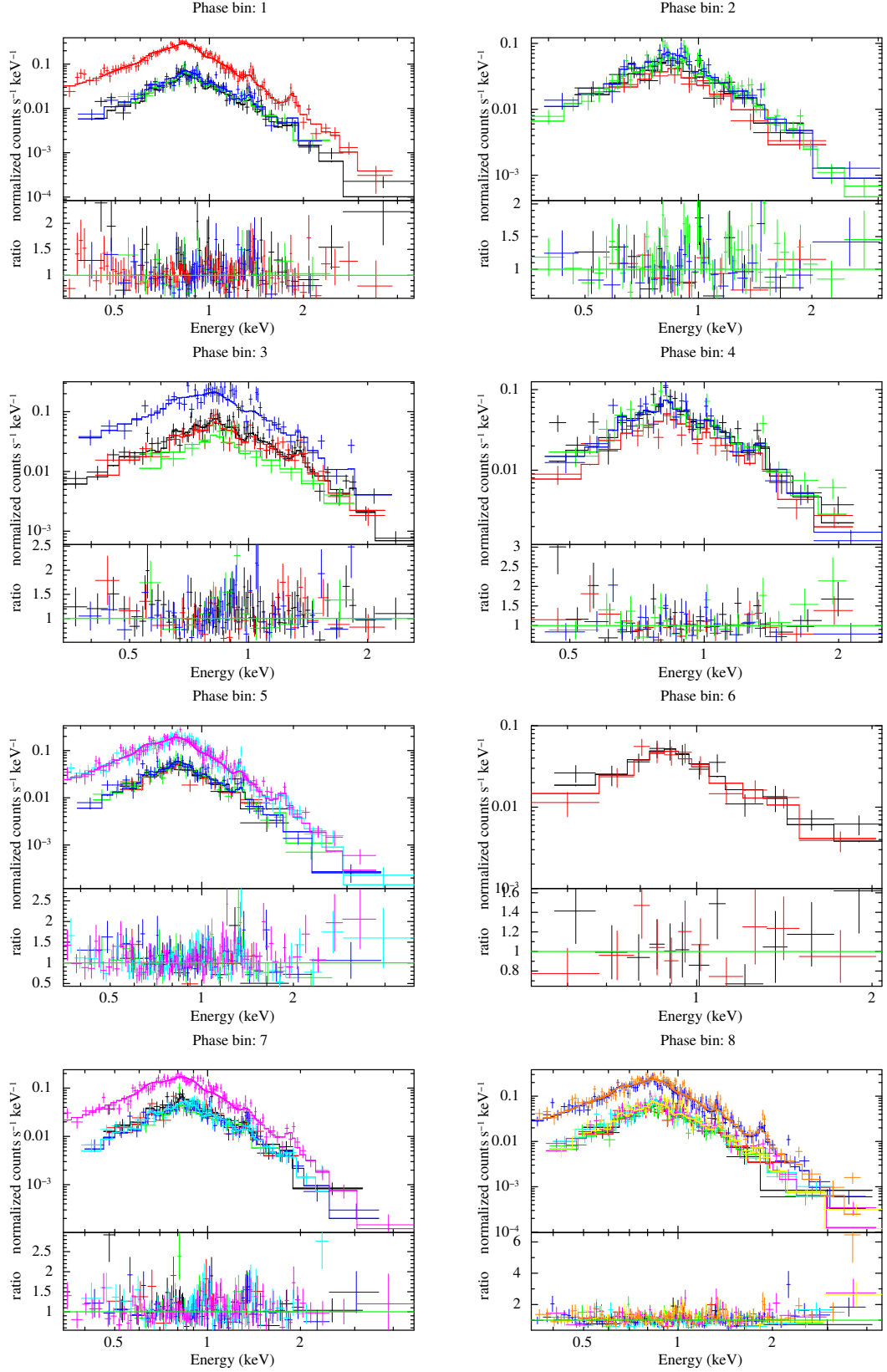


Figure 6.3: X-ray spectra of HD 93205 jointly fitted with the two temperature thermal plasma emission model for all of the eight phase bins defined in Table 6.2. The lower panel of each figure represents the ratio of the data to the model.

6. X-RAY INVESTIGATION AND OPTICAL POLARIMETRY OF MASSIVE O+O BINARIES

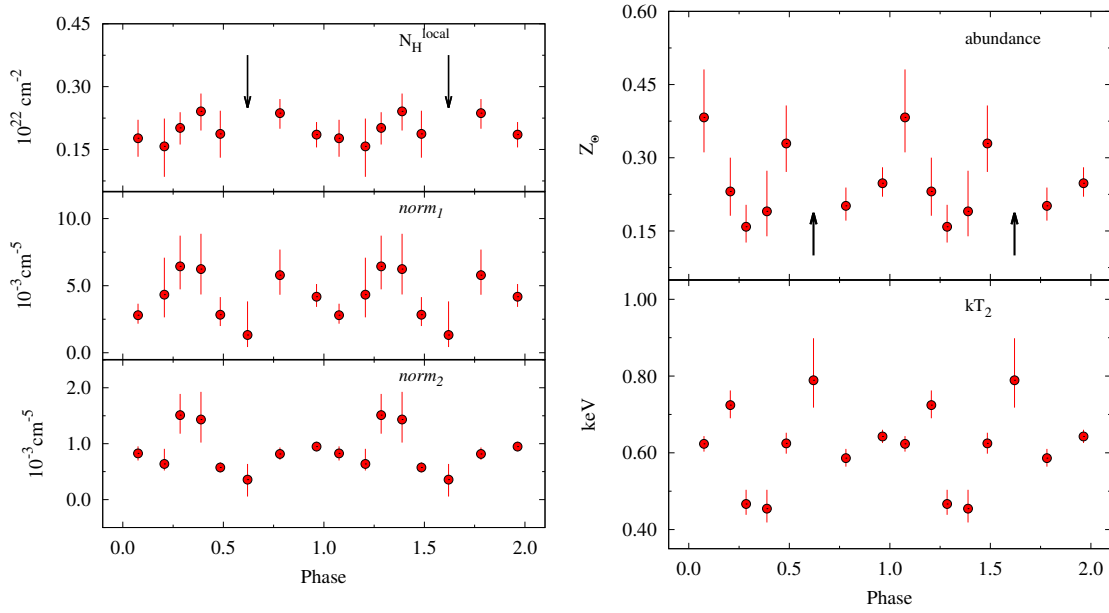


Figure 6.4: Variation of different spectral parameters with orbital phase of HD 93205 obtained after X-ray spectral fitting (see Table 6.2).

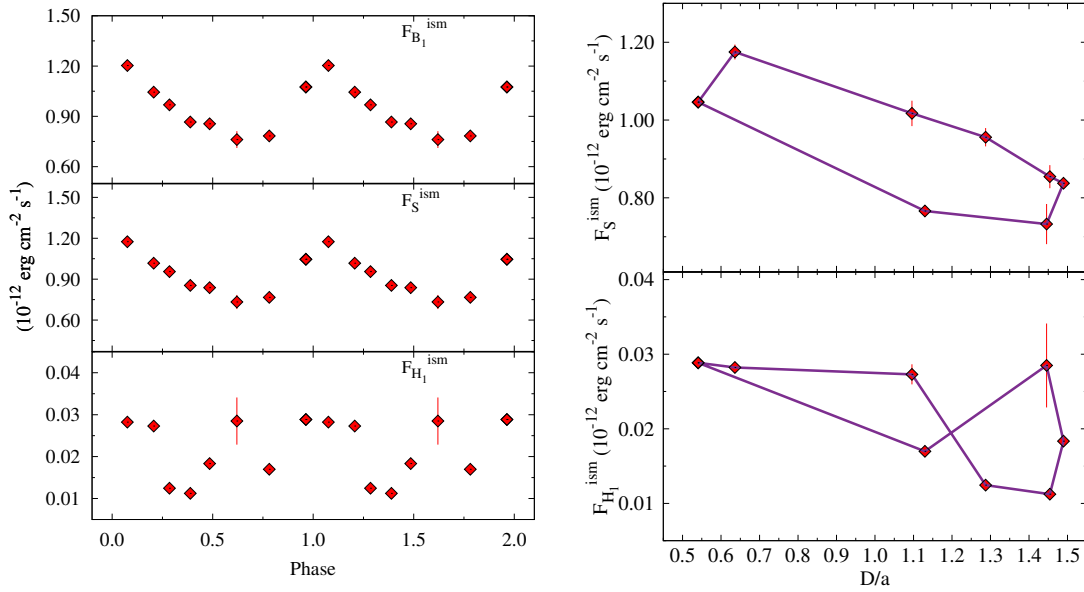


Figure 6.5: Variation of X-ray flux in different energy bands from HD 93205 obtained after X-ray spectral fitting with orbital phase (*left*) and binary separation (D normalized to semi-major axis ‘ a ’) (*right*).

and becomes

Table 6.2: Best fit parameters obtained from spectral fitting of HD 93205 as observed from *XMM-Newton*-EPIC.

Phase bin	ϕ	N_H^{local} (10^{22} cm $^{-2}$)	$norm_1$ (10^{-3} cm $^{-5}$)	$norm_2$ (10^{-3} cm $^{-5}$)	kT_2 (keV)	Z (Z_\odot)	$F_{B_1}^{ism}$ (10^{-12} erg cm $^{-2}$ s $^{-1}$)	F_S^{ism}	$F_{H_1}^{ism}$	$\chi_\nu^2(dof)$
1	0.08	$0.18^{+0.18}_{-0.04}$	$2.79^{+0.86}_{-0.63}$	$0.83^{+0.13}_{-0.13}$	$0.62^{+0.02}_{-0.02}$	$0.38^{+0.09}_{-0.07}$	$1.20^{+0.02}_{-0.02}$	$1.17^{+0.02}_{-0.02}$	$0.03^{+0.001}_{-0.001}$	1.00 (242)
2	0.21	$0.16^{+0.16}_{-0.07}$	$4.33^{+2.75}_{-1.69}$	$0.64^{+0.27}_{-0.12}$	$0.72^{+0.04}_{-0.03}$	$0.23^{+0.07}_{-0.05}$	$1.04^{+0.03}_{-0.03}$	$1.02^{+0.03}_{-0.03}$	$0.03^{+0.001}_{-0.001}$	1.17 (109)
3	0.29	$0.20^{+0.20}_{-0.04}$	$6.44^{+2.29}_{-1.71}$	$1.51^{+0.38}_{-0.33}$	$0.47^{+0.04}_{-0.03}$	$0.16^{+0.03}_{-0.03}$	$0.97^{+0.02}_{-0.02}$	$0.96^{+0.02}_{-0.02}$	$0.01^{+0.001}_{-0.001}$	1.17 (168)
4	0.39	$0.24^{+0.24}_{-0.05}$	$6.24^{+2.63}_{-1.89}$	$1.43^{+0.49}_{-0.41}$	$0.45^{+0.05}_{-0.04}$	$0.19^{+0.08}_{-0.05}$	$0.87^{+0.03}_{-0.03}$	$0.85^{+0.03}_{-0.03}$	$0.01^{+0.001}_{-0.001}$	1.09 (90)
5	0.48	$0.19^{+0.19}_{-0.06}$	$2.83^{+1.31}_{-0.84}$	$0.57^{+0.09}_{-0.09}$	$0.62^{+0.03}_{-0.03}$	$0.33^{+0.08}_{-0.06}$	$0.86^{+0.01}_{-0.01}$	$0.84^{+0.01}_{-0.01}$	$0.02^{+0.001}_{-0.001}$	1.14 (292)
6	0.62	$< 0.38^\dagger$	$1.32^{+2.51}_{-0.90}$	$0.36^{+0.28}_{-0.30}$	$0.79^{+0.11}_{-0.07}$	$> 0.19^\dagger$	$0.76^{+0.05}_{-0.05}$	$0.73^{+0.05}_{-0.05}$	$0.03^{+0.005}_{-0.005}$	0.83 (18)
7	0.78	$0.24^{+0.24}_{-0.04}$	$5.78^{+1.90}_{-1.46}$	$0.82^{+0.11}_{-0.11}$	$0.59^{+0.02}_{-0.02}$	$0.20^{+0.04}_{-0.03}$	$0.78^{+0.01}_{-0.01}$	$0.77^{+0.01}_{-0.01}$	$0.02^{+0.001}_{-0.001}$	1.03 (270)
8	0.96	$0.19^{+0.19}_{-0.03}$	$4.18^{+0.94}_{-0.76}$	$0.95^{+0.09}_{-0.08}$	$0.64^{+0.02}_{-0.02}$	$0.25^{+0.03}_{-0.03}$	$1.07^{+0.01}_{-0.01}$	$1.05^{+0.01}_{-0.01}$	$0.03^{+0.001}_{-0.001}$	1.39 (469)

Notes. Fit parameters are derived from joint spectral fitting of *XMM-Newton*-EPIC spectra of HD 93205 using model PHABS(ISM)*PHABS(LOCAL)*(APEC+APEC) with fixed values of $N_H^{ISM} = 6.5 \times 10^{22}$ cm $^{-2}$ and $kT_1 = 0.20 \pm 0.07$ keV. $norm_1$ and $norm_2$ are the normalization constants for two temperature components. $F_{B_1}^{ism}$, F_S^{ism} , and $F_{H_1}^{ism}$ are the ISM corrected X-ray fluxes of HD 93205 in broad $_1$, soft, and hard $_1$ energy bands, respectively. χ_ν^2 is the reduced χ^2 and dof is degrees of freedom. Errors quoted on different parameters refer to 68% confidence level.

† Mentioned values correspond to the extreme value of the specified parameter.

6. X-RAY INVESTIGATION AND OPTICAL POLARIMETRY OF MASSIVE O+O BINARIES

minimum close to the apastron accompanied by different X-ray fluxes at the same binary separation but different orbital phases.

6.1.3 Discussion: X-ray emission from HD 93205

The X-ray emission properties of HD 93205, a massive O+O binary, have been investigated in the present study. HD 93205 is an eccentric binary system, therefore, X-ray emission from the wind-wind collision is expected from this source additional to the intrinsic X-ray emission from the individual stars arising from their winds instabilities. In the case of adiabatic shocks in the WCR, the variation of X-ray luminosity is expected to be $1/D$ (Stevens et al., 1992; Usov, 1992), where D is the separation between the two stars, as it is already mentioned in the case of WR 25 (Arora et al., 2019a). The X-ray flux modulations shown in Figure 6.5 (left) clearly display the expected behavior where $F_{B_1}^{ism}$ and F_S^{ism} are maximum around the phase (ϕ) ~ 0.07 and minimum at $\phi \sim 0.62$. However, maximum $F_{H_1}^{ism}$ is observed at $\phi \sim 0.95$ and minimum at ~ 0.39 . The ratio of the maximum to minimum flux is found to be 1.58 ± 0.11 , 1.60 ± 0.11 , and 2.57 ± 0.20 for the broad₁, soft, and hard₁ energy bands, respectively. For the eccentric binary systems, the ratio of the flux at the periastron to apastron is expected to be $f_{peri}/f_{ap} \approx (1+e)/(1-e)$. As HD 93205 has $e \approx 0.5$, therefore the expected ratio should be ~ 1.5 . Clearly, the observed increase of flux around periastron passage is in qualitative agreement with the wind-wind collision model. Such phase dependent X-ray flux variations are typical in the CWBs.

The observed X-ray variability is due to the changes in the binary separation at different orbital phases in an eccentric binary. However, F_S^{ism} and $F_{H_1}^{ism}$ show the deviation from the straight line when plotted against D (normalized to semi-major axis) in Figure 6.5 (right). One of the reasons behind such a deviation could be the anisotropic absorption of X-rays in an eccentric binary at different orbital phases. Photo-electric absorption of X-rays is more when the line of sight to the system passes through the denser stellar wind of more massive component of the binary. The change in N_H^{local} throughout the orbital period in Figure 6.4 (left) confirms this assertion. The presence of asymmetries and inhomogeneities in the stellar winds may add further deviations from the expected behavior (Pittard & Stevens, 1997). The variation of $F_{B_1}^{ism}$ shown in Figure 6.6 also infers that X-ray flux is not maximum and minimum at the exact location of periastron and apastron, respectively. It may also give rise to difference in the expected f_{peri}/f_{ap} ratio to the observed value. Other effects that give rise to such an observed phenomenon are being investigated

6.1 Part I: Characteristics of X-ray emission from HD 93205

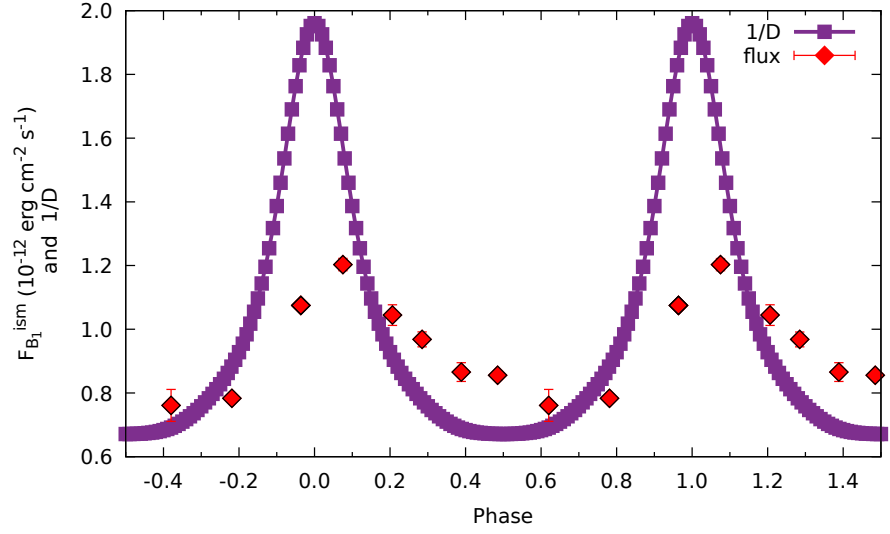


Figure 6.6: Variation of $F_{B_1}^{ism}$ from HD 93205 with orbital phase as observed by *XMM-Newton*-EPIC. The solid line shows the $1/D$ function, where D is the binary separation in terms of the semi-major axis.

and the implications of such effects on the X-ray emission will be considered.

The average values of kT_1 and kT_2 equal to ~ 0.20 keV and ~ 0.60 keV (see Figure 6.4), respectively, indicate that X-ray emission from HD 93205 is rather soft. Comparison of kT_1 and kT_2 derived in the cases of WR 25, WR 121a, and WR 125 (all WR+O binaries) with that of HD 93205 suggests that the strength of wind collision in HD 93205 is not as strong as observed for WR+O binaries explored in this thesis. This indicates that O+O binaries have weaker winds than WR+O systems. The only O+O binaries in the Carina region with hard X-ray spectra ($kT_{avg} > 1$ keV) are HD 93403 (O5 III(fc)+O7 V; Nazé 2009) and HD 93343 (O8 V+O7-8.5 V; Antokhin et al. 2008). They have orbital period > 10 days. However, short orbital period (< 10 days) O+O binaries are generally characterized by $kT_{avg} < 1$ keV (Gagné et al., 2011).

The maximum ISM corrected X-ray luminosity (L_X) of HD 93205 at a distance of 2.32 kpc (Gaia Collaboration et al., 2020) is estimated to be 7.73×10^{32} erg s^{-1} in 0.3-5.0 keV energy band. Upon considering the bolometric luminosity (L_{bol}) of HD 93205 as $\log(L_{bol}/L_{\odot})$ as 5.79 from Gagné et al. (2011), the ratio $\log(L_X/L_{bol})$ is found to be -6.20. The value of $\log(L_X/L_{bol})$ for HD 93205 is large in comparison to typically observed from single O-type stars (≈ -7) (Berghoefter et al., 1997; Nazé et al., 2011). This may be due to the wind interaction region between the two binary components in addition to the embedded wind shocks of individual stars' outflows.

Looking at the above reasonable assertions, one is convinced that HD 93205

6. X-RAY INVESTIGATION AND OPTICAL POLARIMETRY OF MASSIVE O+O BINARIES

is a moderately luminous X-ray source giving rise to mostly soft X-ray emission and a smaller fraction is emitted from the wind-wind collision. One reason for this could be the incapability of detecting hard X-ray spectral tail in comparatively faint CWBs. On the other side, theoretical studies by [Antokhin et al. \(2004\)](#); [Owocki & Gayley \(1995\)](#); [Stevens & Pollock \(1994\)](#); [Walder & Folini \(2003\)](#) of wind-wind collision have suggested that several phenomena like radiative braking or inhibition may considerably reduce the stellar winds speed before entering the WCR. These effects deal with the influence of one stars' radiation field on the wind momentum of its binary companion as investigated for WR 25 and WR 121a also (see [Arora & Pandey 2020](#); [Arora et al. 2019a](#)). Thus, the X-ray luminosity and the hardness of the spectrum are adversely affected since it is directly proportional to the square of the wind velocity reaching the interaction zone. From the present analysis, we conclude that HD 93205 is a CWB where most of its X-ray luminosity of $\sim 10^{32}$ erg s^{-1} is due to the soft energy band emission arising from less strong wind interaction in the WCR of O+O binaries. However, a quantitative analysis of wind collision in HD 93205 is one of the subjects of future programs.

6.2 Part II: Search for intrinsic linear polarization in DH Cep

6.2.1 Motivation

Massive stars winds are dense and extremely ionized consisting of free electrons and ions abundantly. The linear polarization of light occurs through single Thomson scattering by free electrons present in the plasma envelope rotating with the star which is ionized as well as optically thin ([St. -Louis et al., 1988](#)). The polarization study of starlight from the hot objects proves to be a promising manner to systematically probe their wind structure.

No intrinsic linear polarization is expected from the stars having circumstellar envelope in a spherically symmetrical configuration. However, the occurrence of several instabilities in their line-driven outflows gives rise to anisotropic winds in case of massive stars. The polarization of starlight is even more pronounced in case of massive binaries with orbital period of few days. For such systems, the orbital motion of close companion around the primary leads to illumination of the different regions of the electron-rich wind. Therefore, it behaves like a probe and modulates the linear polarization of the system e.g., CQ Cephei (WN6+O9, period=1.64 d,

6.2 Part II: Search for intrinsic linear polarization in DH Cep

Drissen et al. 1986) and V444 Cyg (WN5+O6, period=4.21 d, St. -Louis et al. 1993). The formation of dust in massive stars can further increase the degree of polarization due to the free-free scattering. Polarimetry is, therefore, an important observational technique to study the dust formation and stellar wind structures of massive binaries. Here, we will present polarimetric results obtained for the O+O binary DH Cep.

DH Cep (HD 215835) is a double-lined spectroscopic binary system. It is a member of the cluster NGC 7380 (age ≈ 4 Myr) and has an orbital period of 2.11 d (Lata et al., 2016). This binary star is also an X-ray source with $\log(L_X/L_{bol})$ of -6.7 in 0.3–7.5 keV energy band, perhaps attributed to colliding winds. The presence of the cool (< 1 keV) and hot (> 1.89 keV) temperature components in X-ray spectra of DH Cep could possibly be associated with the instabilities in radiation-driven wind shocks (Bhatt et al., 2010). The main orbital parameters of DH Cep are listed in Table 6.3.

Table 6.3: Basic parameters of the DH Cep system.

Parameter	DH Cep		Reference
	Primary	Secondary	
Distance (kpc)	3.2±0.4		1
V (mag.)	8.61		2
Period (d)	2.11		2
eccentricity	0		2
q (M_1/M_2)	1.15±0.02		2
T_o (HJD)	2456525.564±0.006		2
Spectral type	O5.5 V-III	O6 V-III	2
V_o (km s $^{-1}$)	-46.43 ± 2.47	-51.95 ± 2.65	2
K (km s $^{-1}$)	234.81 ± 3.97	269.70 ± 4.56	2
$a \sin i$ (R $_{\odot}$)	9.79 ± 0.17	11.24 ± 0.19	2
$M \sin^3 i$ (M $_{\odot}$)	15.01 ± 0.66	13.07 ± 0.57	2

Notes: T_o refers to the time of the conjunction (primary in front). The parameters γ , K , $a \sin i$, and $M \sin^3 i$ denote the apparent systemic velocity, the semi-amplitude of the radial velocity curve, the projected distance from the center of the star to the center of mass of the binary system, and the minimum masses of the binary components, respectively.

References: (1) Lindegren et al. (2018), (2) Martins et al. (2017)

6. X-RAY INVESTIGATION AND OPTICAL POLARIMETRY OF MASSIVE O+O BINARIES

6.2.2 Discussion: Linear Polarization of DH Cep

The degree of polarization as well as the polarization angle for DH Cep has been estimated during six nights in 2017 in B, V, R, and I photometric bands. The variation of both of these quantities over different nights was observed. However, to visualize these modulations with the orbital phase, the ephemeris $HJD = 2456525.56 + 2.11E$ has been used (Table 6.3). The variation of degree of polarization and the polarization angle for DH Cep is shown in Figure 6.7 in all the filters. The phase-dependent modulations are clearly visible in these light curves, specifically, in the B and V bands. The amplitude of the degree of polarization modulations is $\sim 0.7\%$ in these bands. The variation of the polarization light curve as well as the polarization angle with wavelength point towards the intrinsically polarized nature of DH Cep. In order to estimate the interstellar linear polarization (p) towards DH Cep, we plotted p versus distance in Figure 6.8. The p values of the stars lying within a 2 deg field of DH Cep were taken from Heiles (2000) while their distances were retrieved from the Gaia DR2 archive (Lindegren et al., 2018). It is anticipated that p increases linearly with the distance because of the presence of the interstellar medium. At the location of DH Cep (distance=3.24 kpc), the p value is $\sim 2\%$. Therefore, the intrinsic polarization of DH Cep is found to be less than 1% in all optical bands, but the trends of Figure 6.7 will remain same.

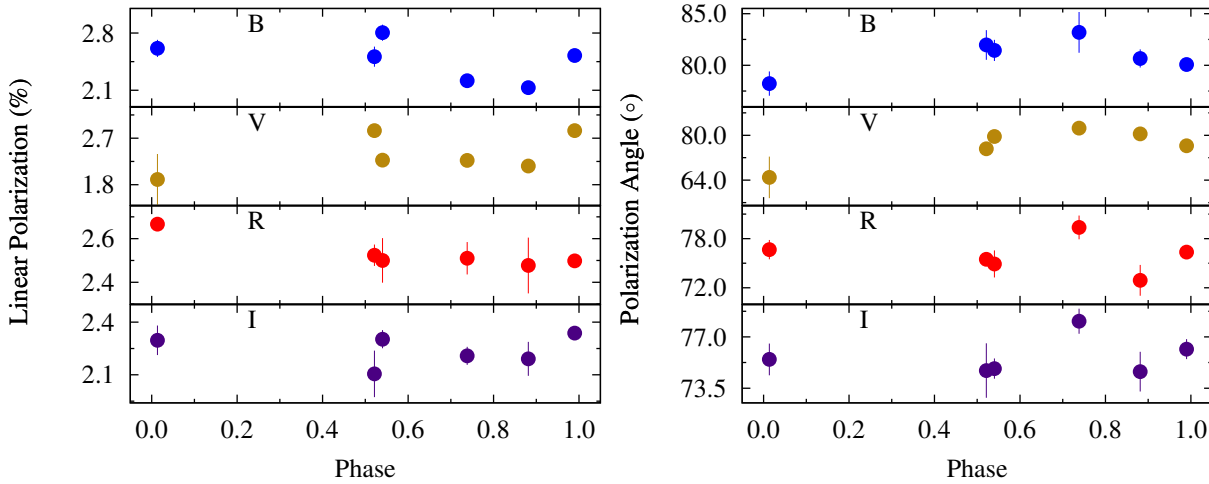


Figure 6.7: Linear polarization (*left*) and polarization angle (*right*) variation of DH Cep with the orbital phase in B, V, R, and I filters running from top to bottom.

The intrinsic polarization of DH Cep may be arising due to any of the following reasons:

1. asymmetric and extended circumstellar/binary envelopes

6.2 Part II: Search for intrinsic linear polarization in DH Cep

2. the presence of instabilities causing inhomogeneities in the massive-star winds (e.g. blobs)
3. the rotation of spots or non-radial stellar pulsations
4. modulations because of the binary motion

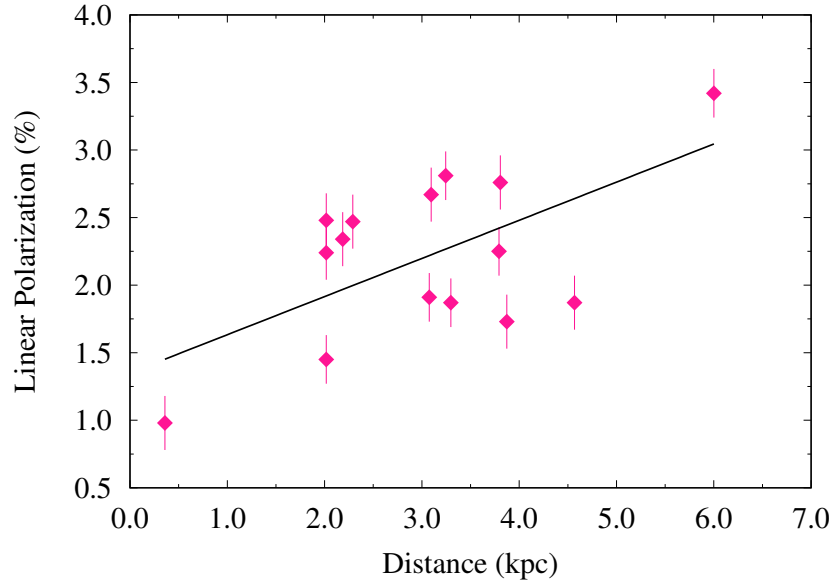


Figure 6.8: Linear polarization (V-band) as a function of distance towards the direction of DH Cep.

The spherically symmetric free electron distribution which is illuminated asymmetrically or isotropic illumination in an aspherical wind may generate the intrinsic linear polarization. For single stars, later effect may cause the polarization. However, the close binaries are affected by any of the causes mentioned. For some cases, even the Roche lobe overflow during certain sporadic periods may lead to polarization of star light due to production of asymmetric wind structures by binary interactions. The variations in the polarization light curves should be strictly periodic due to reason (4) but the presence of the other three effects might also impose several intermittent periodicities (St. -Louis et al., 1987). Significant polarization variability seen in the B and V bands is probably due to the asymmetric circumstellar/binary envelopes. The binary effect is important to study the intrinsic polarization in close massive binaries. Only a few measurements at arbitrary orbital phases cannot completely characterize the time-dependent polarization variations. Therefore, the necessary additional phase-dependent observations of DH Cep are being processed to fill its polarization light curve.

Chapter 7

SUMMARY AND FUTURE PROSPECTS

7.1 Summary

This thesis focuses on the detailed multiwavelength analysis of the massive O- and WR-stars. The main highlight of work done in the thesis is constraining the physical properties of stellar outflows from these early-type, hot stars. A detailed study of radiation emission from massive binaries helped to explain several phenomena active in the individual stellar winds as well as in the wind interaction region in between the component stars of a massive binary. In this thesis, we have studied the objects with diverse spectral types having distinct binary orbital parameters, for example, WR+O or O+O binaries with orbital periods from ~ 2.1 d to 28-29 yr were investigated. The results and inference obtained in each chapter of this thesis are described below –

(i) **Chapter 1 and 2** discusses the detailed overview of the topic, the aim of the thesis, and the adopted methodology to accomplish the goal.

(ii) **Chapter 3** provides the deep exploration of a CWB WR 25 using the > 16 years long X-ray observations from *Suzaku*, *Swift*, *XMM-Newton*, and *NuSTAR*. This is a rare instance where a massive binary is explored till the energy up to 79 keV along with the thermal X-ray emission below 10 keV energy. This was possible because WR 25 was observed by *NuSTAR* along with other X-ray observatories. Below 10 keV, colliding stellar winds of the binary components of WR 25 results in the enhanced X-ray luminosity. The system approaches a brighter X-ray state as the two binary components move close to the periastron passage where the wind interaction is maximum as wind density is largest in that part of the orbit. However, it gradually becomes fainter when the line of sight passes through the denser wind of the WR star in front. The wind collision is mostly adiabatic in WR 25 but significant

7. SUMMARY AND FUTURE PROSPECTS

deviation from the adiabatic cooling is seen around the periastron passage. The main indicator of this effect is the deviation from the expected $1/D$ dependence of the X-ray luminosity for the long period binaries. The inhibited acceleration of massive stars winds close to the periastron before interacting with each other might be a reason for the brief switch of wind plasma to the radiative regime. The sudden radiative braking of the wind of one component by another may further enhance the velocity drop. However, the temperature of post-shock plasma estimated by the spectral fitting of WR 25 at different orbital phases doesn't seem to support this interpretation. Further, WR 25 is unlikely a triple system or it has not gone through major outburst event during the past 16 years of observations as the long-term monitoring suggested the thermal X-ray emission overlaps fairly well when orbits distant in time are compared.

On the other hand, the non-thermal high energy emission has not been revealed for WR 25 in the *NuSTAR* data above 10 keV energy. The upper limits derived for the putative non-thermal X-ray flux from WR 25 belongs to $7-9 \times 10^{-13} \text{ erg cm}^{-2} \text{ s}^{-1}$ range between energy 0.1 and 100.0 keV which is very less than the ISM corrected thermal X-ray flux measured below 10.0 keV. Therefore, either non-thermal high energy radiations are missing in WR 25 or they are below the detection limit of the presently available hard X-ray detectors.

(iii) **Chapter 4** discusses the X-ray emission from a deeply embedded WR star WR 121a lying towards the galactic center. Periodic variations of ~ 4.1 d are observed in the *Chandra* X-ray light curve of WR 121a. The X-rays are emitted by the hot plasma heated by the colliding winds of WR 121a. The modulations of both hard and soft X-ray flux with the orbital phase are due to the eclipsing of WCR by the companion star in WR 121a system. The flux increases by $\sim 53\%$ of the minimum value in the hard X-rays. *Chandra* was not able to resolve two binary components of WR 121a even with its unprecedented spatial resolution ($\sim 0.5''$ per pixel). It was found to be a point source located close to the position of W43 #1b. The two components of the thermal plasma emission model with temperatures of cool and hot components as 0.98 ± 0.34 and 3.55 ± 0.69 keV, respectively, could explain the X-ray spectra of WR 121a. The X-rays are heavily absorbed below 2.5 keV as WR 121a lies in the deeper regions of the galaxy. The most plausible binary orbit of WR 121a is circular with an orbital period of 4.1 d. The winds interact at sub-terminal speeds in this short period massive binary and radiative cooling of the wind plasma is important to explain the observed X-ray emission. The wider shock opening angles derived for WR 121a are in the favor of ongoing radiative braking and inhibition in the WCR for the case of an early O-type companion star.

Multi-wavelength observations of WR 121a are necessary to identify the accurate spectral types of the binary components and to explain the dynamics of winds more precisely in its WCR.

(iv) **Chapter 5** is based on the extensive monitoring of an episodic dust maker, WR 125, using archival and new data in X-rays and in the (near and mid) infrared. The X-ray emission, especially the soft X-rays, is observed to switch to a low state in 2020 pointing toward the next periastron passage in WR 125. The drop in the soft X-ray emission could be attributed to a significant photoelectric absorption close to periastron, when the X-ray emission from the WCR may be more quantitatively absorbed by the dense WC wind. Looking at the previous low X-ray emission observed in the year 1991, an orbital period of 28-29 yrs is suggested for WR 125. This is further supported by enhanced infra-red emission observed in 2019-2021 by our very recent measurements. The excess infra-red emission is attributed to the circumstellar dust formation. The present infra-red outburst is identical to the one observed at the beginning of the 1990s that lasted for about 3-4 yrs due to the formation of dust close to the periastron passage of an eccentric long-period binary. Once again, the time interval between these two events is about 28-29 yrs.

Although the present analysis confirms that periastron passage occurred in 2019-2021, still care has to be taken while estimating the orbital period of WR 125. The lack of data in both the X-ray and infra-red light curves prevents us to completely rule out a period twice as short as of 28-29 yrs. The 2004-2005 epoch has not been covered by the present X-ray and infra-red observations where another un-noticed periastron passage could have occurred. Future observations around the year 2034 would decide which of the short or long period hypothesis for WR 125 is correct.

(v) **Chapter 6** investigates the stellar wind properties of O+O binaries through their X-ray and linear polarimetric observations. We have chosen short period massive binaries for such a study to gather complete information about the radiation emission over the full orbital cycle of the systems. The X-ray study of HD 93205 consisting of O3.5 V((f)) and O8 V star in an eccentric orbit of period 6.08 d suggested that the wind-wind collision is the source of X-ray radiations additional to the intrinsic X-ray emission from the individual stars arising from their winds instabilities. The X-ray flux varies with binary separation and the ratio of the maximum to minimum flux is found to be 1.58 ± 0.11 , 1.60 ± 0.11 , and 2.57 ± 0.20 for the broad₁, soft, and hard₁ energy bands, respectively, in qualitative agreement with wind-wind collision model but few deviations are also reported from the 1/D trend. The average value of temperatures corresponding to the two thermal plasma emission models equal to ~ 0.20 keV and ~ 0.60 keV indicate that X-ray emission from HD 93205 is

7. SUMMARY AND FUTURE PROSPECTS

rather soft.

Another O5.5 V-III+O6 V-III binary called DH Cep has been explored using optical (B, V, R, and I bands) linear polarimetric data-sets. The average intrinsic linear polarization in each of the photometric bands is found to be less than 1% over six nights of observations. The degree of polarization as well as the polarization angle appear to be orbital phase-dependent. The significant polarization variability noticed towards shorter wavelengths (*i.e.* B and V bands) is indicative of the asymmetric circumstellar envelope.

7.2 Future prospects

In this thesis, we focused on massive O-type and WR stars to explore the huge radiation driven outflows from the massive stellar surface of these luminous objects. The aim is fulfilled using the X-ray, optical polarimetric, and infra-red photometric observations of massive binaries. There are few other techniques that might be extremely useful for the characterization of the physical properties of massive stars and their winds. These are the subject of future studies and are explained as follows

–

(i) We have initiated a polarimetric observation campaign of a sample of 12 massive binaries consisting of WR+O as well as O+O systems. In this thesis, the polarimetric results obtained for the O+O binary DH Cep have been presented. Until now, the phase coverage of DH Cep and other sources is sparse. More data-sets are observed to complete the polarization light curves and the data is being processed. Our next aim is to estimate the parameters like inclination (i), mass loss rate, and the distribution of the scattering material around the binary stars by using available standard models (St. -Louis et al., 1987). The inclination of the binary systems can also be found from their photometric light curves. But this method requires a sufficiently high value of i to yield eclipses, either involving the stars themselves or from the phase-dependent diminution of the light from one star as it orbits in the wind of the other star. On the other hand, the phase-dependent linear polarization modulations are used extensively for the low inclination WR+O binaries. Once the value of i is known, accurate masses of the binary components can be estimated, which is difficult otherwise. This method also provides reliable mass-loss rates since intrinsic polarization is largely expected to be originating from the inner parts of the wind, where the density is large. Therefore, the uncertainties of the wind parameters in its outer parts, which are involved in other techniques

of finding the mass-loss rates like radio-based data, do not affect the results (St.-Louis et al., 1988).

(ii) The next goal is comprised of optical and infra-red spectroscopy using 3.6 m DOT. An important aspect of understanding the massive stars is their multiplicity investigations. The mutual interaction between the stars present in short-period binaries, in the form of mass exchange or common envelope formation, may strongly affect them. Further, the wind interaction among components of massive systems is the source of dust formation, particle acceleration, thermal X-ray emission, and other non-thermal emission mechanisms. In order to describe these processes, accurate information about the orbital elements of massive binaries is required which is possible through spectroscopic studies. In this regard, the two spectrographs namely ADFOSC and TANSPEC mounted with 3.6 m DOT can be utilized to investigate massive stellar systems present in the Northern hemisphere. ADFOSC is an optical low-resolution slit spectrograph with imaging capabilities having wavelength sensitivity between $0.35 \mu\text{m}$ to $0.9 \mu\text{m}$. Whereas TANSPEC is the medium resolution spectrograph covering from $0.55 \mu\text{m}$ in optical up to $2.54 \mu\text{m}$ in NIR with a resolving power of ~ 2750 (Sagar et al., 2020). Stellar spectroscopic studies to unravel the orbital motion of the stars through radial velocity measurements leads to the determination of their minimum masses ($M \sin^3 i$) which combined with the optical polarimetric measurements to determine the inclination can lead to absolute masses of the components.

Additionally, the multiple systems deeply embedded in the galactic layers are the appropriate targets to be observed with such large telescopes to inspect their stellar properties. For example, consider the case of WR 121a which is opaque to optical wavelengths. The infra-red spectroscopy and high-resolution imaging of WR 121a with 3.6 m DOT in the future would help to resolve and identify the precise spectral type as well as luminosity class of its components. Further, the techniques to disentangle the spectra may even allow us to separate the spectra of the binary components and confront them to stellar atmosphere models to determine various parameters including element abundances (e.g. Mahy et al. 2017; Sana et al. 2012b).

(iii) As we know that massive binaries are also responsible for accelerating particles to relativistic speeds in their wind interaction region giving rise to radio synchrotron and non-thermal high energy radiation emission. Therefore, the radio spectrum of massive stars is composite having both the components of thermal emission from the winds and non-thermal radio synchrotron emission by the relativistic particles. The lower frequencies observed in the radio spectrum are attributed to the synchrotron emission while above 1 GHz frequency, the spectrum may be dominated

7. SUMMARY AND FUTURE PROSPECTS

by thermal emission (De Becker et al., 2017). Thus, the lower frequency spectral domain is ideal to investigate non-thermal processes which is covered by the upgraded Giant Metrewave Radio Telescope (uGMRT; Gupta et al. 2017) in the frequency range 150 MHz–1.4 GHz. The uGMRT observations would allow identification of new PACWBs to be included in the existing catalogue (De Becker et al., 2017; De Becker & Raucq, 2013) which would further help to investigate the fraction of particle accelerators among massive binaries. The high sensitivity observations from uGMRT below 1.4 GHz are a boon to explore non-thermal radio emission from massive binaries which is few tens of mJy for the brightest sources. Therefore, there might be a pool of non-thermal emitters to be discovered at the sub-mJy level where the uGMRT would be really important.

The particle acceleration may also be explored in the high energy X-rays (above 10 keV) as performed for WR 25 using *NuSTAR* data. A similar approach can also be applied to observe massive binaries with LAXPC onboard *AstroSat* in 3-80 keV energy range. The high energy spectral analysis is important to derive the spectral index of the high energy emission which is directly related to the index of the relativistic electrons population responsible for the radio synchrotron emission as well. Therefore, the optical and infra-red observations from 3.6 m DOT are useful for the determination of the orbital parameters and the characterization of the nature of the components in the multiple systems. This information will further be fed to radio data analysis from uGMRT and hard X-ray investigations with *AstroSat* to identify more particle accelerators and develop sophisticated models to understand the physics of CWBs.

References

- Abbott D. C., Beiging J. H., Churchwell E., Torres A. V., 1986, ApJ, 303, 239 [132](#), [143](#), [144](#)
- Abbott D. C., Bieging J. H., Churchwell E., 1981, ApJ, 250, 645 [22](#)
- Abbott D. C., Bieging J. H., Churchwell E., Cassinelli J. P., 1980, ApJ, 238, 196 [22](#)
- Abbott D. C., Lucy L. B., 1985, ApJ, 288, 679 [15](#)
- Acerro F., Ackermann M., Ajello M., et al., 2013, ApJ, 773, 1, 77 [106](#)
- Albacete-Colombo J. F., Damiani F., Micela G., Sciortino S., Harnden F. R. J., 2008, A&A, 490, 3, 1055 [151](#)
- Albacete Colombo J. F., Méndez M., Morrell N. I., 2003, MNRAS, 346, 3, 704 [151](#)
- Allen D. A., Swings J. P., Harvey P. M., 1972, A&A, 20, 333 [129](#)
- Anders E., Grevesse N., 1989, Geochim. Cosmochim. Acta, 53, 1, 197 [57](#)
- Anderson G. E., Gaensler B. M., Kaplan D. L., et al., 2011, ApJ, 727, 2, 105 [106](#), [115](#), [119](#)
- Antokhin I. I., Owocki S. P., Brown J. C., 2004, ApJ, 611, 1, 434 [160](#)
- Antokhin I. I., Rauw G., Vreux J. M., van der Hucht K. A., 2003, in Magnetic Fields in O, B and A Stars: Origin and Connection to Pulsation, Rotation and Mass Loss, edited by L. A. Balona, H. F. Henrichs, R. Medupe, vol. 305 of Astronomical Society of the Pacific Conference Series, 383 [151](#)
- Antokhin I. I., Rauw G., Vreux J. M., van der Hucht K. A., Brown J. C., 2008, A&A, 477, 2, 593 [151](#), [159](#)

REFERENCES

- Arnaud K. A., 1996, in *Astronomical Data Analysis Software and Systems V*, edited by G. H. Jacoby, J. Barnes, vol. 101 of *Astronomical Society of the Pacific Conference Series*, 17 [54](#)
- Arora B., Pandey J. C., 2020, *ApJ*, 891, 2, 104 [25](#), [105](#), [143](#), [160](#)
- Arora B., Pandey J. C., De Becker M., 2019a, *MNRAS*, 487, 2, 2624 [25](#), [69](#), [107](#), [158](#), [160](#)
- Arora B., Pandey J. C., Joshi A., De Becker M., 2019b, *Bulletin de la Societe Royale des Sciences de Liege*, 88, 287 [25](#), [149](#)
- Baug T., Ojha D. K., Ghosh S. K., et al., 2018, *Journal of Astronomical Instrumentation*, 7, 1, 1850003 [xxviii](#), [59](#), [60](#)
- Beals C. S., 1929, *MNRAS*, 90, 202 [4](#)
- Beals C. S., 1938, *Trans. IAU*, 6, 248 [4](#)
- Bell A. R., 1978, *MNRAS*, 182, 147 [19](#)
- Benaglia P., De Becker M., Ishwara-Chandra C. H., Intema H. T., Isequilla N. L., 2020, *PASA*, 37, e030 [143](#)
- Benaglia P., Romero G. E., 2003, *A&A*, 399, 1121 [29](#)
- Benaglia P., Romero G. E., Stevens I. R., Torres D. F., 2001, *A&A*, 366, 605 [30](#)
- Berghoefer T. W., Schmitt J. H. M. M., Danner R., Cassinelli J. P., 1997, *A&A*, 322, 167 [28](#), [159](#)
- Bhalerao V., Bhattacharya D., Vibhute A., et al., 2017, *Journal of Astrophysics and Astronomy*, 38, 2, 31 [36](#)
- Bhatt H., Pandey J. C., Kumar B., Sagar R., Singh K. P., 2010, *New A*, 15, 8, 755 [161](#)
- Blum R. D., Daminieli A., Conti P. S., 1999, *AJ*, 117, 3, 1392 [105](#), [106](#), [121](#), [126](#)
- Bohannon B., Crowther P. A., 1999, *ApJ*, 511, 1, 374 [4](#)
- Bulgarelli A., Fioretti V., Parmiggiani N., et al., 2019, *A&A*, 627, A13 [106](#)
- Burrows D. N., Hill J. E., Nousek J. A., et al., 2005, *Space Sci. Rev.*, 120, 3-4, 165 [42](#)

REFERENCES

- Cappa C., Goss W. M., van der Hucht K. A., 2004, *AJ*, 127, 5, 2885 [132](#), [143](#), [144](#)
- Cassinelli J. P., Ignace R., Waldron W. L., Cho J., Murphy N. A., Lazarian A., 2008, *ApJ*, 683, 2, 1052 [123](#)
- Cassinelli J. P., Miller N. A., Waldron W. L., MacFarlane J. J., Cohen D. H., 2001, *ApJ*, 554, 1, L55 [28](#)
- Castor J. I., Abbott D. C., Klein R. I., 1975, *ApJ*, 195, 157 [13](#)
- Cazorla C., Nazé Y., Rauw G., 2014, *A&A*, 561, A92 [101](#)
- Chapman J. M., Leitherer C., Koribalski B., Bouter R., Storey M., 1999, *ApJ*, 518, 2, 890 [99](#)
- Chaves R. C. G., Renaud M., Lemoine-Goumard M., Goret P., 2008, in *American Institute of Physics Conference Series*, edited by F. A. Aharonian, W. Hofmann, F. Rieger, vol. 1085, 372–375 [106](#)
- Chené A.-N., St-Louis N., Moffat A. F. J., Gayley K. G., 2020, *ApJ*, 903, 2, 113 [25](#)
- Cherepashchuk A. M., 1976, *Soviet Astronomy Letters*, 2, 138 [16](#), [28](#), [119](#), [129](#)
- Cherepashchuk A. M., 1990, *SvA*, 34, 481 [127](#)
- Cherepashchuk A. M., Karetnikov V. G., 2003, *Astronomy Reports*, 47, 1, 38 [120](#)
- Chiosi C., Maeder A., 1986, *ARA&A*, 24, 329 [9](#)
- Chlebowski T., Garmany C. D., 1991, *ApJ*, 368, 241 [150](#)
- Conti P. S., 1975, *Memoires of the Societe Royale des Sciences de Liege*, 9, 193 [8](#)
- Conti P. S., Walborn N. R., 1976, *ApJ*, 207, 502 [149](#), [150](#), [151](#)
- Corcoran M. F., 1996, in *Revista Mexicana de Astronomia y Astrofisica Conference Series*, edited by V. Niemela, N. Morrell, P. Pismis, S. Torres-Peimbert, vol. 5 of *Revista Mexicana de Astronomia y Astrofisica Conference Series*, 54–60 [150](#)
- Corcoran M. F., Swank J., Rawley G., Petre R., Schmitt J., Day C., 1995, in *Revista Mexicana de Astronomia y Astrofisica Conference Series*, edited by V. Niemela, N. Morrell, A. Feinstein, vol. 2 of *Revista Mexicana de Astronomia y Astrofisica Conference Series*, 97 [150](#)

REFERENCES

- Crowther P. A., 2004, in EAS Publications Series, edited by M. Heydari-Malayeri, P. Stee, J. P. Zahn, vol. 13 of EAS Publications Series, 1–20 [2](#)
- Crowther P. A., 2007, ARA&A, 45, 1, 177 [xxvii](#), [7](#), [8](#), [94](#), [100](#), [122](#), [126](#)
- Crowther P. A., De Marco O., Barlow M. J., 1998, MNRAS, 296, 2, 367 [4](#)
- Crowther P. A., Hillier D. J., Smith L. J., 1995, A&A, 293, 172 [5](#)
- Crowther P. A., Walborn N. R., 2011, MNRAS, 416, 2, 1311 [3](#), [4](#), [69](#)
- Cutri R. M., Skrutskie M. F., van Dyk S., et al., 2003, 2MASS All Sky Catalog of point sources. [109](#)
- De Becker M., 2007, A&A Rev., 14, 3-4, 171 [24](#), [97](#), [98](#)
- De Becker M., 2015, MNRAS, 451, 1, 1070 [133](#)
- De Becker M., 2018, A&A, 620, A144 [100](#)
- De Becker M., Benaglia P., Romero G. E., Peri C. S., 2017, A&A, 600, A47 [100](#), [130](#), [170](#)
- De Becker M., Hutsemékers D., Gosset E., 2014, New Astronomy, 29, 75 [97](#)
- De Becker M., Isequilla N. L., Benaglia P., 2019, A&A, 623, A163 [143](#)
- De Becker M., Raucq F., 2013, A&A, 558, A28 [xxxviii](#), [19](#), [31](#), [96](#), [99](#), [130](#), [170](#)
- De Becker M., Rauw G., Pittard J. M., Sana H., Stevens I. R., Romero G. E., 2007, A&A, 472, 3, 905 [101](#)
- De Becker M., Rauw G., Sana H., et al., 2006, MNRAS, 371, 3, 1280 [101](#), [107](#)
- de Boer K., Seggewiss W., 2008, Stars and Stellar Evolution [6](#), [8](#)
- de Wilt P., Rowell G., Walsh A. J., et al., 2017, MNRAS, 468, 2, 2093 [106](#)
- den Herder J. W., Brinkman A. C., Kahn S. M., et al., 2001, A&A, 365, L7 [44](#)
- Dougherty S. M., Beasley A. J., Claussen M. J., Zauderer B. A., Bolingbroke N. J., 2005, ApJ, 623, 1, 447 [130](#)
- Dougherty S. M., Pittard J. M., Kasian L., Coker R. F., Williams P. M., Lloyd H. M., 2003, A&A, 409, 217 [24](#)

- Dougherty S. M., Williams P. M., 2000, *MNRAS*, 319, 4, 1005 [99](#)
- Drew J. E., 1990, in *Properties of Hot Luminous Stars*, edited by C. D. Garmany, vol. 7 of *Astronomical Society of the Pacific Conference Series*, 230–241 [100](#)
- Drissen L., Moffat A. F. J., Bastien P., Lamontagne R., Tapia S., 1986, *ApJ*, 306, 215 [161](#)
- Drissen L., Robert C., Moffat A. F. J., 1992, *ApJ*, 386, 288 [70](#)
- Drury L. O., 1983, *Reports on Progress in Physics*, 46, 8, 973 [19](#)
- Eichler D., Usov V., 1993, *ApJ*, 402, 271 [17](#), [29](#), [125](#)
- Elmegreen B. G., Lada C. J., 1977, *ApJ*, 214, 725 [1](#)
- Farnier C., Walter R., Leyder J. C., 2011, *A&A*, 526, A57 [98](#)
- Feldmeier A., Puls J., Pauldrach A. W. A., 1997, *A&A*, 322, 878 [28](#), [120](#)
- Fermi E., 1949, *Physical Review*, 75, 8, 1169 [19](#)
- Figer D. F., McLean I. S., Najarro F., 1997, *ApJ*, 486, 1, 420 [5](#)
- Friend D. B., Abbott D. C., 1986, *ApJ*, 311, 701 [15](#)
- Gagné M., Fehon G., Savoy M. R., et al., 2011, *ApJS*, 194, 1, 5 [151](#), [159](#)
- Gagné M., Fehon G., Savoy M. R., Cartagena C. A., Cohen D. H., Owocki S. P., 2012, in *Proceedings of a Scientific Meeting in Honor of Anthony F. J. Moffat*, edited by L. Drissen, C. Robert, N. St-Louis, A. F. J. Moffat, vol. 465 of *Astronomical Society of the Pacific Conference Series*, 301 [119](#), [125](#)
- Gaia Collaboration, Brown A. G. A., Vallenari A., et al., 2020, *arXiv e-prints*, arXiv:2012.01533 [159](#)
- Gamen R., Gosset E., Morrell N., et al., 2006, *A&A*, 460, 3, 777 [27](#), [70](#), [71](#), [82](#), [83](#), [95](#)
- Gamen R., Gosset E., Morrell N. I., et al., 2008, in *Revista Mexicana de Astronomia y Astrofisica Conference Series*, vol. 33, 91–93 [70](#)

REFERENCES

- Garmire G. P., Bautz M. W., Ford P. G., Nousek J. A., Ricker George R. J., 2003, Advanced CCD imaging spectrometer (ACIS) instrument on the Chandra X-ray Observatory, vol. 4851 of Society of Photo-Optical Instrumentation Engineers (SPIE) Conference Series, 28–44 [38](#)
- Gayley K. G., 1995, *ApJ*, 454, 410 [14](#)
- Gayley K. G., Owocki S. P., Cranmer S. R., 1997, *ApJ*, 475, 2, 786 [93](#), [124](#)
- Gehrels N., Chincarini G., Giommi P., et al., 2004, *ApJ*, 611, 2, 1005 [42](#)
- Gehrels N., Ramirez-Ruiz E., Fox D. B., 2009, *ARA&A*, 47, 1, 567 [1](#)
- Georgy C., Ekström S., Hirschi R., Meynet G., Groh J. H., Eggenberger P., 2015, in *Wolf-Rayet Stars*, edited by W.-R. Hamann, A. Sander, H. Todt, 229–232 [9](#)
- Georgy C., Ekström S., Meynet G., et al., 2012, *A&A*, 542, A29 [9](#)
- Giacconi R., Branduardi G., Briel U., et al., 1979, *ApJ*, 230, 540 [66](#)
- Gosset E., 2007, Habilitation thesis. Univ. Liège, Belgium [91](#), [95](#)
- Gosset E., Nazé Y., 2016, *A&A*, 590, A113 [101](#)
- Grave J. M. C., Kumar M. S. N., 2007, *A&A*, 462, 3, L37 [106](#)
- Gupta Y., Ajithkumar B., Kale H. S., et al., 2017, *Current Science*, 113, 4, 707 [170](#)
- H. E. S. S. Collaboration, Abdalla H., Abramowski A., et al., 2018, *A&A*, 612, A1 [106](#)
- Hamaguchi K., Corcoran M. F., Pittard J. M., et al., 2018, *Nature Astronomy*, 2, 731 [101](#)
- Hamann W. R., Gräfener G., Liermann A., 2006, *A&A*, 457, 3, 1015 [5](#)
- Hamann W. R., Gräfener G., Liermann A., et al., 2019, *A&A*, 625, A57 [121](#), [122](#)
- Harnden F. R. J., Branduardi G., Elvis M., et al., 1979, *ApJ*, 234, L51 [27](#)
- Harrison F. A., Craig W. W., Christensen F. E., et al., 2013, *ApJ*, 770, 2, 103 [xxviii](#), [39](#), [40](#), [97](#)
- Heiles C., 2000, *AJ*, 119, 2, 923 [162](#)

- Hiltner W. A., Schild R. E., 1966, *ApJ*, 143, 770 [4](#)
- Horne J. H., Baliunas S. L., 1986, *ApJ*, 302, 757 [110](#), [111](#)
- Iben Icko J., Livio M., 1993, *PASP*, 105, 1373 [11](#)
- Janesick J., Blouke M., 1987, *S&T*, 74, 238 [35](#)
- Jansen F., Lumb D., Altieri B., et al., 2001, *A&A*, 365, L1 [43](#)
- Jenkins E. B., 2019, *ApJ*, 872, 1, 55 [154](#)
- Kahn S. M., Leutenegger M. A., Cottam J., et al., 2001, *A&A*, 365, L312 [28](#)
- Kashi A., Soker N., 2009, *MNRAS*, 394, 2, 923 [xxvii](#), [16](#)
- Kennicutt Robert C. J., 1998, *ARA&A*, 36, 189 [1](#)
- Kennicutt R. C., Evans N. J., 2012, *ARA&A*, 50, 531 [1](#)
- Koyama K., Tsunemi H., Dotani T., et al., 2007, *PASJ*, 59, 23 [41](#)
- Kudritzki R. P., 1996, in *Liege International Astrophysical Colloquia*, edited by J. M. Vreux, A. Detal, D. Fraipont-Caro, E. Gosset, G. Rauw, vol. 33 of *Liege International Astrophysical Colloquia*, 467 [15](#)
- Kumar B., Omar A., Maheswar G., et al., 2018, *Bulletin de la Societe Royale des Sciences de Liege*, 87, 29 [58](#)
- Lamers H. J. G. L. M., Snow T. P., Lindholm D. M., 1995, *ApJ*, 455, 269 [26](#)
- Lata S., Pandey A. K., Panwar N., Chen W. P., Samal M. R., Pandey J. C., 2016, *MNRAS*, 456, 3, 2505 [161](#)
- Le Bouquin J. B., Sana H., Gosset E., et al., 2017, *A&A*, 601, A34 [146](#)
- Leitherer C., Chapman J. M., Koribalski B., 1995, *ApJ*, 450, 289 [99](#)
- Leitherer C., Chapman J. M., Koribalski B., 1997, *ApJ*, 481, 2, 898 [99](#)
- Leyder J. C., Walter R., Rauw G., 2008, *A&A*, 477, 3, L29 [101](#)
- Lindegren L., Hernández J., Bombrun A., et al., 2018, *A&A*, 616, A2 [98](#), [161](#), [162](#)
- Lomax J. R., Nazé Y., Hoffman J. L., et al., 2015, *A&A*, 573, A43 [107](#), [124](#)

REFERENCES

- Lomb N. R., 1976, *Ap&SS*, 39, 2, 447 [82](#), [110](#)
- Longair M. S., 1994, *High energy astrophysics*, vol. 2 [xxvii](#), [20](#)
- Lucy L. B., 1982, *ApJ*, 255, 286 [28](#), [119](#)
- Lucy L. B., Solomon P. M., 1970, *ApJ*, 159, 879 [13](#)
- Lucy L. B., White R. L., 1980, *ApJ*, 241, 300 [28](#)
- Lumb D. H., Schartel N., Jansen F. A., 2012, arXiv e-prints, arXiv:1202.1651 [xxviii](#), [44](#)
- Luo D., McCray R., Mac Low M.-M., 1990, *ApJ*, 362, 267 [91](#), [122](#)
- Luque-Escamilla P. L., Muñoz-Arjonilla A. J., Sánchez-Sutil J. R., Martí J., Combi J. A., Sánchez-Ayaso E., 2011, *A&A*, 532, A92 [105](#), [106](#), [107](#), [109](#), [115](#), [121](#), [122](#)
- Maeder A., Meynet G., 1987, *A&A*, 182, 243 [xxvii](#), [9](#), [10](#)
- Maeder A., Meynet G., 2012, *Reviews of Modern Physics*, 84, 1, 25 [9](#)
- Mahy L., Damerджи Y., Gosset E., et al., 2017, *A&A*, 607, A96 [169](#)
- Mainzer A., Bauer J., Cutri R. M., et al., 2014, *ApJ*, 792, 1, 30 [66](#)
- Mainzer A., Bauer J., Grav T., et al., 2011, *ApJ*, 731, 1, 53 [66](#)
- Marchenko S. V., Moffat A. F. J., Koenigsberger G., 1994, *ApJ*, 422, 810 [124](#)
- Marcote B., Callingham J. R., De Becker M., et al., 2021, *MNRAS*, 501, 2, 2478 [130](#)
- Martins F., Mahy L., Hervé A., 2017, *A&A*, 607, A82 [161](#)
- Mason K. O., Breeveld A., Much R., et al., 2001, *A&A*, 365, L36 [44](#)
- Midooka T., Sugawara Y., Ebisawa K., 2019, *MNRAS*, 484, 2, 2229 [132](#), [133](#), [134](#), [136](#), [142](#)
- Mitsuda K., Bautz M., Inoue H., et al., 2007, *PASJ*, 59, S1 [xxviii](#), [40](#), [41](#)
- Moffat A. F. J., 1978, *A&A*, 68, 41 [69](#)
- Morrell N. I., Barbá R. H., Niemela V. S., et al., 2001, *MNRAS*, 326, 1, 85 [27](#), [151](#)

- Morris P. W., Brownsberger K. R., Conti P. S., Massey P., Vacca W. D., 1993, *ApJ*, 412, 324 [25](#)
- Morton D. C., 1967, *ApJ*, 150, 535 [26](#)
- Muijres L. E., Vink J. S., de Koter A., Müller P. E., Langer N., 2012, *A&A*, 537, A37 [94](#), [100](#), [121](#), [122](#), [126](#)
- Münch G., 1950, *ApJ*, 112, 266 [124](#)
- Murray S. S., Austin G. K., Chappell J. H., et al., 2000, in *X-Ray Optics, Instruments, and Missions III*, edited by J. E. Truemper, B. Aschenbach, vol. 4012 of Society of Photo-Optical Instrumentation Engineers (SPIE) Conference Series, 68–80 [38](#)
- Nazé Y., 2009, *A&A*, 506, 2, 1055 [159](#)
- Nazé Y., Broos P. S., Oskinova L., et al., 2011, *ApJS*, 194, 1, 7 [151](#), [159](#)
- Nazé Y., Gosset E., Mahy L., Parkin E. R., 2017, *A&A*, 607, A97 [101](#)
- Nazé Y., Mahy L., Damerdji Y., et al., 2012, *A&A*, 546, A37 [100](#)
- Nguyen Luong Q., Motte F., Schuller F., et al., 2011, *A&A*, 529, A41 [105](#)
- Ojha D., Ghosh S. K., Sharma S., et al., 2018, *Bulletin de la Societe Royale des Sciences de Liege*, 87, 58 [60](#)
- Omar A., Kumar B., Gopinathan M., Sagar R., 2017, *Current Science*, 113, 4, 682 [58](#)
- Oskinova L. M., 2005, *MNRAS*, 361, 2, 679 [125](#)
- Oskinova L. M., Hamann W. R., 2008, *MNRAS*, 390, 1, L78 [107](#)
- Owocki S., 2013, *Stellar Winds*, vol. 4, 735 [xxviii](#), [27](#)
- Owocki S. P., Castor J. I., Rybicki G. B., 1988, *ApJ*, 335, 914 [28](#), [119](#)
- Owocki S. P., Gayley K. G., 1995, *ApJ*, 454, L145 [160](#)
- Pallavicini R., Golub L., Rosner R., Vaiana G. S., Ayres T., Linsky J. L., 1981, *ApJ*, 248, 279 [27](#)
- Panagia N., Felli M., 1975, *A&A*, 39, 1 [22](#), [99](#), [130](#)

REFERENCES

- Pandey J. C., Pandey S. B., Karmakar S., 2014, *ApJ*, 788, 1, 84 [70](#), [71](#), [72](#), [73](#), [74](#), [80](#), [81](#), [82](#), [95](#), [107](#)
- Parkin E. R., Pittard J. M., Nazé Y., Blomme R., 2014, *A&A*, 570, A10 [101](#)
- Pittard J. M., Dougherty S. M., 2006, *MNRAS*, 372, 2, 801 [29](#)
- Pittard J. M., Dougherty S. M., Coker R. F., O'Connor E., Bolingbroke N. J., 2006, *A&A*, 446, 3, 1001 [xxviii](#), [24](#)
- Pittard J. M., Parkin E. R., 2010, *MNRAS*, 403, 4, 1657 [92](#), [101](#), [129](#)
- Pittard J. M., Stevens I. R., 1997, *MNRAS*, 292, 2, 298 [158](#)
- Plaskett J. S., Pearce J. A., 1931, *Publications of the Dominion Astrophysical Observatory Victoria*, 5, 1 [2](#)
- Podsiadlowski P., 2001, in *Evolution of Binary and Multiple Star Systems*, edited by P. Podsiadlowski, S. Rappaport, A. R. King, F. D'Antona, L. Burderi, vol. 229 of *Astronomical Society of the Pacific Conference Series*, 239 [11](#)
- Pollock A. M. T., 1987, *ApJ*, 320, 283 [28](#), [69](#), [132](#)
- Pollock A. M. T., Corcoran M. F., 2006, *A&A*, 445, 3, 1093 [70](#)
- Pollock A. M. T., Haberl F., Corcoran M. F., 1995, in *Wolf-Rayet Stars: Binaries; Colliding Winds; Evolution*, edited by K. A. van der Hucht, P. M. Williams, vol. 163 of *IAU Symposium*, 512 [69](#), [132](#)
- Prilutskii O. F., Usov V. V., 1976, *SvA*, 20, 2 [16](#), [28](#), [119](#), [129](#)
- Prinja R. K., Barlow M. J., Howarth I. D., 1990, *ApJ*, 361, 607 [26](#)
- Puls J., Springmann U., Lennon M., 2000, *A&AS*, 141, 23 [15](#)
- Puls J., Vink J. S., Najarro F., 2008, *A&A Rev.*, 16, 3-4, 209 [13](#), [100](#)
- Raassen A. J. J., van der Hucht K. A., Mewe R., et al., 2003, *A&A*, 402, 653 [70](#), [119](#)
- Rappoldi A., Lucarelli F., Pittori C., et al., 2016, *A&A*, 587, A93 [106](#)
- Rautela B. S., Joshi G. C., Pandey J. C., 2004, *Bulletin of the Astronomical Society of India*, 32, 3, 159 [xxviii](#), [63](#), [64](#), [65](#)

- Rauw G., Blomme R., Nazé Y., et al., 2016, *A&A*, 589, A121 [101](#), [122](#)
- Rauw G., Nazé Y., 2016, *Advances in Space Research*, 58, 5, 761 [101](#), [120](#)
- Raymond J. C., Smith B. W., 1977, *ApJS*, 35, 419 [56](#), [119](#)
- Reitberger K., Kissmann R., Reimer A., Reimer O., 2014, *ApJ*, 789, 1, 87 [29](#)
- Roberts D. H., Lehar J., Dreher J. W., 1987, *AJ*, 93, 968 [112](#)
- Runacres M. C., Owocki S. P., 2002, *A&A*, 381, 1015 [100](#)
- Sagar R., Kumar B., Sharma S., 2020, *Journal of Astrophysics and Astronomy*, 41, 1, 33 [169](#)
- Sana H., de Mink S. E., de Koter A., et al., 2012a, *Science*, 337, 6093, 444 [16](#)
- Sana H., Evans C. J., 2011, in *Active OB Stars: Structure, Evolution, Mass Loss, and Critical Limits*, edited by C. Neiner, G. Wade, G. Meynet, G. Peters, vol. 272, 474–485 [16](#)
- Sana H., Nazé Y., O’Donnell B., Rauw G., Gosset E., 2008, *New Astronomy*, 13, 4, 202 [101](#)
- Sana H., Stap F. A., de Koter A., et al., 2012b, in *Proceedings of a Scientific Meeting in Honor of Anthony F. J. Moffat*, edited by L. Drissen, C. Robert, N. St-Louis, A. F. J. Moffat, vol. 465 of *Astronomical Society of the Pacific Conference Series*, 263 [169](#)
- Sana H., Stevens I. R., Gosset E., Rauw G., Vreux J. M., 2004, *MNRAS*, 350, 3, 809 [101](#)
- Scargle J. D., 1982, *ApJ*, 263, 835 [82](#), [110](#)
- Schmidt G. D., Elston R., Lupie O. L., 1992, *AJ*, 104, 1563 [64](#)
- Seetha S., Ramadevi M. C., Babu V. C., et al., 2006, *Advances in Space Research*, 38, 12, 2995 [37](#)
- Seward F. D., Chlebowski T., 1982, *ApJ*, 256, 530 [69](#), [150](#)
- Seward F. D., Forman W. R., Giacconi R., et al., 1979, *ApJ*, 234, L55 [27](#), [69](#), [150](#)
- Shenar T., Sablowski D. P., Hainich R., et al., 2019, *A&A*, 627, A151 [xxvii](#), [11](#), [12](#)

REFERENCES

- Singh K. P., 2016, in *Accretion Processes in Cosmic Sources*, 7 [xxviii](#), [37](#)
- Singh K. P., Stewart G. C., Westergaard N. J., et al., 2017, *Journal of Astrophysics and Astronomy*, 38, 2, 29 [36](#), [50](#)
- Singh K. P., Tandon S. N., Agrawal P. C., et al., 2014, in *Space Telescopes and Instrumentation 2014: Ultraviolet to Gamma Ray*, edited by T. Takahashi, J.-W. A. den Herder, M. Bautz, vol. 9144 of *Society of Photo-Optical Instrumentation Engineers (SPIE) Conference Series*, 91441S [36](#)
- Sinvhal S. D., Kandpal C. D., Mahra H. S., Joshi S. C., Srivastava J. B., 1972, in *Optical astronomy with moderate size telescopes*, 20–34 [63](#)
- Skinner S. L., Zhekov S. A., Güdel M., Schmutz W., 2007, *MNRAS*, 378, 4, 1491 [123](#)
- Skinner S. L., Zhekov S. A., Güdel M., Schmutz W., 2015, *ApJ*, 799, 2, 124 [107](#), [125](#)
- Skinner S. L., Zhekov S. A., Güdel M., Schmutz W., Sokal K. R., 2010, *AJ*, 139, 3, 825 [119](#)
- Skinner S. L., Zhekov S. A., Güdel M., Schmutz W., Sokal K. R., 2012, *AJ*, 143, 5, 116 [119](#)
- Skrutskie M. F., Cutri R. M., Stiening R., et al., 2006, *AJ*, 131, 2, 1163 [67](#)
- Smith L. F., 1968, *MNRAS*, 138, 109 [4](#)
- Smith L. F., 1973, in *Wolf-Rayet and High-Temperature Stars*, edited by M. K. V. Bappu, J. Sahade, vol. 49, 15 [4](#)
- Smith L. F., Shara M. M., Moffat A. F. J., 1996, *MNRAS*, 281, 1, 163 [69](#)
- Smith N., 2014, *ARA&A*, 52, 487 [15](#)
- Smith N., Conti P. S., 2008, *ApJ*, 679, 2, 1467 [4](#)
- Smith R. K., Brickhouse N. S., Liedahl D. A., Raymond J. C., 2001, *ApJ*, 556, 2, L91 [56](#)
- Sobolev V. V., 1960, *Moving envelopes of stars* [14](#)
- Sota A., Maíz Apellániz J., Morrell N. I., et al., 2014, *ApJS*, 211, 1, 10 [69](#), [150](#)

REFERENCES

- St. -Louis N., Drissen L., Moffat A. F. J., Bastien P., Tapia S., 1987, ApJ, 322, 870
[163](#), [168](#)
- St. -Louis N., Moffat A. F. J., Drissen L., Bastien P., Robert C., 1988, ApJ, 330,
286 [160](#), [169](#)
- St. -Louis N., Moffat A. F. J., Lapointe L., et al., 1993, ApJ, 410, 342 [161](#)
- Stevens I. R., Blondin J. M., Pollock A. M. T., 1992, ApJ, 386, 265 [17](#), [28](#), [91](#), [93](#),
[119](#), [129](#), [130](#), [158](#)
- Stevens I. R., Pollock A. M. T., 1994, MNRAS, 269, 226 [93](#), [124](#), [160](#)
- Strüder L., Briel U., Dennerl K., et al., 2001, A&A, 365, L18 [43](#)
- Sugizaki M., Mitsuda K., Kaneda H., Matsuzaki K., Yamauchi S., Koyama K., 2001,
ApJS, 134, 1, 77 [106](#)
- Tandon S. N., Subramaniam A., Girish V., et al., 2017, AJ, 154, 3, 128 [36](#)
- Tramper F., Straal S. M., Sanyal D., et al., 2015, A&A, 581, A110 [4](#)
- Truemper J., 1982, Advances in Space Research, 2, 4, 241 [66](#)
- Turner M. J. L., Abbey A., Arnaud M., et al., 2001, A&A, 365, L27 [43](#)
- Usov V. V., 1991, MNRAS, 252, 49 [25](#)
- Usov V. V., 1992, ApJ, 389, 635 [126](#), [158](#)
- van der Hucht K. A., 2001, New A Rev., 45, 3, 135 [xxxiii](#), [5](#), [6](#), [69](#), [106](#), [131](#), [145](#)
- Vink J. S., de Koter A., Lamers H. J. G. L. M., 2000, A&A, 362, 295 [15](#)
- Walborn N. R., 1971, ApJ, 167, L31 [149](#)
- Walborn N. R., 1973, ApJ, 179, 517 [149](#)
- Walborn N. R., 1977, ApJ, 215, 53 [8](#)
- Walborn N. R., 1982, ApJ, 256, 452 [2](#), [8](#)
- Walborn N. R., Nichols-Bohlin J., Panek R. J., 1985, NASA Reference Publication,
1155 [69](#)

REFERENCES

- Walder R., Folini D., 2003, in *A Massive Star Odyssey: From Main Sequence to Supernova*, edited by K. van der Hucht, A. Herrero, C. Esteban, vol. 212, 139 [160](#)
- Weisskopf M. C., Tananbaum H. D., Van Speybroeck L. P., O'Dell S. L., 2000, *Chandra X-ray Observatory (CXO): overview*, vol. 4012 of *Society of Photo-Optical Instrumentation Engineers (SPIE) Conference Series*, 2–16 [38](#)
- Werner M., Reimer O., Reimer A., Egberts K., 2013, *A&A*, 555, A102 [132](#)
- Westerhout G., 1958, *Bull. Astron. Inst. Netherlands*, 14, 215 [105](#)
- White R. L., 1985, *ApJ*, 289, 698 [23](#)
- White R. L., Becker R. H., 1983, *ApJ*, 272, L19 [22](#), [23](#)
- Williams P. M., 1995, in *Wolf-Rayet Stars: Binaries; Colliding Winds; Evolution*, edited by K. A. van der Hucht, P. M. Williams, vol. 163, 335 [25](#), [129](#)
- Williams P. M., 2008, in *Revista Mexicana de Astronomia y Astrofisica Conference Series*, vol. 33 of *Revista Mexicana de Astronomia y Astrofisica Conference Series*, 71–76 [129](#)
- Williams P. M., 2014, *MNRAS*, 445, 2, 1253 [131](#)
- Williams P. M., 2019, *MNRAS*, 488, 1, 1282 [131](#), [140](#)
- Williams P. M., van der Hucht K. A., Bouchet P., et al., 1992, *MNRAS*, 258, 461 [131](#), [132](#), [139](#), [143](#), [144](#)
- Williams P. M., van der Hucht K. A., Kidger M. R., Geballe T. R., Bouchet P., 1994, *MNRAS*, 266, 247 [131](#), [139](#)
- Williams P. M., van der Hucht K. A., Pollock A. M. T., Florkowski D. R., van der Woerd H., Wamsteker W. M., 1990, *MNRAS*, 243, 662 [129](#), [130](#), [142](#)
- Williams P. M., van der Hucht K. A., The P. S., 1987, *A&A*, 182, 91 [25](#)
- Willis A. J., 1982, in *Wolf-Rayet Stars: Observations, Physics, Evolution*, edited by C. W. H. De Loore, A. J. Willis, vol. 99, 87–102 [4](#)
- Wolf C. J. E., Rayet G., 1867, *Academie des Sciences Paris Comptes Rendus*, 65, 292 [3](#)
- Woosley S. E., Bloom J. S., 2006, *ARA&A*, 44, 1, 507 [1](#)

REFERENCES

- Wright A. E., Barlow M. J., 1975, MNRAS, 170, 41 [22](#), [24](#), [99](#), [100](#), [130](#)
- Wright E. L., Eisenhardt P. R. M., Mainzer A. K., et al., 2010, AJ, 140, 6, 1868 [66](#)
- Yadav J. S., Agrawal P. C., Antia H. M., et al., 2016, in Space Telescopes and Instrumentation 2016: Ultraviolet to Gamma Ray, edited by J.-W. A. den Herder, T. Takahashi, M. Bautz, vol. 9905 of Society of Photo-Optical Instrumentation Engineers (SPIE) Conference Series, 99051D [36](#)
- Zhekov S. A., 2012, MNRAS, 422, 2, 1332 [107](#)

Long-term soft and hard X-ray investigation of the colliding wind WN+O binary WR 25

Bharti Arora,^{1,2★} J. C. Pandey^{1★} and M. De Becker^{2★}

¹Aryabhata Research Institute of Observational Sciences, Nainital 263002, India

²Space Sciences, Technologies and Astrophysics Research (STAR) Institute, University of Liège, Quartier Agora, 19c, Allée du 6 Août, B5c, B-4000 Sart Tilman, Belgium

Accepted 2019 May 22. Received 2019 May 22; in original form 2018 July 18

ABSTRACT

We investigated the long-term behaviour in X-rays of the colliding wind binary WR 25, using archival data obtained with *Suzaku*, *Swift*, *XMM–Newton*, and *NuSTAR* spanning over ~ 16 yr. Our analysis reveals phase-locked variations repeating consistently over many consecutive orbits, in agreement with an X-ray emission fully explained by thermal emission from the colliding winds in the 208-d orbit. We report on a significant deviation of the X-ray flux with respect to the $1/D$ trend (expected for adiabatic shocked winds) close to periastron passage. The absence of a drop in post-shock plasma temperature close to periastron suggests this break in trend cannot be explained in terms of reduced pre-shock velocities in this part of the orbit. Finally, *NuSTAR* data reveal a lack of hard X-ray emission (above 10.0 keV) above the background level. Upper limits on a putative non-thermal emission strongly suggest that the sensitivity of present hard X-ray observatories is not sufficient to detect non-thermal emission from massive binaries above 10 keV, unless the wind kinetic power is large enough to significantly feed particle acceleration in the wind–wind interaction.

Key words: radiation mechanisms: non-thermal – binaries: general – stars: early-type – stars: individual: WR 25 – X-rays: stars.

1 INTRODUCTION

Early-type stars with initial masses higher than $10 M_{\odot}$, corresponding to the spectral types from early-B to O, lie in the upper left part of the Hertzsprung–Russell diagram. These objects evolve over short lifetimes (typically of the order of a few to 10 Myr) and during the advanced stages of their evolution, they appear as Wolf–Rayet (WR) stars. Being among the category of massive stars, these hot stars are very luminous and have strong radiatively driven winds. Radiatively driven winds are the winds driven by the transfer of momentum from the photospheric radiation field through photon scattering by strong UV resonance lines. Only a fraction of the ions are directly accelerated by this process; however, other charged particles constituting the stellar wind are dragged along by Coulomb interactions (see e.g. Puls, Vink & Najarro 2008, for a review on this topic). These winds are highly supersonic, travelling with terminal velocities (v_{∞}) ~ 1000 – 3000 km s^{−1} and have mass-loss rates (\dot{M}) in the range from $\dot{M} \sim 10^{-7}$ to $10^{-4} M_{\odot}$ yr^{−1}. As a consequence of these huge stellar winds, massive stars undergo a very significant degree of mass-loss during their lifetime, which not only affects the

evolution of the star itself (e.g. Smith 2014) but also has a strong impact on their surroundings (e.g. Fierlinger et al. 2016).

Massive stars are, more generally, found in binary or higher multiplicity systems with other massive stars. The periods of these binaries range from a couple of days up to many years (or hundreds or thousands of years). When two massive stars are bound together by gravity, their winds interact with each other and part of their kinetic energy is converted into radiation that gives rise to a number of observational signatures spanning a wide range of the electromagnetic spectrum. In this paper, we will focus on the most spectacular observational consequence of the colliding winds which is the X-ray emission that is produced due to the formation of hydrodynamic shocks in the wind collision region (WCR). X-rays provide the invaluable diagnostics of shock physics in colliding-wind massive binaries.

WR 25 (HD 93162) is a bright ($V \sim 8.03$ mag) WR binary system located in the Carina Nebula region. The spectral classification of WR 25 has always been a matter of debate because it displays dilute WN6–7 emission-line spectrum (Walborn, Nichols-Bohlin & Panek 1985) combined with strong absorption features (Moffat 1978). Later on WR 25 was classified as WN6ha by Smith, Shara & Moffat (1996). Looking at various spectral features of WR 25 as observed by many authors, van der Hucht (2001) categorized it as WN6h+O4f. More recently, it has been moved to the class of the ‘hot slash’ objects by Crowther & Walborn (2011) on the basis

* E-mail: bharti@aries.res.in (BA); eewan@aries.res.in (JCP); Michael.DeBecker@uliege.be (MDeB)

Table 1. Orbital parameters of WR 25.

Parameter	Value	Reference
Period (d)	207.85 ± 0.02	1
V_o (km s ⁻¹)	-34.6 ± 0.5	1
K (km s ⁻¹)	44 ± 2	1
Eccentricity	0.50 ± 0.02	1
ω (deg)	215 ± 3	1
$T_{\text{periastron}}$ (HJD)	2451598 ± 1	1
T_{RVmax} (HJD)	2451654 ± 1	1
$a \sin i$ (R _⊙)	156 ± 8	1
$M_{\text{pri}} \sin^3 i$ (M _⊙)	75 ± 7	2
$M_{\text{sec}} \sin^3 i$ (M _⊙)	27 ± 3	2

Notes. Here, V_o is the radial velocity, K is the radial velocity amplitude, ω is the longitude of periastron, $T_{\text{periastron}}$ is the time of periastron passage, T_{RVmax} is the time of maximum radial velocity, $a \sin i$ is the projected semimajor axis, $M_{\text{pri}} \sin^3 i$ and $M_{\text{sec}} \sin^3 i$ are the minimum masses of primary and secondary binary components, respectively. **References:** (1) Gamen et al. (2006); (2) Gamen et al. (2008).

of its P-Cygni H β profile and was given O2.5If*/WN6 spectral type. Sota et al. (2014) detected a visual companion in WR 25 with a separation of 790 mas and V-band magnitude difference of 5.8 mag using the *Hubble Space Telescope* observations. Therefore, the latest spectral classification of WR 25 is O2.5If*/WN6+OB, with no detailed information about the spectral and luminosity class of companion star. WR 25 was seen in X-ray energy range for the first time by Seward et al. (1979) using *Einstein* X-ray observations (0.2–4.0 keV) of the Trumpler 16 open cluster and its surroundings. Later observations of *Einstein* of the same region revealed the ratio of X-ray to bolometric luminosity of $\sim 2 \times 10^{-6}$ for WR 25 is an order of magnitude higher than observed for other WR stars in same region (Seward & Chlebowski 1982). In the X-ray survey of WR stars by Pollock (1987) and Pollock, Haberl & Corcoran (1995), WR 25 was again found to be the brightest X-ray source. Significant variability in the optical polarization was noticed by Drissen, Robert & Moffat (1992) and it was suggested that these modulations were caused by the binary motion of the stars in WR 25. Raassen et al. (2003) attempted to investigate the X-ray emission of WR 25 and could not notice any variability in the emission over a period of 10 yr. But the presence of the Fe XXV emission line in *XMM-Newton* spectrum of WR 25 pointed towards wind collision occurring in the system. Pollock & Corcoran (2006) recognized the variations in the X-ray emission of WR 25 for the first time and suggested that it is a colliding wind binary (CWB) system with a period of about 4 yr. Later in the same year, Gamen et al. (2006) provided the radial velocity solutions for WR 25 and it was found to be a long period (~ 208 d) and eccentric ($e = 0.5$) binary system. Orbital parameters of WR 25 are given in Table 1.

A more detailed X-ray study of WR 25 was performed by Pandey, Pandey & Karmakar (2014) using *Swift* and *XMM-Newton* observations spanning over ~ 10 yr. Looking at enhanced X-ray luminosity accompanied with the phase locked modulations, they concluded that WR 25 is a CWB where the X-ray emission is significantly coming from the hot plasma heated by the colliding winds. Their analysis also pointed towards the hints for a $1/D$ (D is the binary separation) variation of the X-ray luminosity, at least at higher energies (i.e. above 2 keV), while the variations in the softer energy bands were seen to be modulated by absorption effects. In order to investigate these variations, a detailed monitoring of

the X-ray emission as a function of the orbital phase must be conducted. Such an observational study is needed to constrain the stellar winds collision properties and test the present theoretical models which provide a description of the physics of colliding winds. Because colliding-wind binaries span a wide range of stellar and orbital parameters, it is important to study as many such sources as possible in detail, and consequently confront present theories to a significantly relevant sample of observational facts. To date, there are only a few massive binaries with longer periods (longer than ~ 100 d) which were observed with a good phase coverage. In this context, we have executed a deep X-ray study of WR 25 using the long-term archival X-ray data from modern X-ray observatories.

This paper is organized as follows. Section 2 summarizes the observations used and the data-reduction methodology. Section 3 describes the X-ray spectral properties of WR 25. The X-ray light curve analysis is given in Section 4. Our main results are discussed in Section 5, and Section 6 gives the conclusions.

2 OBSERVATIONS AND DATA REDUCTION

We used X-ray observations of WR 25 made by *Suzaku*, *Swift*, *XMM-Newton*, and *NuSTAR* from 2000 July to 2016 August for a total of 226 epochs. A detailed log of these observations is given in Table 2. The orbital phase of each observation was derived by using ephemeris $\text{HJD} = 2451598.0 + 207.85E$ (Gamen et al. 2006). We have also included the *Swift* and *XMM-Newton* data sets that were studied by Pandey et al. (2014). For homogeneity and application of latest calibration, these X-ray data were processed again. The data-reduction procedure adopted for each X-ray observatory is explained as follows.

2.1 *Suzaku*

The *Suzaku* satellite observed Carina Nebula for 10 times from 2005 August to 2013 July taking Eta Carinae at the centre of the X-ray Imaging Spectrometer (XIS–0, 1, and 3) field of view. These data were reprocessed using the currently available calibration data base by running the task AEPipeline (version 1.1.0) for individual observation ID. The data were reduced in accordance with the standard screening criteria. Grade 0, 2, 3, 4, and 6 events were used. Events recorded during the South Atlantic Anomaly passages, Earth elevation angle below 5° and Earth day-time elevation angle below 20° were discarded. Hot and flickering pixels were also removed. Barycentric correction to the clean event files was applied by using the task AEBARYCEN. A circular region of radius 90 arcsec centred at source position was used to extract the source products, which is more than the XIS half power diameter (HPD) of 2 arcmin. However, other circular regions of radius 45 arcsec near the source free region were selected as background regions. Light curves, spectra, and the response files were obtained, from both 3×3 and 5×5 modes collectively, using the XSELECT (version 2.4c) package. Background subtracted light curves and spectra from two front illuminated (FI) XIS chips (XIS–0 and 3) were added using the tasks LCMATH and ADDASCASPEC, respectively. Finally, the back illuminated (BI; XIS–1) and FI XIS spectra were grouped to have minimum 20 counts per energy bin for further spectral analysis.

2.2 *Swift*

WR 25 has been observed frequently by *Swift* X-Ray Telescope (XRT) from 2007 December to 2009 June and 2014 August to 2016

Table 2. Log of observations of WR 25.

Obs. ID	Obs. date	Start time (UT)	Exp./ Eff. Exp. (ks)	Source counts	Phase (ϕ)	Offset (arcmin)
<i>Suzaku</i>						
100012010	2005-08-29	01:48:03	49.8	16771	0.689	7.500
100045010	2006-02-03	09:59:30	21.4	4944	0.450	6.521
402039010	2007-06-23	05:54:08	58.4	24523	0.879	5.312
403035010	2008-06-10	01:51:36	35.4	8363	0.576	5.682
–	–	–	–	–	–	–
–	–	–	–	–	–	–

Notes. Source counts are given for *Suzaku* XIS-1, *Swift* XRT, *XMM–Newton* MOS2, and *NuSTAR* FPMB detectors. A detailed log of observations is available online.

August in photon counting mode. These long-term observations enabled us to investigate the X-ray emission at almost all the phases of this long period binary system. The observations with exposure time less than 1 ks were discarded due to few raw counts (see also Table 2). The data were processed using *Swift* XRTPIPELINE (version 0.13.2). This produced cleaned and calibrated event files using calibration files available in 2016 mid-November. The extraction of image, light curve, and spectrum for every observation was done using XSELECT (version 2.4c) package by selecting standard event grades of 0–12. Source products were extracted from a circular region of 30 arcsec radius. An annular background region of 69 arcsec inner and 127 arcsec outer radius, around the source region, was chosen for the background estimation. The spectra were binned to have minimum 10 counts per energy bin with GRPPHA. The response matrix file (RMF) provided by the *Swift* team (swxpc0to12s6_20130101v014.rmf) was used. In order to take bad columns into account, we calculated an ancillary response file (ARF) for each data set individually using the task XRTMKARF by considering the associated exposure map.

2.3 *XMM–Newton*

WR 25 was observed with *XMM–Newton* 24 times from 2000 July to 2015 July with the three European Photon Imaging Camera (EPIC) instruments, *viz.* MOS1, MOS2, and PN. Observations were made using various configurations of these detectors. The PN image of Eta-Carinae region in 0.3–10.0 keV energy range is shown in Fig. 1. These data were reduced with SAS v15.0.0 using calibration files available in 2017 May. The tasks EPCHAIN and EMCHAIN were used to do pipeline processing of raw EPIC Observation Data Files (ODF). List of event files was extracted using the SAS task EVSELECT which included selecting the good events with pattern 0–4 for PN and 0–12 for MOS data. Each observation ID was checked for pile-up using the task EPATPLOT but none was found to be affected by pile-up. Each data set was checked for high background intervals and excluded from the event file wherever found. The EPIC light curves and spectra of WR 25 were extracted from on-source counts obtained from a circular region centred at the source with a radius of 30 arcsec. Background estimation was done from circular regions of the same size at source-free regions surrounding the source. To apply good time intervals, dead time, exposure, point-spread function, and background correction to the obtained light curves, we used the EPICLCCORRTASK. The task ESPECGET was used to generate the source spectrum. To calibrate the flux and energy axes, the dedicated ARF and RMF response matrices, respectively, were also calculated by this task. Backscaling of the extracted spectra was

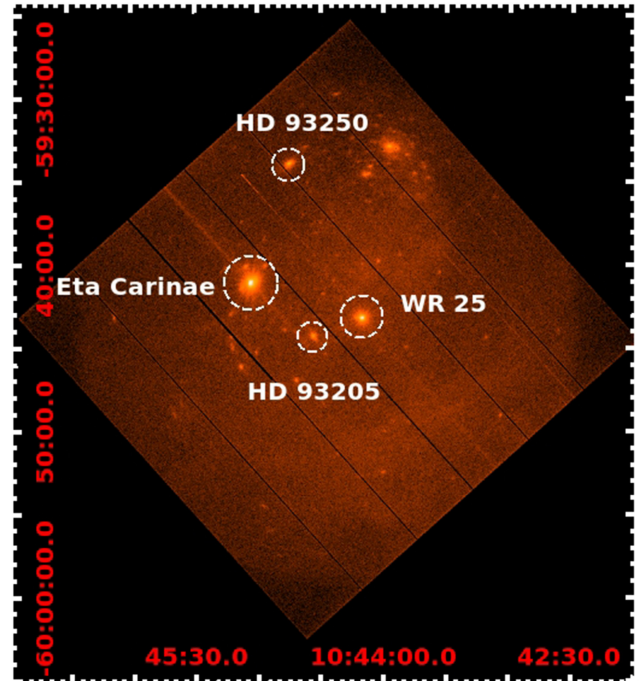


Figure 1. *XMM–Newton*–PN false-colour image of η -Carinae field in 0.3–10.0 keV energy range from observation ID 0112560201. X- and Y-axes correspond to RA (J2000) and Dec. (J2000), respectively.

done using the task BACKSCALE. The EPIC spectra were grouped to have minimum 20 counts per spectral bin.

2.4 *NuSTAR*

NuSTAR observed WR 25 on 10 occasions from 2014 March to 2016 June using both the focal plane modules (FPMA and FPMB). Reduction of *NuSTAR* data was done using data analysis software NUSTARDAS v1.5.1 distributed by HEASARC within HEASOFT 6.18. The calibrated, cleaned, and screened event files were generated by running NUIPELINE (version 0.4.4) task using *NuSTAR* CALDB version 20160824 released on 2016-08-30. To extract the source and background counts, circular regions of 30 arcsec radius at a source and nearby surrounding source-free regions, respectively, on the same detector were selected. The size of the chosen source region is of the order of the HPD (~ 1 arcmin). Light curve and spectrum in 3–79 keV energy range and corresponding response

files were extracted using NUPRODUCTS package within NUSTARDAS with time binning of 10 s. In order to correct the arrival times of the X-ray photons, the barycentric correction was applied to the background subtracted light curves using the task BARYCORR. Spectra were grouped to have 10 counts per spectral bin using the task GRPPHA. Spectra extracted from FPMA and FPMB of individual dataset were fitted jointly.

3 THE SPECTRA

3.1 Look at the X-ray spectra of WR 25

The X-ray spectrum below 10.0 keV presents the typical features of an optically thin thermal plasma emission at high temperature (above 10^6 K), as expected for a colliding wind massive binary (see e.g. Pandey et al. 2014).

The FI *Suzaku*–XIS spectrum of WR 25 at different orbital phases (but at almost same binary separation) are shown in Figs 2(a)–(c). The two spectra in each of the figure show the difference in the source flux when the two components of the binary system move towards and away from each other. Fig. 2(a) shows the source spectra before ($\phi = 0.88$, black in colour) and after ($\phi = 0.12$, red in colour) periastron passage. The system is brighter in X-rays just before periastron passage than after it at all the energies. Similarly the *XMM–Newton*–MOS2 spectra of WR 25, as shown in Fig. 2(d), display the same behaviour. However, as the two components move towards apastron this difference keeps on decreasing (Fig. 2b) and vanishes close to apastron (Fig. 2c).

The *NuSTAR*–FPMA spectrum of WR 25 without background subtraction (black in colour) as well as the background spectrum (red in colour) in 3.0–79.0 keV energy range are shown in Fig. 3. It is evident that after 10.0 keV, both spectra are almost identical which confirms that the source counts are significant only in 3.0–10.0 keV energy range. Background photons are dominating in the extracted spectrum beyond 10.0 keV. The lack of hard X-ray emission is discussed in Section 5.2. Therefore, the *NuSTAR* spectrum of WR 25 was considered in 3.0–10.0 keV energy range only for further spectral analysis.

3.2 X-ray spectral analysis

The fitting of X-ray spectra in 0.3–10.0 keV energy range was done using the models of the Astrophysical Plasma Emission Code (APEC; Smith et al. 2001) in the X-ray spectral fitting package XSPEC (Arnaud 1996) version 12.9.0i. The form of the model used was $phabs(ism)*phabs(local)(vapec + vapec)$. The component $phabs$ used to model the interstellar as well as local absorption effects uses the values of different elemental abundances according to Anders & Grevesse (1989). A similar model was also used by Pandey et al. (2014) for the spectral analysis of WR 25. However, Pandey et al. (2014) used $wabs$ instead of $phabs$. Since the X-ray spectra from *XMM–Newton* have best photon statistics than the others, therefore, first, all the parameters excluding $N_{\text{H}}^{\text{ISM}}$ were free in the spectral fitting. Temperature corresponding to cool component was found to be constant around its mean value of 0.628 keV. Phased variation of temperatures corresponding to hot component (kT_2) is shown in Fig. 4, which is also found to be constant within 1σ level around the mean value of 2.75 keV. The model parameters derived from the current spectral fitting which are based on the latest calibration, software, and larger data sets are found to be similar to that found by Pandey et al. (2014). Therefore, the values of the interstellar equivalent H-column density ($N_{\text{H}}^{\text{ISM}}$), as well as the

temperature and abundances for the two thermal components, were kept fixed at those obtained by Pandey et al. (2014). Only the local equivalent H-column density ($N_{\text{H}}^{\text{local}}$), as well as the normalization constants for the two temperature components, were kept free. χ^2 minimization method was used to best fit the model to the data. The observed (not corrected for any absorption effects, F^{obs}), ISM corrected (F^{ism}), and intrinsic (corrected for both ISM and local wind absorption, F^{int}) X-ray fluxes of WR 25 in soft (0.3–2.0 keV, F_{S}), hard (2.0–10.0 keV, F_{H}), and 3.0–10.0 keV (F_{X}) energy bands were derived using the model $cflux$ in XSPEC. The normalization constants, $norm_1$ and $norm_2$, corresponding to the cool and hot plasma components, respectively, were also estimated. The method used for fitting of the spectra from each satellite, with this model, is explained as follows.

3.2.1 Suzaku

The BI and FI *Suzaku*–XIS spectra of WR 25 were fitted jointly in 0.7–10.0 keV energy range due to poor SNR of data below 0.7 keV. The spectra obtained from each data set were fitted individually. The spectral parameters obtained after the spectral fitting (*viz.* $norm_1$, $norm_2$, $N_{\text{H}}^{\text{local}}$, $F_{\text{S}}^{\text{obs}}$, $F_{\text{H}}^{\text{obs}}$, $F_{\text{S}}^{\text{ism}}$, $F_{\text{H}}^{\text{ism}}$, $F_{\text{S}}^{\text{int}}$, and $F_{\text{H}}^{\text{int}}$) are given in Table 3 and are plotted as a function of orbital phase in Fig. 5(a).

3.2.2 Swift

The fitting of the *Swift*–XRT spectra was done in the 0.5–10.0 keV energy range. Since the signal-to-noise ratio of individual *Swift* spectra is very low, we decided to jointly fit the spectra lying within a phase interval of ≤ 0.02 . But still, we were not able to fit certain phase bins spectra due to very poor SNR. To solve this problem, we had to jointly fit those spectra with those of nearby phase bins. In addition, some orbital phase bins were not covered by observations. As a result, we defined phase bins 1–36 (introduced in the Table 3) and a joint fitting of the spectra taken in the same phase bin was performed. The values of the different spectral parameters obtained are given in Table 3 and their variation with orbital phase is shown in Fig. 5(b). For the five phase bins, *viz.* 32, 33, 34, 35, and 36, we had to fix the $N_{\text{H}}^{\text{local}}$ values to those obtained by the spectral fitting of the nearby phase bins. The open circles in the middle panel of Fig. 5(b) mark these values.

3.2.3 XMM–Newton

The spectra obtained from MOS1, MOS2, and PN detectors of the same data set were fitted jointly in the 0.3–10.0 keV energy range. The spectra obtained from observation IDs 0145740201 and 0145740301 were added since these were observed on the same day. Similarly, spectra from IDs 0145740401 and 0145740501 were also added. Other spectra from different data sets were fitted individually. The spectral parameters obtained after fitting of EPIC spectra are given in Table 3. These parameters are plotted as a function of orbital phase in Fig. 5(c).

3.2.4 NuSTAR

The *NuSTAR* spectrum was fitted in the 3.0–10.0 keV energy range only for the reasons mentioned in the above sub-section. Since the *NuSTAR* spectrum does not include the soft energy range, it was fitted using the single-temperature component with $kT = 2.75$ keV. The form of the model used was $phabs(ism)*phabs(local)*vapec$.

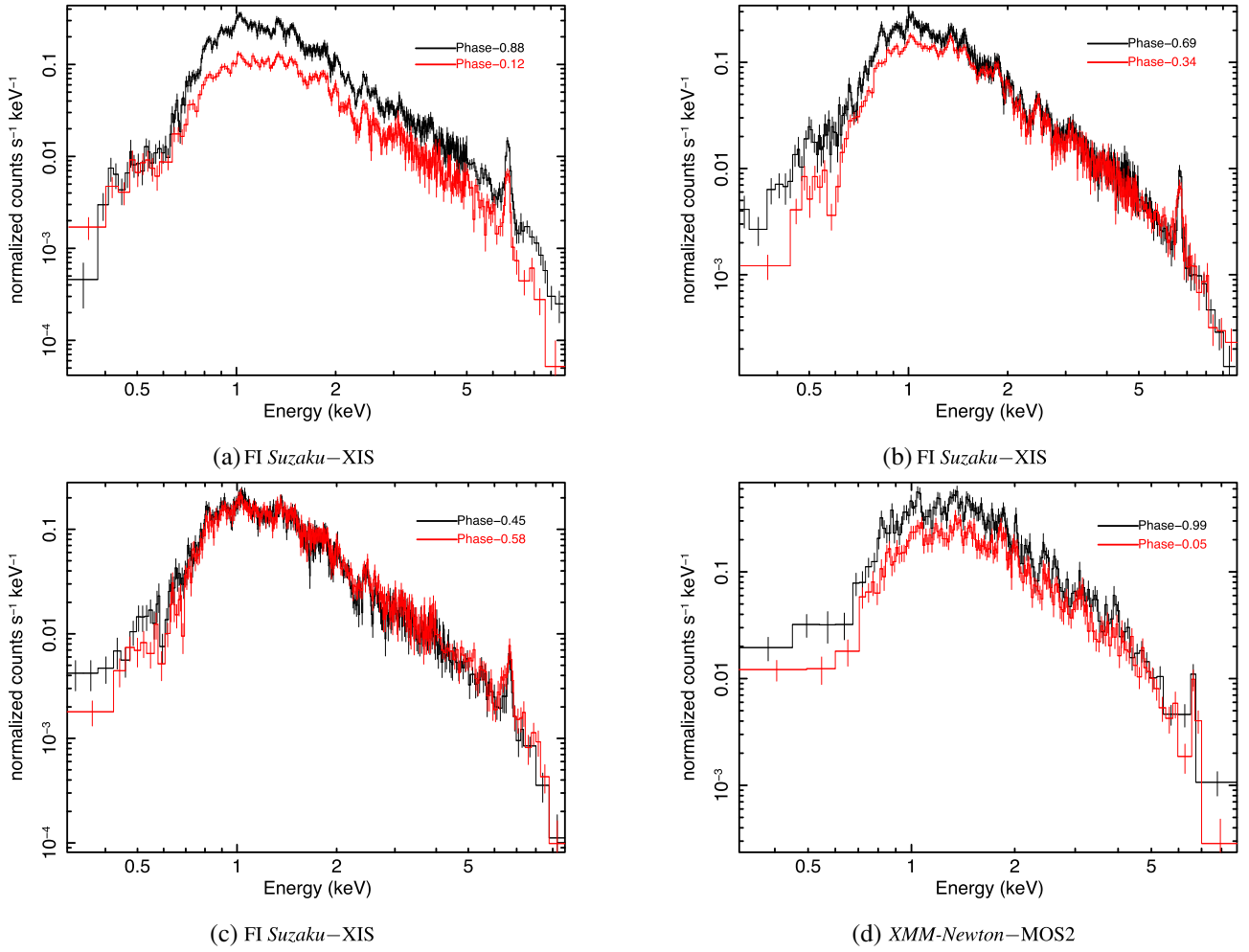


Figure 2. *FI Suzaku*–XIS and *XMM-Newton*–MOS2 spectra of WR 25 at different orbital phases. In each panel the stars are at (almost) identical binary separation but either receding (phase < 0.5) or approaching each other (phase > 0.5).

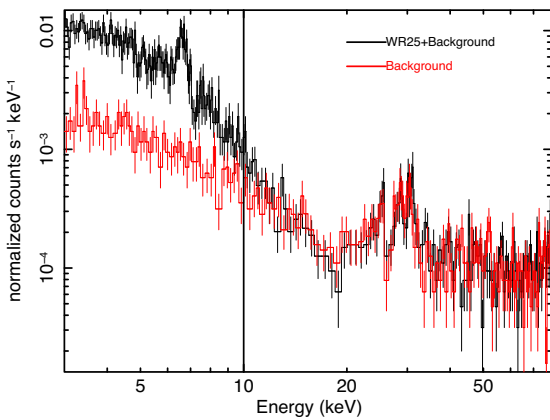


Figure 3. *NuSTAR*–FPMA spectra of WR 25 without background correction (black line) and only background (red line) of observation ID 30002010005.

The spectra obtained by the detectors FPMA and FPMB of the same observation data set were fitted jointly. Additionally, the spectra observed within a phase difference of ≤ 0.02 were also fitted jointly. Since the soft energy range is missing in *NuSTAR* spectra, $N_{\text{H}}^{\text{local}}$

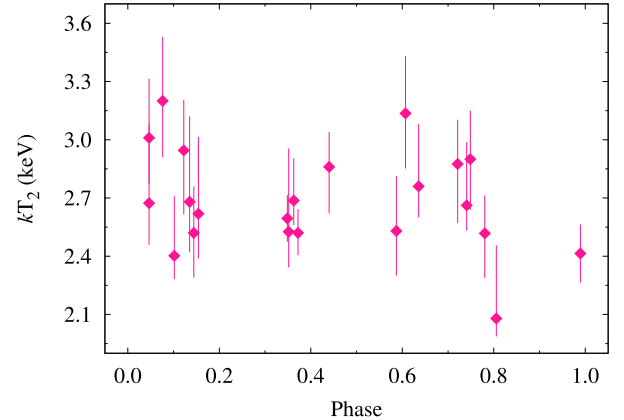


Figure 4. Variation of plasma temperature corresponding to hot component (kT_2) for *XMM-Newton*–EPIC data.

could not be determined through the standard fitting procedure. We had to freeze the $N_{\text{H}}^{\text{local}}$ values, for *NuSTAR* spectra, to those obtained by the fitting of the very close-by phases spectra from other satellites data. The normalization constant ($norm$), and the resulting observed ($F_{\text{X}}^{\text{obs}}$), ISM corrected ($F_{\text{X}}^{\text{ism}}$) as well as intrinsic

Table 3. Best-fitting parameters obtained from *Suzaku*, *Swift*, and *XMM-Newton* spectral fitting of WR 25.

Obs. ID / Phase bin	ϕ	$N_{\text{H}}^{\text{local}}$ (10^{22} cm^{-2})	$norm_1$ (10^{-3} cm^{-5})	$norm_2$ (10^{-3} cm^{-5})	$F_{\text{S}}^{\text{obs}}$	$F_{\text{H}}^{\text{obs}}$	$F_{\text{S}}^{\text{ism}}$ ($10^{-12} \text{ erg cm}^{-2} \text{ s}^{-1}$)	$F_{\text{H}}^{\text{ism}}$ ($10^{-12} \text{ erg cm}^{-2} \text{ s}^{-1}$)	$F_{\text{S}}^{\text{int}}$	$F_{\text{H}}^{\text{int}}$	χ^2_{ν} (dof)
<i>Suzaku</i>											
100012010	0.689	$0.29^{+0.02}_{-0.02}$	$3.67^{+0.25}_{-0.25}$	$3.45^{+0.07}_{-0.07}$	$3.29^{+0.03}_{-0.03}$	$3.32^{+0.03}_{-0.03}$	$4.68^{+0.04}_{-0.04}$	$3.39^{+0.03}_{-0.03}$	$12.23^{+0.11}_{-0.11}$	$3.55^{+0.03}_{-0.03}$	1.32 (775)
100045010	0.450	$0.30^{+0.02}_{-0.02}$	$3.82^{+0.32}_{-0.32}$	$2.64^{+0.09}_{-0.09}$	$2.99^{+0.04}_{-0.04}$	$2.62^{+0.03}_{-0.04}$	$4.27^{+0.06}_{-0.06}$	$2.69^{+0.04}_{-0.04}$	$11.72^{+0.16}_{-0.16}$	$2.81^{+0.04}_{-0.04}$	1.39 (753)
402039010	0.879	$0.35^{+0.01}_{-0.01}$	$6.09^{+0.29}_{-0.29}$	$4.89^{+0.08}_{-0.08}$	$4.59^{+0.03}_{-0.03}$	$4.74^{+0.03}_{-0.03}$	$6.39^{+0.05}_{-0.05}$	$4.85^{+0.03}_{-0.03}$	$19.42^{+0.14}_{-0.14}$	$5.12^{+0.04}_{-0.04}$	1.46 (730)
403035010	0.577	$0.29^{+0.03}_{-0.03}$	$3.41^{+0.32}_{-0.32}$	$2.99^{+0.08}_{-0.08}$	$2.97^{+0.04}_{-0.04}$	$2.89^{+0.04}_{-0.04}$	$4.22^{+0.05}_{-0.05}$	$2.97^{+0.04}_{-0.04}$	$11.13^{+0.14}_{-0.14}$	$3.09^{+0.04}_{-0.04}$	1.11 (634)
-	-	-	-	-	-	-	-	-	-	-	-
-	-	-	-	-	-	-	-	-	-	-	-

Notes. The fitted model has the form $phabs(ism)*phabs(local)(vapec + vapec)$, with $N_{\text{H}}^{\text{ISM}}$ fixed to $3.7 \times 10^{21} \text{ cm}^{-2}$ and the temperatures fixed to 0.628 and 2.75 keV. Abundances are given in table 4 of Pandey et al. (2014). χ^2_{ν} is the reduced χ^2 and dof is degrees of freedom. Errors quoted on different parameters refer to 90 per cent confidence level. The $N_{\text{H}}^{\text{local}}$ values for 32–36 phase bins of *Swift* were fixed to those of the nearby phase bins. The *XMM-Newton* spectra obtained from observation IDs 0145740201 and 0145740301 as well as 0145740401 and 0145740501 were added. Full table is available online.

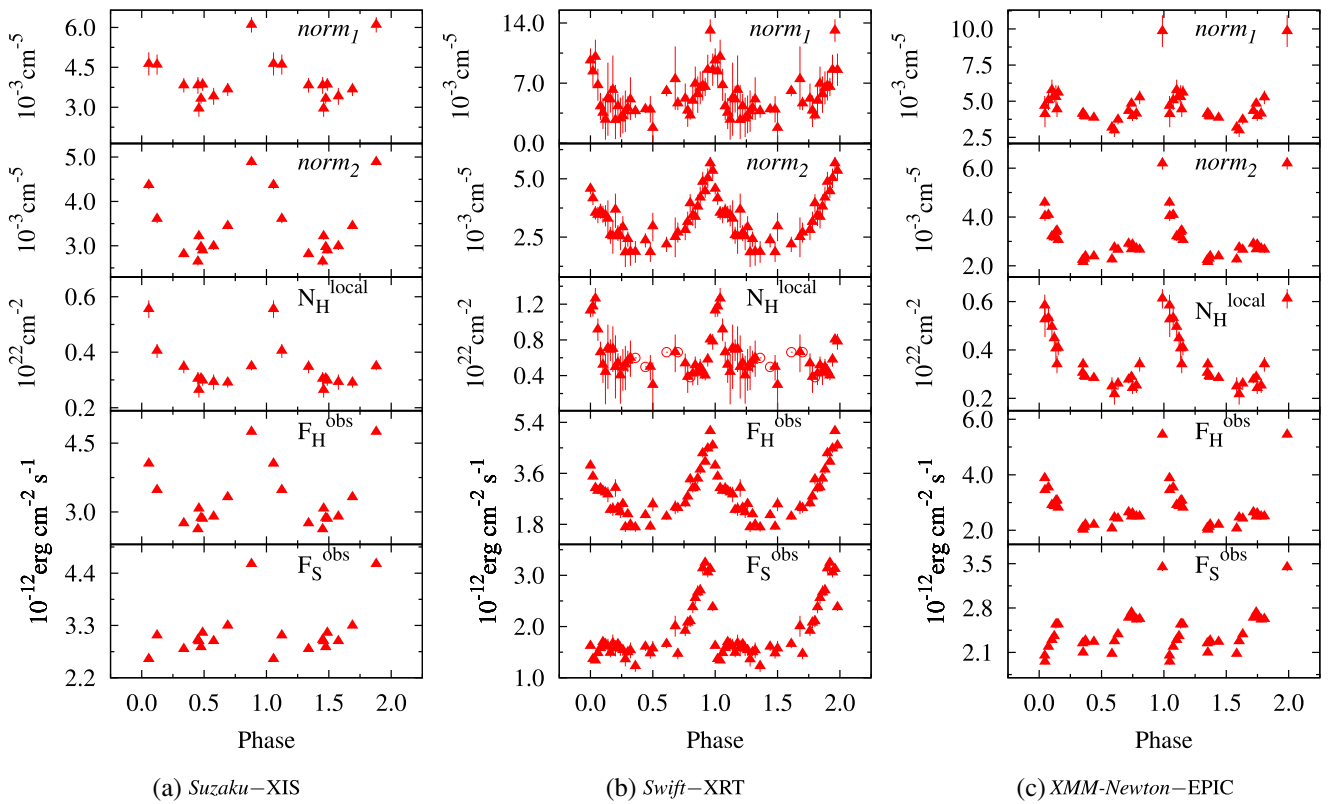


Figure 5. Spectral parameters as a function of orbital phase as observed by (a) *Suzaku*–XIS, (b) *Swift*–XRT, and (c) *XMM-Newton*–EPIC. Open circles in the middle panel of the middle figure correspond to the fixed values of $N_{\text{H}}^{\text{local}}$ to those of the nearby phase bins.

($F_{\text{X}}^{\text{int}}$) X-ray fluxes were determined and are given in Table 4. The variation of $norm$ and $F_{\text{X}}^{\text{obs}}$ with orbital phase is shown in Fig. 6.

4 X-RAY LIGHT-CURVES ANALYSIS

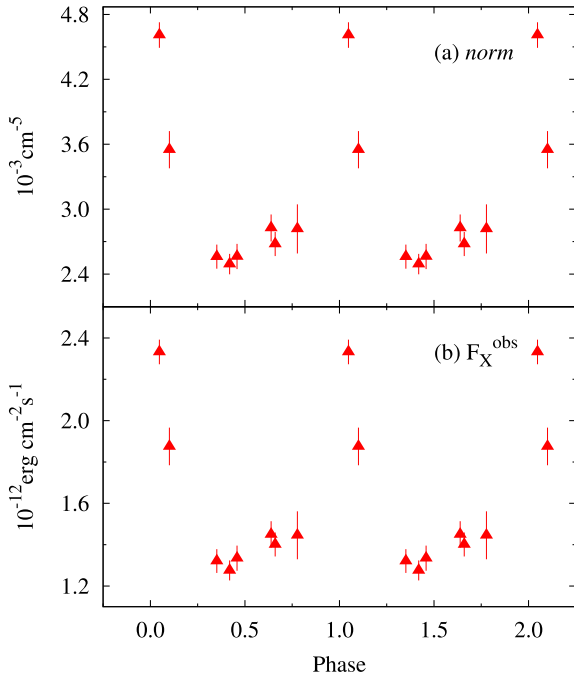
The background subtracted X-ray light curves as observed by *Swift*–XRT in broad (0.3–10.0 keV), soft (0.3–2.0 keV), and hard (2.0–10.0 keV) energy bands are shown in Fig. 7, where each data point represents an average count rate of the corresponding observation. Blue triangles mark the data observed during 2007 December to 2009 June which was studied by Pandey et al. (2014). However, red filled circles correspond to the data observed continuously from

2014 August to 2016 August. A time span of 250 d is covered between JD 245 7370.0 and 245 7620.0. The time period of this binary system is estimated to be 207.85 ± 0.02 d by Gamen et al. (2006) from radial velocity measurements of WR 25 using N IV $\lambda 4058$ emission line. Pandey et al. (2014) also found a period of 207.5 ± 3.4 d on the basis of X-ray light curves. The present 250 d continuous monitoring of WR 25 covers more than one orbital cycle in Fig. 7. Therefore, count rate initially increased (at around JD = 245 7370.0) to the maximum and then decreased (at around JD = 245 7495.0) to the minimum and then again increased towards the end of the light curve in all the energy bands mentioned here. However, the change in the hard energy band is not as steep as that in the soft energy band.

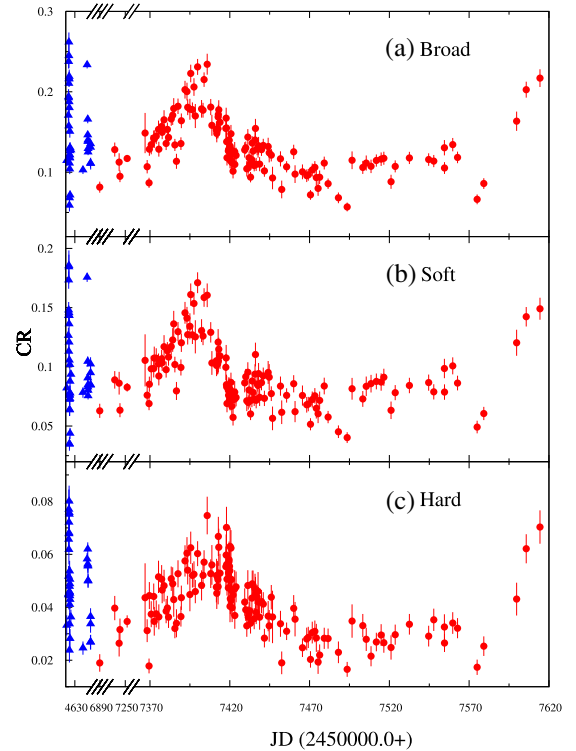
Table 4. Best-fitting parameters obtained from *NuSTAR* spectral fitting of WR 25.

Obs. ID	ϕ	$N_{\text{H}}^{\text{local}}$ (10^{22} cm^{-2})	$norm$ (10^{-3} cm^{-5})	$F_{\text{X}}^{\text{obs}}$	$F_{\text{X}}^{\text{ism}}$ ($10^{-12} \text{ erg cm}^{-2} \text{ s}^{-1}$)	$F_{\text{X}}^{\text{int}}$	$\chi_{\nu}^2(\text{dof})$
30002010002	0.777	0.29	$2.82^{+0.23}_{-0.23}$	$1.45^{+0.12}_{-0.12}$	$1.48^{+0.12}_{-0.12}$	$1.50^{+0.12}_{-0.12}$	1.26 (31)
30002010005 30101005002	0.048	0.99	$4.61^{+0.12}_{-0.12}$	$2.33^{+0.06}_{-0.06}$	$2.38^{+0.06}_{-0.06}$	$2.52^{+0.06}_{-0.06}$	1.34 (63)
30002040004	0.351	0.34	$2.56^{+0.11}_{-0.11}$	$1.32^{+0.06}_{-0.06}$	$1.35^{+0.06}_{-0.06}$	$1.38^{+0.06}_{-0.06}$	1.04 (31)
30002010007 30002010008	0.419	0.32	$2.49^{+0.09}_{-0.09}$	$1.28^{+0.05}_{-0.05}$	$1.30^{+0.05}_{-0.05}$	$1.33^{+0.05}_{-0.05}$	1.35 (63)
30002010010	0.458	0.26	$2.56^{+0.12}_{-0.12}$	$1.33^{+0.06}_{-0.06}$	$1.36^{+0.06}_{-0.06}$	$1.39^{+0.06}_{-0.06}$	1.03 (31)
30002010012	0.639	0.28	$2.83^{+0.12}_{-0.12}$	$1.45^{+0.06}_{-0.06}$	$1.48^{+0.07}_{-0.07}$	$1.51^{+0.07}_{-0.07}$	1.69 (31)
30002040002	0.101	0.45	$3.55^{+0.17}_{-0.17}$	$1.87^{+0.09}_{-0.09}$	$1.92^{+0.09}_{-0.09}$	$1.97^{+0.09}_{-0.09}$	0.82 (31)
30201030002	0.660	0.32	$2.68^{+0.11}_{-0.11}$	$1.40^{+0.06}_{-0.06}$	$1.43^{+0.06}_{-0.06}$	$1.46^{+0.06}_{-0.06}$	1.49 (31)

Notes. The fitted model has the form $phabs(ism)*phabs(local)*vapeac$, with $N_{\text{H}}^{\text{ISM}}$ fixed to $3.7 \times 10^{21} \text{ cm}^{-2}$ and the temperature fixed to 2.75 keV. Abundances are given in table 4 of Pandey et al. (2014). χ_{ν}^2 is the reduced χ^2 and dof is degrees of freedom. Errors quoted on different parameters refer to 90 per cent confidence level. The spectra obtained from observation IDs 30002010005 and 30101005002 as well as 30002010007 and 30002010008 were fitted jointly. The $N_{\text{H}}^{\text{local}}$ values for *NuSTAR* spectra were fixed to those obtained by the spectral fitting of the very close-by phases spectra from other observatories data.


Figure 6. Normalization constant ($norm$) and observed X-ray flux ($F_{\text{X}}^{\text{obs}}$) as a function of orbital phase for *NuSTAR*–FPMs data.

The long-term observation of WR 25 also enabled us to determine its orbital period more accurately than the previous studies. Lomb–Scargle periodogram (Lomb 1976; Scargle 1982) was used to perform the period analysis from *Swift* light curves. The peak with the highest power lies at frequency $0.00481 \pm 0.00005 \text{ cycles d}^{-1}$ in broad energy band. This corresponds to $207.8 \pm 3.4 \text{ d}$ orbital period which is consistent with the previous findings also. The power spectra of *XMM–Newton* light curves also showed a similar orbital period of $208.3 \pm 2.2 \text{ d}$.


Figure 7. X-ray light curves in broad (0.3–10.0 keV), soft (0.3–2.0 keV), and hard (2.0–10.0 keV) energy bands as observed by *Swift*–XRT. Blue triangles mark the data observed during 2007 December to 2009 June and the red filled circles correspond to 2014 August to 2016 August observations.

The light curves from other observatories (*NuSTAR*, *Suzaku*, and *XMM–Newton*) data are not shown here because none of them presents a continuous monitoring of the source. Only a few observations of WR 25 were made at random orbital phases and hence no regular pattern was visible in their light curves.

4.1 Folded X-ray light curves

The background subtracted light curves as observed by FPMA and FPMB onboard *NuSTAR* were obtained in 3.0–10.0 and 10.0–78.0 keV energy bands. The median of the ratio of the count rate to the corresponding error in 3.0–10.0 keV energy range was estimated to be 3.51 while it was 2.00 in 10.0–78.0 keV energy band. Therefore, we have considered *NuSTAR* light curves only in 3.0–10.0 keV energy band for further analysis (see also Section 3.1). The background subtracted X-ray light curves were folded using the ephemeris $HJD = 2451598.0 + 207.85E$ given by Gamen et al. (2006). The zero phase in the folded light curves corresponds to the time of the periastron passage. The X-ray light curves observed by FI *Suzaku*–XIS, *Swift*–XRT, and *XMM–Newton*–MOS2 were folded in (a) broad, (b) soft, and (c) hard energy ranges and are shown in Figs 8(a)–(c), respectively. Each point in the folded light curves corresponds to the average count rate of an observation ID. In Fig. 8(b), the folded X-ray light curve of *Swift*–XRT, red filled circles and blue triangles mark the observations made with a time gap of ~ 7 yr as in Fig. 7. It is evident that the count rates before and after this gap overlap fairly well, suggesting a reasonably stable behaviour of the phase-dependent X-ray emission over several orbits. Moreover, it also points towards the absence of any third component on a wider orbit, which would have been a potential cause of longer term modulations (on top of that of the 208-d binary) in the X-ray light curve. Phase locked variations were seen in all the folded X-ray light curves and a similar kind of trend is observed. In the folded light curves of FI *Suzaku*–XIS, *Swift*–XRT, and *XMM–Newton*–MOS2, initially the count rate increases around the periastron passage followed by a very sharp decrease in broad and soft energy bands just after the periastron and then it recovers to an average value around the apastron. On the other hand, the folded light curves as observed by *NuSTAR*–FPMA and FPMB in 3.0–10.0 keV energy band are as shown in Fig. 9. Here again, the count rate decreases gradually while moving from periastron to apastron. The ratio of the maximum to the minimum count rate in broad, soft, and hard energy bands were found to be 2.48, 2.48, and 2.47 for FI *Suzaku*–XIS, 4.46, 5.37, and 4.83 for *Swift*–XRT, and 2.2, 1.9, and 3.2 for *XMM–Newton*–MOS2 observations, respectively. However, for *NuSTAR*–FPMA and FPMB observations in 3.0–10.0 keV energy range, this ratio is 2.1 and 2.5, respectively.

4.2 Flux versus binary separation

The variation of observed and intrinsic X-ray fluxes in soft (F_S) and hard (F_H) energy bands with binary separation (D , i.e. the binary separation normalized to the semimajor axis a) as observed by *Suzaku*, *Swift*, and *XMM–Newton* is shown in Fig. 10. The orbital phases corresponding to a few observations are also mentioned in the figure. It is evident from these plots that the intensity of the X-ray emission varies as the two components of this binary system move towards and away from each other. These variations were found to be deviated from the linear trend. In order to find the significance of deviations from the linear trend a χ^2 -test was performed on the best-fitting straight line. We found that deviation was more than 99.9 per cent confidence level from linear trend for all the observations in both soft and hard energy bands. F_S seem to be more affected as compared to F_H . The most pronounced variation in the emission occurs close to periastron passage; however, around the apastron, there is not much difference. *Swift* observations have the dense coverage of the orbital period of WR 25 than other satellites’ observations. Therefore, it will be more appropriate to discuss the

Swift observations. For *Swift*, the maximum value of F_S^{obs} occurred at phase 0.92 and dropped sharply to the phase 0.04. However, for F_H^{obs} , the maximum and minimum values were measured at phases 0.96 and 0.48 (Fig. 10b), respectively. Both F_S^{int} and F_H^{int} were highest at phase 0.96 (Fig. 10e) i.e. before the periastron passage but these were lowest at phases 0.50 and 0.48, respectively. The plots for *Suzaku* (Figs 10a and d) and *XMM–Newton* (Figs 10c and f) also express a similar variation pattern but the poorer orbital sampling (especially close to periastron) prevents any accurate determination of the position of F_S and F_H extrema. We do not show the variation of F_S and F_H with D for all satellites data together since there are some differences between the individual satellite results, probably because of noise and cross-calibration effects, but a similar trend is followed by each.

The variation of F_X^{obs} and F_X^{int} as a function of normalized D as observed by *NuSTAR* is shown in Figs 11(a) and (b), respectively, and there is not much difference in both values at all the orbital phases. It appears that F_X varied with D almost linearly and there is not any significant deviation in X-ray emission as two components of WR 25 move around the periastron. But a careful inspection of plots reveals that *NuSTAR* observations did not cover much of the orbit around the periastron passage. After the phase 0.78, *NuSTAR* observed WR 25 at phase 0.05 and then at phase 0.1. Therefore, the flux information in between the orbital phases 0.78–0.05 is missing in the part of the orbit where the most pronounced changes in the X-ray emission are expected.

5 DISCUSSION

5.1 Variability of the thermal X-ray emission

Our analysis, in general agreement with previous studies, emphasizes a few features deserving to be discussed and commented in their appropriate context.

The folded X-ray light curve of *Swift*–XRT measurements (which offers the best orbital sampling) presents a peaked maximum close to the periastron passage, followed by a decrease of the emission on the way to apastron, suggesting an X-ray emission dependent on the stellar separation. This maximum is observed at orbital phases 0.943, 0.943, and 0.973, respectively, in the broad, soft, and hard energy bands. The investigation of the separation-dependent variations must be based on quantities independent of the ISM as well as local absorption by the stellar wind (see below). A first indicator should be the X-ray flux measured in the hard band, weakly affected by photoelectric absorption. It is clear that the hardest emission is produced by the colliding-wind region and therefore should be affected by the varying separation, while the soft emission is produced by both the individual stellar winds and the wind–wind interaction region. The evolution of the hard X-ray flux as a function of distance is shown in the lower panels of Figs 10(a)–(c), and in Fig. 11(a). An alternative way would consist in plotting the intrinsic values (i.e. corrected for both local and interstellar absorptions) as a function of distance as shown in Figs 10(d)–(f) and in Fig. 11(b). A third approach is to follow the evolution of the normalization constant corresponding to the hard component ($norm_2$, relevant for the colliding winds emission) as a function of distance. The general trends shown by these three indicators, especially when only hard X-ray fluxes are considered, are indeed very similar as expected.

Hydrodynamic models of wind interactions in massive binaries predict that WCR can behave either adiabatically or radiatively (Stevens et al. 1992). In shorter period systems, instabilities arise

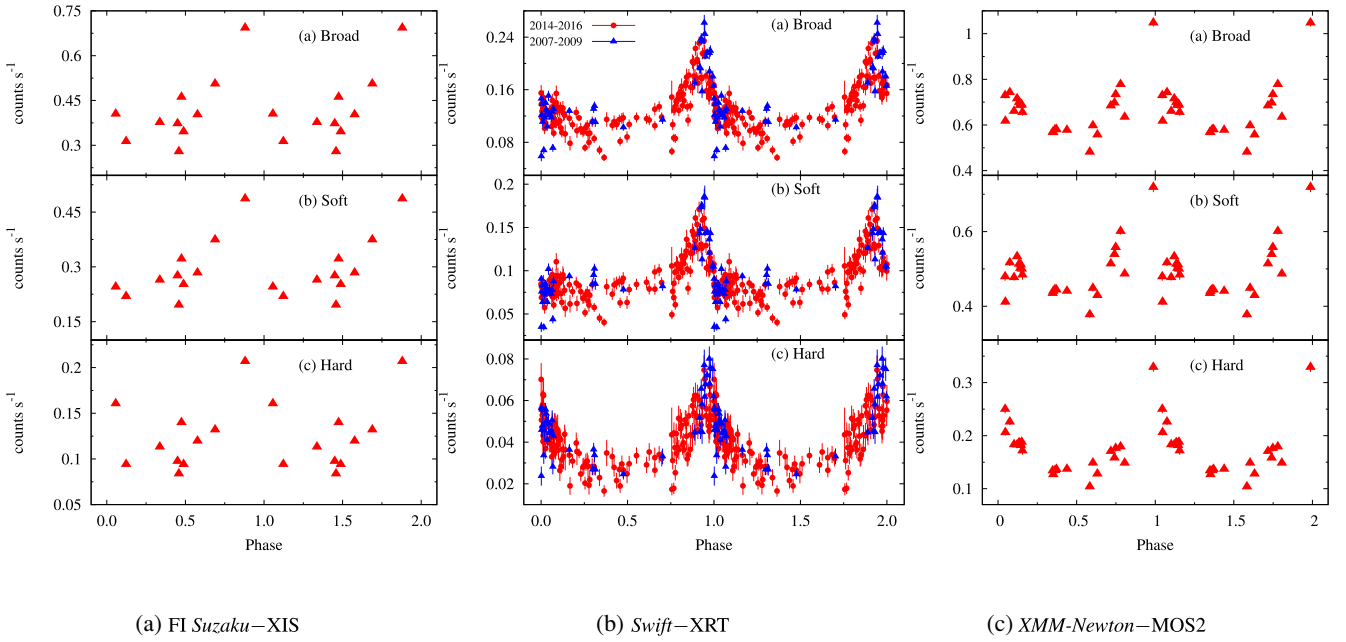


Figure 8. Folded X-ray light curves in broad, soft, and hard energy bands as observed by (a) *FI Suzaku* – XIS, (b) *Swift* – XRT, and (c) *XMM–Newton* – MOS2.

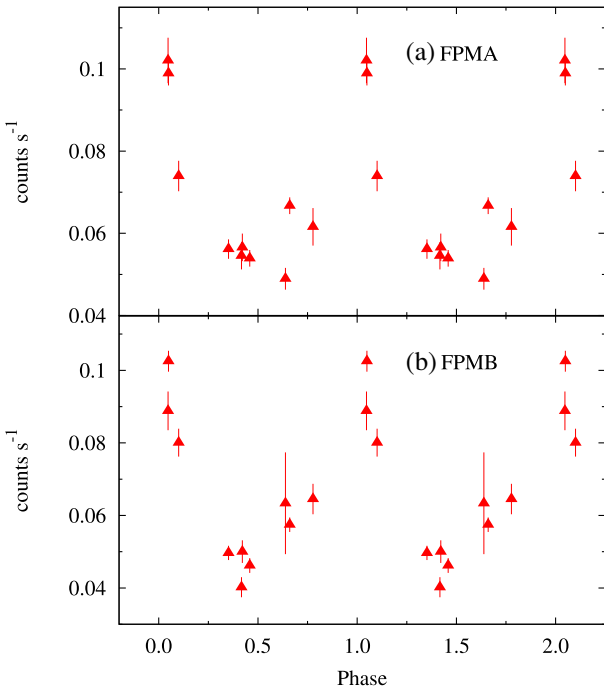


Figure 9. Folded X-ray light curves in 3.0–10.0 keV energy range as observed by *NuSTAR* – FPMA (upper panel) and FPMB (lower panel).

in the interaction region which leads to a quite turbulent wind collision and the X-ray luminosity then follows a relation of the form $L_X \propto f \dot{M} v^2$, where f is the fraction of the wind involved in the collision, \dot{M} is the mass-loss rate, and v is the pre-shock wind velocity. However, in the adiabatic regime, the interaction appears smoother and the X-ray luminosity scales as $L_X \propto \dot{M}^2 v^{-3.2} D^{-1}$, where D is the binary separation (Luo et al. 1990). This behaviour

is expected for binaries with orbital periods longer than few days. Since WR 25 has the orbital period of ~ 208 d, therefore, it should follow the latter X-ray luminosity relation and hence the intrinsic flux is expected to be maximum at periastron, where the plasma density is higher. Based on the limited data set, Gosset (2007) found that the hard X-ray flux of WR 25 increases linearly with the inverse of the relative binary separation using *XMM–Newton* data, in full agreement with the expected behaviour for an adiabatic case.

Light curves presented in Fig. 10 present a behaviour reminiscent of a hysteresis, even though this is not well supported by Fig. 11 characterized by a poorer orbital phase sampling. Pittard & Parkin (2010) predicted hysteresis behaviour in the variation of the X-ray luminosity from colliding winds as a function of the binary separation for eccentric systems. Though the model of Pittard & Parkin (2010) is designed for eccentric O+O binaries with period less than 10 d and weaker stellar winds, we find the similar features in the X-ray emission of WR 25. The origin of this effect is an asymmetry in the wind collision region about the line of centres, especially close to periastron passage. In the specific case of WR 25, the orbital velocity close to periastron reaches its maximum, while radiative effects (such as radiative inhibition and sudden radiative breaking, see below in this section) can reduce substantially the pre-shock wind velocity. The combination of these two effects is expected to result in an increase of the ratio between the orbital and wind velocities at periastron, which favours a distortion of the wind collision region. Such a distortion is expected to lead to a significant departure with respect to pure symmetry about the line of centres, causing the hysteresis. If the trends shown in Fig. 10 are real, one may thus tentatively transpose the case described by Pittard & Parkin (2010) to provide a likely interpretation context to our observations, provided we remember the basic idea behind this effect has to be slightly adapted to take into account some specificities of the system. The emission is brighter when the two components move towards each other than when they separate again. It may happen because of a higher pre-shock wind velocities

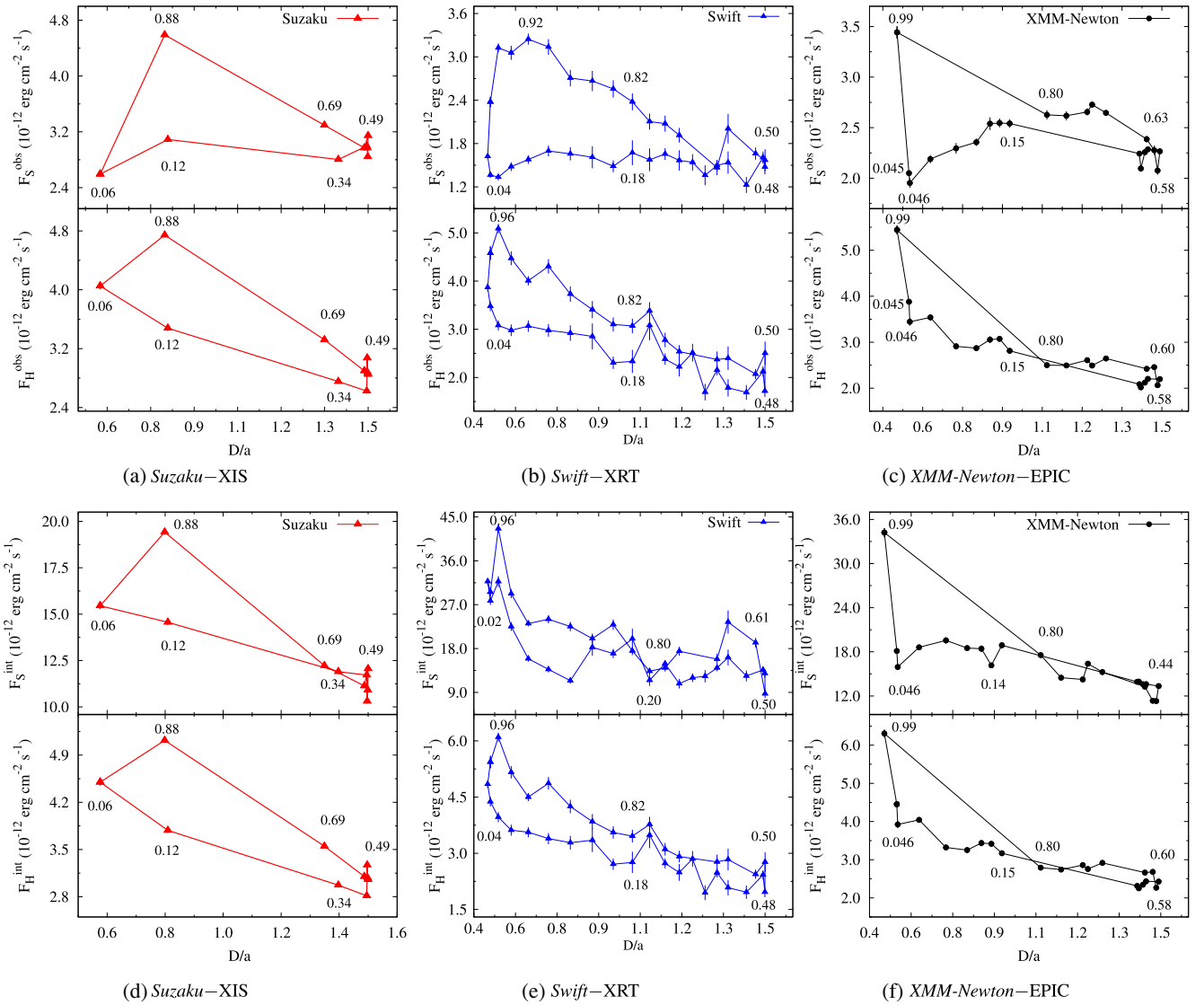


Figure 10. Observed (top row) and intrinsic (bottom row) X-ray flux of WR 25 as a function of binary separation in soft (F_S) and hard (F_H) energy bands as observed by *Suzaku*–XIS, *Swift*–XRT, and *XMM-Newton*–EPIC. The orbital phases corresponding to a few data points have also been mentioned in the figures.

when stars are getting closer, favouring a brighter hard X-ray component. As the two stars come close to each other, their winds collide with lower terminal velocities. The lower pre-shock velocity is less favourable to the hard X-ray emission that appears thus weaker. Therefore, the maximum X-ray luminosity is observed before the periastron passage. When the two components move away from each other after periastron, less hard X-ray emission is observed which reflects the smaller pre-shock wind velocities attained at earlier orbital phases, reducing the emission measure of the plasma that is warm enough to produce radiation significantly above 2 keV. We have however to caution that this interpretation relies notably on a significant phase-locked variation of the pre-shock velocity, which is not fully supported by our measurements of the post-shock plasma temperature, as detailed in the discussion below in this section.

Our analysis show that the X-ray emission deviates from the linear $1/D$ trend close to periastron, suggesting a departure from the adiabatic regime when the stellar separation is shorter. It is worth

checking the evolution along the orbit of the cooling parameter (χ) defined by Stevens et al. (1992) as the ratio of the cooling time of the post-shock gas to the typical escape time from the shock region. It is expressed as $\chi = v^4 D / \dot{M}$, where v is the pre-shock wind velocity in 1000 km s^{-1} units, D is the distance from the star to the shock in 10^7 km and \dot{M} is the mass-loss rate in $10^{-7} M_{\odot} \text{ yr}^{-1}$ (Stevens et al. 1992). For $\chi \ll 1$, the gas cools rapidly and the collision is considered to be radiative while for the adiabatic case, $\chi \geq 1$. The switch of χ down to radiative values can be further enhanced by radiative effects such as radiative inhibition and sudden radiative braking. These are related to the presence of the radiation field of the companion star and it has been shown that they may reduce the pre-shock velocity of colliding winds. Radiative inhibition involves the reduction in the initial acceleration of the stellar wind by the radiation field of its companion (Stevens & Pollock 1994). It is more suitable for close O + O binaries with comparably strong optically thin winds. However, sudden radiative braking is more favoured in WR + O binaries where the wind of the primary star is suddenly

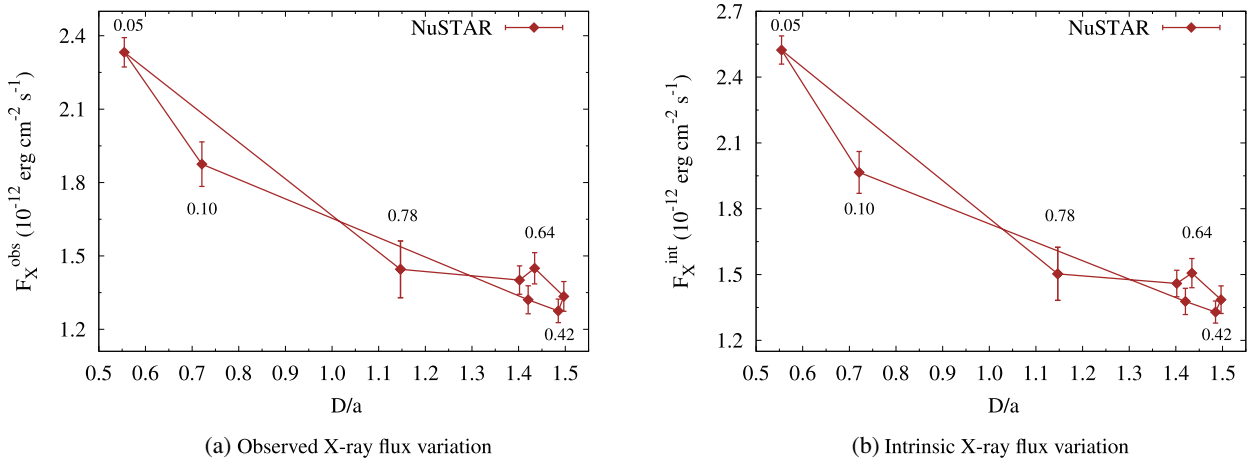


Figure 11. (a) Observed and (b) intrinsic X-ray flux as a function of binary separation in 3.0–10.0 keV (F_X) energy band as observed by *NuSTAR*–FPMs. The orbital phases corresponding to a few data points have also been mentioned in the figures.

decelerated by the radiative momentum flux of its companion as it approaches the surface of that star (Gayley, Owocki & Cranmer 1997). It constitutes a more severe interaction that can significantly alter the bow-shock geometry close to periastron passage. Since the cooling parameter is proportional to v^4 , the lowering of the pre-shock velocity through this effect can have a significant impact on the shock regime, leading to a reinforcement of the radiative regime around periastron.

We estimated v and χ for both components of WR 25 at the position of the WCR by using the standard β -velocity law (thus without any influence by radiative effects mentioned in the previous paragraph). To achieve this, the typical values of the various stellar parameters for the WN6ha (primary) and O4 (secondary) stars were considered as given in Table 5. χ is expected to change as a function of the orbital phase because (i) the stellar separation changes and (ii) the pre-shock velocity is likely to change if the winds collide before they reach their terminal velocity. Our estimates show that within a 0.10 phase interval around periastron, both shocked winds should become slightly radiative with a χ value slightly lower than 1, especially if the O4 star is assumed to be a supergiant. χ remains higher than 1 during the remaining parts of the orbit for both winds. The evolution of v and χ with the orbital phase for both components of WR 25 is shown in Fig. 12 assuming secondary star as an O4 supergiant. Here, we see that v decreases by 25 per cent and 34 per cent for WN- and O-star, respectively, from apastron to periastron. One should however caution that the above discussion is valid for expectations based on simple principles, but one has to note a clear discrepancy between the expected trend of the pre-shock velocity illustrated in Fig. 12 and the measurements of the post-shock plasma temperature reported on in Fig. 4. As the post-shock plasma temperature should scale with the square of the pre-shock velocity, a significant and smooth phase-locked evolution of the plasma temperature should be measured, but this is not observed. Provided the measured plasma temperature is an adequate proxy of the pre-shock velocity in the wind–wind interaction region, the simple interpretation context described here fails to explain all the emission properties described in this study. In order to achieve a more appropriate interpretation of the X-ray emission of WR 25 and of its variability, the support of more sophisticated modelling is strongly required. In particular, the pre-shock velocity along

the colliding-wind region appears as a critical physical quantity strongly influencing the overall X-ray emission of the system. An adequate dynamical modelling is needed to reconcile the apparent contradiction between the trends shown by Figs 12 and 4.

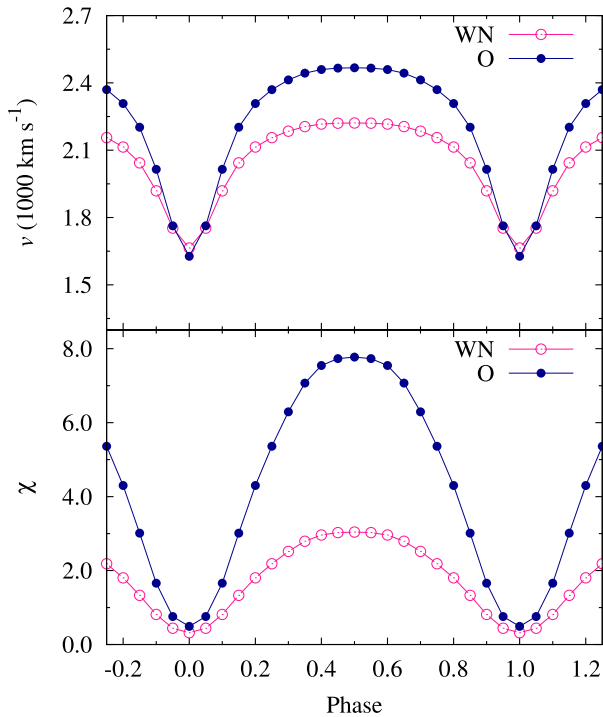
Besides the trend discussed above related to the change of stellar separation, local absorption by the stellar winds material is also important to interpret X-ray light curves. The impact of this local absorption is clearly measured as a sudden and sharp drop in the X-ray flux that occurs shortly after periastron passage, in the broad and soft energy bands. According to the radial velocity curve of WR 25, presented by Gamen et al. (2006), primary component of this binary remains towards the observer from phase ~ 0.95 to 0.27. A sharp minimum is observed in F_5^{ism} at orbital phase 0.04 ± 0.01 of WR 25. Therefore, this drop is the resultant of the strong local absorption faced when the WN wind is in front of the colliding-wind region, around this phase, from the observer’s point of view. This feature was not so obvious in the results presented in the previous studies (Gosset 2007; Pandey et al. 2014) because of a sparser orbital sampling. This post-periastron minimum is not observed in the hard energy band, which is basically unaffected by photoelectric absorption.

We want to caution that the results obtained from this study represent a very approximate picture of the actual physical condition of the system. In particular, one knows that the plasma temperature derived from our modelling approach consists of a rough average. Actually, the X-ray emitting region is made of the distribution of cells spreading over wide ranges of density and temperature. The post-shock temperature distribution is expected to peak along the line of centres where the pre-shock velocity of the colliding winds is the highest, with lower typical temperatures away from the apex of the shocks. Such a more realistic representation would be much too detailed considering the accuracy of the data used in this study. Our approach focuses thus on average and typical values, easily represented by the models and the modelling tools we used in this study. On the other hand, one also has to clarify that freezing the post-shock plasma temperature across the full spectral time-series is at first sight at odd with the expectation of a varying pre-shock velocity in an eccentric system. In particular, the hardest component significantly accounting for the X-ray emission close to the line of centres should in principle be affected. However, the change in pre-

Table 5. List of the stellar parameters adopted for the estimation of cooling parameter (χ) at the WCR of WR 25.

Parameter	WN6ha	O4 (secondary)			Reference
	(primary)	Dwarf	Giant	Supergiant	
Mass (M_{\odot})	–	46.16	48.80	58.03	2
Radius (R_{\odot})	20	12.31	15.83	18.91	1, 2
Mass-loss rate ($M_{\odot} \text{ yr}^{-1}$)	10^{-5}	$10^{-5.836}$	$10^{-5.540}$	$10^{-5.387}$	1, 2
Terminal wind velocity (km s^{-1})	2500	3599	2945	2877	1, 2
β -velocity law	1.00	0.90	0.90	0.92	1, 2

Notes. The radius of the primary component was derived using the values of luminosity ($10^{6.18} L_{\odot}$) and temperature (45 000 K) for WN6ha star from Crowther (2007) assuming the black body emission. **References:** (1) Crowther (2007); (2) Muijres et al. (2012).


Figure 12. Expected evolution of the pre-shock wind velocity (v) and cooling parameter (χ) with the orbital phase for both components of WR 25. Here, secondary component of WR 25 is an O4 supergiant.

shock velocity is not high enough to completely lead to dramatic changes in plasma temperatures, at least in a large part of the orbit and at the level of accuracy of the measurements allowed by the data (see Fig. 4). As a result, this approximation does not compromise the validity of our general interpretation. Concerning the element abundances, one should also keep in mind that the emitting plasma is coming from both stellar winds, and this is not straight forward to anticipate in which proportion, especially as a function of the orbital phase. In addition, the abundances of the absorbing plasma are also expected to vary depending on which stellar wind is in front. The required improvements in the spectral analysis to account for such effects are far beyond the information content of our data series and out of reach of our modelling tools. Our approach offers thus the advantage to provide a relevant description with a reasonably low number of free parameters, which constitutes a convenient requirement to perform the variability analysis described in this study.

Finally, the long-time basis of the data series investigated in this paper (about 16 yr) suggests a fairly good consistency of the phase-

folded X-ray emission even when observations distant by several years are considered. This indicates that the binary system scenario is fully satisfactory to explain the temporal behaviour of WR 25, rejecting the idea that it might be a higher multiplicity system with an additional colliding-wind region (on a wider orbit) contributing to the overall thermal X-ray emission.

5.2 Lack of non-thermal emission

It has been noticed that some colliding wind binaries also act as sources of particle acceleration in their wind collision region through the diffusive shock acceleration (DSA) mechanism which leads to the production of relativistic particles (De Becker & Rauq 2013). Relativistic electrons travelling in the magnetic field may give rise to synchrotron radio emission or they may also inverse Comptonize the photospheric stellar light to X-rays or even soft γ -rays. This opens up the possibility that some non-thermal X-ray emission may be measured in colliding-wind binaries. As emphasized in this paper, and the same holds for other colliding-wind binaries, the soft X-ray emission (below 10 keV) is dominated by thermal emission from the wind–wind interaction region. As a result, attempts to measure such a non-thermal X-ray emission should focus on hard X-rays, above 10 keV (see e.g. De Becker 2007). However, the lack of significant X-ray emission revealed by *NuSTAR* between 10 and 78 keV provides evidence that no inverse Compton scattering emission is produced by WR 25 above the background level.

The availability of hard X-ray data allows, however, to derive upper limits on the count rate of the putative non-thermal X-ray emission between 10 and 78 keV for FPMA and FPMB instruments. We applied the procedure applied by De Becker, Hutsemékers & Gosset (2014) to *NuSTAR* data sets obtained at two extreme orbital phases, respectively, close to periastron ($\phi = 0.049$) and apastron ($\phi = 0.458$). We filtered event lists using a circular spatial filter with a radius of 30 arcsec to measure the associated number of counts (C). This radius was selected because it corresponds to the half the Half Power Diameter (HPD) given by Harrison et al. (2013). This extraction region is large enough to collect a count number still significant for Poisson statistics, and it is small enough to avoid any significant contamination by adjacent imaging resolution elements. This count number was then corrected for the encircled energy fraction corresponding to the extraction radius (50 per cent, as we adopted an extraction radius corresponding to that fraction), and it was further corrected for the position dependent effective area of the FPMs. For the latter correction, we considered a median energy, i.e. 40 keV. According to Harrison et al. (2013), at a distance of about 5.5 arcmin from the on-axis position (see the observation log in Table 2) the effective area is about 45 per cent of its maximum (on-

Table 6. Estimates of the upper limits on the count rate for *NuSTAR* instruments at the position of WR 25.

	FPMA	FPMB
$\phi = 0.049$		
C (cnt)	189	194
C_{cor} (cnt)	839	861
C_{max} (cnt)	969	993
$C_{\text{max}} - C_{\text{cor}}$ (cnt)	130	132
Eff. exp. time (s)	79400	79400
CR (cnt s ⁻¹)	1.6×10^{-3}	1.6×10^{-3}
$\phi = 0.458$		
C (cnt)	144	126
C_{cor} (cnt)	639	559
C_{max} (cnt)	753	666
$C_{\text{max}} - C_{\text{cor}}$ (cnt)	114	107
Eff. exp. time (s)	54500	54500
CR (cnt s ⁻¹)	2.0×10^{-3}	2.0×10^{-3}

axis) value. We thus obtain a corrected count number (C_{cor}). We then determined a count threshold (C_{max}) corresponding to a logarithmic likelihood (L) of 12, translating into a probability (P) to find a count number in excess of C_{max} of about 6×10^{-6} ($L = -\ln P$), under the null hypothesis of pure background Poisson fluctuations. This criterion is frequently adopted as a threshold for statistical fluctuations. In practice, we iteratively estimated the logarithmic likelihood assuming Poisson statistics on the basis of the corrected count number and adopting a first guess for C_{max} . At every iteration, C_{max} was adapted to converge to a logarithmic likelihood of 12, for a fixed C_{cor} value. The difference between these two quantities (C_{max} at $L = 12$ and C_{cor}) gives the maximum expected count excess. The division of the latter quantity by the effective exposure time gives the count rate (CR) upper limit on the putative emission, as shown in Table 6. This approach has the benefit to estimate a count excess on a statistically relevant basis.

The upper limits on the count rate for a hypothetical inverse Compton scattering X-ray emission can be converted into physical flux units assuming an adequate emission model. The non-thermal spectrum should be a power law, slightly affected by interstellar and local absorption in the softer energy band. Even though our upper limits on the count rate relies on the 10–78 keV range, the IC process should contribute over the full X-ray range, and we estimated the flux between 0.1 and 100 keV. We used the WebPIMMS online tool¹ assuming two different values of the photon index: 1.5 (the standard value for DSA in strong shocks, e.g. De Becker 2007) and 1.7 (valid for the likely leptonic component in Eta Car’s soft γ -ray spectrum, Farnier, Walter & Leyder 2011). Depending on the orbital phase, on the instrument and on the assumed photon index, we obtain intrinsic non-thermal X-ray fluxes in the range $7\text{--}9 \times 10^{-13}$ erg cm⁻² s⁻¹. For a distance of 2.1 kpc (Gaia DR2; Lindgren et al. 2018), this converts into upper limits on the intrinsic luminosities in the range $3.6\text{--}4.7 \times 10^{32}$ erg s⁻¹.

These numbers deserve to be discussed in the context of the energy budget of colliding-wind massive binaries, and of their participation in non-thermal processes. The IC process (over the full X-ray domain) and the thermal X-ray emission (measured below 10 keV) share the same energy reservoir, i.e. the fraction of the wind kinetic power that is injected in the colliding winds. On the basis of previous measurements on colliding-wind binaries, the fraction of

that energy that is converted into thermal X-rays emerging from the winds is of the order of 1–10 per cent. A similar fraction is expected to apply for the energy injection into non-thermal particles, on the basis of theoretical considerations and of a comparison with the case of supernova remnants which share the same physics. However, IC scattering comes only from the energy injected into electrons, which constitutes only a fraction of the energy of the non-thermal particles, i.e. likely a few per cent of the energy injected in relativistic particles (see De Becker & Rauqc 2013, for a discussion of the energy budget of particle-accelerating colliding-wind binaries). Considering the high radiative energy density in the particle acceleration region, the energy injected in relativistic electrons should be dominantly radiated through IC scattering. The amount of energy injected into the IC process should thus, roughly, be at most equivalent to a few per cent of the energy radiated in thermal X-rays and escaping from the winds. However, our upper limits on the non-thermal X-ray emission are only a few per cent of the intrinsic thermal X-ray fluxes reported in this paper, and about a factor 10 lower than the thermal X-ray fluxes corrected for ISM absorption only (see Table 3). These upper limits do not therefore provide better constraints than the anticipated educated guesses proposed by previous studies. Consequently, the limitations due to the sensitivity of *NuSTAR* lead to quite loose upper limits, which do not provide stringent constraints on the non-thermal physics. Only systems with higher kinetic power, hence with a more abundant mechanical energy reservoir, would have a chance to be detected as non-thermal emitters in hard X-rays with *NuSTAR*. As a result, present-day non-detection constitute by no means a severe drawback for the scenario of non-thermal high-energy emission from massive binaries.

On the other hand, the most active indicator for particle acceleration in massive binaries is synchrotron radio emission. Previous radio continuum observations of Southern massive stars allowed to measure a flux density of 0.90 ± 0.15 mJy at a wavelength of 3 cm for WR 25 (Leitherer, Chapman & Koribalski 1995; Chapman et al. 1999). Only upper limits to the flux density could be obtained at longer wavelengths. No formal determination of the nature (thermal or non-thermal) of the radio emission from WR 25 could be achieved as it was detected at only one frequency, preventing therefore any spectral index determination (Leitherer, Chapman & Koribalski 1997). However, by combining all the measurements, Dougherty & Williams (2000) gave a lower limit of $\alpha = -1.26$ to the radio spectral index of WR 25 (for a flux density dependence on the frequency defined as $S_\nu \propto \nu^\alpha$). Leitherer et al. (1995) argued that the observed 3 cm emission from WR 25 is of thermal nature by comparing the mass-loss rate of WR 25 using models given by Wright & Barlow (1975) and Panagia & Felli (1975) to those obtained by some independent techniques which assumed thermal nature of the emission. We calculated the expected thermal free-free radio emission from the WN wind following the Wright & Barlow (1975) approach, adopting the stellar parameters for a WN star wind quoted in Table 5. We also adopted an electron temperature equal to 50 per cent of the effective temperature (Drew 1990), for an effective temperature of 45 000 K (for a WN6ha classification, Crowther 2007). Our estimate of the flux density was corrected to take into account wind clumping, following the same approach as De Becker (2018). As noted by Puls et al. (2008), mass-loss determinations on the basis of radio flux density measurements should be reduced by a factor \sqrt{f} to account for clumping (where f is the clumping factor). Accordingly, a clumped stellar wind characterized by a given mass-loss rate will generate thermal radio emission with a flux density a factor $f^{2/3}$ greater than for a smooth, un-clumped configuration. We assumed a clumping factor of 4, valid for the outer parts of the

¹<https://heasarc.gsfc.nasa.gov/cgi-bin/Tools/w3pimms/w3pimms.pl>

wind where the thermal radio emission is produced (Runacres & Owocki 2002). The same procedure was followed to estimate the contribution from the O-star wind, using the wind parameters given in Table 5 and an effective temperature of about 40 000 K (Muijres et al. 2012). As a result, we estimate that the observed cumulative flux density at 3 cm for both components winds, at a distance of 2.1 kpc, should be of the order of 0.60 mJy (about 0.50 and 0.10 mJy for the WN and the O components, respectively), in fair agreement (within uncertainties) with the measurement at that wavelength. This provides some significant support to the idea that the radio measurement of WR 25 is more likely made of thermal emission only, without the need to call upon any additional non-thermal contribution to interpret the measurements. The lack of non-thermal radio emission associated to WR 25 may be attributed either to an inefficient acceleration process or to a strong free-free absorption by the WN (and to some extent O) stellar wind material. The latter process constitutes indeed a very likely turn-over process for synchrotron spectra produced by massive binaries (see e.g. De Becker et al. 2017). At this stage, no hint for particle acceleration has been revealed for WR 25.

5.3 Comparison with other systems

CygOB2#9 is another wind interacting source (O5–5.5I+O3–4III, $e = 0.71$, $P_{\text{orb}} = 858.4$ d) which shows a very clear $1/D$ variation of the X-ray flux as expected for very long period binary systems (Nazé et al. 2012). A small deviation with respect to the $1/D$ trend was observed for the hard X-ray flux at periastron. Nazé et al. (2012) suggested that this might be a consequence of the collision becoming slightly radiative around the periastron due to increased wind density. They also found that the emission was somewhat softer near periastron and suggested that radiative inhibition and/or braking became efficient when the two binary components were closest. Parkin et al. (2014) confirmed this assertion for CygOB2#9 and showed that wind acceleration is inhibited at all phases by the radiation field of the companion star. 9 Sgr (O3.5 V((f*))+O5–5.5 V((f)), $e = 0.71$, $P_{\text{orb}} = 9.1$ yr, Rauw et al. 2016) is another long period CWB with a significant deviation from the expected $1/D$ behaviour close to periastron. Among shorter period systems, some massive binaries display a clear hysteresis effect in the dependence of the X-ray emission as a function of stellar separation (Pittard & Parkin 2010). These systems include CygOB2#8a (O6If+O5.5III(f), $e = 0.21$, $P_{\text{orb}} = 21.9$ d, De Becker et al. 2006; Cazorla, Nazé & Rauw 2014); HD 152248 (O7.5(f)III+O7(f)III, $e = 0.13$, $P_{\text{orb}} = 5.816$ d, Sana et al. 2004; Rauw & Nazé 2016); HD 152218 (O9IV+O9.7V, $e = 0.26$, $P_{\text{orb}} = 5.60$ d, Sana et al. 2008; Rauw & Nazé 2016); WR 21a (WN5h+O3V, $e = 0.69$, $P_{\text{orb}} = 31.680$ d, Gosset & Nazé 2016); HD 166734 (O7.5If+O9I(f), $e = 0.618$, $P_{\text{orb}} = 34.53$ d, Nazé et al. 2017). All of these systems, with shorter orbital periods, show larger X-ray flux values around apastron than periastron with a maximum value in between apastron and periastron. But in the case of CygOB2#9 and WR 25, lower X-ray fluxes are observed at apastron than periastron with a maximum close to periastron only. This is expected as shorter period systems undergo stronger deviations from the expected $1/D$ behaviour as compared to longer period binary systems: on the one hand shorter period systems are more prone to be radiative, and on the other hand the dynamics of the shocks is more sensitive to the distortion produced by the higher orbital velocity in short period binaries (Pittard & Parkin 2010).

From the point of view of non-thermal X-ray emission, our results are in line with previous non-detection already reported for massive binaries in the Cygnus region on the basis of *INTEGRAL*

observations (De Becker et al. 2007). However, our upper limits are more constraining than those derived with *INTEGRAL* by about two orders of magnitude, thanks to the better sensitivity of *NuSTAR*. The only massive binary system with a reported non-thermal high-energy emission is Eta Car, with a hard X-ray luminosity of about 7×10^{33} erg s $^{-1}$ (Leyder, Walter & Rauw 2008, on the basis of *INTEGRAL* observations), thus significantly brighter than the upper limit we derived for WR 25. More recently, Hamaguchi et al. (2018) reported even on phase-locked non-thermal hard X-ray emission from Eta Car using *NuSTAR* data. This lends support to the idea already mentioned in Section 5.2 that only systems with a significantly high wind kinetic power (such as Eta Car) may reveal their non-thermal high-energy emission, given the sensitivity of current instruments.

6 CONCLUSIONS

We carried out a deep X-ray study of WR 25 using the archival X-ray data from *Suzaku*, *Swift*, *XMM-Newton*, and *NuSTAR*. The time basis of the observations we investigated is more than 16 yr, thus much longer than previous studies on this object.

In the soft X-ray domain below 10 keV, WR 25 is an overluminous X-ray source as a result of the colliding stellar winds of the two components of the binary system. The system is brighter before periastron passage and becomes fainter when the line of sight passes through the dense wind of the WR star in front. Since harder X-rays are less affected by the enhanced column density, this atmospheric eclipse-like effect is not observed above 2 keV. The analysis of this data shows the wind collision is more or less adiabatic but with a significant deviation with respect to the expected $1/D$ dependence of the X-ray luminosity around periastron passage. This deviation may tentatively be explained by a lower pre-shock velocity close to periastron favouring a brief switch to the radiative regime, especially if the velocity drop is enhanced by sudden radiative braking. However, this interpretation is not supported by our measurements of post-shock plasma temperatures as a function of the orbital phase, which do not present any measurable drop close to periastron. Our long-term monitoring suggests the thermal X-ray emission overlaps fairly well when orbits distant in time are compared. This indicates that WR 25 is unlikely a triple system where an additional colliding-wind region in a wider orbit may contribute to the overall thermal X-ray emission.

Above 10 keV, *NuSTAR* data do not reveal any X-ray emission attributable to a non-thermal high-energy component due to inverse Compton scattering. The upper limits we derived on the putative non-thermal X-ray flux are in the range of $7\text{--}9 \times 10^{-13}$ erg cm $^{-2}$ s $^{-1}$ (between 0.1 and 100.0 keV), which is about a factor 10 lower than the ISM corrected thermal X-ray flux we measure below 10.0 keV. Considering one may expect the non-thermal energy injection into relativistic electrons (responsible for IC scattering) is at most a few per cent of the energy radiated in thermal X-rays, the presently accessible upper limits provide only loose constraints on the non-thermal high-energy emission. A measurable IC emission could, however, be envisaged from systems characterized by quite large wind kinetic power, as in the case of Eta Car for instance. Non-thermal energy budget consideration for colliding-wind binaries show that even a significant energy injection would lead to a putative non-thermal emission below the sensitivity of *NuSTAR* for most known systems. A sensitivity improvement of at least one order of magnitude is needed to access more stringent limits on the IC emission, or even have a chance to detect it for massive star systems with the most powerful winds.

ACKNOWLEDGEMENTS

The present research work has used data obtained from the *Suzaku* satellite, a collaborative mission between the space agencies of Japan (JAXA) and the USA (NASA), as well as from the *NuSTAR* mission, a project led by the California Institute of Technology, managed by the Jet Propulsion Laboratory and funded by the National Aeronautics and Space Administration. These results are also based on the observations obtained with *XMM-Newton*, an ESA science mission with instruments and contributions directly funded by ESA Member States and NASA. We acknowledge the use of public data from the *Swift* data archive. The authors want to thank Dr. Eric Gosset for helpful discussions. We thank the anonymous referee for reading our paper and his/her useful comments.

REFERENCES

- Anders E., Grevesse N., 1989, *Geochim. Cosmochim. Acta*, 53, 197
- Arnaud K. A., 1996, in Jacoby G. H., Barnes J., eds, ASP Conf. Ser. 101, Astronomical Data Analysis Software and Systems V. Astron. Soc. Pac., San Francisco, CA, p. 17
- Cazorla C., Nazé Y., Rauw G., 2014, *A&A*, 561, A92
- Chapman J. M., Leitherer C., Koribalski B., Bouter R., Storey M., 1999, *ApJ*, 518, 890
- Crowther P. A., 2007, *ARA&A*, 45, 177
- Crowther P. A., Walborn N. R., 2011, *MNRAS*, 416, 1311
- De Becker M., 2007, *A&AR*, 14, 171
- De Becker M., 2018, *A&A*, 620, A144
- De Becker M., Raucq F., 2013, *A&A*, 558, A28
- De Becker M., Rauw G., Sana H., Pollock A. M. T., Pittard J. M., Blomme R., Stevens I. R., van Loo S., 2006, *MNRAS*, 371, 1280
- De Becker M., Rauw G., Pittard J. M., Sana H., Stevens I. R., Romero G. E., 2007, *A&A*, 472, 905
- De Becker M., Hutsemekers D., Gosset E., 2014, *New Astron.*, 29, 75
- De Becker M., Benaglia P., Romero G. E., Peri C. S., 2017, *A&A*, 600, A47
- Dougherty S. M., Williams P. M., 2000, *MNRAS*, 319, 1005
- Drew J. E., 1990, in Garmany C. D., ed., ASP Conf. Ser. Vol. 7, Properties of Hot Luminous Stars. Astron. Soc. Pac., San Francisco, p. 230
- Drissen L., Robert C., Moffat A. F. J., 1992, *ApJ*, 386, 288
- Farnier C., Walter R., Leyder J. -C., 2011, *A&A*, 526, A57
- Fierlinger K. M., Burkert A., Ntormousi E., Fierlinger P., Schartmann M., Ballone A., Krause M. G. H., Diehl R., 2016, *MNRAS*, 456, 710
- Gamen R. et al., 2006, *A&A*, 460, 777
- Gamen R. et al., 2008, *RMxAC*, 33, 91
- Gayley K. G., Owocki S. P., Cranmer S. R., 1997, *ApJ*, 475, 786
- Gosset E., 2007, Habilitation thesis. Univ. Liège, Belgium
- Gosset E., Nazé Y., 2016, *A&A*, 590, A113
- Hamaguchi K. et al., 2018, *Nat. Astron.*, 2, 731
- Harrison F. A. et al., 2013, *ApJ*, 770, 103
- Leitherer C., Chapman J. M., Koribalski B., 1995, *ApJ*, 450, 289
- Leitherer C., Chapman J. M., Koribalski B., 1997, *ApJ*, 481, 898
- Leyder J. -C., Walter R., Rauw G., 2008, *A&A*, 477, L29
- Lindgren L. et al., 2018, *A&A*, 616, A2
- Lomb N. R., 1976, *Ap&SS*, 39, 447
- Luo D., McCray R., Mac Low M. -M., 1990, *ApJ*, 362, 267
- Moffat A. F. J., 1978, *A&A*, 68, 41
- Mujires L. E., Vink J. S., de Koter A., Müller P. E., Langer N., 2012, *A&A*, 537, A37
- Nazé Y., Mahy L., Damerdjy Y., Kobulnicky H. A., Pittard J. M., Parkin E. R., Absil O., Blomme R., 2012, *A&A*, 546, A37
- Nazé Y., Gosset E., Mahy L., Parkin E. R., 2017, *A&A*, 607, A97
- Panagia N., Felli M., 1975, *A&A*, 39, 1
- Pandey J. C., Pandey S. B., Karmakar S., 2014, *ApJ*, 788, 84
- Parkin E. R., Pittard J. M., Nazé Y., Blomme R., 2014, *A&A*, 570, A10
- Pittard J. M., Parkin E. R., 2010, *MNRAS*, 403, 1657
- Pollock A. M. T., 1987, *ApJ*, 320, 283
- Pollock A. M. T., Corcoran M. F., 2006, *A&A*, 445, 1093
- Pollock A. M. T., Haberl F., Corcoran M. F., 1995, in van der Hucht K. A., Williams P. M., eds, Proc. IAU Symp. 163, Wolf-Rayet Stars: Binaries, Colliding Winds, Evolution. Kluwer, Dordrecht, p. 512
- Puls J., Vink J. S., Najarro F., 2008, *A&AR*, 16, 209
- Raassen A. J. J., van der Hucht K. A., Mewe R., Antokhin I. I., Rauw G., Vreux J.-M., Schmutz W., Güdel M., 2003, *A&A*, 402, 653
- Rauw G., Nazé Y., 2016, *Adv. Space Res.*, 58, 761
- Rauw G. et al., 2016, *A&A*, 589, A121
- Runacres M. C., Owocki S. P., 2002, *A&A*, 381, 1015
- Sana H., Stevens I. R., Gosset E., Rauw G., Vreux J. -M., 2004, *MNRAS*, 350, 809
- Sana H., Nazé Y., O'Donnell B., Rauw G., Gosset E., 2008, *New Astron.*, 13, 202
- Scargle J. D., 1982, *ApJ*, 263, 835
- Seward F. D., Chlebowski T., 1982, *ApJ*, 256, 530
- Seward F. D., Forman W. R., Giacconi R., Griffiths R. E., Harnden F. R., Jones C., Pye J. P., 1979, *ApJ*, 234, L55
- Smith N., 2014, *ARA&A*, 52, 487
- Smith L. F., Shara M. M., Moffat A. F. J., 1996, *MNRAS*, 281, 163
- Smith R. K., Brickhouse N. S., Liedahl D. A., Raymond J. C., 2001, *ApJ*, 556, L91
- Sota A., Apellániz J. M., Morrell N. I., Barbá R. H., Walborn N. R., Gamen R. C., Arias J. I., Alfaro E. J., 2014, *ApJS*, 211, 10
- Stevens I. R., Pollock A. M. T., 1994, *MNRAS*, 269, 226
- Stevens I. R., Blondin J. M., Pollock A. M. T., 1992, *ApJ*, 386, 265
- van der Hucht K. A., 2001, *New Astron. Rev.*, 45, 135
- Walborn N. R., Nichols-Bohlin J., Panek R. J., 1985, International Ultraviolet Explorer Atlas of O-type Spectra from 1200 to 1900 Å, Vol. 1155, NASA Reference Publ., USA
- Wright A. E., Barlow M. J., 1975, *MNRAS*, 170, 41

SUPPORTING INFORMATION

Supplementary data are available at [MNRAS](https://www.mnras.org) online.

[Table2.txt](#).

[Table3.txt](#).

Please note: Oxford University Press is not responsible for the content or functionality of any supporting materials supplied by the authors. Any queries (other than missing material) should be directed to the corresponding author for the article.

This paper has been typeset from a $\text{\TeX}/\text{\LaTeX}$ file prepared by the author.



Unraveling the Nature of the Deeply Embedded Wolf–Rayet Star WR 121a

Bharti Arora^{1,2} and J. C. Pandey¹

¹ Aryabhata Research Institute of Observational Sciences (ARIES), Nainital-263 002, India; bharti@aries.res.in

² School of Studies in Physics & Astrophysics, Pt. Ravishankar Shukla University, Raipur-492 010, India; jeewan@aries.res.in

Received 2019 November 28; revised 2020 February 4; accepted 2020 February 4; published 2020 March 11

Abstract

An X-ray study of the deeply embedded Wolf–Rayet star WR 121a has been carried out using long-term (spanning over ~ 12 yr) archival observations from *Chandra* and *XMM-Newton*. For the first time, a periodic variation of 4.1 days has been detected in the X-ray light curve of WR 121a. No companion is seen in a merged and exposure-corrected *Chandra* X-ray image of WR 121a, as found in other previous observations in the *J* band. The X-ray spectrum of WR 121a is well explained by a thermal plasma emission model with temperatures of 0.98 ± 0.34 keV and 3.55 ± 0.69 keV for the cool and hot components, respectively, and nonsolar abundances. The present study indicates that WR 121a is an X-ray-bright massive binary with an X-ray luminosity of $\sim 10^{34}$ erg s⁻¹, which can be explained by active wind collision between its components. Phase-locked modulations have been seen in the flux variation of WR 121a where the flux increases by a factor of ~ 1.6 from minimum to maximum in the 0.3–10.0 keV energy band. These variations could be caused by the wind collision region being eclipsed by the secondary star in a binary orbit. The winds of both components of WR 121a appear to be radiative. Radiative inhibition and radiative braking are the most likely processes that are severely affecting the wind collision in this short-period massive binary system.

Unified Astronomy Thesaurus concepts: Wolf–Rayet stars (1806); WN stars (1805); Binary stars (154); Early-type stars (430); X-ray stars (1823); Stellar winds (1636)

1. Introduction

Hot stars with spectral type from early B to O lie on the upper-left part of the Hertzsprung–Russell diagram. The evolution of these objects happens over short timescales (typically of the order of a few to 10 Myr), and they appear as Wolf–Rayet (WR) stars during the end stages of their evolution. The typical initial mass of the progenitors of WR stars is greater than $25 M_{\odot}$ (Crowther 2007). WR stars are set apart by powerful outflows of matter from their surfaces, fed by their extreme radiation fields in the form of stellar winds (Puls et al. 2008). These stellar winds travel with large terminal velocities ($1000\text{--}3000$ km s⁻¹) and lead to enormous mass-loss rates ($10^{-7}\text{--}10^{-4} M_{\odot}$ yr⁻¹). The presence of these potent outflows gives rise to many observational signatures, which can be observed over a wide range of the electromagnetic spectrum.

Massive stars in our Galaxy are born predominantly within the dense cores of giant molecular clouds. They start affecting their environment very soon after a star has formed through their intense ionizing radiation fields and strong stellar winds. W43 (=G30.8–0.2) is one such star-forming complex, which was first discovered in the radio domain by Westerhout (1958). It lies in the first galactic quadrant with galactic longitude of $30^{\circ}8$ and latitude of $-0^{\circ}2$ along the connecting point of the Scutum–Centaurus arm and the Galactic bar. The distance estimated for the W43 complex is ~ 6 kpc from the Sun, and it contains a total mass of $\sim 7.1 \times 10^6 M_{\odot}$ (Nguyen Luong et al. 2011). The core of W43 hosts a well-known giant H II region powered by an open cluster of young and luminous stars embedded in it (named in the SIMBAD³ database as the [BDC99] W43 cluster). A detailed study of this region was performed in infrared wavelength by Blum et al. (1999), and they pointed out that the W43 cluster is totally obscured in the

optical band with an estimated value of A_V of ~ 34 mag, which is equivalent to a hydrogen column density of about 6.5×10^{22} cm⁻² (Luque-Escamilla et al. 2011). Blum et al. (1999) also showed that the three brightest members of this cluster are massive stars, one of which is a WR star (named W43 #1 = WR 121a) and the other two belonging to the category of O-type giants/supergiants (named W43 #2 and #3). Using these spectral classifications, the dust extinction (A_K) to the individual object could be estimated to be close to 3.5 mag for all of them.

WR 121a was classified as WN7+abs owing to the similarity of its *K*-band spectrum with that of WR 131 (Blum et al. 1999). The “abs” component was added to the spectral type of this object because of the presence of diluted emission lines in its spectrum, which might be originating from the unseen companion of this star. In the seventh catalog of Galactic WR stars, WR 121a was placed in the category of probable binary systems and was specified as having WN7+a/OB? spectral type (van der Hucht 2001). WR 121a was seen in X-ray for the first time by Sugizaki et al. (2001) during the ASCA Galactic Plane Survey (AGPS). They detected this source (AX J184738–0156) in the 0.7–10.0 keV energy band with a $>5\sigma$ significance level, and it was unidentified at that time. Grave & Kumar (2007) also pointed out hints toward the binary nature of WR 121a using the spectro-astrometric technique. Anderson et al. (2011) investigated previously unidentified X-ray sources during the AGPS with *Chandra X-ray Observatory* data. They pointed out that the source AX J184738–0156 is coincident with WR 121a, which was discovered by Blum et al. (1999). Based on the *Chandra* and *XMM-Newton* spectral features of WR 121a, Anderson et al. (2011) suggested that this object belongs to a class of colliding wind binaries. However, they did not find any hint of variability in the data. Later, in the same year, Luque-Escamilla et al. (2011) studied the infrared and radio properties of the

³ <https://simbad.u-strasbg.fr/simbad/>

W43 cluster. They reported that two components (W43 #1a and W43 #1b) of WR 121a have been resolved with a separation of 598 ± 3 mas and a position angle of $255^\circ \pm 1^\circ$ using *J*-band observations from the ESO Very Large Telescope (VLT). Based upon the position of W43 #1b, which was found to be exactly coincident with the position of the X-ray source CXO J184736.6–015633, they have also speculated that W43 #1a is likely the WR member of the system, while W43 #1b is the O-type companion as the X-ray-emitting region generally lies closer to the star with relatively weaker wind in a colliding wind binary (CWB). Nonthermal synchrotron radiation was also found to emerge from an extended region of the cluster but with a peak offset from the position of WR 121a by $\sim 3''$ (much closer to W43 #3). As suggested by Luque-Escamilla et al. (2011), this nonthermal radio emission originates from the cumulative effect of stellar outflows from the WR and O stars in the cluster. There are several other pieces of evidence as well which associate very high-energy sources (MeV to TeV) to the surrounding star formation region of WR 121a (see Chaves et al. 2008; Acero et al. 2013; Rappoldi et al. 2016; de Wilt et al. 2017; H. E. S. S. Collaboration et al. 2018; Bulgarelli et al. 2019).

Our motivation to carry out the study of WR 121a is to explain the underlying mechanism of its X-ray emission. Speculation about this object being a massive binary system has been made many times, but a systematic confirmation is required. If it is a CWB, then it should reveal some hints of variability in its long-term observations. This information will help us classify this source among the category of other massive binaries. An observational study of this kind is necessary to constrain the stellar wind interaction features of as many objects as possible and to present some inputs to existing theoretical models that describe the physics of colliding winds to make more accurate predictions. The studies carried out previously based on a similar approach have enriched us with valuable information (e.g., De Becker et al. 2006; Oskinova & Hamann 2008; Zhekov 2012; Pandey et al. 2014; Lomax et al. 2015; Skinner et al. 2015; Arora et al. 2019, etc.). Also, WR 121a lies in a rich complex of a star-forming region toward the galactic center; therefore, it is important to know about the nature of massive stars present in that region to quantify their contribution toward different dynamical processes occurring there.

This paper is organized as follows. Section 2 presents the observations used and the data reduction methodology. The X-ray timing analysis is given in Section 3. In Section 4, we present the X-ray spectral analysis of WR 121a. Our main results are discussed in Section 5, and Section 6 presents the conclusions.

2. Observations and Data Reduction

We have made use of archival X-ray data of WR 121a observed with *Chandra* and *XMM-Newton* for a total of 10 epochs from 2004 October to 2016 July. The detailed log of observations is given in Table 1. The procedure followed to process and reduce these data sets has been mentioned in this section below.

2.1. Chandra

W43-Main cluster was observed with *Chandra* (Weisskopf et al. 2000) several times during 2016 June–July with different

configurations of the Advanced *Chandra* Imaging Spectrometer (ACIS)-I (Garmire et al. 2003). The PI of these observations was Leisa K. Townsley. WR 121a was present almost at the aimpoint of the detector for these data sets. The exposure times of these observations were in the range of 13.9–77.5 ks. The pointing R.A. and decl. of the telescope were almost the same for all of these observations, but the satellite roll pointing angle was different for the data observed in 2016 June from that of the 2016 July data sets (see Table 1). WR 121a was also observed by *Chandra*-ACIS-S in 2008 May with a relatively shorter exposure time and at a position with a larger offset from the detector aimpoint (PI: Stephen Murray).

Chandra data sets were reduced using the standard reduction techniques⁴ with CIAO version 4.11 and CALDB version 4.8.2. The level = 1 event files were reprocessed using the script CHANDRA_REPRO. In order to correct the arrival time of the X-ray photons, the barycentric correction was applied to the reprocessed, level = 2 event files using the CIAO task AXBARY. Subsequently, the background light curves for each observation were produced, and none was found to be affected significantly by high background rates.

To determine the position of WR 121a accurately in the observed X-ray frames, we have merged different *Chandra* observations. Another aim of merging different data sets is to increase the signal-to-noise ratio and search for the binary companion to WR 121a, shown in ESO-VLT *J*-band images by Luque-Escamilla et al. (2011), so that even if it is X-ray faint, it could be detected. The data sets with different pointing roll angles were merged separately. The first set is made up of observation IDs with S.N. 3–7 (set 1), and another, set 2, was made with S.N. 8–10 in Table 1. Next, we ran WAVDETECT on each exposure independently to determine the position of various sources for matching between different exposures. The observation IDs 18867 and 18887 were chosen as references to align the different images of sets 1 and 2, respectively, due to their maximum exposure time compared to others in their respective sets. We then ran WCS_MATCH between all other exposures of each set with their respective reference image using sources returned from WAVDETECT. Subsequently, the aspect solutions as well as event files were updated with WCS_UPDATE for each observation to align them with their respective reference image.

Finally, we produced two merged, exposure-corrected images for these two sets in the 0.5–7.0 keV energy band, which are shown in Figure 1. The individual exposures of a set were first reprojected onto the frame of their respective reference image and then merged using CIAO task REPROJECT_OBS. The merged images were then exposure corrected and binned into $\sim 0''.5 \times 0''.5$ pixels (1×1 binning) using the task FLUX_OBS. Further, the source detection algorithm WAVDETECT was run on the merged data, and the position of the various sources detected is shown with green ellipses in Figure 1.

WR 121a was detected at an average position of R.A. (J2000) = 18:47:36.643 and decl. (J2000) = $-01:56:33.77$. The detected position of this X-ray source is closest to the position of WR 121a as given in the 2MASS All-Sky Catalog of Point Sources (Cutri et al. 2003). No nearby X-ray source was detected toward the northeast direction of the position of WR 121a in the merged images as shown by Luque-Escamilla et al. (2011)

⁴ <http://cxc.harvard.edu/ciao/threads/>

Table 1
Log of Observations of WR 121a

Sr. No.	Satellite	Obs. ID	Obs. Date	Start Time (UT)	Detector	Livetime (ks)	Source ^a Counts	Offset ^b (')	Roll Pointing Angle (°)
1	<i>XMM-Newton</i>	0203850101	2004 Oct 22	05:48:23	PN	21.8	4303	0.136	258.74 ^c
					MOS1	25.3	2064		
					MOS2	25.3	1892		
2	<i>Chandra</i>	9612	2008 May 27	16:58:20	ACIS-S	1.6	121	0.489	121.26
3	<i>Chandra</i>	18868	2016 Jun 13	16:27:05	ACIS-I	13.9	674	0.008	144.20
4	<i>Chandra</i>	17716	2016 Jun 14	03:33:28	ACIS-I	43.5	2370	0.008	144.20
5	<i>Chandra</i>	18870	2016 Jun 16	02:09:55	ACIS-I	32.7	1746	0.008	144.20
6	<i>Chandra</i>	18867	2016 Jun 16	19:28:17	ACIS-I	47.4	2429	0.008	144.20
7	<i>Chandra</i>	18869	2016 Jun 19	07:33:11	ACIS-I	39.5	2516	0.008	144.20
8	<i>Chandra</i>	18887	2016 Jul 28	09:05:55	ACIS-I	77.5	3425	0.008	235.20
9	<i>Chandra</i>	17717	2016 Jul 29	15:25:49	ACIS-I	45.5	2559	0.008	235.20
10	<i>Chandra</i>	18888	2016 Jul 31	09:47:19	ACIS-I	45.0	2332	0.008	235.20

Notes.

^a Background-corrected net source count has been estimated in the 0.5–10.0 keV energy range for *XMM-Newton* while in 0.5–8.0 KeV for *Chandra*.

^b Offset between the WR 121a position and the telescope pointing.

^c The position angle of the telescope has been mentioned for the *XMM-Newton* data set.

in the *J*-band image. The coordinates (R.A., decl.) of W43 #1a and #1b as provided by Luque-Escamilla et al. (2011) are 18:47:36.691, –01:56:33.06 and 18:47:36.653, –01:56:33.22, respectively. The detected position of WR 121a lies closer to W43 #1b toward its south. Further, we have also checked the possible structure of the X-ray source WR 121a. A simulated *Chandra* point-spread function (PSF) image using the MARX⁵ software tool was generated following the CIAO science thread procedure as instructed. The CIAO task SRCEXTENT was used to determine the structure of the source using this simulated PSF. The X-ray source centered at the position of WR 121a was found to be point-like with 90% confidence level. The average position of the source detected nearest to WR 121a has the coordinates (R.A., decl.) 18:47:36.677, –01:56:36.72. It is at a distance of $\sim 3''.0$ toward the south of the detected position of WR 121a. The observed position of this closest source suggests that it is probably W43 #3, which is an O+O binary system (Luque-Escamilla et al. 2011). A detailed investigation is required to determine the exact identity of this object.

In order to generate the source light curves and spectra, a circular source region of radius $1''.72$ was selected with the center on WR 121a. For background estimation, another source-free circular region of radius $4''.92$ was chosen, close to the source region, on the same ACIS-CCD chip for all the data sets. The background-subtracted X-ray light curves were extracted from these regions using the task DMEXTRACT in three energy bands, viz. 0.5–8.0 keV, 0.5–2.0 keV, and 2.0–8.0 keV. The spectra and the associated response matrices (ARF and RMF) were extracted using the task SPEXTRACT. Individual spectra were grouped to have a minimum of 15 counts per energy bin.

2.2. XMM-Newton

WR 121a was observed with *XMM-Newton* (Jansen et al. 2001) for a single epoch in 2004 October (PI: David Helfand) with the European Photon Imaging Camera (EPIC; Strüder et al. 2001; Turner et al. 2001) instrument. EPIC consists of three CCDs, namely MOS1, MOS2, and PN. The EPIC data

were reduced with SAS version 17.0.0 using the latest calibration files. The SAS tasks EMCHAIN and EPCHAIN were used to produce processed event lists from the raw Observational Data Files (ODF) for the EPIC-MOS and EPIC-PN detectors, respectively. The SAS task EVSELECT was used to extract the list of event files with pattern 0–4 for PN and 0–12 for MOS data. The data were checked for pileup using the task EPATPLOT, and it was found to be unaffected by this effect. Further, the data were also checked for the presence of high background intervals, and it was found to be free from background flaring.

The X-ray light curves and spectra of WR 121a from EPIC instruments were generated from a circular region centered at the source position with a radius of $15''$ (equal to the half-power diameter). In order to ascertain that no nearby sources contaminate the X-ray products generated for WR 121a, we have also identified sources present in the field using the task EDETECT_CHAIN. The source detected closest to the position of WR 121a lies outside the selected source region of $15''$ radius at a distance of $\sim 26''$. However, *Chandra* detected three sources using observation ID 18869 (at the nearest phase) within the selected $15''$ radius of WR 121a. These sources contribute only 3.5% to the total count rate of WR 121a in the $15''$ source radius of *Chandra* observation. Further, we have converted count rates of all three *Chandra*-detected sources to the EPIC –PN of *XMM-Newton* using the WebPIMMS.⁶ The corresponding count rates from the EPIC-PN instrument for each source are equivalent to or less than the background count rate of the EPIC-PN for the present observation of 21.8 ks. This could be a probable reason why these sources were not detected by *XMM-Newton*. Under these circumstances, there is a low probability of contamination from neighboring sources to WR 121a in its $15''$ source radius in this *XMM-Newton* observation. Nevertheless, we caution readers to take the results obtained from *XMM-Newton* with care against possible contamination (if any) from neighboring sources. Background estimation was also done from a circular region of the same size at source-free regions near the source on the same CCD. Light curves extracted from the EPIC instrument were also corrected for

⁵ http://cxc.harvard.edu/ciao/threads/marx_sim/

⁶ <https://heasarc.gsfc.nasa.gov/cgi-bin/Tools/w3pimms/w3pimms.pl>

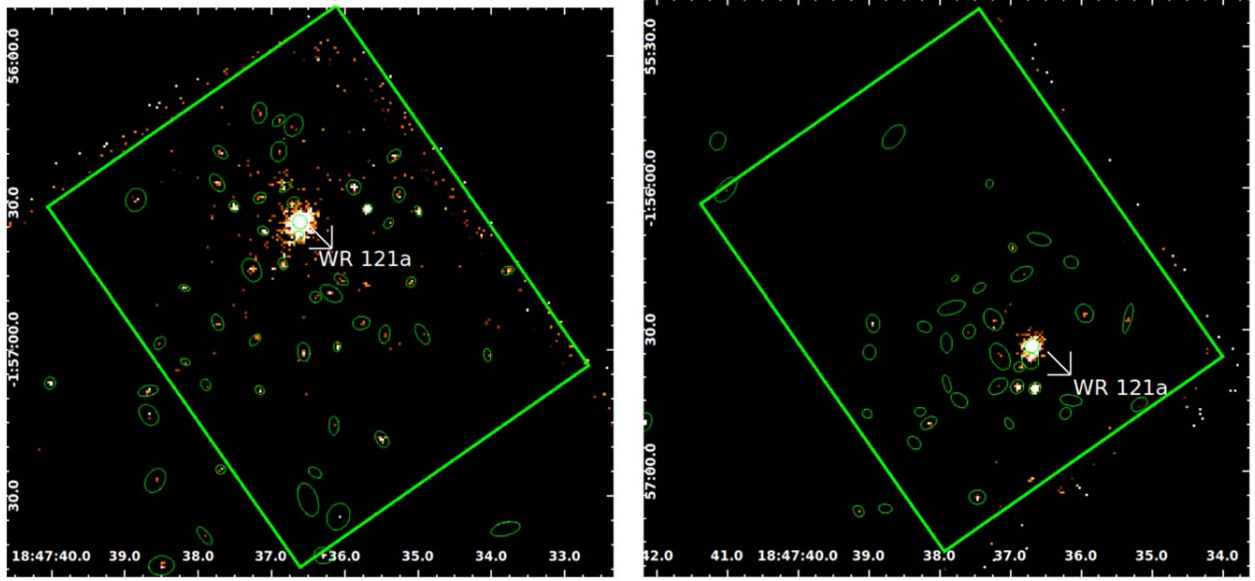


Figure 1. Merged and exposure-corrected images of W43-Main from observation IDs 18868, 17716, 18870, 18867, and 18869 (left) and 18887, 17717, and 18888 (right) of *Chandra*-ACIS-I observations in the 0.5–7.0 keV energy band. The images are binned into $\sim 0.5'' \times 0.5''$ pixels (1×1 binning). The $1.5'' \times 1.2''$ region around the center of W43-Main is marked by a rectangle. The X- and Y-axes correspond to R.A. (J2000) and decl. (J2000), respectively. The position of WR 121a as well as various other sources detected in the field is also marked in the figures.

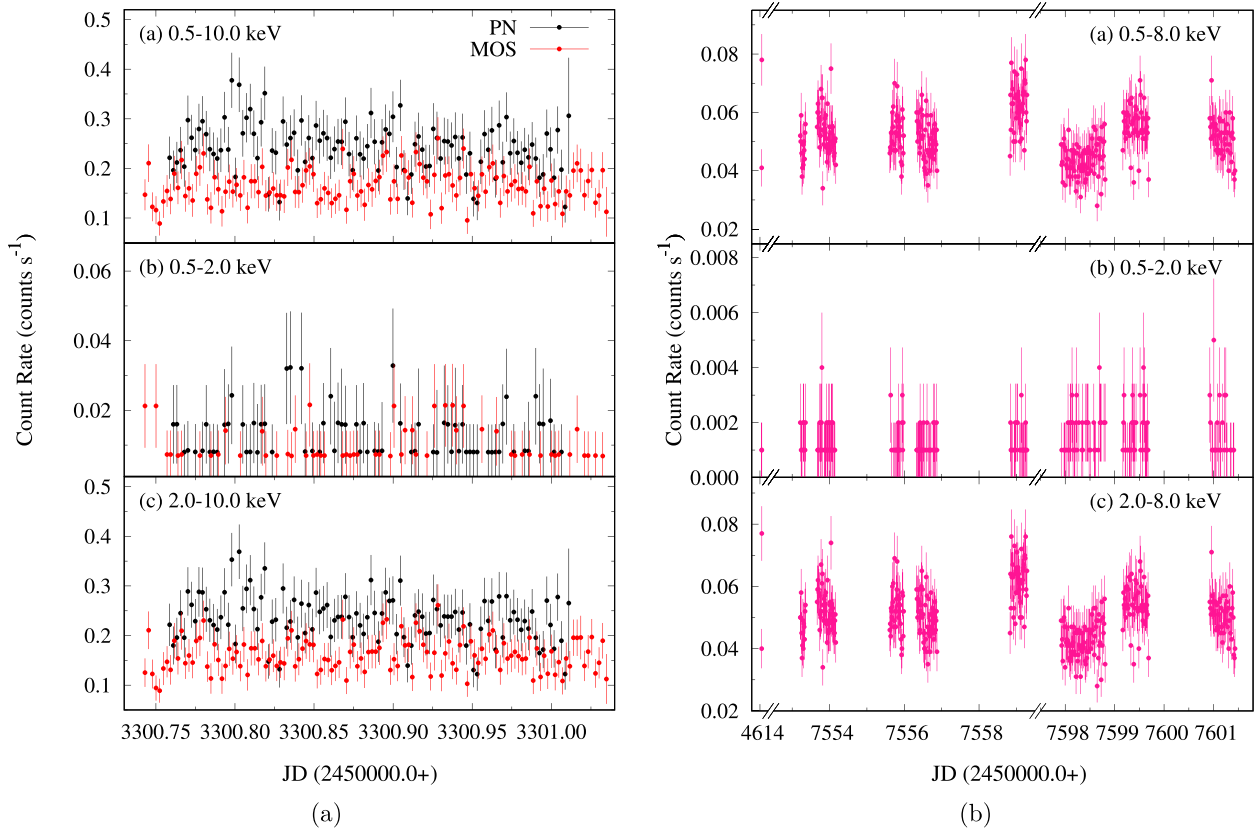


Figure 2. X-ray light curves of WR 121a in different energy bands as observed by (a) *XMM-Newton*-EPIC and (b) *Chandra*-ACIS.

good time intervals, dead time, exposure, point-spread function, and background using the SAS task EPICLCCORR. The MOS1 and MOS2 light curves were added using LCMATH of HEASOFT version 6.21. The task EVSELECT was used to generate the source as well as the background spectra. To

calibrate the flux and energy axes, the dedicated ARF and RMF response matrices were also calculated by the tasks ARFGEN and RMFGEN, respectively. Back scaling of the extracted spectra was done using the task BACKSCALE. The EPIC spectra were grouped to have minimum 15 counts per spectral bin

using GRPPHA. Further temporal and spectral analyses were performed using HEASOFT version 6.21.

3. X-Ray Timing Analysis

The background-subtracted X-ray light curves as observed by *XMM-Newton*-EPIC and *Chandra*-ACIS were produced in the three energy bands and have been shown in Figure 2. The *XMM-Newton* light curves were binned with 200 s while the *Chandra* light curves were binned with 1000 s. The smaller number of count rates in the 0.5–2.0 keV energy band is indicative of the high absorption toward the source. However, the count rate in the other two energy bands follows a similar pattern. As shown in Figure 2(b), a hint of variability is clearly seen in the 0.5–8.0 and 2.0–8.0 keV energy bands.

3.1. Search for Variability

We have examined the collective *Chandra*-ACIS light curve of WR 121a in the 0.5–8.0 keV energy range using the χ^2 test of variability defined as

$$\chi^2 = \sum_{i=1}^N \frac{(C_i - \bar{C})^2}{\sigma_i^2}, \quad (1)$$

where \bar{C} is the average count rate, C_i is the count rate of the i th observation, and σ_i is the error corresponding to C_i . The value of χ^2 obtained for the *Chandra*-ACIS light curve in the 0.5–8.0 keV energy band is 1346 for 379 degrees of freedom. The χ^2 statistic was compared against a critical value (χ_{ν}^2) for the 0.1% significance level, obtained from the χ^2 probability distribution function. The χ^2 value obtained is very large compared to the χ_{ν}^2 of 470 for 379 degrees of freedom. This confirms that WR 121a was essentially variable with a 99.9% confidence level during these observations. Light curves of the individual epoch of observations were also examined for the presence of variability using the χ^2 test. None of them was found to be significantly variable.

Further, we have performed a Fourier transform (FT) of the *Chandra*-ACIS light curve in the 0.5–8.0 keV energy band using the Lomb–Scargle periodogram (Lomb 1976; Scargle 1982; Horne & Baliunas 1986) to find any periodic signal. This is particularly effective in determining periodicities in those time series which are obtained over unequally spaced intervals of time. The top panel of Figure 3 shows the Lomb–Scargle power spectra of the *Chandra* light curve in the 0.5–8.0 keV energy band, where a peak power corresponding to a period of 4.1 ± 0.1 days was noticed. We have also calculated a false-alarm probability (see Horne & Baliunas 1986) to check the significance of detected peaks. It is shown by the horizontal line in the top panel of Figure 3. Several other peaks were also present in the Lomb–Scargle power spectra, which may be due to the aliasing. To verify whether the identified peak in the periodograms is caused by the purely periodic signal or by the sampling, we have obtained the periodogram called the data window as shown in the middle panel of Figure 3. It has been determined by setting all the data values as well as its variance to unity which were used to estimate the Lomb–Scargle periodogram of the light curve. Therefore, it simply depends upon how the sampling of the signal was performed and does not depend upon the signal itself. The identified peak in the Lomb–Scargle power spectra did not fall under the window function, indicating that the derived periodicity is real. We have also performed a

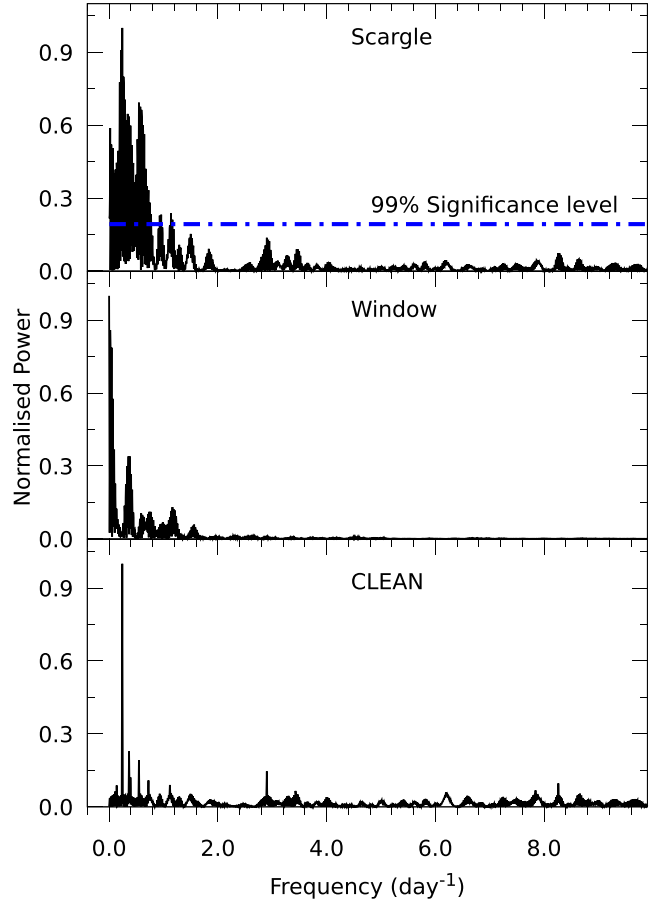


Figure 3. Lomb–Scargle (top), data window (middle), and CLEAN (bottom) power spectra of WR 121a in the 0.5–8.0 keV energy range using data from *Chandra*-ACIS. The dashed–dotted line in the top panel shows the false-alarm probability corresponding to 99% significance level.

periodogram analysis of the data using the CLEAN algorithm (Roberts et al. 1987). The CLEAN power spectrum was obtained by using a loop gain of 0.1 and the number of iterations of 100. Similar to the Lomb–Scargle periodogram, a peak corresponding to a period of 4.1 ± 0.1 days was also found in the CLEAN power spectra (see bottom panel of Figure 3).

3.2. Folded X-Ray Light Curves

X-ray light curves of WR 121a were folded using the ephemeris $\text{HJD} = 2457553.27 + 4.1E$, where zero phase corresponds to a minimum X-ray count rate as observed for the Obs. ID 18868 and are shown in Figure 4. The average count rate of an individual observation was taken as a single data point in the folded light curve as the light curve of individual observations was nonvariable. In the energy band 0.5–2.0 keV, the average count rate belonging to Obs. ID 9612 was found to be significant at the 1.4σ level, whereas average count rates for other Obs. IDs were significant at more than the 3σ level. The light curves in the individual bands show phase-locked variability. X-ray light curves in the 0.5–8.0 keV and 2.0–8.0 keV energy bands show similar behavior. In both of these energy bands, the count rate increased from phase ~ 0.0 to phase ~ 0.4 and then decreased to phase ~ 1.0 . However, in the 0.5–2.0 keV energy band, initially, the count rates increased from phase 0.0 to phase ~ 0.23 . Then, it dropped in the later

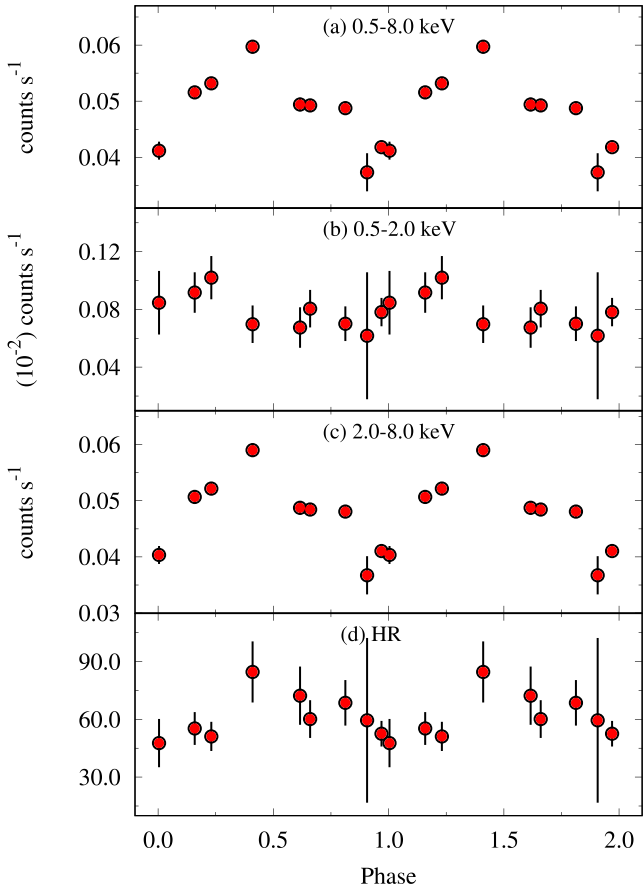


Figure 4. Folded X-ray light curves of WR 121a in different energy bands as observed by *Chandra*-ACIS.

phase and became constant up to phase ~ 1.0 within a 1σ level. The ratio of the maximum to the minimum count rates in the 0.5–8.0 keV, 0.5–2.0 keV, and 2.0–8.0 keV energy bands was found to be 1.60 ± 0.15 , 1.51 ± 0.38 , and 1.61 ± 0.15 , respectively.

The hardness ratio (HR), which is defined as the ratio of count rates in the 2.0–8.0 keV and 0.5–2.0 keV energy bands, can reveal information about the spectral variations. The HR curve as shown in panel (d) of Figure 4 displays similar behavior to that of the light curve in the 2.0–8.0 keV energy band. The maximum value of the HR near orbital phase ~ 0.4 indicates a harder spectrum relative to other orbital phases.

4. X-Ray Spectral Analysis

The *Chandra*-ACIS-I spectra of WR 121a at different orbital phases are shown in Figure 5. Several emission lines are visible in the X-ray spectrum of WR 121a. The two spectra in the Figure 5 display the difference in source flux when the two components of the binary system were ~ 0.5 phases apart. The soft-energy part is highly absorbed, as predicted for this deeply embedded object. But the system appears to be slightly brighter around phase 0.41 than phase 0.97 while this difference vanishes below ~ 4 keV. The HR curve shown in the bottom panel of Figure 4 also displays a similar feature.

The best-fit model to fit the X-ray spectrum of WR 121a was obtained using *XMM-Newton* data as the X-ray spectra from EPIC instruments have better photon statistics than the *Chandra* data (see Table 1). We even attempted to fit combined

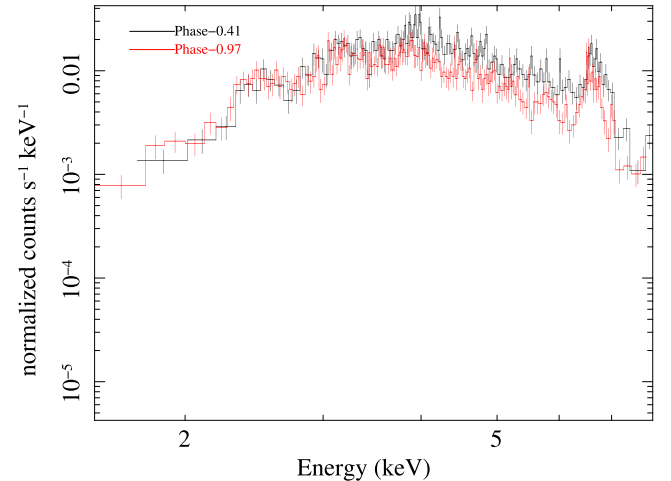


Figure 5. Comparison of *Chandra*-ACIS spectra of WR 121a at two different orbital phases. Black points correspond to orbital phase ~ 0.41 and red points refer to phase ~ 0.97 .

spectra from all nine data sets of *Chandra* to obtain the best-fit parameters. But it returned some bizarre values after spectral fitting. Therefore, we began with the fitting of MOS and PN spectra of WR 121a jointly in the 0.5–10.0 keV energy range using the models of the Astrophysical Plasma Emission Code (APEC; Smith et al. 2001) implemented in the X-ray spectral fitting package XSPEC (Arnaud 1996) version 12.9.1. We could not derive the abundances of individual elements using the *XMM-Newton* spectra of WR 121a by using the model “vapec” in XSPEC as the best-fit model returned unphysical values of abundances. Therefore, we decided to fit the spectrum with a model in the form of $\text{phabs(ism)*phabs(local)(apec+apec)}$. The components phabs(ism) and phabs(local) were used to model the interstellar absorption and the local wind absorption effects, respectively, with elemental abundances according to Anders & Grevesse (1989). The parameter $N_{\text{H}}^{\text{ISM}}$ corresponding to the model component “ phabs(ism) ” was frozen at the value of $6.5 \times 10^{22} \text{ cm}^{-2}$ (Luque-Escamilla et al. 2011). The abundances (Z) were tied for both components of “ apec ” model. All other parameters along with Z were kept free in the fitting. A χ^2 statistics was used for the spectral fitting. The best-fit model on *XMM-Newton*-EPIC spectra returned the values of two temperatures (i.e., kT_1 and kT_2) as 0.98 ± 0.34 keV and 3.55 ± 0.69 keV, respectively. However, Z was found to be 0.8 ± 0.1 times solar photospheric abundances. The blending of various emission lines in the low-resolution X-ray spectrum of WR 121a, as well as the nondetection of a few lines below 2.5 keV due to heavy absorption, leads to subsolar global abundances in the spectral fitting. Therefore, high-resolution grating spectra are needed for precise abundance determinations. The X-ray spectra of WR 121a as observed by MOS and PN along with the best-fit model are shown in Figure 6. Various spectral lines along with the continuum have been fitted properly with a reduced χ^2 of 0.99 for 351 degrees of freedom. The strong emission line has been detected between 6 and 7 keV. The centroid of the line has been estimated by fitting a Gaussian profile and found to be at 6.66 ± 0.01 keV with an equivalent width of 1.38 ± 0.15 keV, which is similar to that found by Anderson et al. (2011). This line has been identified as Fe XXV and remains unresolved in the *XMM-*

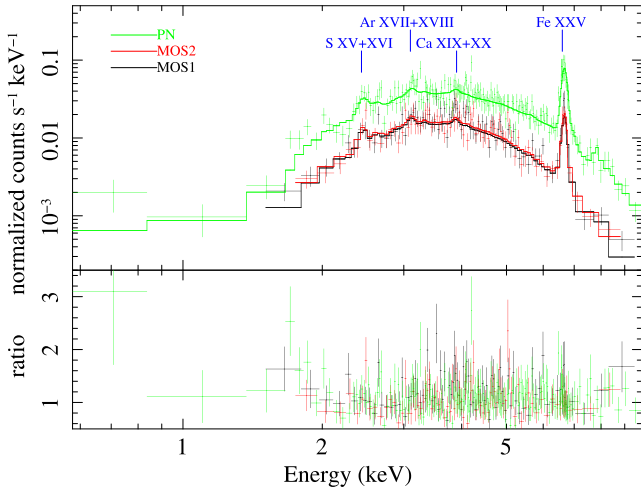


Figure 6. X-ray spectra of WR 121a as observed from MOS and PN detectors on board *XMM-Newton* along with the best-fit folded two-temperature plasma emission model (*2T APEC*). The lower panel shows the residual in terms of the ratio of the data and model.

Newton spectrum of WR 121a as *XMM-Newton* possesses an energy resolution of $\sim 135\text{--}140$ eV (FWHM) around 7 keV.

While fitting the *Chandra* spectrum from individual observations, initially we have followed the same procedure applied to fit the EPIC spectra. But the temperatures of both components over all phases were found to be consistent. Thus, *Chandra* spectra of WR 121a at different epochs of observations were fitted by keeping the parameters $N_{\text{H}}^{\text{ISM}}$, kT_1 , kT_2 , and Z fixed to the best-fit values obtained from the EPIC spectra, whereas the local equivalent H column density ($N_{\text{H}}^{\text{local}}$) along with the normalization constants of both temperature components (norm_1 and norm_2) were free parameters. Each spectrum from *Chandra-ACIS* was fitted individually except one from Obs. ID 9612 due to its poor photon counts. Therefore, it was fitted jointly with the spectrum of Obs. ID 18887, which lies at its closest phase. The ISM-corrected X-ray fluxes of WR 121a in the broad- (0.3–10.0 keV, $F_{\text{B}}^{\text{ISM}}$), soft- (0.3–2.0 keV, $F_{\text{S}}^{\text{ISM}}$), and hard-energy (2.0–10.0 keV, $F_{\text{H}}^{\text{ISM}}$) bands were derived using the model CFLUX in XSPEC. The intrinsic X-ray flux (i.e., corrected for both the galactic as well as local absorption) has also been estimated in the broad-energy ($F_{\text{B}}^{\text{int}}$) band. The values of the best-fit parameters are given in Table 2. The variation of spectral parameters with orbital phase is shown in Figure 7, where the red filled circles and green filled triangles correspond to *Chandra-ACIS* and *XMM-Newton-EPIC* data, respectively. The parameters norm_1 and $N_{\text{H}}^{\text{local}}$ were found to vary along with the orbital phase within the 1σ level, whereas the parameters norm_2 , $F_{\text{B}}^{\text{ISM}}$, and $F_{\text{H}}^{\text{ISM}}$ varied in a similar fashion. A secular variation in these parameters was noticed, they increased from phase 0.0 to a phase near ~ 0.4 , and then decreased to phase 1.0. However, the variation in $F_{\text{S}}^{\text{ISM}}$ was found to be different from that seen in $F_{\text{H}}^{\text{ISM}}$. At first, $F_{\text{S}}^{\text{ISM}}$ increased from phase 0.0 to a phase near 0.36, then suddenly dropped to phase 0.41. After this phase, $F_{\text{S}}^{\text{ISM}}$ increased again to phase ~ 0.6 then showed a decreasing trend afterward.

5. Discussion

A detailed investigation of WR 121a using long-term X-ray data from the *Chandra* and *XMM-Newton* satellites was carried

out for the first time. The X-ray spectrum of WR 121a below 10.0 keV represents the typical characteristics of an X-ray emission from an optically thin thermal plasma at temperature $> 10^6$ K (see Figure 6). These features are expected to arise from plasma heated in the wind collision region (WCR) of a colliding wind massive binary where supersonic winds from the two massive stars produce shock-heated gas (Stevens et al. 1992). This results in the production of thermal hard X-ray emission. Anderson et al. (2011) fitted *XMM-Newton* spectra of WR 121a with a simpler one-temperature Raymond & Smith (1977) model, which they attributed to the presence of a likely thermal component to the X-ray emission. The values of temperature and abundances they derived are consistent with our estimates. Analyzing the X-ray spectrum of WR 121a, Anderson et al. (2011) also suggested that it belongs to the category of CWBs. The current study verifies this fact by looking at the following details:

1. The maximum ISM-corrected X-ray luminosity ($L_{\text{X}}^{\text{ISM}}$) of WR 121a in the 0.3–10.0 keV energy band is estimated to be 1.54×10^{34} erg s $^{-1}$ (corresponding to a distance of 6 kpc), while the ISM and local wind absorption-corrected X-ray luminosity ($L_{\text{X}}^{\text{int}}$) has been estimated to be 1.70×10^{35} erg s $^{-1}$. This belongs to the typical X-ray luminosity range of $\sim 10^{32}\text{--}10^{35}$ erg s $^{-1}$ for WR + O binary systems (e.g., Gagné et al. 2012). The derived X-ray luminosity for WR 121a is also found to be more than the typical X-ray luminosity of several single WN stars (Skinner et al. 2010, 2012).
2. The presence of a strong 6.7 keV Fe XXV emission line further supports this fact as its generation requires high-temperature plasma (approximately 10^7 K), which is present in the WCR as pointed out by Raassen et al. (2003).
3. The current theoretical models about CWBs suggest that a substantial amount of X-rays originate from the collision of dense and highly supersonic stellar winds of binary components (Cherepashchuk 1976; Prilutskii & Usov 1976). However, individual stars may also have a considerable intrinsic soft X-ray emission due to the relatively less stronger shocks that develop as an outcome of line-driven instabilities (Lucy 1982; Owocki et al. 1988). Therefore, fitting the X-ray spectra of bright WR + O binaries requires at least two thermal components, which is also seen in the case of WR 121a (see Section 4). The two temperatures derived from the spectral fitting of WR 121a are well within a range typically found for massive binaries, e.g., ≤ 1 keV for cool and 2.0–4.0 keV for hot temperature components (Feldmeier et al. 1997; Rauw & Nazé 2016).
4. Another important aspect of CWBs is the phase-locked variability of the flux and/or the hardness of the X-ray emission. This depends upon the amount of absorption suffered by the X-rays through the orbit. As soft X-rays are more strongly absorbed, increasing absorption therefore reduces the observed flux but increases the hardness. Figures 4, 5, and 7 display clear signatures of variability along the orbit and hence supports CWB status of WR 121a.

The X-ray light curves of WR 121a in the 0.5–8.0 keV energy band shows periodicity corresponding to 4.1 ± 0.1 day period. For the WR+O binaries, Cherepashchuk & Karetnikov (2003) suggested that the orbits of WR+O binaries are circular

Table 2
Best-fit Parameters Obtained from *Chandra*-ACIS and *XMM-Newton*-EPIC Spectral Fitting of WR 121a

Obs. ID	Orbital Phase	norm ₁ (10 ⁻³ cm ⁻⁵)	norm ₂	$N_{\text{H}}^{\text{local}}$ (10 ²² cm ⁻²)	$F_{\text{B}}^{\text{ISM}}$	$F_{\text{S}}^{\text{ISM}}$ (10 ⁻¹² erg cm ⁻² s ⁻¹)	$F_{\text{H}}^{\text{ISM}}$	$F_{\text{B}}^{\text{int}}$	χ_{ν}^2 (dof)
0203850101	0.36	10.60 ^{+3.86} _{-3.44}	4.49 ^{+0.18} _{-0.18}	4.15 ^{+0.73} _{-0.73}	3.57 ^{+0.08} _{-0.08}	0.22 ^{+0.01} _{-0.01}	3.35 ^{+0.07} _{-0.07}	32.74 ^{+2.5} _{-2.5}	0.99 (351)
18868	0.00	14.26 ^{+17.99} _{-13.66}	3.34 ^{+0.54} _{-0.68}	7.17 ^{+3.29} _{-4.18}	2.26 ^{+0.16} _{-0.16}	0.04 ^{+0.01} _{-0.01}	2.22 ^{+0.16} _{-0.16}	39.53 ^{+8.74} _{-8.77}	1.61 (36)
17716	0.16	4.54 ^{+6.23} _{-4.20}	4.13 ^{+0.25} _{-0.26}	4.41 ^{+1.67} _{-1.54}	2.76 ^{+0.09} _{-0.09}	0.11 ^{+0.02} _{-0.02}	2.65 ^{+0.09} _{-0.09}	17.62 ^{+3.24} _{-3.25}	1.25 (120)
18870	0.62	16.22 ^a	4.44 ^{+0.30} _{-0.34}	5.07 ^{+2.94} _{-1.86}	2.72 ^{+0.11} _{-0.11}	0.07 ^{+0.01} _{-0.01}	2.65 ^{+0.11} _{-0.11}	17.10 ^{+4.08} _{-4.08}	0.99 (93)
18867	0.81	8.32 ^{+8.55} _{-6.14}	4.25 ^{+0.27} _{-0.29}	6.49 ^{+1.91} _{-1.82}	2.55 ^{+0.09} _{-0.09}	0.04 ^{+0.01} _{-0.01}	2.51 ^{+0.09} _{-0.09}	26.89 ^{+4.25} _{-4.25}	1.16 (121)
18869	0.41	11.53 ^{+10.81} _{-8.12}	5.52 ^{+0.35} _{-0.38}	7.19 ^{+1.84} _{-1.83}	3.16 ^{+0.11} _{-0.11}	0.04 ^{+0.01} _{-0.01}	3.12 ^{+0.11} _{-0.11}	36.66 ^{+5.75} _{-5.76}	1.03 (127)
17717	0.23	5.97 ^{+5.36} _{-4.26}	4.07 ^{+0.25} _{-0.26}	4.13 ^{+1.29} _{-1.31}	2.93 ^{+0.10} _{-0.09}	0.15 ^{+0.02} _{-0.02}	2.79 ^{+0.09} _{-0.09}	20.97 ^{+3.18} _{-3.19}	0.99 (130)
18888	0.66	10.42 ^a	4.21 ^{+0.25} _{-0.25}	4.68 ^{+1.81} _{-1.63}	2.68 ^{+0.09} _{-0.09}	0.08 ^{+0.01} _{-0.01}	2.59 ^{+0.09} _{-0.09}	16.27 ^{+3.25} _{-3.25}	1.00 (119)
18887	0.97	6.37 ^{+3.51} _{-2.96}	3.01 ^{+0.17} _{-0.18}	4.20 ^{+1.01} _{-0.99}	2.32 ^{+0.07} _{-0.07}	0.13 ^{+0.01} _{-0.01}	2.19 ^{+0.06} _{-0.06}	20.19 ^{+2.25} _{-2.26}	1.25 (175)
9612	0.91	6.37 ^{+3.51} _{-2.96}	3.01 ^{+0.17} _{-0.18}	4.20 ^{+1.01} _{-0.99}	2.32 ^{+0.07} _{-0.07}	0.13 ^{+0.01} _{-0.01}	2.19 ^{+0.06} _{-0.06}	20.19 ^{+2.25} _{-2.26}	1.25 (175)

Notes. Fit parameters are based on a two-temperature APEC model with two absorption components, $N_{\text{H}}^{\text{ISM}}$ (for galactic absorption) and $N_{\text{H}}^{\text{local}}$ (for local wind absorption). The fitted model has the form $\text{phabs(ism)} * \text{phabs(local)} * (\text{apec} + \text{apec})$ with $N_{\text{H}}^{\text{ISM}} = 6.5 \times 10^{22} \text{ cm}^{-2}$, the two temperatures $kT_1 = 0.98 \pm 0.34 \text{ keV}$ and $kT_2 = 3.55 \pm 0.69 \text{ keV}$, and abundance $Z = 0.8$ fixed to values derived from fitting the *XMM-Newton*-EPIC spectra of WR 121a. norm₁ and norm₂ are the normalization constants for two temperature components. $F_{\text{B}}^{\text{ISM}}$, $F_{\text{S}}^{\text{ISM}}$, and $F_{\text{H}}^{\text{ISM}}$ are the ISM-corrected X-ray fluxes of WR 121a in the broad-, soft-, and hard-energy bands, respectively. $F_{\text{B}}^{\text{int}}$ is the intrinsic X-ray flux corrected for both $N_{\text{H}}^{\text{ISM}}$ as well as $N_{\text{H}}^{\text{local}}$ in the broad-energy band. χ_{ν}^2 is the reduced χ^2 , and dof is degrees of freedom. Errors quoted on different parameters refer to 90% confidence level. The spectra obtained from Obs. IDs 18887 and 9612 have been fitted jointly.

^a Mentioned values correspond to the upper limits of the specified parameter.

if their orbital periods are less than ~ 14 days. Figure 8 shows the plot between eccentricity and the orbital period of WR+O binaries. The location of WR 121a is shown by a dashed line. From this figure, it appears that circularization occurs in the orbital period between 10 and 20 days. Thus, the orbit of WR 121a can be considered circular. Further, it appears that the circular orbit implies phase-independent wind collision between stars. If we consider a circular orbit, the phase variation in X-ray flux could be due to the change in absorption by the variable wind density along the line of sight and/or occultation of the X-ray-emitting region. Because hard X-rays are mainly generated in the WCR, the minimum $F_{\text{H}}^{\text{ISM}}$ at phase 0.0, as shown in Figure 7, could therefore be due to the eclipsing of WCR behind the O-type companion. We suggest that the WCR is eclipsed by the O star as the location of WCR is close to the O star (as explained later in this section) and the size of the O star is larger than its companion WN star. After the maximum flux at ~ 0.36 , $F_{\text{H}}^{\text{ISM}}$ decreases gradually until the orbital phase ~ 1.0 . This is also evident from the larger HR ratio as well as the harder *Chandra* X-ray spectrum of WR 121a near phase ~ 0.4 as seen in Figures 4 and 5, respectively. $F_{\text{S}}^{\text{ISM}}$ also follows a similar trend to that of $F_{\text{H}}^{\text{ISM}}$ during the orbital phases 0.0 to 0.36. But it shows instances of increased/decreased values around other orbital phases, which is exactly opposite to the trend followed by $N_{\text{H}}^{\text{local}}$. Although it is difficult to anticipate anything from the variation of $N_{\text{H}}^{\text{local}}$, owing to its large error bars, still it presents hints about our line of sight passing through stellar winds of different densities. Because $N_{\text{H}}^{\text{local}}$ mostly affects the soft X-rays, this might therefore be giving rise to orbital variations in $F_{\text{S}}^{\text{ISM}}$. The estimation of $N_{\text{H}}^{\text{local}}$ with large uncertainty, along with the sparse orbital sampling, does not allow us to accurately determine the geometry of the binary components as well as of the WCR during the orbital period. Therefore, further observations of WR 121a with dense orbital sampling in different wavebands are urgently required to understand its binary nature more deeply.

Luque-Escamilla et al. (2011) has suggested that the separation between the two components of WR 121a is

$\sim 0''.598$. Using this separation, we estimated the orbital period (P) of the WR 121a system using Kepler's third law:

$$P^2 = \frac{4\pi^2 a^3}{G(M + m)}, \quad (2)$$

where a is the linear separation corresponding to $0''.598$ angular separation at a distance of 6 kpc, G is the universal gravitational constant, and M and m represent the masses of the primary and secondary stars of the binary, respectively. Because of the similarity of the K -band spectra of WR 121a and WR 131, as noted by Blum et al. (1999), the value of M is taken to be the same as that for the WN7 star of WR 131 i.e., equal to $44 M_{\odot}$ (Hamann et al. 2019). Using several values of m for typical O-type dwarf/giant/supergiant star from Muijres et al. (2012), the value of P is found to be more than 2700 yr. Further, it is very unlikely for the faraway companions to give rise to a strong wind-wind collision to emit significant X-rays. Until now, massive binaries having an orbital period of only up to a few years have been seen to harbor X-ray-bright wind-wind collision (e.g., 9 Sgr with an orbital period of 9.1 yr; Rauw et al. 2016). Therefore, either the companion of the WN7 star in WR 121a as described by Luque-Escamilla et al. (2011) may not be correct or this may be a triple system where X-ray modulations of 4.1 days observed in this study are originating from the shorter orbital components. The radius of the WN7 star has been estimated to be $7.85 R_{\odot}$ using its typical values of luminosity as $10^{5.54} L_{\odot}$, temperature as 50,000 K (Crowther 2007), and assuming blackbody emission, whereas there is a large spread in the mass of the WN7-type star, in the range of $7-49 M_{\odot}$ (Hamann et al. 2019). The mass, and the radius of the O-type companion have been noted to lie in the range of $16.46-66.89 M_{\odot}$ and $7.39-23.11 R_{\odot}$, respectively, by considering all possible cases of dwarf/giant/supergiant star (Muijres et al. 2012). Assuming a circular orbit scenario and the above-mentioned mass estimations, the linear separation from the center of the WN7 star to the

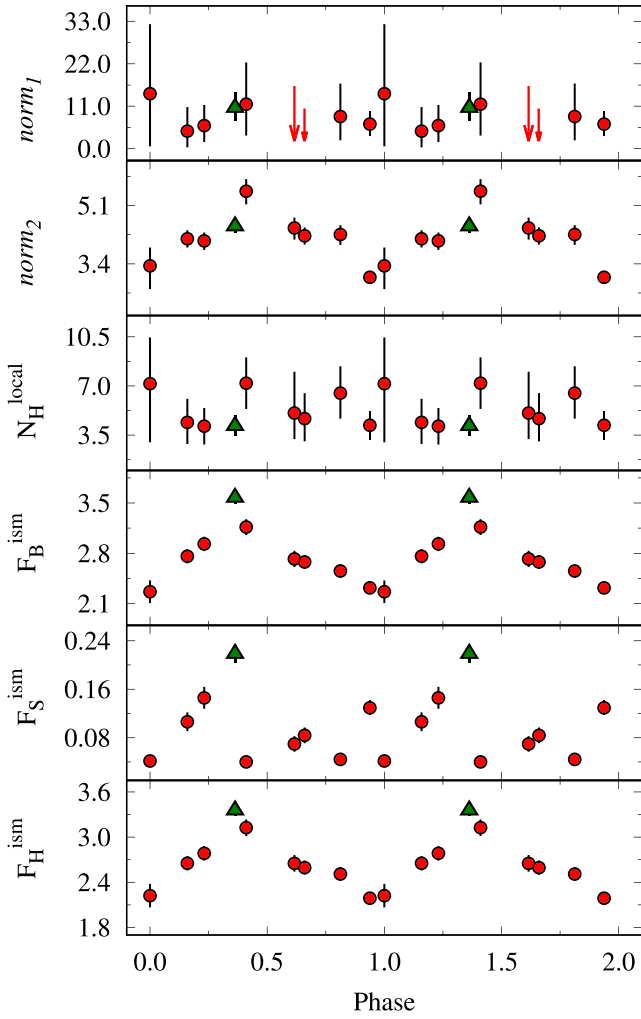


Figure 7. Spectral parameters as a function of the orbital phase of WR 121a obtained from *Chandra*-ACIS (red filled circles) and *XMM-Newton*-EPIC data (green filled triangles). Here, $norm_1$ and $norm_2$ are in units of 10^{-3} cm^{-5} , N_H^{local} in 10^{22} cm^{-2} , and F_B^{ism} , F_S^{ism} , as well as F_H^{ism} in units of $10^{-12} \text{ erg cm}^{-2} \text{ s}^{-1}$. The downward arrows in the top panel mark the upper limits of $norm_1$ for two *Chandra* Obs. IDs (see Table 2).

center of the O-type star of the WR 121a system is found to lie in the range of $30.90\text{--}52.75 R_\odot$ which translates to an angular separation of $0.024\text{--}0.041 \text{ mas}$ at a distance of 6 kpc. The WR 121a system appears to be either detached or semidetached, where the O-type star is filling its Roche lobe especially when it is in supergiant state.

To explore the nature of wind collision in WR 121a, the value of the cooling parameter (χ) at the position of wind collision in between two stars has also been estimated. χ is defined as the ratio of the cooling time of the postshock gas to the typical escape time from the shock region by Stevens et al. (1992) as

$$\chi = \frac{v^4 D}{\dot{M}}, \quad (3)$$

where v is the preshock wind velocity in units of 1000 km s^{-1} , D is the distance from the star to the shock in units of 10^7 km , and \dot{M} is the mass-loss rate in units of $10^{-7} M_\odot \text{ yr}^{-1}$. If $\chi \ll 1$, then the wind collision is considered radiative where the gas

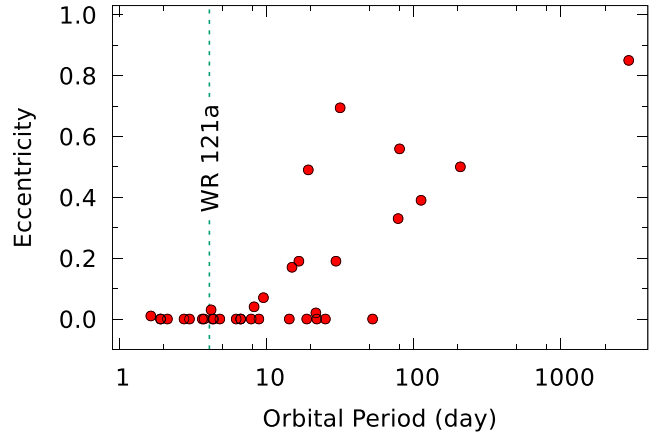


Figure 8. Plot of eccentricity as a function of the orbital period of WR+O binaries. The location of WR 121a is shown by the dashed line.

cools through rapid radiation emission. However, $\chi \geq 1$ indicates an adiabatic cooling regime. Because the spectral features of WR 121a are similar to those of WR 131, the mass of WN7 star has been adopted as $44 M_\odot$ for the rest of the analysis. However, a range of masses as mentioned above for the O-type star has been considered. Additionally, by assuming the typical values of mass-loss rate, radius, and terminal-wind velocity for a WN7 and O-type dwarf/giant/supergiant star (Crowther 2007; Muijres et al. 2012; Hamann et al. 2019), the position of the WCR was estimated, and correspondingly, the wind speeds of two stars were calculated at the WCR using the standard β -velocity law. It was seen that the stellar winds of both components of WR 121a interact at subterminal speeds, and the value of χ for a circular orbit of period 4.1 days is estimated to be $\ll 1$ for the winds of both WN and O stars at the position of the WCR. This is as expected as the shocked wind has not had enough time to escape the WCR and cool down via adiabatic expansion in short-period massive binaries; therefore, it cools rapidly through radiation emission.

The plasma temperature derived from the spectral fitting of WR 121a can also be used to estimate the preshock velocity by using the relation from Luo et al. (1990):

$$kT_{\text{sh,max}} = 1.95 \mu v_{\perp,1000}^2 \text{ keV}, \quad (4)$$

where μ is the mean mass per particle in units of the proton's rest mass, which is 1.16 for a WN star (Skinner et al. 2007) and 0.62 for an O-type star (Cassinelli et al. 2008), and $v_{\perp,1000}$ is the wind-velocity component perpendicular to the shock front in units of 1000 km s^{-1} . The average values of preshock velocities corresponding to the cool temperature (which is mostly generated due to the radiation-driven wind shock of individual components of the binary) for the WN and O components of WR 121a are found to be ~ 658 and $\sim 900 \text{ km s}^{-1}$, respectively, whereas the preshock velocities in the WCR corresponding to the hot temperature are estimated to be 1253 and 1714 km s^{-1} for the WN- and O-type components of the WR 121a system, respectively. These values are lower than the typical terminal velocity observed for the single WN- and O-type stars. This may be happening because of two reasons. One is that a wide range of temperatures is covered by the shocked plasma in WCR. The hottest plasma is expected to lie near the stagnation point while

the cooler plasma is present along the wings of the shock front. But the X-ray spectral fitting gives the average temperature prevailing in the WCR, which will be less than the maximum shock temperature mentioned in the relation (4). Another probable reason could be that if the winds of individual binary stars have not reached terminal speeds before colliding, as it is likely for short-period binaries, then the maximum shock temperature will further be decreased.

In addition to the presence of hydrodynamic shocks in the CWBs, some other effects have to be considered as well. These include alterations of the characteristics of preshock flow along with the microscopic phenomena prevailing in postshock plasma. For massive binaries, the interaction of the stellar wind with the strong radiation fields of the component stars inhibits the acceleration of one star's wind and prohibits it from reaching v_∞ (Stevens & Pollock 1994). On the other hand, another outcome of the radiation pressure of the companion star, called radiative braking, was examined by Gayley et al. (1997). This effect is most favorable for those binary configurations in which the wind momenta of the component stars are highly imbalanced, e.g., WR + O binaries. For those systems, as the dominant star wind approaches close to the surface of companion star, the radiative momentum flux of the companion star suddenly decelerates it. This process leads to significant modification of the bow shock geometry and the wider opening angle of the shock cone. In some situations, it is impossible for the companion wind to sustain the momentum of the dominant wind. Radiative braking prevents the collision of incoming wind onto the surface of the companion star for those scenarios. For example, consider the case of V444 Cyg (WR 139). It is a massive binary where the primary is a WN5 star whereas the secondary is an O6 star. They move around an orbit that is almost circular (eccentricity = 0.03), with an orbital period of ~ 4.2 days (Münch 1950; Marchenko et al. 1994). Owing to the shorter period and strong stellar winds of its components, it was suggested by Lomax et al. (2015) that both radiative braking and inhibition are required to explain the X-ray light curves of V444 Cyg. They have also estimated the shock-opening angle for wind collision in V444 Cyg, and it was found to be approximately 75° . The large value of the shock-opening angle confirmed that these two mechanisms play an important role in the stellar wind interaction of two components of this binary. Our analysis reveals that WR 121a is also similar to V444 Cyg in terms of its orbit. Their periods are almost the same. We also noticed that while calculating χ , the position of the WCR was found to coincide with the position of the secondary star in the orbit for the O-type star later than O6.0, O5.5, and O5.0 for dwarfs, giants, and supergiant, respectively. This indicates that the WCR might just be collapsing onto the surface of the secondary star of WR 121a. The ratio of the companion star radius to the binary separation is found to lie in the range of 0.22–0.51, where the WR wind is shocking onto the companion surface. To explore this scenario further, we estimated the shock-opening angle (θ) for various combinations of WN7 and an O-type star in a 4.1 day circular orbit according to Eichler & Usov (1993) as

$$\theta \simeq 2.1 \left(1 - \frac{\eta^{\frac{2}{5}}}{4} \right) \eta^{\frac{1}{5}} \quad \text{for } 10^{-4} \leq \eta \leq 1, \quad (5)$$

where $\eta = (\dot{M}v_\infty)_O / (\dot{M}v_\infty)_{WN}$ is the wind momentum ratio. It has been seen that η varies from 0.018 to 0.73 for all

combinations of WN7 primary with different O-type secondaries, and correspondingly, θ was found to lie in the range of $\sim 30^\circ$ – 84° . The larger value of η , and hence θ , observed for early O-type companions indicates that radiative braking plays an important role in the WCR of WR 121a as early O-type stars carry sufficient wind momentum to reduce the effect of the WN wind momentum. However, as the secondary star moves to the later O-type stars, the decreasing shock-opening angle points toward the scenario of either no or low radiative braking, and hence, the WN star wind overpowers the O-star wind and the shock forms at or very near the O-star surface as also inferred from χ calculations.

As mentioned in the beginning of this section, WR 121a lies toward the high end of the L_X range observed for massive binaries. Therefore, it is one of the brightest WR+O binary in X-rays. It was noted by Gagné et al. (2012) that generally all of the binary systems with WR stars having supergiant early O-type secondaries have $L_X > 10^{33} \text{ erg s}^{-1}$. However, systems with a supergiant late O-type star as a companion of the WR star have $L_X^{\text{int}} \sim 10^{33} \text{ erg s}^{-1}$, e.g., CQ Cep (WN6+O9II-Ib; Skinner et al. 2015) and WR 133 (WN5+O9I; Oskinova 2005). Because the L_X^{int} of $\sim 10^{35} \text{ erg s}^{-1}$ for WR 121a is much higher than that of WR systems with a late-type supergiant companion, we therefore anticipate that the WR 121a system may have an early O-type supergiant companion with a WN7 primary. If it is so, then radiative braking, as well as inhibition, would certainly be playing an important role in the WCR of the WR 121a system. The denser wind of the WN7 star may hide spectral features specific to an O-type companion as the bolometric luminosity of an O-type star is almost similar to that of a WN7 star (Crowther 2007; Muijres et al. 2012). The K -band spectrum of WR 121a also provides a hint about the presence of a companion, in spite of the large extinction toward the source direction (Blum et al. 1999), which suggests that the companion may be a bright object. However, detailed investigation into the matter is necessary.

An estimate of the intrinsic luminosity from the wind collision in a binary system containing WN7 and an O-type dwarf/giant/supergiant star has been made using the theoretical relations given by Usov (1992). It has already been mentioned that for all combinations of a WN7 and O-type star, the stellar winds of two binary components interact at subterminal speeds either in between the stars or on the surface of the secondary star. Therefore, WR 121a with an orbital period of ~ 4.1 days can be regarded as one of the very close or close binary systems according to Usov (1992). However, the predicted intrinsic X-ray luminosity is found to lie in the range of ~ 0.5 – $6.0 \times 10^{35} \text{ erg s}^{-1}$, from Equation (81) of Usov (1992), where the WR wind is shocking onto the companion surfaces. On the other hand, when the stellar winds interact in between the stars at subterminal speeds, the predicted X-ray luminosity belongs to the ~ 14 – $152 \times 10^{35} \text{ erg s}^{-1}$ range, which is one to two orders of magnitude larger than typically seen for CWBs and the value determined here for WR 121a. However, the value of L_X^{int} for WR 121a derived from observations is subjected to uncertainties in the distance to the source and the hydrogen column density used to correct for X-ray absorption. The imprecise estimation of mass-loss rates, as well as clumped winds, might also be possible explanations for this discrepancy (Cherepashchuk 1990).

6. Conclusions

A deep exploration of the X-ray emission from the WR star WR 121a using long-term archival data is presented in this paper. WR 121a is found to be a periodic variable in X-rays with a period of ~ 4.1 days, where a significant amount of X-rays originate from the hot plasma heated by the colliding winds. This periodic variation is also found in both soft- and hard-energy bands where the X-ray flux was increased by $\sim 53\%$ of the minimum flux in hard X-rays. These variations are explained due to the eclipsing of the WCR by the companion star in the WR 121a system. The two binary components of WR 121a could not be resolved by *Chandra*, and WR 121a was detected as a point-like source close to the position of W43 #1b. The X-ray spectra of WR 121a below 2.5 keV is heavily absorbed and have been well modeled with two-temperature plasma emission models with the temperature of the cool and hot components being 0.98 ± 0.34 and 3.55 ± 0.69 keV, respectively. The stellar winds from binary components of WR 121a interact at subterminal speeds, and the wind collision is found to be radiative. The derived values of the opening angles for WR 121a suggest that processes like radiative braking and inhibition must be significantly affecting the wind collision if the companion is an early O-type star. We encourage more multiwavelength observations of WR 121a to identify the accurate spectral types of the binary components and to explain more precisely the dynamics of winds in its WCR.

We thank the anonymous referee for the careful reading of the manuscript and giving us constructive comments and suggestions. The scientific results reported in this article are based on data obtained from the *Chandra* Data Archive along with observations obtained with *XMM-Newton*, an ESA science mission with instruments and contributions directly funded by ESA member states and NASA.

Facilities: *Chandra*, *XMM-Newton*.

Software: CIAO (v4.11); Fruscione et al. 2006), SAS (v17.0.0; Gabriel et al. 2004), XSPEC (v12.9.1; Arnaud 1996).

ORCID iDs

J. C. Pandey  <https://orcid.org/0000-0002-4331-1867>

References

- Acero, F., Ackermann, M., Ajello, M., et al. 2013, *ApJ*, **773**, 77
- Anders, E., & Grevesse, N. 1989, *GeCoA*, **53**, 197
- Anderson, G. E., Gaensler, B. M., Kaplan, D. L., et al. 2011, *ApJ*, **727**, 105
- Arnaud, K. A. 1996, in ASP Conf. Ser. 101, *Astronomical Data Analysis Software and Systems V*, ed. G. H. Jacoby & J. Barnes (San Francisco, CA: ASP), 17
- Arora, B., Pandey, J. C., & De Becker, M. 2019, *MNRAS*, **487**, 2624
- Blum, R. D., Damiani, A., & Conti, P. S. 1999, *AJ*, **117**, 1392
- Bulgarelli, A., Fioretti, V., Parmiggiani, N., et al. 2019, *A&A*, **627**, A13
- Cassinelli, J. P., Ignace, R., Waldron, W. L., et al. 2008, *ApJ*, **683**, 1052
- Chaves, R. C. G., Renaud, M., Lemoine-Goumard, M., & Goret, P. 2008, in AIP Conf. Ser. 1085, *High Energy Gamma-Ray Astronomy*, ed. F. A. Aharonian, W. Hofmann, & F. Rieger (Melville, NY: AIP), 372
- Cherepashchuk, A. M. 1976, *SvAL*, **2**, 138
- Cherepashchuk, A. M. 1990, *SvA*, **34**, 481
- Cherepashchuk, A. M., & Karetnikov, V. G. 2003, *ARep*, **47**, 38
- Crowther, P. A. 2007, *ARA&A*, **45**, 177
- Cutri, R. M., Skrutskie, M. F., van Dyk, S., et al. 2003, *2MASS All Sky Catalog of Point Sources* (Washington, DC: NASA)
- De Becker, M., Rauw, G., Sana, H., et al. 2006, *MNRAS*, **371**, 1280
- de Wilt, P., Rowell, G., Walsh, A. J., et al. 2017, *MNRAS*, **468**, 2093
- Eichler, D., & Usov, V. 1993, *ApJ*, **402**, 271
- Feldmeier, A., Puls, J., & Pauldrach, A. W. A. 1997, *A&A*, **322**, 878
- Fruscione, A., McDowell, J. C., Allen, G. E., et al. 2006, *Proc. SPIE*, **6270**, 62701V
- Gabriel, C., Denby, M., Fyfe, D. J., et al. 2004, in ASP Conf. Ser. 314, *The XMM-Newton SAS—Distributed Development and Maintenance of a Large Science Analysis System: A Critical Analysis*, ed. F. Ochsenbein, M. G. Allen, & D. Egret (San Francisco, CA: ASP), 759
- Gagné, M., Fehon, G., Savoy, M. R., et al. 2012, in ASP Conf. Ser. 465, *Proceedings of a Scientific Meeting in Honor of Anthony*, ed. F. J. Moffat & L. Drissen (San Francisco, CA: ASP), 301
- Garmire, G. P., Bautz, M. W., Ford, P. G., Nousek, J. A., & Ricker, G. R. J. 2003, *Proc. SPIE*, **4851**, 28
- Gayley, K. G., Owocki, S. P., & Cranmer, S. R. 1997, *ApJ*, **475**, 786
- Grave, J. M. C., & Kumar, M. S. N. 2007, *A&A*, **462**, L37
- Hamann, W. R., Gräfener, G., Liemann, A., et al. 2019, *A&A*, **625**, A57
- H. E. S. S. Collaboration, Abdalla, H., Abramowski, A., et al. 2018, *A&A*, **612**, A1
- Horne, J. H., & Baliunas, S. L. 1986, *ApJ*, **302**, 757
- Jansen, F., Lumb, D., Altieri, B., et al. 2001, *A&A*, **365**, L1
- Lomax, J. R., Nazé, Y., Hoffman, J. L., et al. 2015, *A&A*, **573**, A43
- Lomb, N. R. 1976, *Ap&SS*, **39**, 447
- Lucy, L. B. 1982, *ApJ*, **255**, 286
- Luo, D., McCray, R., & Mac Low, M.-M. 1990, *ApJ*, **362**, 267
- Luque-Escamilla, P. L., Muñoz-Arjonilla, A. J., Sánchez-Sutil, J. R., et al. 2011, *A&A*, **532**, A92
- Marchenko, S. V., Moffat, A. F. J., & Koenigsberger, G. 1994, *ApJ*, **422**, 810
- Muijres, L. E., Vink, J. S., de Koter, A., Müller, P. E., & Langer, N. 2012, *A&A*, **537**, A37
- Münch, G. 1950, *ApJ*, **112**, 266
- Nguyen Luong, Q., Motte, F., Schuller, F., et al. 2011, *A&A*, **529**, A41
- Oskinova, L. M. 2005, *MNRAS*, **361**, 679
- Oskinova, L. M., & Hamann, W. R. 2008, *MNRAS*, **390**, L78
- Owocki, S. P., Castor, J. I., & Rybicki, G. B. 1988, *ApJ*, **335**, 914
- Pandey, J. C., Pandey, S. B., & Karmakar, S. 2014, *ApJ*, **788**, 84
- Prilutskii, O. F., & Usov, V. V. 1976, *SvA*, **20**, 2
- Puls, J., Vink, J. S., & Najarro, F. 2008, *A&ARv*, **16**, 209
- Raassen, A. J. J., van der Hucht, K. A., Mewe, R., et al. 2003, *A&A*, **402**, 653
- Rappoldi, A., Lucarelli, F., Pittori, C., et al. 2016, *A&A*, **587**, A93
- Rauw, G., Blomme, R., Nazé, Y., et al. 2016, *A&A*, **589**, A121
- Rauw, G., & Nazé, Y. 2016, *AdSpR*, **58**, 761
- Raymond, J. C., & Smith, B. W. 1977, *ApJS*, **35**, 419
- Roberts, D. H., Lehar, J., & Dreher, J. W. 1987, *AJ*, **93**, 968
- Scargle, J. D. 1982, *ApJ*, **263**, 835
- Skinner, S. L., Zhekov, S. A., Güdel, M., & Schmutz, W. 2007, *MNRAS*, **378**, 1491
- Skinner, S. L., Zhekov, S. A., Güdel, M., & Schmutz, W. 2015, *ApJ*, **799**, 124
- Skinner, S. L., Zhekov, S. A., Güdel, M., Schmutz, W., & Sokal, K. R. 2010, *AJ*, **139**, 825
- Skinner, S. L., Zhekov, S. A., Güdel, M., Schmutz, W., & Sokal, K. R. 2012, *AJ*, **143**, 116
- Smith, R. K., Brickhouse, N. S., Liedahl, D. A., & Raymond, J. C. 2001, *ApJL*, **556**, L91
- Stevens, I. R., Blondin, J. M., & Pollock, A. M. T. 1992, *ApJ*, **386**, 265
- Stevens, I. R., & Pollock, A. M. T. 1994, *MNRAS*, **269**, 226
- Strüder, L., Briel, U., Dennerl, K., et al. 2001, *A&A*, **365**, L18
- Sugizaki, M., Mitsuda, K., Kaneda, H., et al. 2001, *ApJS*, **134**, 77
- Turner, M. J. L., Abbey, A., Arnaud, M., et al. 2001, *A&A*, **365**, L27
- Usov, V. V. 1992, *ApJ*, **389**, 635
- van der Hucht, K. A. 2001, *NewAR*, **45**, 135
- Weisskopf, M. C., Tananbaum, H. D., Van Speybroeck, L. P., & O'Dell, S. L. 2000, *Proc. SPIE*, **4012**, 2
- Westerhout, G. 1958, *BAN*, **14**, 215
- Zhekov, S. A. 2012, *MNRAS*, **422**, 1332

**ARYABHATTA RESEARCH INSTITUTE OF OBSERVATIONAL
SCIENCES, MANORA PEAK, NAINITAL**

**FIRST BELGO-INDIAN NETWORK FOR ASTRONOMY & ASTROPHYSICS
(BINA) INTERNATIONAL WORKSHOP**

15-18 NOVEMBER 2016

Certificate

This is to certify that *Ms. Bharti Arora* of Aryabhata Research Institute of Observational Sciences (ARIES), Nainital presented her research work entitled "*X-ray observations of a colliding wind binary WR 25*" during the first Belgo-Indian Network for Astronomy & Astrophysics (BINA) International Workshop on "*Instrumentation and Science with the 3.6-m DOT and 4-m ILMT telescopes*" held at ARIES, Nainital from 15 to 18 November, 2016.

Convener

Santosh

Dr. Santosh Joshi
Scientist - E
ARIES, Nainital

Scientist "E"
ARIES, Nainital.

X-ray observations of the colliding wind binary WR 25

Bharti Arora*, Jeewan Chandra Pandey

Aryabhata Research Institute of Observational Sciences (ARIES), Nainital 263002, India

Abstract: Using the archival data obtained from *Chandra* and *Suzaku* spanning over ~ 8 years, we present an analysis of a WN6h+O4f Wolf-Rayet binary, WR 25. The X-ray light curves folded over a period of ~ 208 d in the 0.3-10.0 keV energy band showed phase-locked variability where the count rates were found to be maximum near the periastron passage. The X-ray spectra of WR 25 were well explained by a two-temperature plasma model with temperatures of 0.64 ± 0.01 and 2.96 ± 0.05 keV and are consistent with previous results. The orbital phase dependent local hydrogen column density was found to be maximum just after the periastron passage, when the WN type star is in front of the O star. The hard (2.0-10.0 keV) X-ray luminosity was linearly dependent on the inverse of binary separation which confirms that WR 25 is a colliding wind binary.

1 Introduction

Wolf-Rayet (WR) stars are evolved hot massive O-type stars, close to the end of their nuclear burning phase. It is their hot stellar winds, with velocities in the range $1000-3000 \text{ km s}^{-1}$ and mass loss rates of $10^{-6}-10^{-4} M_{\odot}$ per year (Hamann et al. 2006), that characterizes the Population I WR stars. Spectroscopically, WR stars are spectacular in appearance with strong and broad emission lines ($\sim 10^3 \text{ km s}^{-1}$). X-rays from massive stars are thought to be produced in two ways: via embedded shocks in the radiatively driven winds close to the stars and in massive binaries via shocks in the wind collision zone between two stars (Stevens et al. 1992). Therefore, in a binary system, X-ray emission might display phase-locked variability, either as a consequence of the changing wind opacity along the line of sight or as a result of variable orbital separation in the case of an eccentric binary system.

WR 25 (HD 93162) is a bright ($V = 8.1$) WR star located in the Carina Nebula region and is classified as WN6h+O4f (van der Hucht 2001). Gamen et al. (2006) studied the radial velocity profile of WR 25 and suggested that it has an eccentric binary orbit ($e = 0.5$) with an orbital period of about 208 days. Also, the ratio of X-ray to bolometric luminosity of $\sim 10^{-6}$ (Seward & Chlebowski 1982) for WR 25 is an order of magnitude higher than observed for single WR stars, suggesting it to be a very likely candidate of colliding wind binary systems. Previous X-ray studies of WR 25 were done by Raassen et al. (2003), Pollock et al. (2006), and Pandey et al. (2014). These studies are based on limited X-ray observations. Therefore, in order to investigate this system deeply, we have carried out an X-ray study using the observations made by *Chandra* (Weisskopf et al. 2000) and *Suzaku* (Mitsuda et al. 2007) of WR 25.

This paper is organised as follows. Section 2 summarizes the observations. In Section 3 and 4, X-ray light curves and X-ray spectra obtained from *Suzaku* data are discussed. In Section 5, the de-

*email: bharti@aries.res.in

pendence of X-ray luminosity on binary separation is investigated followed by conclusions in Section 6.

2 Observations

WR 25 has been observed by *Suzaku* on 10 occasions from August 2005 to July 2013 taking η Carinae at the centre of the field of view of the X-ray Imaging Spectrometer (XIS). *Chandra* made one observation of WR 25 in August 2006. Collectively, the observations made by these two satellites from 2005 to 2013 at 11 different epochs were used for the present study. The data was analysed using standard packages of X-ray analysis and the latest version of calibration files for both satellites.

3 X-ray Light Curves

The background subtracted X-ray light curves, as observed by the front illuminated (FI) XIS units *viz.* XIS-0 and XIS-3 onboard *Suzaku*, were added. The X-ray light curves obtained were folded using an ephemeris $HJD = 2451598.0 + 207.85E$ (Gamen et al. 2006), where $HJD = 2451598.0$ corresponds to the zero phase in the folded light curves at the time of periastron passage. The folded X-ray light curves in the broad (0.3-10.0 keV), soft (0.3-2.0 keV) and hard (2.0-10.0 keV) energy bands are shown in panels (a), (b), and (c) of Fig. 1, respectively. The light curves in the individual energy bands show phase locked variability. The count rate drops suddenly after the periastron passage in the broad- and soft-band light curves and then increase again up to the phase ~ 0.88 . However, in the hard energy band, the count rate decreased systematically while moving away from periastron, being minimum at apastron. The hardness ratio (HR), defined as $(\text{Hard-Soft})/(\text{Hard+Soft})$ and shown in panel (d) of Fig. 1, reveals information about the spectral variations. The larger value of HR near phase ~ 0.06 indicates a harder spectrum at that phase.

4 X-ray Spectra

The X-ray spectra of WR 25 as observed by FI XIS-0 and XIS-3 were added and strong emission lines from various species were identified. The spectra were fitted using the models of Astrophysical Plasma Emission Code (APEC; Smith et al. 2001) in the X-ray spectral fitting package XSPEC. The form of model used for spectral fitting was $\text{PHABS(ISM)*PHABS(LOCAL)*(VAPEC+VAPEC)}$ and the χ^2 minimization method was applied to optimize the fit of the model to the data. While performing spectral fitting, abundances of He, C and N were fixed at 2.27, 0.15 and 5.9 respectively (obtained by Crowther et al. 1995 from optical spectra of WR 25). The temperature for both components, the interstellar medium hydrogen column density (N_H^{ISM}) as well as the abundances of various species were found to be almost constant at all the orbital phases and their average values were similar to those obtained by Pandey et al. (2014). Therefore, further spectral fitting was done by fixing these parameters to the values of Pandey et al. (2014). The local hydrogen column density (N_H^{local}) and normalization constant for both the components were kept free. The emission measures (EMs), EM_1 and EM_2 corresponding to the cool and hot plasma components, respectively, were calculated from the associated normalization parameters. The X-ray fluxes of WR 25 at different orbital phases were estimated using the CFLUX model in XSPEC in the soft (0.3–2.0 keV) and hard (2.0–10.0 keV) energy bands. The luminosities in the soft (L_S) and hard (L_H) energy bands were derived from the corresponding flux values at a source distance of 3.24 kpc (van der Hucht 2001). The variations of EM_1 , EM_2 , N_H^{local} , L_H and L_S with orbital phase are plotted in Fig. 2.

The maximum values of L_H and L_S are found near the phase of 0.88, close to the periastron passage. L_S drops suddenly to the phase ~ 0.06 where N_H^{local} is maximum. Furthermore, N_H^{local} decreases to the phase ~ 0.5 with a corresponding increase in L_S . After that, N_H^{local} as well as L_S become almost constant until L_S again increases near the periastron passage at a phase ~ 0.88 . The minimum value of L_S is obtained just after its maximum value that is 1.9 times more than the minimum value. However, L_H decreases gradually from phase ~ 0.06 to the phase ~ 0.5 and again increases to the phase ~ 0.88 , near the periastron passage. The maximum value of L_H obtained is 1.8 times more than its minimum value. The EMs, EM_1 and EM_2 corresponding to the cool and hot plasma components, are also found to be phase dependent, being minimum at phase ~ 0.5 and maximum at phase ~ 0.88 .

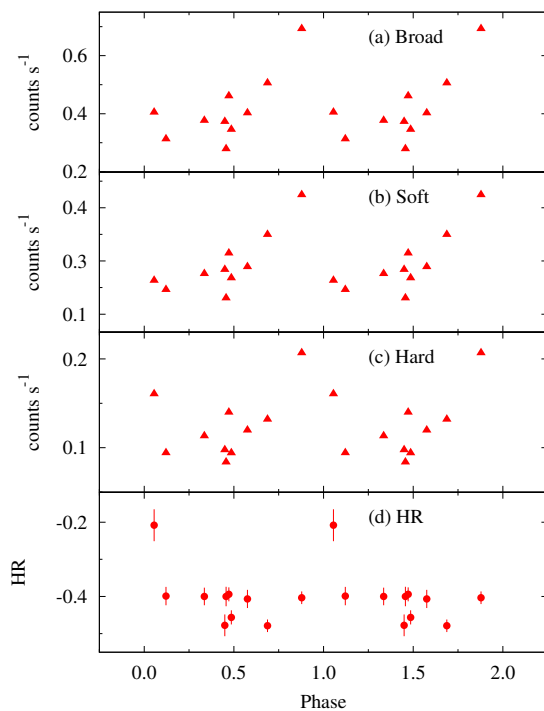


Figure 1: Top: Folded X-ray light curves in different energy bands: (a) broad (0.3-10.0 keV), (b) soft (0.3-2.0 keV), and hard (2.0-10.0 keV). Bottom: Folded values of the hardness ratio (d). In each panel, the reference epoch HJD = 2 451 598.0 corresponds to periastron passage.

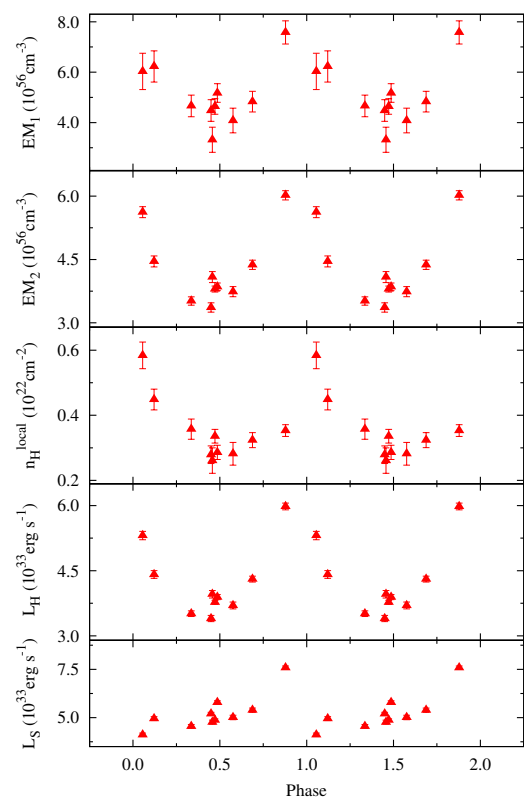


Figure 2: Spectral parameters as a function of orbital phase. In each panel, the reference epoch HJD = 2 451 598.0 corresponds to periastron passage.

5 L_X versus binary separation

The phase-locked variability in the X-ray light curves and spectral parameters of WR 25 could be a consequence of the changing binary separation in its eccentric orbit. The variation of X-ray luminosity in the soft (0.3-2.0 keV) (L_S) and hard (2.0-10.0 keV) (L_H) energy bands with the inverse of the normalized binary separation (the binary separation D normalized to the semi-major axis a), as observed by *Chandra*, *Suzaku*, *Swift* and *XMM-Newton* is shown in Fig. 3. The *Swift* and *XMM-Newton* luminosities were taken from Pandey et al. (2014). L_H varies with the inverse of D : L_H increases

when D decreases (and vice versa) but there is a deviation from a linear trend. L_S doesn't seem to follow a similar trend as L_H .

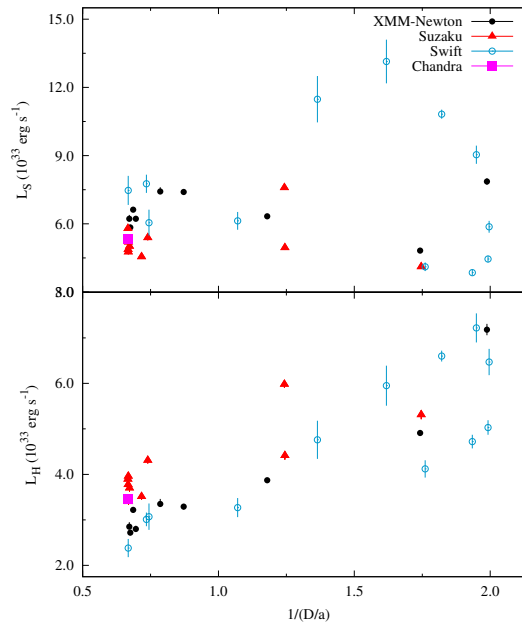


Figure 3: X-ray luminosity as a function of inverse of binary separation in soft and hard X-ray energy bands.

6 Conclusions

Using the data from *Chandra* and *Suzaku*, we have investigated the wind properties of WR 25. We found that the X-ray emission is stronger as the stars approach periastron in the 2.0-10.0 keV energy band, while the emission is stronger in the 0.2-2.0 keV energy band when they recede. A hysteresis of the intrinsic X-ray emission appears to be present when the luminosity is plotted against the binary separation. With the high-resolution spectrograph proposed for the 3.6-m Devasthal Optical Telescope (DOT), a continuous spectroscopic monitoring of colliding wind binaries could provide information about the wind properties at various orbital phases and help to get an in-depth understanding of their dynamics.

Acknowledgements

This research has made use of data obtained from the *Suzaku* satellite, a collaborative mission between the space agencies of Japan (JAXA) and the USA (NASA), as well as from Chandra Data Archive and the Chandra Source Catalog, and software provided by the Chandra X-ray Center (CXC) in the application packages CIAO, ChIPS, and Sherpa.

References

- Crowther P. A., Hillier D. J., Smith L. J. 1995, *A&A*, 293, 403
Gamen R., Gosset E., Morrell N. et al. 2006, *A&A*, 460, 777
Hamann W.-R., Gräfener G., Liermann A. 2006, *A&A*, 457, 1015
Mitsuda K., Bautz M., Inoue H. et al. 2007, *PASJ*, 59, S1-S7
Pandey J. C., Pandey S. B., Karmakar S. 2014, *ApJ*, 788, 84
Pollock A. M. T., Corcoran M. F. 2006, *A&A*, 445, 1093
Raassen A. J. J., van der Hucht K. A., Mewe R. et al. 2003, *A&A*, 402, 653
Seward F. D., Chlebowski T. 1982, *ApJ*, 256, 530
Smith R. K., Brickhouse N. S., Liedahl D. A., Raymond J. C. 2001, *ApJ*, 556, 91
Stevens I. R., Blondin J. M., Pollock A. M. T. 1992, *ApJ*, 386, 265
van der Hucht K. A. 2001, *NewAR*, 45, 135
Weisskopf M. C., Tananbaum H. D., Van Speybroeck L. P., ODeil S. L. 2000, *Proc. SPIE Conf. Ser. Vol. 4012, X-Ray Optics, Instruments, and Missions III*. SPIE, Bellingham, p. 2

OBSERVATOIRE ROYAL
DE
BELGIQUE



KONINKLIJKE STERRENWACHT
VAN
BELGIË

Avenue Circulaire 3 -1180 Bruxelles

DIRECTION OPÉRATIONNELLE
ASTRONOMIE ET
ASTROPHYSIQUE

Ringlaan 3 - 1180 Brussel

OPERATIONELE DIRECTIE
ASTRONOMIE EN
ASTROFYSICA

Name: Arora Bharti
Institute: Aryabhata Research Institute of Observational Sciences (ARIES)
Address: Manora Peak, 263002 Nainital, India
E-mail: bharti@aries.res.in

Contact persons	E-mail	Telephone	Date
P. De Cat	Peter.DeCat@oma.be	+32 2 373 67 85	07/09/20

Subject: Poster presentation at the 2nd BINA workshop

To whom it may concern,

I hereby confirm that **Arora Bharti** presented a poster presentation entitled "*Polarization study of massive binaries with ARIES-1.04 m telescope*" during the 2nd BINA workshop "BINA as an expanding international collaboration" that was held in the Meridian room of the Royal Observatory of Belgium from October 9, 2018 to October 12, 2018 (<http://aa.oma.be/18bina>).

Sincerely yours,

Peter De Cat

Polarization study of massive binaries with the ARIES-1.04 m telescope

Bharti Arora^{1*}, Jeewan Chandra Pandey¹, Arti Joshi¹, Michaël De Becker²

¹ Aryabhata Research Institute of Observational Sciences (ARIES), Nainital–263 002, India

² Space Sciences, Technologies and Astrophysics Research (STAR) Institute, University of Liège, Quartier Agora, 19c, Allée du 6 Août, B5c, B-4000 Sart Tilman, Belgium

Abstract: We present preliminary results obtained from optical (B, V, R, and I) linear polarimetric observations of the O+O massive binary DH Cep. The observations were made on six nights in 2017 with the Aries IMaging POLarimeter (AIMPOL) mounted at the back of the 1.04-m Sampurnanand Telescope of ARIES. The average intrinsic linear polarization in each of the B, V, R, and I photometric bands is found to be less than 1%. The degree of polarization as well as the polarization angle appear to be orbital phase dependent. The significant polarization variability noticed towards shorter wavelengths (i.e. B and V bands) is indicative of the asymmetric circumstellar envelope.

Keywords: Stars: early-type – Optical wavelength: stars – massive binaries: individual – DH Cep: technique – linear polarization

1 Introduction

Massive stars (O-type and Wolf-Rayet stars) are hot and luminous objects which are characterized by their huge stellar winds that lead to high mass loss rates (10^{-7} to $10^{-5} M_{\odot}$ per year). These stellar winds are dense and strongly ionized, thus abundant in free electrons and ions. This fact opens the door to a promising way of systematically probing the wind structure of these stars, namely via the polarization of starlight. In particular, free electrons can lead to linear polarization of light through single Thomson scattering in an ionized and optically thin plasma envelope co-rotating with the star (St.-Louis et al. 1988).

Most stars have a spherically symmetric circumstellar envelope, and therefore no intrinsic linear polarization is observed. However, for massive stars, which are known to have anisotropic winds as a result of the inherent instability of their line-driven mass loss, this is not the case. Further, this effect is even more significant in the case of short-period massive binaries, where the close companion acts like a probe and modulates the linear polarization as it orbits around the primary star and illuminates different regions of the electron-rich wind, e.g., CQ Cephei (WN6+O9, period–1.64 d, Drissen et al. 1986) and V444 Cyg (WN5+O6, period–4.21 d, St.-Louis et al. 1993). Some of the massive binaries have also been identified as dust producers despite their strong radiation fields. Their dust

*e-mail: bharti@aries.res.in

formation is associated with the presence of strong colliding winds. Hence, these are expected to be highly polarized due to the free-free scattering. Polarimetry is, therefore, an important observational technique to study the dust formation and stellar winds of massive binaries.

We have initiated a polarimetric observation campaign of a sample of 12 massive binaries consisting of WR+O as well as O+O systems. Here, we will present preliminary results obtained for the O+O binary DH Cep.

DH Cep (HD 215835) is a double-lined spectroscopic binary system. It is a member of the cluster NGC 7380 (age ≈ 4 Myr) and has an orbital period of 2.11 d (Lata et al. 2016). This binary star is also an X-ray source with $\log(L_X/L_{bol})$ of -6.7 in 0.3–7.5 keV energy band, perhaps attributed to colliding winds. The presence of the cool (< 1 keV) and hot (> 1.89 keV) temperature components in X-ray spectra of DH Cep could possibly be associated with the instabilities in radiation-driven wind shocks (Bhatt et al. 2010). The main orbital parameters of DH Cep are listed in Table 1.

Table 1: Basic parameters of the DH Cep system.

Parameter	DH Cep		Reference
	Primary	Secondary	
Distance (kpc)	3.2±0.4		1
V (mag.)	8.61		2
Period (d)	2.11		2
eccentricity	0		2
q (M_1/M_2)	1.15±0.02		2
T_o (HJD)	2456525.564±0.006		2
Spectral type	O5.5 V-III	O6 V-III	2
γ (km s $^{-1}$)	-46.43± 2.47	-51.95± 2.65	2
K (km s $^{-1}$)	234.81± 3.97	269.70± 4.56	2
$a \sin i$ (R_\odot)	9.79±0.17	11.24± 0.19	2
$M \sin^3 i$ (M_\odot)	15.01±0.66	13.07± 0.57	2

Notes: T_o refers to the time of the conjunction (primary in front). The parameters γ , K , $a \sin i$, and $M \sin^3 i$ denote the apparent systemic velocity, the semi-amplitude of the radial velocity curve, the projected distance from the center of the star to the center of mass of the binary system, and the minimum masses of the binary components, respectively.

References: (1) Lindegren et al. (2018), (2) Martins et al. (2017)

2 Observations and data reduction

The optical polarimetric observations of massive binaries were acquired using AIMPOL mounted at the Cassegrain focus of the 1.04-m Sampurnanad telescope of ARIES. The telescope is an RC reflector with a focal ratio of $f/13$. AIMPOL is coupled with a TK 1K×1K CCD camera which is cooled by liquid-N $_2$. AIMPOL consists of an achromatic half-wave plate (HWP) modulator and a Wollaston prism beam-splitter. Hence, for each object within the field-of-view, two images (ordinary and extra-ordinary) are formed. After alignment of the optical axis of AIMPOL with the North-South (NS) direction of the telescope, observations were done at four positions of HWP (0°, 22.5°, 45°, and 67.5°).

The standard aperture photometry technique was used to estimate fluxes of the ordinary and extraordinary beams of the target at each position of HWP with the IRAF package. Two normalized

Stokes parameters, Q and U, were calculated corresponding to the four positions of the HWP (see Rautela et al. 2004).

DH Cep was observed in the B, V, R, and I photometric bands having $\lambda_{eff} = 0.44, 0.55, 0.66,$ and $0.80 \mu\text{m}$, respectively, on the nights of 15, 16 October, and 12, 20, 21 November, as well as 14 December, 2017. Polarized and un-polarized standard stars from Schmidt et al. (1992) were also observed to perform the zero point calibration of the estimated polarization angles of the target and the correction for instrumental polarization, respectively.

3 Preliminary Results

The variations of the degree of polarization and the polarization angle of DH Cep with orbital phase are shown in Fig. 1. The phase-dependent modulations are clearly visible in these light curves, specifically, in the B and V bands. The amplitude of the degree of polarization modulations is $\sim 0.7\%$ in these bands. The variation of the polarization light curve as well as the polarization angle with wavelength point towards the intrinsically polarized nature of DH Cep. In order to estimate the interstellar linear polarization (p) towards DH Cep, we plotted p versus distance in Fig. 2. The p values of the stars lying within a 2 deg field of DH Cep were taken from Heiles (2000) while their distances were retrieved from the Gaia DR2 archive (Lindgren et al. 2018). It is anticipated that p increases linearly with the distance because of the presence of the interstellar medium. At the location of DH Cep (distance=3.24 kpc), the p value is $\sim 2\%$. Therefore, the intrinsic polarization of DH Cep is found to be less than 1% in all optical bands, but the trends of Fig. 1 will remain same.

The modulations in intrinsic polarization of DH Cep may be arising due to any of the following reasons:

1. asymmetric and extended circumstellar/binary envelopes
2. the presence of instabilities causing inhomogeneities in the massive-star winds (e.g. blobs)
3. the rotation of spots or non-radial stellar pulsations
4. modulations because of the binary motion

The variations in the polarization light curves should be strictly periodic due to reason (4) but the presence of the other three effects might also impose several intermittent periodicities (St.-Louis et al. 1987). Significant polarization variability seen in the B and V bands is probably due to the asymmetric circumstellar/binary envelopes.

Until now, the phase coverage of DH Cep is sparse. We are observing this source continuously during the current and future observation cycles to complete its polarization light curve. Our next aim is to estimate the parameters like inclination i , mass loss rate and the distribution of the scattering material around the binary stars by using available standard models (St.-Louis et al. 1987). The inclination of the binary systems can also be found from their photometric light curves. But this method requires a sufficiently high value of i to yield eclipses, either involving the stars themselves or from the phase-dependent diminution of the light from one star as it orbits in the wind of the other star. On the other hand, the phase-dependent linear polarization modulations are used extensively for the low inclination WR+O binaries. Once the value of i is known, accurate masses of the binary components can be estimated, which is difficult otherwise. This method also provides reliable mass loss rates since intrinsic polarization is largely expected to be originating from the inner parts of the wind, where the density is large. Therefore, the uncertainties of the wind parameters in its outer parts, which are involved in other techniques of finding the mass loss rates like radio-based data, do not affect the results (St.-Louis et al. 1988).

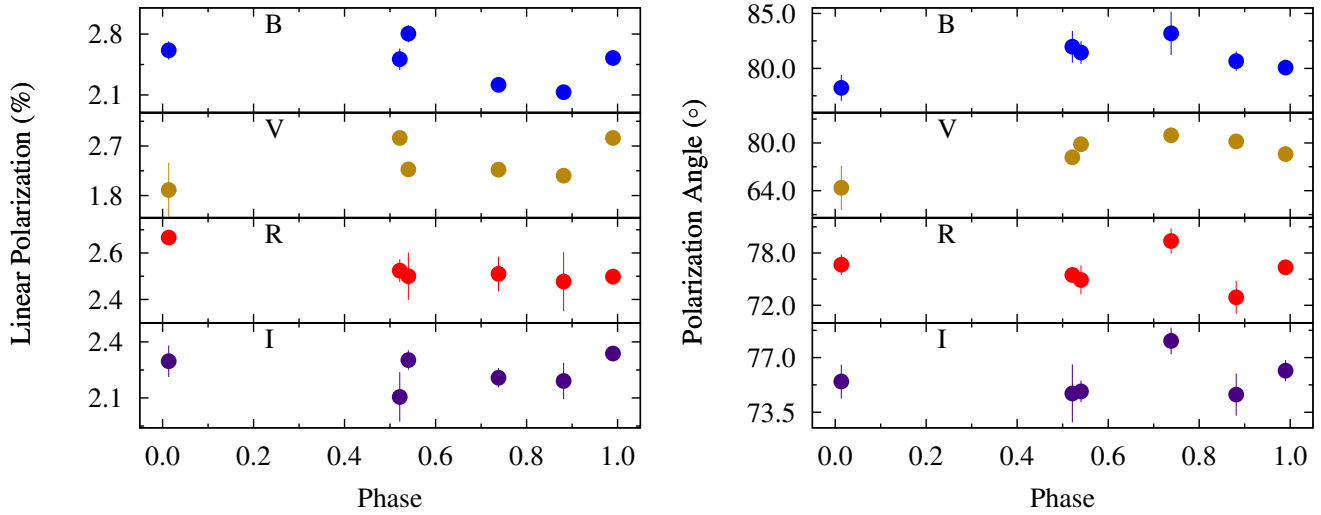


Figure 1: Linear polarization (left) and polarization angle (right) variation of DH Cep with the orbital phase in B, V, R, and I filters running from top to bottom.

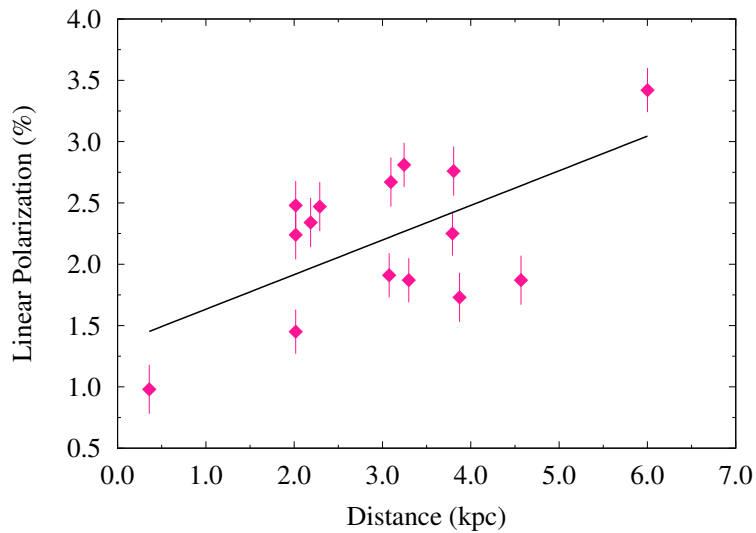


Figure 2: Linear polarization (V-band) as a function of distance towards the direction of DH Cep.

References

- Bhatt H., Pandey J. C., Kumar B. et al. 2010, *NewA*, 15, 755
 Drissen L., Moffat A. F. J., Bastien P. et al. 1986, *ApJ*, 306, 215
 Heiles C. 2000, *AJ*, 119, 923
 Lata S., Pandey A. K., Panwar N. et al. 2016, *MNRAS*, 456, 2505
 Lindegren L., Hernández J., Bombrun A. et al. 2018, *A&A*, 616, A2
 Martins F., Mahy L., Hervé A. 2017, *A&A*, 607, A82
 Rautela B. S., Joshi G. C., Pandey J. C. 2004, *BASI*, 32, 159
 Schmidt G. D., Elston R., Lupie O. L. 1992, *AJ*, 104, 1563
 St.-Louis N., Drissen L., Moffat A. F. J. et al. 1987, *ApJ*, 322, 870
 St.-Louis N., Moffat A. F. J., Drissen L. et al. 1988, *ApJ*, 330, 286
 St.-Louis N., Moffat A. F. J., Lapointe L. et al. 1993, *ApJ*, 410, 342